Dissertation thesis

Absorption power cycle with aqueous salt solution for low temperature heat utilization

Ing. Václav Novotný

Thesis submitted for the dual degree of Doctor of Philosophy to the Faculty of Mechanical Engineering, Czech Technical University in Prague; College of Engineering, National Tsing Hua University

Supervisors:
prof. Michal Kolovratník (CTU)
prof. Hung-Yin Tsai (NTHU)

February 4, 2022

Acknowledgements

I would like to express my appreciation to those who supported this work and provided me with the possibility and encouragement to pursue it. First I would like to thank my advisors, prof. Michal Kolovratnik and prof. Hung-Yin Tsai for their guidance. Additionally, I would also like to thank prof. Andreas Weiß, who has been an example of approach to research and professional life. There are also many colleagues I would like to thank for their help, consultation, and camaraderie, primarily from LORCA, UCEEB at the Czech Technical University. Jakub Maščuch has provided excellent further guidance. Jan Špale is a great colleague, friend and teammate in many projects, who is excited about the research similarly as I am. On the way through exploration APC systems I must acknowledge work performed with colleagues and previously students Dávid J. Szucs, Daniel Suchna and Jan Pavlíčko. Special thanks goes to Radka Vopatová for her invaluable help with thesis formatting.

I would like to also acknowledge the support of my family, especially Jan Novotny for assistance with measurement and power load systems. Finally, and most importantly, I want to thank my wife Jen-Mei for her continuous support during this work. Without it, I doubt that I would have reached this achievement.

Acknowledged need to be also research projects, in which were investigated some parts of this thesis:

- TJ01000090 Research of additive manufacturing (3D print) possibilities for manufacturing of expanders for low temperature decentralized energy applications, 2017-2019, Provider: Technology Agency of the Czech Republic, position: principal investigator

- BTHA-JC-2018-56 (also 8E18B012) Low cost turboexpanders for decentralized energy applications – possibilities of 3D print manufacturing from modern plastic materials, (international project), 2018-2020, Provider: The Bavarian-Czech Academic Agency, position: principal investigator
- TO01000160 Optimised expanders for small-scale distributed energy systems, (international project) 2020-2024, Provider: Technology Agency of the Czech Republic, position: principal investigator
- TJ04000326 Waste heat utilization for energy storage based on the concept of Carnot batteries, 2020-2022, Provider: Technology Agency of the Czech Republic, position: principal investigator
- EG15_019/0004976 Utilization of waste heat by its transformation into electric energy, 2015-2020, Provider: Ministry of Industry and Trade, Czech Republic, position: researcher
- LO1605 - University Centre for Energy Efficient Buildings e Sustainability Phase, National Sustainability Programme I (NPU I), Provider: Ministry of Education, Youth and Sports, Czech Republic, position: researcher
- SGS16/147/OHK2/2T/12 Design and construction of experimental rig for verification of function of advanced absorption power cycle components, 2016-2017, Provider: Grant Agency of the CTU in Prague, position: principal investigator
- SGS18/128/OHK2/2T/12 Modification and extension of experimental rig for advanced absorption power cycles, 2018-2019, Provider: Grant Agency of the CTU in Prague, position: principal investigator
- SGS21/111/OHK2/2T/12 Micro-scale turbines for distributed energy systems, 2021-2022, Provider: Grant Agency of the CTU in Prague, position: principal investigator
- NF-CZ08-OV-1-003-2015 Study of CCS Pilot Technologies for Coal Fired Power Plants in the Czech Republic. (international project) 2015-2016, Provider: Norway Grants via Ministry of Finance Czech Republic, position: researcher

Highlights

- Utilization of low temperature heat for power production combines challenges of low cycle efficiency while requiring simple and feasible technical solution
- Absorption cycle provides theoretically a thermodynamic benefit over other cycles as absorption power cycle (APC) or combined power and cooling cycle, especially owing to working fluid temperature glide
- Aqueous solution of salts as lithium bromide proposed as working fluid for specific range of low temperature (namely heat source below 120°C) and decentralized applications
- Experimental APC unit designed and built with nominal power output 370 W as probably world's first LiBr APC
- Actual operation data are related to predicted including measured temperature profiles during non-isothermal phase change, prospect of utilization efficiency reached 0.5% and cycle efficiency up to 5% with source-sink temperature difference below 70 K
- Plastic 3D printed turboexpanders experimentally verified as a feasible solution with single stage air and low pressure steam in experimental APC, unoptimized turbines reached isentropic efficiency around 15-35%

Declaration

I hereby declare that the presented thesis is my own work and that I have cited all sources of information in accordance with the Guideline for adhering to ethical principles when elaborating an academic final thesis.

I acknowledge that my thesis is subject to the rights and obligations stipulated by the Act No. 121/2000 Coll., the Copyright Act, as amended, in particular that the Czech Technical University in Prague and National Tsing Hua University have the right to conclude a license agreement on the utilization of this thesis as a school work under the provisions of Article 60 (1) of the Act.

In Prague on February 4, 2022 . . . . . .

Czech Technical University in Prague

Faculty of Mechanical Engineering

Citation of this thesis

Novotný, Václav. *Absorption power cycle with aqueous salt solution for low temperature heat utilization.* Dissertation thesis . Czech Technical University in Prague, Faculty of Mechanical Engineering, 2022.

Abstract

Absorption cycles have been proposed not only for cooling but also for power generation, such as well-known Kalina cycle utilizing water-ammonia mixture working fluid. Among advantages of this these absorption power cycles (APC) is that the multicomponent mixture working fluid can provide low exergy destruction in heat exchangers through variable temperature during phase change (temperature glide), thus achieve higher efficiency than thermodynamic cycles with constant temperature phase change. Use of other working fluids than water-ammonia has however stood aside of mainstream research. Specifically, using aqueous salt solutions, such as LiBr found in absorption chillers, is proposed in this work.

A comprehensive theoretical investigation based on pinch point analysis has shown the largest benefits of salt APC in low temperature applications (below about 120°C), mainly for waste heat recovery (WHR). The comparison has been performed with a steam Rankine cycle, a water-ammonia APC, and organic Rankine cycles (ORC) with a range of working fluids and configurations (recuperation, sub/trans-critical). Second application of APC was investigated as a combined power and cooling system, where salt solutions can bring a simplification against some water ammonia systems. For given low temperature system, again, it outperforms water-ammonia under same configuration and benchmark ORC with vapour compression chiller. The analyses include a parasitic load for heat rejection such as fans and pumps. These can have a similar power rating as the expander output at low temperature systems. Configurations explored in this work are purposefully rather simple, so that they are technically feasible. The salt-based APCs also carry environmental benefits, as the salts utilized in the working fluids are non-toxic.

According to the literature review, operation of no salt solution APC has ever been reported. Therefore, this work embarks also on an experimental task to

validate technical feasibility. World's first LiBr solution APC proof-of-concept unit has been designed and built with 20 kW nominal thermal input and sub-kW power output. The experimental works point out at specific aspects of the design with respect to the theoretical models' assumptions. Temperature glide during phase change has been measured and it is in desorber (vapour generator) significantly lower, than theoretical one. In the absorber, significant subcooling of the solution is required and absorption rate is lower than predicted. On the other hand, desorber heat transfer is higher than predicted and steam separated from the solution is naturally superheated due to boiling point elevation.

Specific part of the experimental work is then focused on turboexpander development. As the vapour is at low pressure in the APC (vacuum, typically several to dozens kPa at turbine inlet) with high volumetric flowrate, turbines are the suitable expander choice. Low temperatures further suggested use of polymer materials and additive manufacturing. Together with permanent magnet motor as a generator, this concept was proposed and shown as a cost effective solution for small turboexpanders. First, several configurations of air turbines were developed and tested. Following, a turbine with rotor and stator flow components made of nylon by powder bed fusion has been used for the APC unit. It serves as a proof of concept system, while further engineering development can improve the performance for applications in APC or combined power and cooling systems.

Need for simplicity of designed system is indeed stressed throughout the work. Slightly better theoretical performance is often practically not worth of added complexity. The overall results outline possibilities of (rather limited) actual applicability of the LiBr APC for waste heat recovery. Proposed combined power and cooling system can, however, largely help for the widespread of LiBr chillers, provide for them better capacity factor, utilize currently uneconomical low temperature heat and save primary resources.

Keywords Absorption chiller, Kalina cycle, absorption power cycle, low temperature, waste heat recovery, experimental, temperature glide, LiBr, proof of concept, expander, additive manufacturing

Abstrakt (Abstract in Czech)

Absorpční cykly byly navrženy nejen pro účely chlazení, ale také jako produkční pro výrobu práce a elektřiny. Mezi takové patří Kalinův oběh využívající směs vody a čpavku jako pracovní látku. Mezi výhody těchto termodynamických oběhů (absorption power cycle – APC) je, že vícesložková pracovní látka může poskytnout nízkou destrukci exergie ve výměnících díky proměnné teplotě fázové změny (teplotnímu skluzu), a tím dosáhnout lepší účinnosti, než tepelné oběhy s konstantní teplotou při vypařování a kondenzaci. Využití dalších pracovních látek, než pouze vody se čpavkem, ale stálo stranou zaměření většiny výzkumu. V této práci je navrženo využití vodných roztoků solí, jako např. LiBr využívaného v absorpčním chlazení. Zevrubná teoretická analýza založena termodynamických modelech s minimálním teplotním rozdílem ukázala vysoký přínos APC se solnými roztoky v nízkoteplotních aplikacích (pod cca 120°C), primárně pro využití odpadního tepla. Porovnání bylo provedeno s parním Rankinovo oběhem, APC se směsí vody a čpavku a s organickými Rankinovo oběhy (ORC) pracujícími s řadou pracovních látek a různých konfigurací (rekuperace, pod/nad-kritické). Druhou zkoumanou aplikací APC je systém kombinované výroby elektřiny a chladu, kde použití solného roztoku může přinést i zjednodušení oproti některým systémům s vodou a čpavkem. Navržený systém předčí alternativy využívající vody se čpavkem v totožné konfiguraci i referenční systém ORC s kompresorovým chlazením. V analýzách je zahrnuta vlastní spotřeba pro odvod tepla jako ventilátory a čerpadla. Pro nízkoteplotní systémy může být vlastní spotřeba v podobných hodnotách, jako samotný výkon expandéru. Konfigurace zkoumané v této práci jsou cíleně spíše jednodušší, aby byly technicky realizovatelné. Použití APC se solnými roztoky v neposlední řadě má environmentální pozitiva neboť používané soli nejsou toxické.

Na základě dostupné literatury nebyl nikdy publikován provoz APC s roztoky soli. Proto se tato práce také zaměřuje na experimentální ověření technické realizovatelnosti. Pravděpodobně první LiBr APC systém na světě byl navržen

a postaven s nominálním příkonem 20 kW tepla a výkonem pod 1 kW. Experimentální práce poukazují na specifické aspekty návrhu s ohledem na teoretické předpoklady. Teplotní skluz během změny fáze byl experiemntálně určen a v desorbéru (generátoru páry) je výrazně nižší, než je teoretický. V absorbéru je zapotřebí výrazné podchlazení roztoku a intenzita absorpce je nižší, než předpovězená. Na druhou stranu přestup tepla v desorbéru je lepší, než předpovězený, a separovaná pára z roztoku je přirozeně přehřátá díky zvýšení bodu varu v roztoku.

Specifická část experimentálních prací se poté zaměřuje na vývoj turboexpandéru. Tím, že pára v APC je na nízkém tlaku (vakuum, typicky jednotky až desítky kPa na vstupu turbíny) s vysokým objemovým tokem, turbíny jsou vhodným typem expandéru. Nízké teploty dále nabízejí použití polymerních materiálů a aditivní výroby. Spolu s motorem s permanentními magnety jako generátorem byla tato koncepce navržena a ukázána jako nákladově efektivní řešení pro malé turboexpandéry. Nejprve bylo vyvinuto a testováno několik konfigurací vzduchových turbín. Následně byla pro jednotku APC použita turbína s rotorem a průtočnými částmi statoru vyrobenými z nylonu pomocí 3D tisku. Systém slouží pro ověření možností, přičemž dalším technickým vývojem lze zlepšit parmatery pro aplikace v systémech APC nebo kombinovaných systémech výroby elektřiny a chlazení.

Potřeba jednoduchosti navrženého systému je zdůrazněna v celé práci. Mírně lepší teoretický výkon často prakticky nestojí za přidanou složitost systému. Celkové výsledky nastiňují možnosti (spíše omezené) skutečné použitelnosti LiBr APC pro využití odpadního tepla. Navržený kombinovaný systém výroby elektřiny a chlazení však může do značné míry napomoci k rozšíření LiBr absorpčních chladičů, zajistit pro ně lepší roční využití, využít jinak ekonomicky neperspektivní nízkoteplotní teplo a ušetřit primární zdroje.

Klíčová slova Absorpční chladič, Kalinův oběh, absorpční oběh, nízkoteplotní, využití odpadního tepla, experiment, teplotní skluz, LiBr, ověření technologie, expandér, 3D tisk

摘要(Abstract in Chinese)

吸收式循環不僅被提用於冷卻，也被提用於發電，例如利用水氨混合液當工作流體的Kalina循環。這些吸收式能源循環（APC）的優點之一是，多重組合的混合工作流體可以藉由相變時的溫度變化（溫度滑落）在熱交換器中提供較低熵的產生(entropy production)，從而達到比恆溫相變的熱力循環擁有更高的效率。然而，除了水-氨之外，其他工作流體的使用已被主流研究所忽視。具體來說，本工作提出使用水鹽溶液，如吸收式製冷機中的溴化鋰(LiBr)。

基於夾點分析的綜合理論調查顯示，鹽APC在低溫應用中（低於120°C）的最大好處，主要是餘熱回收（WHR）。將朗肯循環、水-氨APC及有機朗肯循環（ORC）進行了比較，有一系列的工作液體和配置（蓄熱、亞/跨臨界）。APC的第二種應用被研究爲聯合動力和冷卻系統，其中鹽溶液可以帶來對一些水氨系統的簡化。對於給定的低溫系統，在相同的配置和帶有蒸汽壓縮冷卻器的基準ORC下，它再次優於水-氨。該分析包括用於熱排斥的寄生負載，如風扇和泵。在低溫系統中，這些負載的額定功率與膨脹機的輸出功率相似。在這項工作中探討的配置故意相當簡單，以便它們在技術上是可行的。鹽基APC還具有環境效益，因爲工作液體中使用的鹽是無毒的。

根據文獻回顧，還沒有關於鹽溶液APC運行的報導。因此，這項工作也開始了一項實驗任務，以驗證技術可行性。世界上第一個溴化鋰(LiBr)溶液APC概念驗證裝置已被設計和建造，其額定熱輸入20千瓦，功率輸出低於千瓦。實驗工作指出了設計中與理論模型假設有關的具體方面。測量了相變過程中的溫度滑移，它在解吸器（蒸汽發生器）中明顯低於理論值。在吸收器中，需要對溶液進行明顯的過冷處理，吸收率比預測的要低。另一方面，解吸器的傳熱比預測的要高，由於沸點升高，從溶液中分離出來的蒸汽自然過熱。

然後，實驗工作的具體部分集中在渦輪擴張器的開發上。由於蒸汽在APC中處於低壓狀態（眞空，通常在渦輪機入口處爲幾十千帕），體積流量大，渦

輪機是合適的膨脹機選擇。低溫進一步建議使用聚合物材料和增材製造。與作爲發電機的永磁電機一起，這個概念被提出，並被證明是小型渦輪膨脹機的一個成本效益的解決方案。首先，開發和測試了幾種配置的空氣渦輪機。隨後，一個由尼龍製成的轉子和定子流動部件的渦輪機被用於APC單元。它作爲一個概念驗證系統，而進一步的工程開發可以提高APC或聯合動力和冷卻系統的應用性能。

在整個工作中，確實強調了設計系統簡單性的必要性。稍微好一點的理論性能往往不值得增加複雜性。總體結果概述了LiBr APC在餘熱回收方面的實際應用可能性（相當有限）。然而，擬議的聯合動力和冷卻系統可以在很大程度上幫助LiBr冷風機的普及，爲它們提供更好的容量係數，利用目前不經濟的低溫熱量，並節省初級資源。

Keywords 吸收式製冷，卡林那循環，吸收式動力循環，低溫，廢熱回收，實驗，溫度驟降，LiBr，概念驗證，膨脹機，3d列印

Contents

Chapter 1

Introduction

Energy transformation offers many challenges as well as opportunities. Recovery of low temperature sources as waste heat is one of the fields with a potential to bring notable benefits to the new clean and sustainable power production systems. General peculiarities of this topic are introduced after a brief overview of the author's work reaching to multiple aspects of research in energy engineering and after introducing the thesis structure.

1.1 Current energy engineering and author's research

Current world tries to focus its future in the energy field into new, renewable and environmentally friendly resources and energy savings as well as better utilization of current resources. Various topics related to these issues are subject of the author's interest and research. One of the examples is the water-energy nexus where is very active research for new membrane materials which should lead into less energy intensive fresh water production or even energy production via pressure retarded osmosis from enormous potential of salinity gradients. In this topic author has cooperated on a work [1] suggesting an innovation in membrane design and fabrication by development of methods in a quickly developing field of nano-technology. The energy market itself is quickly transforming towards distributed power generation, where micro-cogeneration could play a role. A specific analysis of micro-cogeneration for family house in the Czech Republic has been explored in another author's work [2] although current economic conditions make microcogeneration feasible only under specific circumstances [3]. One of them with a niche market appears to be somewhat larger size microcogeneration systems combusting low quality (cheap) biomass, feasible for municipalities and small industries. For them and ORC system is being developed [4, 5, 6] and within it a specific expander

of a rotary vane type [7, 8]. Alternatively there are explored novel ORC configuration for maximization of waste heat utilization from combustion engines [9]. Supposedly environmentally friendly area, somewhat controversial, but offering large scale means to mitigate climate change, is carbon capture and sequestration (CCS). In this topic, focusing mainly on integrated gasification combined cycle with CCS but also on general CCS aspects, mostly related to the Central Europe region, were conducted several works and case studies [10, 11, 12]. Energy storage is yet another topic with large potential, not only within currently already common electrochemical batteries. Large scale medium duration systems as Carnot batteries of various forms might provide another part of the puzzle of the future low carbon dispatchable resilient energy systems [13, 14, 15].

Among these various topics, waste heat recovery and low temperature heat utilization is another topic, which holds large potential for electricity production and thus saving primary energy resources. In order tackle this, a concept of absorption cycles, primarily absorption power cycles (APC) and combined power and cooling cycles, utilizing aqueous solutions of salts such as LiBr as a working fluid, is tackled in this work.

1.2 Thesis structure

The work provides first an introduction to low temperature waste heat utilization by power cycles, review of absorption power cycles, its history and current status. It includes Kalina cycles with water-ammonia mixture, as well as ones considering alternative working fluids. Reviewed applications are not only for power production, but also combined power and cooling. Focus is made on LiBr solution, commonly considered in absorption cooling, along with other aqueous salt solutions. Following are theoretical investigations, showing the potential superiority of the LiBr based cycle for low temperature waste heat recovery power cycles. Combined cycle for power and cooling is proposed as a solution to better utilize available heat by absorption system in time of fluctuating demand between power and cooling. Configuration of this cycle is also much simpler than many others proposed, which is suitable for future practical implementation. Need for simplicity of designed system is indeed stressed throughout the work. Slightly better theoretical performance is often practically not worth of added complexity.

Design and investigation of a laboratory scale proof of concept system is another part of the thesis. Several design approaches were explored. The world's first reported LiBr solution APC is described from design, commissioning and operation point of view followed by performance analysis. Specific part of the development was focused to expanders with investigation of turbines with plastic 3D printed components. Therefore, it is described in a separate chapter.

This expander design was successfully tested with air and adopted in the APC unit. The overall results, discussed at the end of experimental analyses, outline future possibilities and actual applicability of the LiBr APC for waste heat recovery and combined cooling and power applications, as well as use of developed expanders for other applications.

Due to the extent of the work, the thesis is, after the literature review, organized into multiple chapters, each with their separate description of the methods, followed by results and their discussion. Then Appendices contain information important for the work, which would however negatively affect overall readability of the thesis as a whole.

1.3 Low temperature waste heat recovery

Utilization of the low temperature and waste heat resources, especially at temperature below 200°C and in decentralized applications at the industrial sites, is field of research and development holding a large and mostly untapped potential [16, 17, 18, 19]. This is regardless a low conversion efficiency due to thermodynamic limitations of the power cycles. Effective utilization of this heat could contribute to significant savings of primary energy sources. The most versatile form of energy into which the heat can converted is electricity and the conversion methods are heat engines. Conversion to other useful temperature levels (thermally activated cooling or heat pumps) may be also considered. The conversion systems require technologies different than those used in conventional power production, either due to the very low heat source temperatures as well as due to the nature of these resources distributed across various, mostly industrial, sites with limited size (capacity) of the conversion system. These systems therefore belong among the decentralized energy systems.

As several authors point out, cycle efficiency is not the most important parameter in the waste heat recovery, but the power production is [20, 21]. To get this value, cycle efficiency is multiplied by the amount of heat that can be extracted from the heat source. In order to describe the issues of waste heat recovery and the difference between the efficiency of a thermodynamic cycle and utilization efficiency for given (waste) heat source, Figure 1.1 provides four illustrative $T - S$ diagrams of different thermodynamic cycles for conversion of the same heat source into the electricity (for illustration the entropy of the heat source is positioned and scaled so that the figure would correspond also to a $\dot{Q}$T diagram). All of these cases operate with the same pinch point, which limits the heat transfer from the heat source into the cycle, represented by the length of the red line. The ideal cycle for this case is a trilateral cycle, where the entropy production is minimal. Carnot cycle is on the other hand actually the worst one. Rankine cycle without superheating might be already better

than the Carnot cycle while a Rankine cycle operating with a zeotropic mixture and thus variable boiling temperature is one of the methods to approach the trilateral cycle.

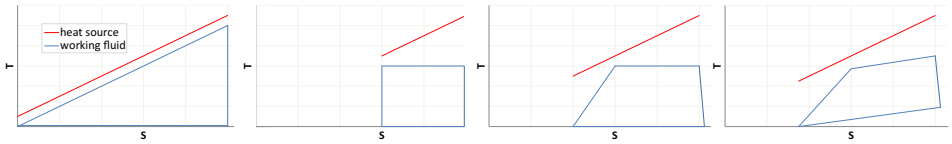

Figure 1.1: Illustration of waste heat recovery with a same value of pinch point by (from left) (a) ideal trilateral cycle, (b) Carnot cycle, (c) Rankine cycle, (d) Rankine cycle with non-isothermal boiling and condensation fluids.

Heat rejection into a secondary fluid further limits the thermodynamic limits of work that a cycle can provide. It is illustrated in following Figure 1.2, where additionally a counter-flow heat exchanger is considered along with a constant temperature rise of the heat rejection fluid (the entropy of the heat rejection fluid is again for illustration scaled and positioned to correspond to a $\dot{Q}$T diagram). All the cycle provide less work. The ideal cycle utilizing all available potential within given constraints is a representation of a Lorenz cycle (with ideally zero temperature rise corresponding to a compression from the coldest point of the cycle). Now, the previous apparent decrease of cycle work due to a temperature glide during heat rejection turned into an advantage, allowing for a higher cycle work between given temperature limits.

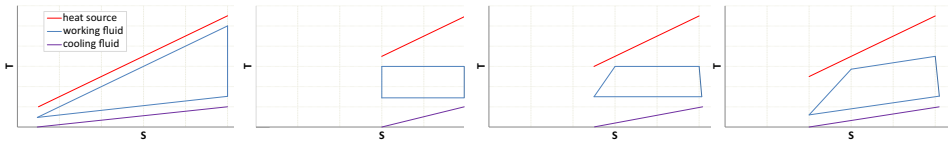

Figure 1.2: Illustration of waste heat recovery with a same value of pinch point and constant heat rejection fluid temperature rise by (from left) (a) ideal Lorenz cycle, (b) Carnot cycle, (c) Rankine cycle, (d) Rankine cycle with non-isothermal boiling and condensation fluids.

Additional aspect that need to be considered is the parasitic load, especially associated with secondary fluids for the heat input and heat rejection. This can largely affect the net power output in low temperature waste heat recovery and parasitic load can be in the order of gross power output [22, 23]. Here, on the other hand, note that the trilateral cycle from Figure 1.1a or Lorenz cycle from Figure 1.2a has also the highest amount of rejected heat.

Looking at the conversion systems for low temperature waste heat sources, standard technologies of thermal power plants and water Rankine cycle cannot be applied and scaled down due to many techno-economic limitations. Organic

Rankine cycle (ORC) with subcritical parameters is the most commonly employed technology for distributed heat to power systems. It has been widely documented and is widely used [16, 24, 25, 26]. Therefore it should be considered as a benchmark compared to which the performance of other cycles is compared to. As such is used in this work. Supercritical ORC has a high potential of increased efficiency; however, it is still mostly in the research phase [16, 27], and pilot applications are appearing only slowly [28]. A key task in ORC design is the selection of the working fluid, which takes into account not only thermodynamic behaviour but also aspects such as safety, toxicity, long-term chemical stability and cost. ORC is generally considered the best technology for utilizing heat sources in the temperature range of 200–400°C [29]. Even heat sources of temperature less than 100°C are nowadays considered for power production [30] and even commercially developed with ORC units [31]. Net efficiency of such units as well as exergetic efficiency is often deep below the thermodynamic limits of the trilateral or Lorenz cycles. It is mainly due to high exergetic losses during isothermal boiling and condensation and high parasitic load required for heat rejection. Therefore, these low temperature ORC are often too expensive with respect to efficiency and obtained power output.

In a pursuit to improve the performance for heat sources at very low temperatures, especially below 200°C, alternative options can be advantageous. Among such options are power cycles using zeotropic mixtures as working fluids and particularly absorption power cycles, foremost of which is the Kalina cycle, with a handful of installations around the world. Several variations of absorption power cycles (APCs) exist also; they are discussed separately in the next section. Other thermodynamic cycles for low-temperature heat sources discussed next are not yet in commercial use. An indirectly heated Brayton cycle results in very low efficiency, especially at low temperatures. There have been studies of an air bottoming cycle, such as in [32], but the temperature of the heat source used is still relatively high, and the efficiency is low. An interesting, but as-yet undeveloped technology is the inverted Brayton cycle [33], which should be able to utilize waste heat at lower temperatures with good efficiency in real devices. In this cycle, a clean hot gas at ambient pressure is first expanded in a turbine; the heat is then rejected, after which the gas is compressed back to ambient pressure to be discharged. Applications of the Stirling cycle are at very low unit outputs and high cost; the Stirling engine has not been widely commercialized for low-temperature heat sources [33, 34]. Furthermore, isothermal heat input was discussed as often not feasible. A trilateral cycle is a cycle with expansion starting from a saturated liquid state rather than a vapour phase, giving a much higher theoretical efficiency compared with the ORC, as it was shown above. However, it is hampered by a lack of research on the two phase expander [27, 35]. Finally, technologies for direct conversion, such as thermoelectric, have many difficulties with perfor-

mance and in commercialization while others as piezoelectric, thermionic or thermo-photovoltaic generation, are largely in the fundamental research phase [16].

Low temperature systems might be also suitable for cooling cycles such as absorption, adsorption or desiccant chillers, which operate in that region [36, 37, 38]. Some systems offer a transformation of primary energy resources for the generation of more than one product, which can be viewed as more beneficial as it may increase the utilization of the resources and it may sometimes help to adjust the products of the system depending on the current needs of the customers. Cogeneration of electricity with a by-product of heat (Combined Heat and Power – "CHP") is a well-known concept. Increasing interest is, however, also paid to other options of cogeneration, such as combined cooling and power ("CCP"), or trigeneration - cooling, heat and power ("CCHP"). Electricity, heat and cold energy are the three products that represent different significance depending on the season, ambient temperature and other factors, while all are often consumed at the same place. Combination of power production and cooling in appears to be a suitable and beneficial step.

Chapter 2

Absorption power cycles

In this chapter is at first introduced the concept of absorption power cycles (APC). Following is the review of APC with primary focus on alternative working fluids than ammonia water mixture, with the largest focus on aqueous salt solutions. This review as a one of a kind tracing origins of consideration of alternative APC working fluids and many previously overseen works has been first published in author's work. As the APC can be combined with regular absorption chiller into cogeneration systems for power and cooling, such systems are introduced as well with a developed comprehensive classification. Following section brings a summary of working fluids consideration.

2.1 Absorption power cycle concept

In a typical Rankine power cycle, boiling and condensation both take place at a constant temperature specific to the pressure of the working fluid. The turbine outlet pressure for the given fluid is controlled by the heat rejection temperature. When the working fluid is a (zeotropic) mixture of two components with different boiling points, the actual boiling point of the mixture becomes a function of component concentration. Reports have been made on cycles utilizing this feature simply to obtain a temperature profile better matched to the heat source [39]. Apart from these uses, the absorption process takes advantage of the different temperature levels at which the absorbent interfaces with the absorbed fluid at the same pressure. In cooling cycles, this effect makes it possible to achieve a very low evaporation pressure (and temperature) of a liquid while keeping the heat rejection temperature at a reasonable level without the need of compressor. Similarly, in a power cycle, this is used to lower the turbine exhaust pressure while maintaining the heat rejection temperature. The following section provides a classification of APCs based on their working fluids. Typical working fluids include a water-ammonia mixture and aqueous salt solutions (mainly LiBr), but other concepts have emerged

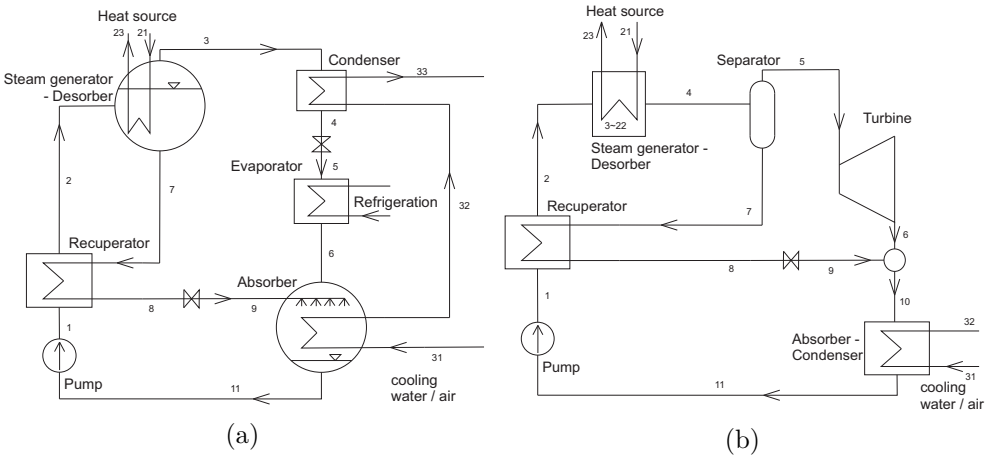

Figure 2.1: Process flow diagrams of a) simple absorption cooling cycle and b) absorption power cycle.

recently, such as the use of ionic liquids and various refrigerants. The schemes of a typical simple cooling cycle and a simple APC for comparison are shown in Figure 2.1. In a typical absorption cooling cycle, steam is generated in the desorber (also known as vapour generator) in state 3 by pool boiling at a constant temperature. It is then condensed (state 4) and throttled down to low pressure (state 5) so that it can provide cooling duty while evaporating to state 6, before getting absorbed into stream 9, resulting in a weak solution (stream 11). The amount of liquid returning from the desorber (from state 7) through the recuperator is relatively large compared with the steam flow, and recirculation of part of stream 11 to another spraying level is usually included to promote absorption [36]. The APC differs from the cooling cycle mainly in that it substitutes the condenser, throttling valve, and evaporator for an expander (turbine). The proposed power cycle, in contrast to a typical cooling cycle, also anticipates using the steam generator and absorber as a counterflow heat exchanger (HX) with a gradual change of temperature during phase change (state 2 to 4 for heat addition, followed by isothermal adiabatic separation, then state 10 to 11 for absorption).

2.2 Review of APC with various working fluids

The review of APC is first briefly tackling the applications with water-ammonia mixture as a well known Kalina cycle. Following on that is a summary of works with aqueous solutions of salts such as LiBr, where much less work has been performed to date. There are other possibilities of working fluids for APC, specifically based on ionic liquids or alcohol mixtures and these are reported at last.

2.2.1 Water-ammonia absorption power cycles

Maloney and Robertson were among the first to study absorption power cycles using an ammonia-water mixture as a working fluid, but because of the thermal boundary conditions considered (using a desorber and absorber of the same design as in the typical cooling cycle), they found no significant thermodynamic benefit [40, 41]. Later, in several patents [42, 43], Kalina described a cycle with a slightly different configuration that exploited the temperature change throughout the evaporation and condensation process. In the cycle, the concentration of working fluid is controlled separately for evaporation and for condensation (by distillation). In the theoretical field, the Kalina cycle brought a revolution in the exergetic efficiency of resource utilization. The cycle has been commercialized with many modifications developed, and the licence holder, Wasabi Energy [44], offers a wide range of applications from high to very low temperature heat sources. Numerous theoretical works have explored various applications and system modifications; some of them are mentioned in [45, 46, 47, 48, 49]. The basic configuration for low-temperature application is the same as in Figure 2.1b; examples of more complex Kalina cycle systems for geothermal applications at different temperatures are shown in Figure 2.2. Globally, nearly 25 MWe of capacity has been installed using this cycle, with more than 15 MWe of capacity is under development [50] in 2016. The Kalina cycle however does not always provide the best performance. Guzovic et al. [51, 52] theoretically compared an ORC and a Kalina cycle for two low-temperature geothermal sources in Croatia, and a higher power output was obtained from the ORC. The reason given was the relatively high condensing temperature resulting from cooling by an air-cooled condenser (ACC) at an ambient temperature of 15°C.

2.2.2 Salt-water absorption power cycles

The first proposal for the use of aqueous salt solutions in absorption power cycles came from the previously mentioned study of Maloney and Robertson [40] in 1953 in which LiCl-water was mentioned as a possible alternative to water-ammonia. It has the potential for improved performance, but nonetheless remained outside the focus of most research. The first known consideration of a LiBr solution as a working fluid can be found in Aly's theoretical work on a solar fuel-assisted power cycle from 1988 [53], in which the working fluid is heated by solar heat to approximately 100°C and flashed; the steam is separated and superheated to 600°C using a fuel-fired superheater. The cycle showed substantially (44%) higher power output compared with other solar fuel-assisted power cycles. In 1991, several modifications of LiBr/LiCl/KOH aqueous-solution absorption power cycle were patented by Ishida et al. [54, 55]. The proposed system always consists of an absorber condenser. The basic configuration of the cycle is the standard APC from Figure 2.1b (with a fuel-

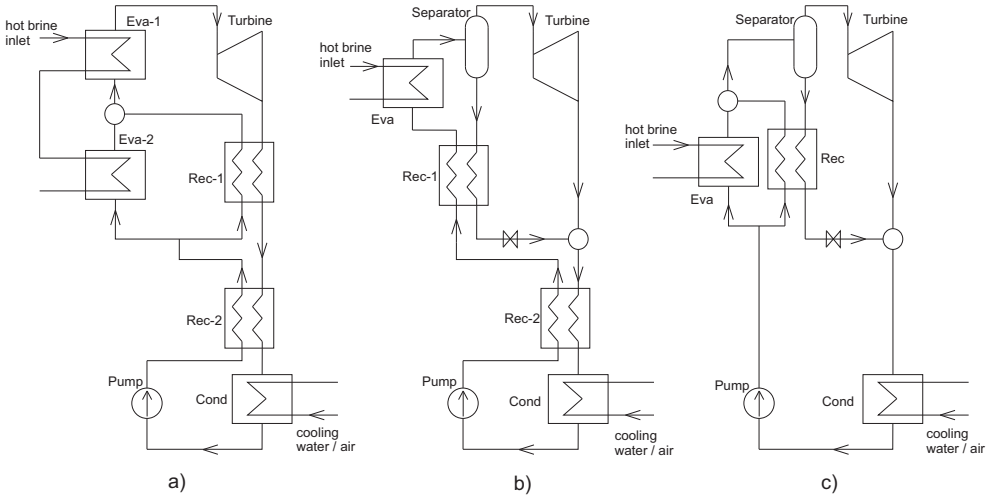

Figure 2.2: Process flow diagrams of (a) high-, (b) middle- and (c) low-temperature geothermal source Kalina cycles (Eva: Evaporator, Cond: Condenser, Rec: Recuperator). Modified from [45].

fired boiler serving as the heat source), in which separation is placed after evaporation. Other proposed modifications circulate the absorbent through the absorber/condenser only in the low pressure part of the cycle, using distillation similarly to high-temperature Kalina cycles (shown in Figure 2.3) or alternative methods, such as reverse osmosis or an electric dialyzer. The setup in Figure 2.3 uses the heat of the steam exiting the turbine to heat up the distillation. As there is pure water vapour before absorption, which should generally increase the mixture temperature, this setup appears to not work properly, but the possibility of using turbine bleed as the distillation heat source is also mentioned. Authors proposed this cycle for standard fuel-fired plants, assuming relatively high temperatures and pressures. In 1995, Styliaras' work [56] provided results for a cycle that uses a solution of LiBr:ZnBr:$CaBr_2$ (1.2:1:0.3) and H_2O with properties derived via the Antoine equation. With an upper steam generator temperature of 70°C, the cycle has an efficiency of 6%, whereas a comparable Rankine steam cycle has only 2%. Issues with working at very low pressures are mentioned. An interesting result is the potential of heat loss in non-ideal HXs, which may be very large for cases in which the concentration of the solution changes only by several percent (high amount of heat is recycled).

Recently, a basic energy and exergy analysis of Garcia-Hernando et al. [57] in 2013 renewed interest in cycles using salt solutions. The authors investigated the same basic scheme as in Figure 2.1b with a LiBr solution. Properties were calculated using the Dühring rule [58]. A substantial increase in the exergetic efficiency of the cycle (the cycle only, with the calculation including the thermal

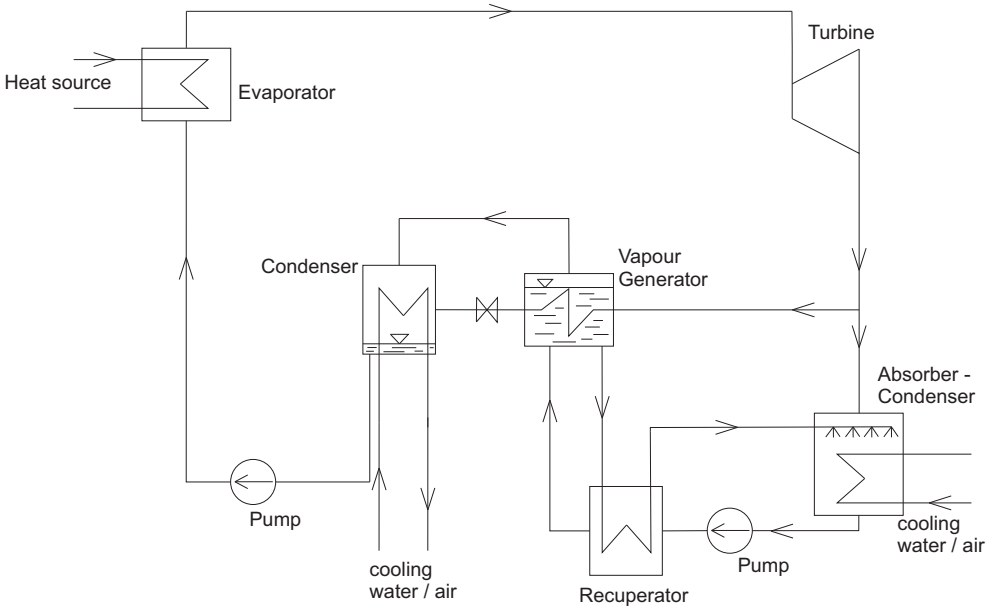

Figure 2.3: Scheme of a LiBr absorption power cycle in which the absorbent circulates only in the low pressure part of the cycle, modified from [54]. Note that unlike in this figure, heat must enter the vapour generator (distiller) from a different source, such as from bleed or other waste heat, as the turbine outlet is already very near or even below ambient temperature.

exergy outflow of the cooled heat source stream) was identified when compared with the reference Rankine cycle for the given heat source and heat sink parameters and admission parameters of the steam. Cycle performance was also compared with several referenced ORCs, showing that the cycle has energy efficiency comparable with the best of them, while providing a better environmental impact. This work is also the first to stress the phenomenon of variable temperatures of boiling and condensation (temperature glide), which is associated with higher exergy conservation in HXs. This work was followed up by an extensive exergo-economic study in 2014 [59]. The H_2O-LiBr cycle was compared with a simple Rankine cycle and with NH_3-H_2O power cycles using the specific exergy costing method. The heat source was designated as saturated water vapour at 150°C, for which a cost was chosen as well. However, this heat source selection hampers one of the cycle's major advantages – temperature match in HXs and use of low to no value waste heat. Even in the case of this heat source, the LiBr-H_2O cycle proved to have the highest efficiency of the three. However, as the LiBr-based cycle operates at very low pressures and high volumetric flows, contrary to the high pressure of the water-ammonia mixture, the analysis logically resulted in an economic disadvantage for the LiBr cycle. It is important to note that the applied costing formulas were taken from references often used for large plants without

the best context (e.g. the formula for the steam turbine cost is in the chain of references used for gas turbines, often with an output range of hundreds MW, and the different properties of the fluid and their effect on the design of turbine are not taken into account). Scaling laws from large power plants do not apply exactly in the scope of small units suitable for distributed power generation [60], for which LiBr APC appears as suitable. The results should be therefore taken with caution. Lastly, the potential of salt solution-based APCs was included in a chapter on the Kalina cycle in a 2015 book by Rogdakis and Lolos [46], which remarked on the potential of salts such as LiBr, LiCl and $CaCl_2$, but no calculations have been performed. In addition to summarizing previous findings, they note the presence of superheated vapour immediately after boiling and separation, and of the necessity of using a counter-current absorber design. A design with several reheaters is furthermore suggested though it again adds up system complexity.

After the author's theoretical investigations, this topic of APC was extended by further works of other authors, often again growing into more complex theoretical systems such as double effect APC system with LiBr [61] or addition of ejector into the system (and combining with electrolyser for "increase in novelty") [62].

Special attention should be paid to work [63], which has surprisingly similar literature review to the one of a kind review from previous work of author. Except for identical text flow and order of citations (not always exactly even in chronological order), there are identical even mistakes in incorrect spelling of authors.

2.2.3 Other absorption power cycles working fluids

Nearly all absorption power cycles use a water-ammonia mixture, possibly a salt solution, as their working fluid. Li et al. [64] also mention that until recently, research had focused only on modifications and adjustments of cycles using a water-ammonia mixture, ignoring the possible use of other working fluids. Amyl acetate-CO_2 has been used in the APC analysis reported in [65] with properties developed on the theoretical basis of the Peng-Robinson method. The paper reported a desorber final temperature of 150°C and absorption terminal temperature of 25°C (subsequently subcooled by 5°C). The cycle efficiency achieved was 14%. The cycle was suggested for waste heat recovery, but comparison of performance with other standard power production systems was not made.

A work of Eller et al. [66] investigated alcohol mixtures as working fluids for Kalina cycle configuration KCS-34 with two recuperators; using sensible heat source and specified inlet and outlet temperature of a heat sink. In

comparison with pure component ORC and mixture ORC at both subcritical and supercritical pressures and for a heat source temperature range 200-400°C, the best performance is provided by zeotropic mixtures, nearly identical for both sub- and super-critical pressures. Pure fluids ORC and alcohol mixtures APC have relatively similar performance with slightly different results for different temperatures; supercritical pure fluids achieve such performance only in selected temperatures fitting to a specific fluid. Ammonia-water APC performance is limited here due to adopted limitations on maximal system pressure.

2.3 Review of absorption power and cooling combined cycles

In the combined cooling and power systems the sorption chillers are the most common thermally activated systems in majority of the works. Looking at the options of absorption cycles, the standard option is a different power cycle as prime mover where the absorption chiller serves as a bottoming cycle [67, 68, 69]. When focusing on deeper integration for combined cooling and power (CCP) cycles, they have been discussed in previous studies with a comprehensive review being brought by [41, 70]. It shows a wide range of cycles' complexity; in some cases, pursuing theoretical improvement in performance results in a system hardly possible to build and operate. Still, nor combined system, nor just absorption chillers, are very widespread. Literature offers several possibilities on how to assess and compare performance of power production and chiller heat duty, since the two are typically in different order. Mostly the solution is found using of a weight factor between the two. Also it was summarized, that most of the systems utilize water-ammonia mixture as working fluid with just few exceptions such as mixture of ammonia and lithium nitrate or ammonia and sodium thiocyanate mixtures.

Ejector cooling can be used as well for thermally activated chillers in CCP systems [71], where one sub-cycle is used to get the driving force of the ejector, thus creating vacuum and cooling in the other sub-cycle. Then the work potential does not need to run only the ejector. It can be converted to useful power in expander, which is then used for running a compressor in standard vapour compression chiller as in [72], thus combine power cycle and compressor chiller into a thermally activated chiller.

The range of the CCP systems based on thermodynamic cycles found in the literature, regardless of the often high level of complexity, can be by its general working principle classified into four main categories. These categories, outlined in Figure 2.4 by illustrative $T - s$ diagrams and example schematics, are following:

- Separate thermodynamic cycles coupled by heat
- Separate thermodynamic cycles coupled by work
- Single-branch thermodynamic cycle for both power and thermally activated cooling
- Branched thermodynamic cycle for power or thermally activated cooling

2.3.1 Separate thermodynamic cycles coupled by heat

A thermally activated cooling cycle can be used as a bottoming cycle in the cogeneration configurations schematically described in diagram in Figure 2.4a. Almost any power cycle can be used as the topping cycle, as long as the heat rejected at sufficient level can drive thermally activated cooling. Therefore this system is feasible for a rather higher heat source temperature. This configuration is beneficial when two technologies available on the market, typically power production system and absorption chiller, are combined. The research then typically focuses on overall performance, annual utilization of power, cold and heat, system's economic performance or on optimal control regimes for maximal utilization of products. [37, 67, 68, 69, 75, 76, 77] The coefficient of performance (COP) of the chiller is then around 0.7 (in case of typical single effect absorption chiller), while the efficiency of power production is depending on heat source temperature and type of topping cycle(s).

The cycles can also be more integrated, as the utilisation of only a part of rejected heat from compressor intercooling [78] or as a complex set of recuperation heat exchangers in a combination of the Kalina power cycle and bottoming H_2O–LiBr absorption chiller [73, 79], which is depicted as the example in Figure 1a. The benefits of such integrated systems are typically an improvement in overall efficiency and a possible reduction in cogeneration annual costs.

2.3.2 Separate thermodynamic cycles coupled by work

Power and cooling cycles can be coupled by produced work instead of heat, as illustrated in Figure 2.4c. In this review, three forms are differentiated: mechanical work, electricity, and motion of the fluid in ejector cooling.

Mechanical and electrical coupling of the systems is primarily considered as a combination of existing technologies. Studies have often focused on the overall performance or experimental validation. In an experimental study on mechanical coupling and application of a motor generator [80], a 1 kWe experimental solar energy system based on an organic Rankine cycle (ORC) and vapour compression cycle (VCC) was constructed using mainly the off-the-shelf

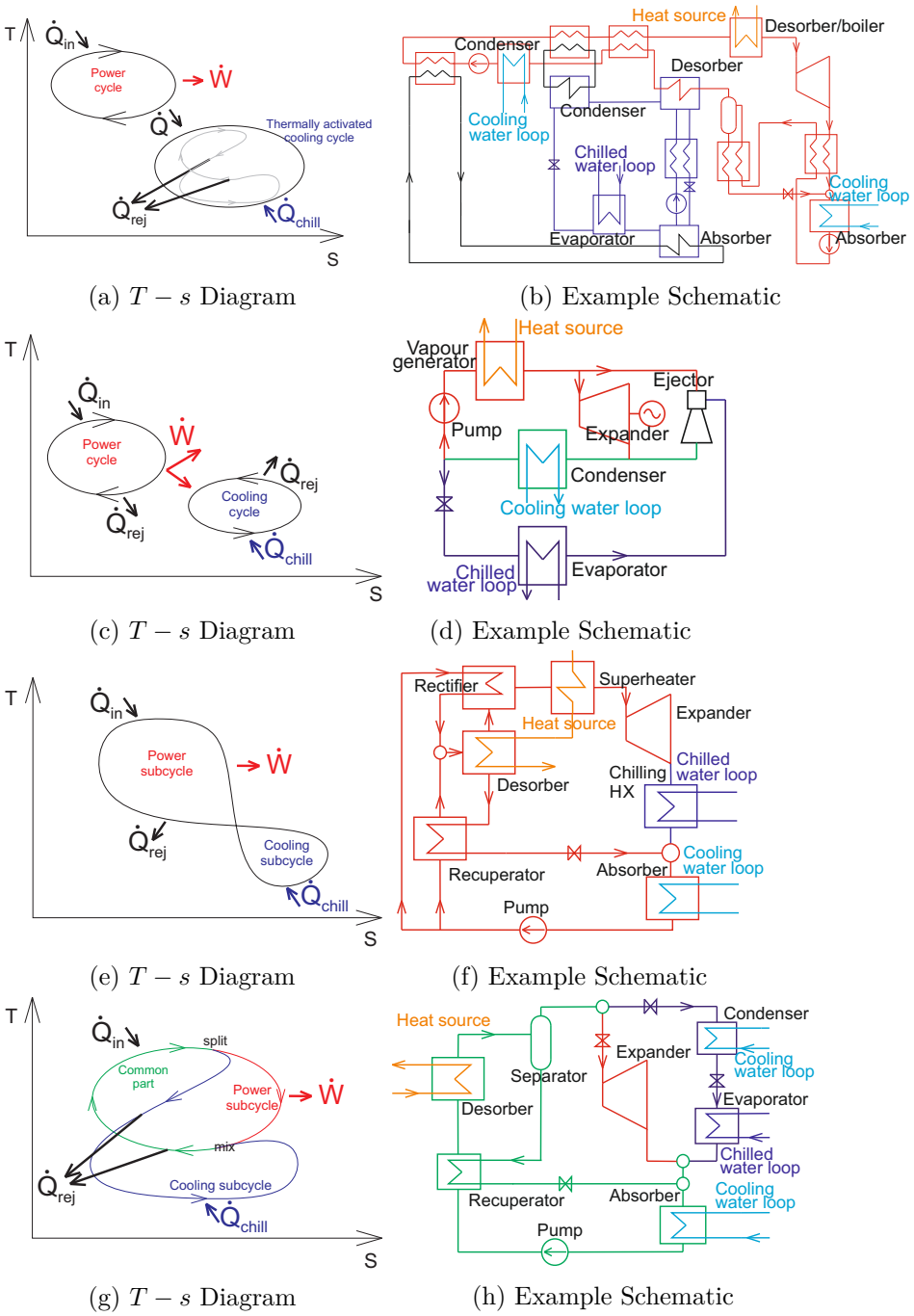

(a) $T-s$ Diagram (b) Example Schematic

(c) $T-s$ Diagram (d) Example Schematic

(e) $T-s$ Diagram (f) Example Schematic

(g) $T-s$ Diagram (h) Example Schematic

Figure 2.4: Schematic T-s and process diagrams of CCP systems with: **(a-b)** two separate cycles coupled by heat (example redrawn from [73]), **(c-d)** two separate cycles coupled by work (ex. from [74]), **(e-f)** single-branch thermodynamic cycle (ex. from [41]), and **(g-h)** two-branch thermodynamic cycle

components. The unit used a 93°C heat source and exhibited a chiller regime COP of 0.71, similar to absorption chillers. The authors of the aforementioned study stated that greater benefits could be achieved with higher-temperature heat sources. A similar system was explored in another study [81], although with a fixed mechanical coupling of the expander and compressor. Thus, no power could be produced; nevertheless, the resulting COP was less than 0.6. A specific case of cycle combinations for trigeneration from waste heat has been reported [82], where an additional absorption chiller is used between the ORC and VCC to ensure that the condenser of the VCC remains at a lower temperature. All the systems were coupled electrically, which provides flexibility, making a purely power or cooling regime possible. The system had a COP of 0.2 and a thermal efficiency of 57%. For electricity production, the efficiency was 6%.

This concept can be simplified using the same working fluid and condenser for both cycles. Such a solar ORC–VCC system was proposed [83] with an expander, compressor, and generator on the same shaft so that electricity or cooling loads can be preferred. Additionally, in winter, the condenser heat can be used for heating in a heat pump regime. A recuperator can also be added to the ORC and VCC to improve the efficiency, thus, the COP, for example, up to 0.66 [29]. Other researchers considered similar systems with combined condensers but without the generator and electricity output. A piston expander–compressor unit proposed in [84] (COP between 0.1 and 0.6, based on the heat source temperature and working fluid) or an ORC heat pump [72] can serve as examples. For a more detailed summary of ORC–VCC systems, the reader is referred to a previous report [83].

The ejector cycles can be combined with power production cycles in several configurations. The simplest and most flexible configuration is a parallel configuration, where the steam at the boiler outlet is routed between the expander and ejector based on the required share between the two products. The vacuum port of the ejector is then connected to the evaporator of the chilling circuit, as shown in Figure 2.4c. The simplicity of such a system allowed for experimental verification of a small system with cooling capacity up to 5 kW and electrical output up to 1.5 kW (COP around 0.3, electricity production 3% to 4%) [74]. When the heat source temperature and vapour generator pressure are higher than needed for the ejector, extraction turbines have been proposed with the vapour extraction fit for the ejector [85, 86]. Another option is to design the expander operating between the vapour generator pressure and optimal ejector driving pressure so that these two are connected serially [87, 88, 89], where flexibility between the products is, however, lost. To maximise the theoretical output, more complex configurations have also been proposed and investigated [90].

2.3.3 Single-branch Thermodynamic Cycle for Both Power and Thermally Activated Cooling

Absorption cycles can be designed in a way that a vapour stream exiting vapour generator is used first for power production and then for cooling, as it is illustrated in Figure 2.4e. The most commonly considered here is the Goswami cycle and its modifications, theoretically explored in numerous works such as [91, 92, 93, 94, 95, 96, 97, 98, 99, 100]. This cycle is based on simple absorption power cycle (APC) with utilization of sub-ambient temperatures at the expander outlet, thus providing some additional cooling on top of produced power (typically one third of turbine work as cooling output). Water ammonia mixture is considered almost exclusively with just few exceptions [94, 101, 102], that operate with different working fluids such as amyl acetate, propane-decane or isobutane-decane. The advantage of the Goswami cycle is in its simplicity, utilizing one additional heat exchanger added at the expander outlet as its temperature can be below ambient. Among the disadvantages are pressure loss at the vapour side or limited control of the chilling output parameters. The cycle has a fixed chilling output to power ratio with rather low share of cooling, performance of which is highly dependent on ambient conditions and expander efficiency.

The Goswami cycle with ammonia has been experimentally explored on a lab scale system with expander power output around 40-120 W at nominal temperature of vapour generator 55-85°C using water-ammonia mixture [38, 103, 104]. In this small scale due to thermal losses and low expander efficiency it was however complicated to obtain sub-ambient temperature at the expander outlet.

Among the modifications of the Goswami cycle, a recuperator has been also proposed between the outlet of the expander and evaporator to boost the cooling performance [105]. Another configurations suggest addition of a condenser after the turbine, thus effectively splitting the pressure potential by the saturation temperature to reject the heat [106]. Turbine work is partly limited, but the cooling load can be then ensured. This concept with added condenser was suggested not only for the water-ammonia mixture, but also for LiBr-water solution [107]. Cooling load can be further boosted by adding a flashing tank on the stream of returning solution, routing thus more vapour to the condenser [108].

2.3.4 Branched Thermodynamic Cycle for Power or Thermally Activated Cooling

Finally, the components of the APC and absorption chiller can be arranged into two branches, as illustrated in Figure 2.4g. The simple form of the cycle shown as an example corresponds to the proposal in an earlier work [109].

This configuration provides very high flexibility because the splitter can freely specify the ratio of vapour passing to the expander or chiller branch. When a water–ammonia mixture is used, a rectifier is typically considered for improved performance, even for simple configurations [110]. Such a system has been experimentally analysed [111], providing a chiller regime COP of approximately 0.6 from a 133°C temperature of the generated vapour. The expander was only simulated using only an orifice. Several authors have proposed the addition of a superheater upstream of the expander to improve its performance [112] and change the configuration to a generator–absorber–exchanger (GAX) cycle for higher heat source temperatures, as other studies [110, 113], or with a separate boiler for turbine and vapour generator [114]. In addition to the water–ammonia mixture, a mixture of ammonia and salts, such as $LiNO_3$ or NaSCN, has been proposed [112, 115], where the configurations are simplified by omitting the rectifier.

An alternative approach for the water–ammonia system is to route all purified ammonia from the rectifier into the chiller branch of the system. The lean stream of ammonia is then fully evaporated in a separate boiler, and the vapour is fed to the expander and follows as lean input into the absorber [116, 117, 118]. However, this approach does not allow for control of the ratio between cooling and power. The opposite approach to the cycle configuration [119] excludes the rectifier and routes vapour from the generator into a turbine. The lean solution is flashed at an intermediate pressure, and the vapour is condensed and throttled to the evaporator in the chiller branch.

2.3.5 Prospects For for Aqueous Salt Solution Systems

An aqueous solution of several salts, but mainly LiBr, has been widely used for absorption chillers, especially when a low-temperature heat source is available and chilled temperatures above 0°C (refrigerant is water) are required. Such a working fluid is environmentally friendly and has low toxicity. Overall, the low pressure level of the system results in fewer legal requirements for installation [36]. However, absorption chillers cost more than double the vapour compression chillers and more expensive is also auxiliary equipment [120]. For example, only less than 2000 of solar absorption cooling systems are installed annually worldwide [121], which also confirms our experience that absorption chillers are not widely used when the cooling load is required only temporarily, mainly because of economic reasons.

Absorption cycles used solely for power production typically adopt an H_2O–NH_3, have been the focus of many researchers and were reviewed in previous sections. The salt solutions were proposed for power cycles as alternatives and as will be shown also later, when applied to low-temperature heat sources below approximately 120°C, i.e., a domain of single-effect LiBr chillers, these

APCs have a superior performance to ORC with respect to cycle efficiency and utilisation efficiency referenced to the heat source. These APCs appear also more suitable for small distributed energy systems rather than large-scale systems. One reason, among others, are the low pressures and associated large volumetric flows of vapour allowing for an efficient turbo-expander design for systems with a small power output (will be shown later).

As one of thermodynamic cycles with two branches, the absorption combined power and cooling cycle (APCC) using an aqueous salt solution (Figure 2.4g) can enable a potentially beneficial variability in the power and chiller output, allowing for higher annual utilisation of absorption system. Technical implementation of this system has not indicated any major obstacles. Regardless of the apparent advantages, a detailed analysis of this system has not been reported in the literature. Hence it is selected for investigation in this thesis.

2.4 Working fluids

The review shows the fact explicitly stated also by Li et al. [64] that until recently, research had focused only on modifications and adjustments of cycles using a water-ammonia mixture, ignoring the possible use of other working fluids. Aqueous solutions of salts, especially LiBr, has been proposed much less, but still it is considered probably due to its common application in absorption chillers. The other working fluids are considered rather exceptionally, where Amyl acetate-CO_2 was theoretically explored for APC [52]. Wider range of working fluids was theoretically explored for APCC, namely ammonia mixtures with either lithium nitrate or sodium thiocyanate [41, 70] or ionic liquids or organic fluids such as amyl acetate, propane-decane or isobutane-decane working with various refrigerants [94, 101, 102]. Specifically in ionic liquids as absorbents is seen by some researchers a future of thermodynamic absorption cycles. They can be paired with absorbates as H_2O, NH_3, hydrofluorocarbons, hydrocarbons and alcohols. [122, 66] For that purpose, Li et al. [64] formulated the properties of three new working pairs based on organic and ionic liquids.

2.4.1 Water-ammonia

The water-ammonia (Kalina) cycle will be used as one of the references in thermodynamic comparison. This working fluid is in use already for considerable amount of time and properties formulation can be considered to be relatively well developed. In [41] are listed 12 formulations of the mixture properties. Some discrepancies between different formulations are mentioned where difference in saturation temperature was found for certain correlations as high as 20% and in saturation enthalpy 100% for pressure 20 MPa. Problems are identified especially in the high pressure domain and for cycles using low temperature sources should not pose major problem. Primarily for this work

will be considered correlation of Ibrahim & Klein from 1993 [123] default to EES. There exist newer and more accurate correlations for ammonia-water mixture properties from 1998 by Roth [124] is part of REFPROP 9 program and is subject to availability, but experience shows a failure to provide results in certain low quality two phase region domain. It can be however used for purposes such as to check final accuracy. To illustrate the properties of this zeotropic mixture, Figure 2.5 shows a phase diagram of the mixture at pressure 1 MPa. If a solution has a concentration 80% of ammonia, it would start boiling at the point (a) at 32°C and the first molecules of vapour are nearly pure ammonia. If the temperature of the boiling solution is further increased, for example to 100°C, liquid concentration is shown by the point (c) and the vapour by the point (d). Finally, the solution gets fully evaporated when reaching the point (b).

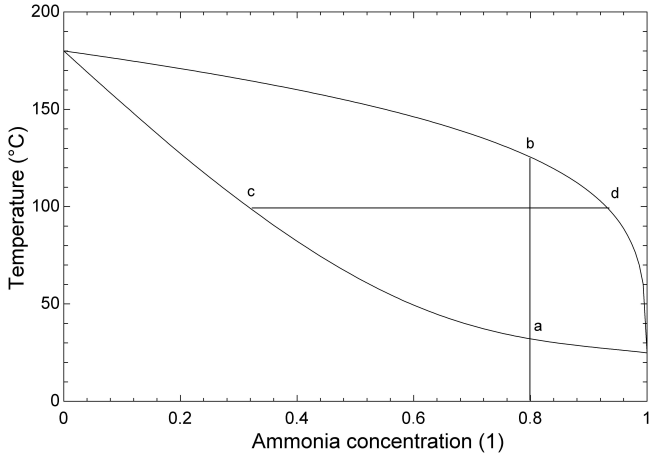

Figure 2.5: Phase diagram of water-ammonia mixture at 1 MPa

2.4.2 Water-salt

This work will be focused mainly to assess potential of aqueous salt solutions. Aqueous solution of several salts, but mostly LiBr, has been widely used for absorption chillers, especially when there is available low temperature heat source and chilled water above zero degree (no freezing as refrigerant is water) is required. The benefits of salts in comparison with ammonia systems is environmentally friendly and safe fluid with low toxicity and low pressure of the system, resulting in less formal requirement for installation. [36] In these solutions, the absorbent salt (LiBr) is non-volatile. The relationship between concentration, temperature and phase composition can be depicted using a Dühring plot to show boiling-point elevation. A Dühring plot for a cooling cycle and the below-calculated case of APC is shown in Figure 2.6. The weak solution is heated and separated into pure vapour (left side of the figure)

and rich solution (right side). When both streams reach a lower temperature and pressure level (via the recuperator, condenser and evaporator, or via the turbine), they are mixed to create again the weak solution. The difference between power cycle for waste heat recovery and between refrigeration cycles can be observed in the figure in the pressure levels, the distance from the crystallization line, as well as in the extent of a change in solution concentration.

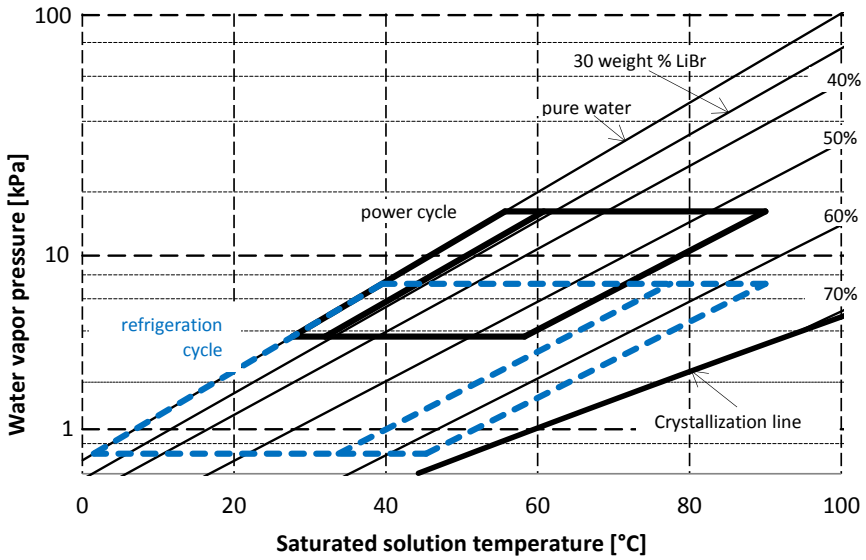

Figure 2.6: A Dühring diagram for a LiBr aqueous solution, highlighting a typical absorption refrigeration cycle from [36] and the power cycle presented here, both with a highest solution temperature of 90°C.

Dühring rule and related diagram sets have been often used to obtain fluid properties [125]. These can be developed theoretically however come with an error. Based on experiments with real solution, there exist several properties formulations. For water - LiBr solution, in the past several formulation were developed, though usually valid only in narrow range and with various success in the industry [126]. Currently are in use mainly two or three formulations. The first one by Pátek and Klomfar [127] is given for the entire composition range and temperature range from 0°C to 227°C (500K), but gives only the properties on the vapour-liquid equilibrium curve. Second frequently used formulation is formulation of Kim and Ferreira [126]. This one is valid from 0°C to 210°C, up to 1 MPa and 0 to 70% LiBr concentration. This formulation will be used as primary in the study in a form of an interpretation from Hochschule Zittau as an external routine into Engineering Equation Solver (EES) used for the calculations [128]. Another often used formulation for LiBr is provided by Sorption Systems Consortium at the University of Maryland [129].

Other salts in aqueous solution are often considered in absorption systems as well as certain additives (e.g. glycerol, where glycerol mixed with LiBr solution is known as Carrol [130]). Among other salts are mostly considered LiCl and $CaCl_2$. LiCl - water properties at vapour-liquid equilibrium have been experimentally measured and correlated by Pátek and Klomfar [131] with validity to 127°C (400K), which is currently also implemented in EES. The properties of the $CaCl_2$ solution are taken from [132], but are significantly disadvantaged by the absence of enthalpy. This increases the potential for error; caution should thus be used when assessing the solution's results.

2.4.3 Ionic liquids – refrigerants, alcohol mixtures and other

Ionic liquids are another promising option as it appears they can mix well with another refrigerants (have good affinity) and be used for absorption process. Ionic liquids can combine with water, ammonia, alcohols, and hydrofluorocarbons to form an absorption working pair.

Considering hydrofluorocarbons as refrigerants there have been even experimentally determined properties of vapour-liquid equilibrium. Specifically for APC was developed non-random two-liquid (NRTL) model of R245fa with absorbents DMF, DMEDEG and NMP (N,N-dimethylformamide , diethylene glycol dimethyl ether and N-methyl-2-pyrrolidone) from 20°C to 80°C [64]. As another can be mentioned vapour-liquid equilibrium for R32 with DMAC and DMEDEG (N,N-Dimethylacetamide) and then R152a with DMEDEG over same temperature range [133]. Deeper and more comprehensive description of ionic liquids with refrigerants and characteristics of these species and their suitability are described in [122]. This is currently rather active field of research and other works describing new working pairs can be found or are expected to be soon developed and published.

One option to predict the properties if formulations are not available is to use known equations of states based on known parameters of pure fluids. Peng-Robinson method has been used in [65] for CO_2 as a refrigerant with absorbent amyl acetate. The method needs critical pressure and temperature of each fluid and experimentally determined acentric factor and interaction term between the two fluids. For this work, amyl acetate-CO_2 mixture is chosen based on reference [65], methanol-heptanol is chosen as most perspective alcohol mixture [66]. Ionic liquids are included by 1-ethyl-3-methylimidazolium tetrafluoroborate with refrigerant R134a (R134a-[EMIM][BF4]) and with water (H_2O-[EMIM][BF4]), as suggested by decent COP performance in absorption cooling regime [122]. These systems in this thesis are modelled in Aspen Plus, where for amyl acetate-CO_2 is used Peng-Robinson equation of state and alcohol mixture uses NRTL model. Ionic liquid mixtures are based on Peng-Robinson equation of state as well. Parameters for ionic liquids that are

not in Aspen Plus databases are obtained from references [134, 135].

For other fluids, standard available formulations exist with minor differences between each other. In this work are used properties default to the database NIST Refprop and to the calculation program EES.

For many mixtures, mainly of refrigerants or alcohols, property databases REFPROP and Coolprop (computationally less convenient for mixtures) can be also used, with more complex equations of state that provide supposedly more accurate properties. These tools are for mixtures implementing primarily Helmholz equation of state.

2.5 Experimental and commercial APC

No experimental APC with salt solution has been reported in the available literature before author's work. Therefore, two separate chapters focus on review of the components needed to implement such system. Experience with experimental systems and installations with APC exists and is limited to water-ammonia mixture reviewed here. Kalina cycle with water-ammonia mixture has been experimentally explored and partly commercialized with most of the units in MW scale. A list of Kalina cycle installations is shown in Table 2.1.

The low temperature geothermal application are in a range of temperatures from less than 100°C in the 50 kW plant EcoGen [137] to approximately 120°C for the Húsavík plant [140] or in Unterhaching. The reliability of these plants appears however, especially for the low temperature geothermal systems, poor. There have been reports of problems with commissioning and operating the machines, with corrosion proving to be a significant issue in the cycle [141, 142] or technical issues due to very high pressures [142]. The most documented are issues of the plant in Húsavík, but the plant in Unterhaching is decommissioned after less than 10 years of operation [143]. This raises questions about suitability of ammonia water mixture in power cycles, but optimistic view on Kalina cycle applications until now along with material consideration is given [136].

The most documented Kalina cycle plant in the literature is the Húsavík plant. Focusing on plant components, larger Kalina cycles are mostly using plate exchangers as mentioned in [143, 144]. Relatively comprehensively are some design features in Húsavík described in [140]. It states that *The evaporator is a shell-and-tube exchanger utilizing low-fin carbon steel tubes. The HT recuperator is a carbon steel shell-and-tube exchanger. The LT recuperator is a welded plate exchanger. The plates are stainless steel surrounded by a carbon steel housing. The condensers are plate-type heat exchangers with welded pairs*

Table 2.1: Overview of Kalina cycle past and present installations [49, 136, 137, 138, 139]

Name	**Country**	**Power output (MWe)**	**Operation (start / current state)**	**Type of unit / heat source**
Canoga park	USA	3.2	1992, refurb. 1996 Out of order	Experimental unit Bottoming cycle to gas fired system
Fukuoka	Japan	4	1998 Out of order	Experimental unit Waste incineration
Kashima Steel Works	Japan	3.45	1999 Operational	Commercial Waste heat from steel plant
Húsavík	Iceland	2	2000 Out of order	Commercial Geothermal
Fuji Oil	Japan	3.9	2005 Operational	Commercial Waste heat from refinery
Bruschal	Germany	0.6	2009 Operational	Commercial Geothermal
Unterhaching	Germany	0.7-3.36	2009 Out of order	Commercial Geothermal
Shanghai Expo (later QuingShui)	China / Taiwan	0.05	2010 Out of order	Experimental demo Solar, later geothermal
EcoGen Tōkamachi	Japan	0.05	2011 Operational	Commercial Geothermal (hot spring)
DG Khan	Pakistan	8.6	2013 Operational	Commercial Waste heat from cement plant
Star Cement	Dubai	4.75	2013 Operational	Commercial Waste heat from cement plant

on the ammonia-water process side to minimize leakage. Plates are stainless steel.' Also it says that the separator is an impingement-type vane module and turbine is derived from standard steam turbine single-stage radial-flow Curtis wheel design with two rows of blades operating over 11000 rpm geared to 1500 rpm generator. Sealing is provided by nitrogen gas generated on site. The sealing issue has been identified as one of the causes of plant failure. The

new website of company producing Kalina cycle units as well as details of tender for components sale after shutdown [143, 145] shows in information about the 3.4 MWe Kalina Cycle Geothermal Power plant in Unterhaching, Germany that all heat exchangers are of vertical plate type, while turbine is multistage axial. Additionally Table 2.2 summarizes main parameters of these two geothermal plants. The micro sized 50 kW geothermal unit uses a high speed turboexpander (58 000 rpm) with magnetic bearings [137]. The layout shows that plate heat exchanger as probably a condenser (absorber), desorber and recuperator are used while probably a large rectifier is also present. [146] Photography and physical layout of this system are in Figure 2.7.

Table 2.2: Summary of main parameters of the two Kalina cycle geothermal plants

	Húsavík test 1	**Húsavík test 2**	**Unterhaching**
Gross electrical output (kW)	1 823	1 826	3 360
Net electrical output (kW)	1 696	1 709	n.a.
Hot water temperature (°C)	122	121	122
Hot water flow rate (kg/s)	90	90	125
Cooling water temp. (°C)	5	5	11
Cooling water flow rate (kg/s)	122	121	630
Working fluid composition	n.a.	n.a.	89% NH_3 11% H_2O

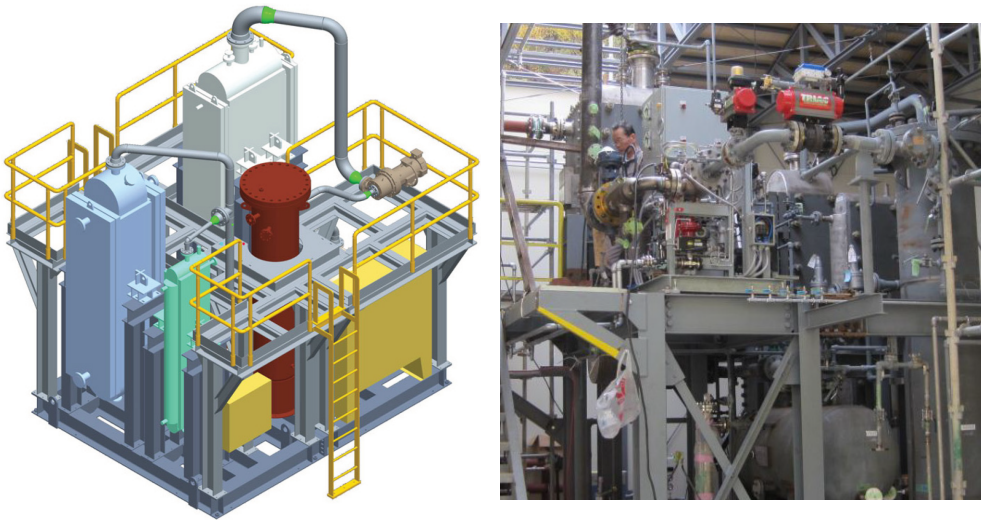

Figure 2.7: EcoGen 50 kW Kalina cycle unit [146, 137]

The second experimentally explored system is the Goswami APCC. It has been performed in three phases described in detail in dissertations between 2003 and 2011 [38, 147, 148] with thermal input of about 10.5 kW in hot water heating for desorber and additional power for electrical superheater. Purpose

of the systems was as a proof of concept demonstration and an analysis of operation regimes. Boiler, recuperator and cooling heat exchanger were based on plate heat exchangers. In the first system the absorber was made of a bank of aluminium finned heat exchangers surrounded with a packing, all enclosed in a vessel with a sprayer at the top. Consequently the bank of exchangers was changed to a microchannel heat exchanger and counterflow configuration, with vapour introduced into a pool under the heat exchanger. Expander was at first simulated by a throttling valve and heat exchanger. Later it was changed to a radial cantilever single stage turbine. This turbine was converted from micro turbine components originally used in an aircraft air-cooling system, which was ordered as a spare part and modified to partial admission system by blocking off most of the nozzles by epoxy. The isentropic efficiency of the turbine was estimated from the measurements in range 20-30% though testing was successful only with air. It turned out inconclusive from ammonia-water testing, mainly due to mechanical transfer of power output and sealing issues. The latest work used a converted off the shelf truck refrigeration scroll compressor as is typical method in many ORC systems. With measured 30-50% efficiency the expander successfully extracted 40-120 W of power output. The system contained a separator tank at the top of which was a rectifier with cooled reflux and Berl saddle packing. The pump was first of a rotary vane type, followed by multi stage until finally a magnetically coupled gear pump was used.

These works successfully demonstrated possibility of obtaining sub-ambient temperatures. Though in reality the cooling effect was lower than predicted, partly due to low expander efficiency, partly due to departure of measured values from modelled thermodynamic equilibrium. Vapour flow rates were also lower than predicted, attributed here mostly to thermal losses. Expander was tested with operation regimes with saturated vapour, superheated vapour and rectified and superheated vapour. Superheating provided the best expander performance. Generally the predicted operation trends were verified.

2.6 Summary of the APC review

Absorption power cycles were extensively studied from theoretical point with water-ammonia mixture, i.e. Kalina cycle. Research at certain point started to focus on potential of highly complex layouts where prospects of commercialization are rather low. Experience from experimental, pilot and first commercial systems with Kalina cycle shows, that system needs to be simple and still it is prone to many issues. It is unlikely that for high temperature and high power output region Kalina cycle would squeeze out current mature systems based on Rankine or even Brayton cycle. By the potential of exergy efficiency it however is promising for low temperature and waste heat recovery in applications, where ORC (regular or with zeotropic fluid) is not feasible. This is seen

also in the development of the Kalina cycle systems applied to waste heat or geothermal resource with power output range of 50 kW to 5 MW. The review shows also prospects of combined systems of power and cooling production. Applications have not been seen probably due to the environmental, material and regulatory issues with water-ammonia chillers or in case of experimentally explored Goswami cycle due to low flexibility of cooling output.

Regarding alternative working fluids the previous research is much less extensive. Several alternatives to the water-ammonia mixture have been proposed in theoretical studies. Specifically, interesting is use of alcohol mixtures or aqueous salt solutions and among them solution of LiBr. The LiBr solution is a working fluid applied in many commercial absorption chillers but only several studies considered it for power production and waste heat recovery or similar open loop heat source application with stress on utilization efficiency. Low pressures (vacuum) in all cycle determine that LiBr solution can never be a competition in field of large power output systems, however it can be beneficial in small distributed systems due to less strict legal requirements or possibility of designing efficient turboexpander for very small mass flow rates, but large volumetric flow rates. Due to the application extent of LiBr chillers, this working fluid also offers a large potential for combined cooling and power systems. It is documented by a large range of principles and configurations of these combined systems, which were by the author classified into the four major groups, which are:

a) Separate thermodynamic cycles coupled by heat

b) Separate thermodynamic cycles coupled by work

c) Single branch thermodynamic cycle for both power and thermally activated cooling

d) Branched thermodynamic cycle for power or thermally activated cooling

Systems coupled by heat refer primarily to utilization of thermally activated chiller as the bottoming cycle. Coupling by work (mechanical or electricity) means in principle two completely standalone systems, though some components can be used for both of them in integrated configurations. The temperature and pressure potential of the expander or condenser, throttling valve and evaporator can be used in a serial configuration. However, it provides a trade-off between cooling and power or one product can be available just in small overall ratio to the other as a result of the thermodynamic peculiarities (cooling in Goswami cycle). The last configuration is the domain of the absorption systems, where either a very flexible system can smoothly switch the evaporated refrigerant between expander and the chiller branch, or a system can utilize the rich

solution from the desorber in various methods (with or without additional heat input) but the flexibility is sacrificed.

Regardless of this wide range of systems and extensive research in each of them, it appears that the works of the author are the first to propose the simple configuration with the parallel chiller loop in one branch and the expander loop in another using LiBr solution (or any aqueous salt solution). This configuration was therefore selected for a detailed analysis of its potential. Lastly the power cycle with LiBr (and generally any salt solution) has, based on available literature, never been experimentally explored. Insufficient attention in the literature is also paid to the experimental investigation of the temperature glide in absorption systems in general. An experimental investigation of LiBr APC should serve to verify the theoretically predicted benefits and show potentially yet unforeseen obstacles. Therefore, an experimental study is suggested to better clarify application potential of this system.

Chapter 3

Review of prospective components design

In order to be able to successfully design the proposed APC, a review for consideration on construction of absorption systems and their major components of the cycle is performed and presented in this section. A separate chapter is then dedicated to the expander. The reason is that expander is a key and specific component, to development of which is in this thesis devoted special effort and specific novel approach.

One of the key aspects of design of heat exchangers is the temperature glide of the bulk temperature in the phenomena of desorption and absorption. It is often taken as a given fact for both water-ammonia and LiBr-water systems [36]. The available literature although failed to provide experimental confirmation of the actual temperature profile in the heat exchangers with the temperature glide during phase change. The available information for commercial Kalina plants are limited to statements of boiling (desorption) taking place in a Shell & Tube or plate type heat exchanger and absorber being of a plate heat exchanger type [49, 136, 139, 140]. This situation persists even though a number of theoretical studies on the Kalina cycle are quite high and it has been even partially commercialized. Similar is the situation in the literature regarding LiBr systems and the phenomena of desorption and absorption. Regardless number of heat and mass transfer investigation, the actual temperature profile has either not been measured or the obtained temperature change was minimal [149, 150]. Limited experimental information reporting the actual temperature profile (but not within absorption/desorption) and usually a decrease in heat transfer coefficients can be taken from studies of refrigerant mixtures as in [151, 152, 153, 154, 155].

Regardless these shortcomings in reported information, the range of experience

and possibilities with components and whole absorption systems is very high, especially in field of absorption cooling. The review of these components primarily with respect to applicability in LiBr APC below includes both standard solution from absorption chillers as well as several options in research phase, which appear prospective for the concept of the APC. Schematic representation illustrating types and configuration of major components in a typical LiBr chiller is in Figure 3.1.

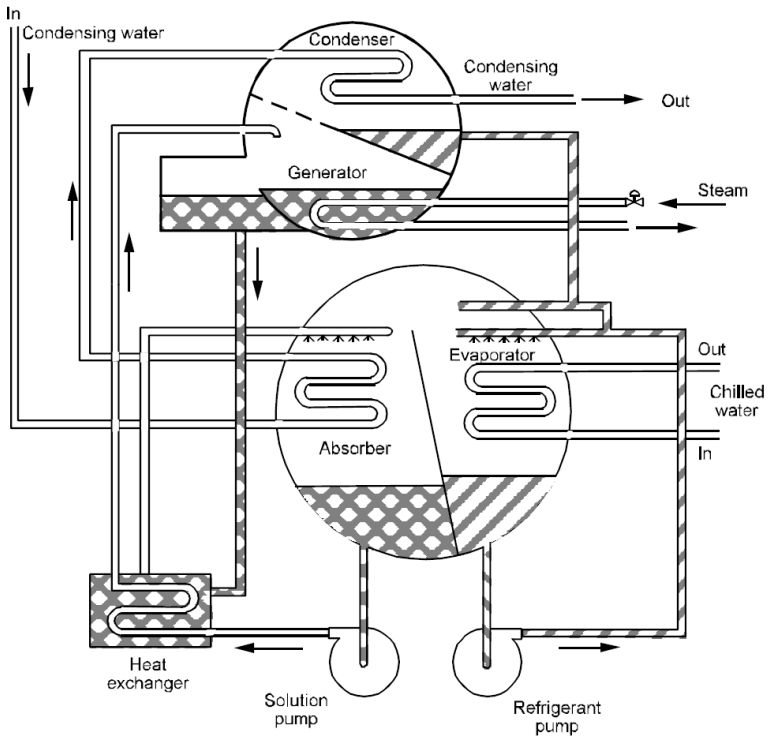

Figure 3.1: Schematic design of typical commercial LiBr absorption refrigerators. Reprinted from [156]

3.1 Absorber / Desorber

Absorber design is identified as the crucial point of absorption heat engines with complicated phenomenon of simultaneous mass and heat transfer. Several designs has been developed, their summary for absorption heat pumps is given in [149] and they are also discussed below together with desorber (steam generator) designs. In any absorber design the following points are most important.

- The interface surface between vapour and absorbent has to be as large as possible.

- The boundary layer of the absorbent film has to be refreshed continuously.
- The absorption heat is to be withdrawn at nearly the same place as it is developed.

In typical absorption cooling the most common absorber and desorber heat exchanger design is of shell & tube type, along with the type with evaporator and condenser. These are often integrated within a single tank (shell) with open space between compartments and processes driven by local concentration and pressure differences as in Figure 3.1. It is important to note, that steam generator (desorber) is here of a pool boiling type thus the temperature glide can be hindered by mixing and convection within the large volume of liquid. Mass transfer in absorber, which relates to its size, is the issue of the boundary layer thickness between the vapour and solution (absorbate and absorbent) [157], therefore designs decreasing the film thickness or promoting intermediate mixing of the solution to "recharge" surface absorption capacity result in higher absorption rates. As [36] mentions, it's suitable for good absorber performance that the absorbent film is no more than 2 mm thick. To promote heat and mass transfer, surfactants such as octyl alcohol might be added into the solution in periodic dosing. It causes change of flow pattern into "Maragoni convection" where as surface tension forces are significantly lowered and the mixing between the layers of liquid is highly promoted. Specific design cases are further discusses below.

3.1.1 Falling Film Absorbers

Falling film type of absorber can be considered as a standard solution, especially for commercial absorption cooling systems. There are two basic common designs which are horizontal tube bank and vertical tube design, as seen on Figure 3.2. For vertical tube design is often applied counter-current flow between vapour and the film, while for best theoretical temperature glide in APC, co-current flow is required.

A thorough review of experimental investigations of LiBr solution absorbers in [149] provides parameters for tubes outer diameter from about 9.5 to 20 mm. Horizontal tube banks are giving heat transfer coefficient of liquid side of 571-803 $W \cdot m^{-2} \cdot K^{-1}$ and mass transfer coefficients 2-3 $E^{-5} \cdot ms^{-1}$. Smallest tubes show highest heat and mass transfer performance. Example of small helical absorber achieved parameters of 400 $W \cdot m^{-2} \cdot K^{-1}$ and mass transfer coefficients 1-4 $E^{-5} \cdot ms^{-1}$. Helical tubes HX is also mentioned as providing highest surface per unit volume. Vertical tube absorber operating with LiBr and other Lithium salts solution, where the cooling water was in annular space around the tube, has resulted in heat transfer coefficients of 200-500 $W \cdot m^{-2} \cdot K^{-1}$ and mass transfer coefficients 2-6 $e^{-5} \cdot ms^{-1}$. Introducing film

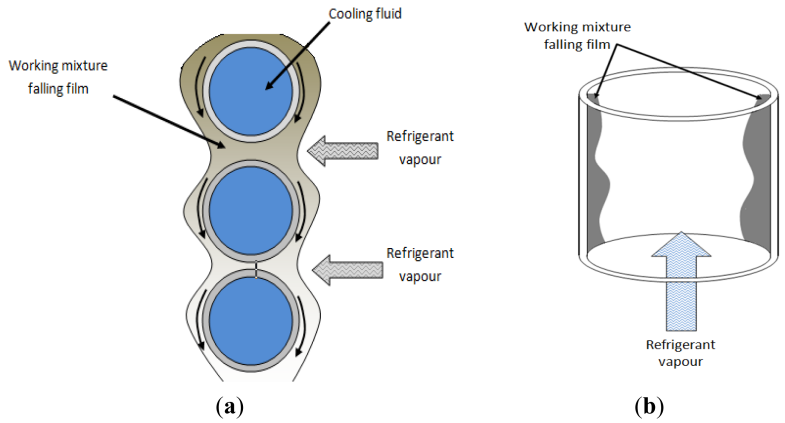

Figure 3.2: Two basic types of falling film absorber: a) horizontal tube bank, b) vertical tube. Reprinted from [149]

guiding fins can result in 100% increase in absorption rate, similarly using floral or hydrophilic tube instead of bare ones increases wetted area by 20-110 %. Surfactants can also improve absorber performance. Alternatively there were explored possibilities of design with structured vertical plates [158, 159] or conical discs [160] but manufacturing of full scale absorbers with these features appears as rather costly.

3.1.2 Adiabatic Absorbers

In adiabatic absorbers the mass transfer process of absorption is separated from the heat transfer that takes place beforehand in a rich solution heat exchanger. Although it is in absorption cooling devices possible to subcool the rich solution enough to absorb all the refrigerants vapour, for proposed LiBr based APC in WHR applications, the amount of solution might be so small it becomes impossible to absorb all vapour with subcooled solution. It can be however perspective as a first stage of absorption where the bulk temperature is increased before the heat transfer to the heat rejection fluid takes place. For LiBr, spraying and flat-fan sheets absorbers have been reported with relatively similar reported performance results. Atomization nozzles might require additional energy input. [149]

3.1.3 Bubble Absorbers

Bubble absorbers have high wetted area and generally provide better performance than falling film absorbers, especially for low solution flow rate. Vapours are introduced into the liquid by nozzles or openings in the bottom or walls of the absorber (porous wall can be thought as alternative process to further explained membrane based absorber). Design of absorber based on commercial

plate heat exchangers or concentric pipes is possible. Bubble absorbers are reported primarily for water-ammonia systems (perhaps due to high volumetric flow in LiBr systems) with heat transfer coefficients between 800 and 5400 $Wm^{-2}K^{-1}$ and mass transfer coefficients possibly above 0.001 $m \cdot s^{-1}$. It is necessary though to ensure proper operation and limit backwards flow of the solution to vapour path during non-steady and non-nominal states. [149] Bubble absorber was also used in experimental Goswami cycle [138].

3.1.4 Flat plate desorbers

Serially manufactured flat plate exchangers have prospect of lowering system cost. They were not found to be applied as absorbers (except for bubble type and Kalina cycle without construction details) with obvious reason being the issue of liquid solution distribution equally to all plates. Using a flat plate exchanger has been however proposed for desorber in [161]. When using LiBr solution, calculated pressure drop may be of a similar order as the absolute values of outlet pressure and the boiling temperature of the solution may be considerably changed. Experiments were performed at relatively high temperatures (190°C heating fluid) in co-current configuration and temperature differences larger than 38°C. A significant increase in surface area was suggested to improve the performance. Similarly a pressure drop of 20 kPa and higher has been measured in high temperature flat plate desorber in [162]. It can be summarized, that this heat exchanger type does not seem as very suitable one for low temperature APC, where turbine inlet pressures are around 10 kPa and good temperature match with low temperature differences in desorber to decrease exergy destruction is required.

3.1.5 Membrane absorber and desorber

Shell & Tube configuration usually results large and heavy equipment limiting economic applicability. There is however another approach based on membranes processes. This concept promises to intensify mass and heat transfer, thus enable smaller size, lighter and cheaper system. Membrane is used to separate liquid and vapour in absorber and desorber (generator), allowing only vapour to pass through. The schematic representation of the process with membrane is in Figure 3.3a. For this purpose, hydrophobic membranes with high liquid entry pressure are required. [163]. Improvement in membrane performance can be linked to nanotechnology as with a preparation of a superhydrophobic nanofibrous structure of membrane reported in [157]. Membrane based generator (desorber) could in some extent solve several APC issues. First, concentration of solution is changing over the membrane length. This is often considered to have a negative effect on system performance. However in the proposed concept of counterflow heat exchange this is brings a benefit of securing solution temperature glide. Another advantage is constraining of the

liquid solution and separating it from vapour, thus eliminating the separator and limiting risk of salt transfer along the vapour to the turbine. Care should be however taken regarding pressure drop, where the pressure drop across the membrane may be of a similar order as the absolute pressure of the generated vapour, similar as for the flat plate desorber.

Using membrane as generator has been reviewed and theoretically and experimentally investigated in [164]. Limiting aspect of the process is found in mass diffusion. Unlike in pure water, bubble growth rate is small and inhibited. Relatively good performance is reported with falling film desorber, though for boiling inception rather high wall temperature is necessary. Two processes can occur in membrane, first is direct diffusion desorption from liquid through membrane, second is creation of bubbles and two-phase flow from which vapour bubbles transfer through the membrane wall. Direct diffusion desorption takes place even when solution pressure is significantly higher (e.g. 23 kPa vs. vapour 6 kPa). Once the solution temperature is increased above solution saturation temperature, boiling takes place, increasing the mass transfer significantly as bubble formation rapidly increases solution-vapour surface area (effect similar to bubble absorber). Experimentally there is currently ongoing research in membrane absorption chillers in Spain with example for absorber and desorber membrane experimental rig in [165]. In the experimental rig there is however not considered potentially beneficial effect of variable composition and temperature along the length. Research project focused on absorption mini chillers based on membrane technology was also undertaken by E-ON with testing of 25 membranes. Conclusion was however that further improvement in membrane technology would be preferred [166]. A work describing whole experimental membrane based chiller [167] suggests possibility of pore size up to 5 μm for absorber (for desorber the proposed range was up to 1 μm) with low pressure drop (at absorption rate 0.002 $kg \cdot m^{-2} \cdot s^{-1}$). This work also mentions that for desorber the main driving force is vapour pressure difference based on temperature (in non-boiling mode). The solution pressure and thus also pressure drop are in this regime relatively irrelevant, see Figure 3.3b. For the absorber however the difference between vapour pressure and saturated solution (pressure potential) is in range 0.5-1.5 kPa.

3.2 Separator

Several approaches can be taken regarding separation of vapour and liquid phase of the fluid, where the vapour phase is routed to a turbine or chiller branch and the liquid phase to recuperator. The natural gravity based separation is used in shell & tube desorber as their integral design, where there are separate liquid (in bottom) and vapour (in top) outlets. [36] It is also visible in Figure 3.1. Additionally, vanes can be used as it was reported for the case of the vane

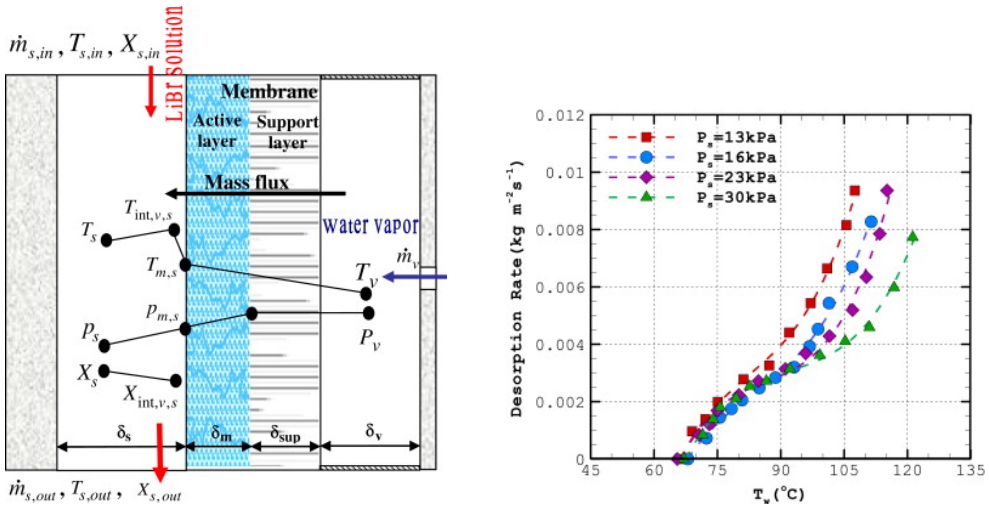

(a) (b)

Figure 3.3: (a) Representation of membrane processes when used for absorption into LiBr solution. Reprinted from [163] and (b) effect of solution pressure and temperature on desorption rate. Reprinted from [167]

type separator in the Húsavík Kalina plant. [140]

Separator of the two phase mixture with a high liquid content is also tackled in geothermal industry where cyclone and gravity types of separators are used. Gravity separator may be designed based on a minimal allowed diameter of droplets passing to the vapour outlet and gravity force acting on it as it travels across. A comprehensive review of cyclone separator design is given in [168] while general information about two phase separation processes in geothermal field are summarized in [20]. In case of once-through heat exchangers with high fluid velocity at the outlet, the geothermal separators appear as a suitable choice of design, but care should be taken regarding possible pressure drop.

3.3 Pumps

Regarding the choice of suitable pump type, a work of author's group [169] reviews different types of pumps for small volumetric flowrate in ORC systems. Among the requirements are decent efficiency, reliable steady operation without pulses and low net positive suction head requirement to limit cavitation. Gear pump appears to satisfy well these requirements. Gear pump with a motor connected via a magnetic coupling was also the pump choice after several trials in experimental Goswami cycle [38]. In standard absorption chillers, use of variable frequency drives for pumps is suggested for efficient operation [36], in experimental system possibility to control a pump is a must.

3.4 Other

The reference [36] provides a useful set of practical information about absorption chillers of which many are applicable also into a concept of absorption power cycle. These include information about addition of corrosion inhibitors, with which and with noncondensible gas purging life expectancy is about 20 years. The purging can be realized by automatic system typically based on hydro ejector. Only after long term shutdown or before first use is used a separate vacuum pump. It is mentioned that for long term shutdowns it's suitable to pressurize the system by inert N2 gas. From material point of view, commonly used materials are carbon steel and copper while stainless steel might be subject to pit corrosion. Rubber is used for sealing. For cooling machines air cooled condenser is not recommended and not common as rather higher temperature of absorber would result in higher LiBr concentration in desorber with risk of crystallization of rich solution, especially after recuperator when it cools down.

Additional component in LiBr absorption chillers is a recuperator heat exchanger. This is in both experimental and commercial system basically always of a flat plate type.

Chapter 4

Review of micro-expanders and additive manufacturing technologies

An expander is an essential component for power cycles regarding both cost and efficiency. An argument for the choice of the impulse turbine is made based on a prospect of a cost-effective turboexpander, assuming the utilization of additive manufacturing (AM) technologies. A review of previous considerations of AM in turbomachinery, therefore, is the main focus of this chapter.

4.1 Expander type consideration

An expander is the essential component for power cycle regarding both cost and efficiency. In distributed energy systems there are two fundamental choices of expanders. The first is a volumetric expander including piston, scroll, screw, rotary vane or Wankel types. The advantage is that these expanders may often be derived from compressors. They are considered to be well fitted for small volumetric flow rates, while achieving decent efficiency and reasonable rotational speed. [170, 171]

The APC with aqueous salt solutions has very low pressures and thus high volumetric flow rates in the expander, suggesting the use of a dynamic expander, i.e. a turbine. Turbo-expanders are a standard for applications with a higher power output than about 500 - 1000 kW_{el}. In smaller applications they are rather rare. Their major types are radial inflow turbines (90 ° IFR), radial cantilever turbines and axial turbines. In the author's view, small turbines have some significant advantages in terms of a micro expander construction kit compared to volumetric expanders (see [172]). In a turbine the fluid volume change during expansion is not just implemented by changing a chamber volume

but by simultaneously increasing flow velocity and area. High expansion ratios can be implemented even in a single stage. This is the reason why a turbine design with fixed main dimensions (e. g. diameter, length) can cover a wide range of boundary conditions (different fluids, mass flow rate, expansion ratio etc.) just by adapting nozzle length and area, blade height and/or degree of admission. Partial admission (p. a.) is a measure to handle part load or low flow rates. In a turbine, there are no contact seals. Hence, no continuous flow of a lubricant is necessary which could spoil the working fluid. More details are given in [172].

For small and micro systems, generally single stage turbines are considered. Currently 90° IFR turbines are often favoured, for example [173, 174, 175, 176, 177, 25]. The reasons for this include its mass application in turbochargers for internal combustion engines and the theoretically achievable high efficiency. The design point of these turbines is at a very high rotational speed. The issues for the limited number of actual commercial applications of this turbine type include the availability, costs and life span of bearings for high rotational speeds, together with a complex geometry, where the customization of very small series is too expensive and time-consuming. Attempts of some companies to design a single design of a small unit for modular application (such as formerly offered Siemens SST-050 50 kW axial steam turbine) have not experienced the expected widespread either.

Generally it is unlikely that the micro turboexpanders in decentralized units (not only and necessarily APC) are going to be ever produced in large series. Especially for waste heat recovery, customization is key for quality performance. A possibility to effectively tailor the turboexpander design to the desired operating conditions of the cycle is a necessity. That comes with increased costs mainly on two fronts – the turbomachinery design and its manufacturing. In the ORC systems, an approach solving both modularity and uniformity of general turbine design together with customization to specific needs at the level of blading modifications has been proposed with primary application in ORC. This effort resulted for example in the micro-turbine-generator-construction-kit (MTG-c-kit) for power output of 5-200 kW_{el}. It achieved a commercialization (DEPRAG SCHULZ GMBH u. CO) though with a costly price tag about 1000 €/kW_{el} and figure depending further on the number of turbines ordered. [178, 179].

Regardless of the modularity and other favourable features of the MTG-c-kit, it has not reached its full potential for wider applications. Low temperature and micro power systems (<10 kW_{el}) can be named as the field with major obstacles. In order allow for greater widespread, the following aspects should be tackled:

- Reduction of specific costs, especially for low power applications
- Reduction of manufacturing lead times, including tests of multiple blading design
- Improvement of the design and customization of blading for specific applications
- Further reduction of the number of components (e.g. wheel with shroud in a single piece)

Cost-effective manufacturing of even single-piece produced customized turbines rotors and stators has some interesting possibilities via additive manufacturing (AM). It was not until the last decade since AM technology allowed to produce technically feasible products while being a cost-effective option in comparison with conventional manufacturing technologies. In low temperature APC, the expected low blade loading stress and low operating temperatures suggest even use of polymeric plastic materials for nozzles and rotor buckets. Regarding polymeric materials, Zywica et al. discussed the possibilities of heat resistant plastics for a high-speed microturbine for a domestic ORC system. [180, 181] In order to show the current state-of-the-art, a review of major additive technologies and their micro-turbine applications are shown below.

4.2 Additive manufacturing methods for turbomachinery

To present the current state-of-the-art of AM for turbomachinery, a brief overview is presented. Summary of the possible additive manufacturing methods and their division according to ISO/ASTM 52900:2015 terminology is presented on a tree chart in Figure 4.1.

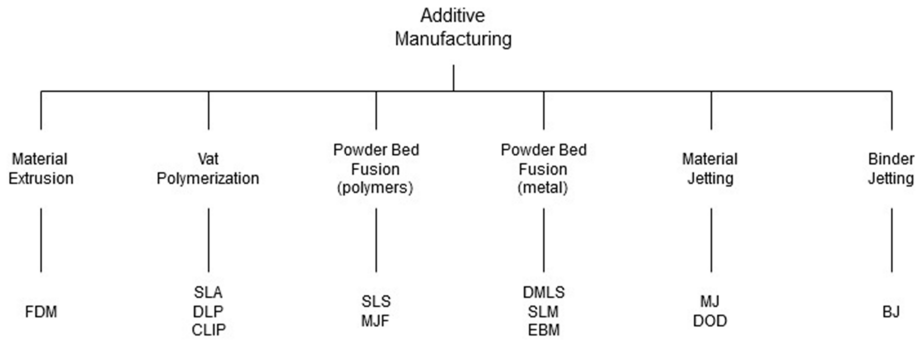

Figure 4.1: A tree chart of additive manufacturing technologies according to ISO/ASTM 52900:2015

Additive manufacturing has found its way towards large-scale turbines and major industrial manufacturers but not as a manufacturing technology for entire wheels or blades, but rather repairs, maintenance and overhaul of the current machines. The author's research group sees further interesting potential of some of the above-mentioned technologies also for small to micro scale low temperature applications, as plastics can be utilized and lower mechanical loading is usually present. Based on the literature review as well as on in-house tests, an overview of AM applicability for micro turboexpanders was created and presented in Table 4.1.

Table 4.1: Summary of AM technologies for small turbines

Technology	**Possible applications**	**Materials**	**Max. T**	**Advantages**	**Drawbacks**
FDM	Low demand parts, other parts with limits	(Ultra) ABS, PETG, composites	∼100 °C	Cheap, widely available	Rough surface in as-printed, need of supports, non-uniform properties
SLS	Any part	Nylon, carbon, TPU, PP	∼80 °C	Cheap, no support, good accuracy	Limited T ∼ 80 °C
SLA	Stationary parts, rotor with limits	Resins	>200 °C	Good resolution and surface quality	Most expensive plastic method, needed supports, fine features and tolerances are a problem
DMLS	Flow components	Metals (steel, Al, Ti)	>1000 °C	Most available metal AM technology	Expensive, sensitive to fine-tuning, Rough surface in as-printed, need of supports
MJF	Any part	Nylon based	∼80 °C	Cheap, no support, best tolerances, fastest	Limited T ∼ 80 °C; domain only of company HP
EBM	Flow components	Metals (steel, Al, Ti)	>1000 °C	Fast, well-tuned properties	Very expensive

4.2.1 Stereolithography

One of the first AM technologies was *stereolithography (SLA)*, whose core functional principle is UV curing of a liquid resin. Most of the resins have a temperature limit of around 70 °C which significantly reduces its potential for turbomachinery applications, but special high-temperature resins that can withstand temperatures up to 290 °C for low loaded parts exist. Novel modifications of SLA such as continuous liquid interface polymerization (CLIP) promise fine tuning of properties of the end product, improved precision and print speed. [182, 183] Radial inflow air turbine of a kW-scale made entirely by SLA was reported. [184] Please note that maximal rotational speed in the experiments was below the nominal design point, suggesting issues either in bearings the material or the construction design. In addition, SLA was tested as a method to manufacture diffusor vanes for a small scale experimental centrifugal air compressor [185] or for models and cold aerodynamic tests in fluid dynamics research of companies and research institutes. [184, 186]

SLA has obvious advantages in surface quality similar to glass, rather high precision provided by print with layer thickness up from 25 μm and thin sharp structures useful for trailing edges of blades, which suggest good applicability. On the contrary, regardless being the most expensive plastic AM method, the main drawback was found in the accuracy of the product. The circular tolerance can be up to 0.5 mm for a wheel of 120 mm in diameter with a state-of-the-art SLA printing machine. The accuracy according to the author's experience hasn't improved regardless of trials with various materials and settings. Support structures are also needed for SLA, leaving burrs, which need to be manually polished. Lastly, the resin components are rather brittle and fragile, which has also been experienced by the author by several incidents resulting even in complete shattering of one turbine wheel.

4.2.2 Fused Deposition Modelling

Fused Deposition Modelling (FDM) is certainly the most common AM technology amongst the domestic applications and is widespread at the market for reasonable prices. Nonetheless, the quality of its prints is usually not able to fulfil requirements and criteria for turbomachinery operation. The product inhomogeneity is rather large, which is a significant issue for rotating parts. The minimum layer thickness is also rather high, up from around 80 μm (typical >150 μm) and thermal effects cause large deterioration of accuracy. The circular tolerance on a wheel of 120 mm in diameter with professional FDM manufacturing exceeded 0.5 mm. Support structures are essential, especially for overhanging structures and they leave burrs after removal. In general, the surface quality is quite rough and requires additional treatment. Concerning the materials and their temperature resistance, FDM prints can sustain temperatures of over 80 °C and exceptionally above 100 °C (Ultra ABS

material). A reference for small-scale turboexpander – a prototype of a 90° IFR 1 kW scale turbine – was found in [187]. An experimental investigation of another FDM manufactured turbomachine was presented in [186], FDM was used only for nozzles while the rotor was machined from glass reinforced polyether-ether-ketone (PEEK). Air tests have proven operation at speed of more than 32 000 rpm, maximum aerodynamic efficiency around 65% and predicted efficiency in ORC with R245fa up to 66%. This AM technology finds many application in less stressed turbine parts, where surface quality is not critical, such as radial inflow turbine casings [187, 188]. Suggestions to use this method mostly for stator components can be supported also by studies of NASA, which tested the possibility to manufacture guide vanes for turbojet engines by FDM from materials as thermoplastics or Ultem$^{\text{ő}}$ with carbon fiber. [189, 190]

4.2.3 Selective Laser Sintering

Selective Laser Sintering (SLS) is an AM method of selective sintering of a polymer powder – usually nylon powder and composite mixtures – by a high-power laser. This technology provides and interesting option for small-scale turbomachinery. The height of individual layers could start from about 60 μm. Together with no need for supporting structures, it provides decent surface quality, even without further polishing. The circular tolerance on a test piece of 120 mm in diameter proved some of the best numbers out of the tested AM technologies, reaching under 0.25 mm out of several test prints. The temperature resistance of the materials is usually around 80 – 100 °C and a bit over 100 °C for composite materials. No turbomachinery applications nor references have been found in the literature. In the authors' research group, it is however of a high interest as its features, such as accuracy, rigidity, price and surface quality make SLS a truly promising technology for small to micro scale low temperature turbomachinery applications.

A very similar technology to SLS is Hewlett-Packard's *Multi Jet Fusion (MJF)*. It also belongs to the polymer powder bed fusion family of the AM methods and uses nylon as the main material. The main difference between MJF and SLS is the heat source. SLS uses a laser to scan and sinter each cross-section, while in MJF an ink (fusing agent) is dispensed on the powder that promotes the absorption of infrared light. An infrared energy source then passes over the building platform and fuses the inked areas. Essentially, MJF is a combination of the SLS and Binder Jetting technologies. The fusing agent currently used in MJF systems is black in colour because dark materials absorb radiation more effectively. As a result, MJF parts have a grey appearance. This technology has the advantages of nylon SLS technology and is cheaper per printed piece. Also, the dimensional accuracy is highest amongst all of the additive manufacturing methods. This makes this technology excellent for prototyping of turbine flow

components.

4.2.4 Direct Metal Laser Sintering

Last but not least, *Direct Metal Laser Sintering (DMLS)* technology is presented as one of the major AM technologies, which works on a similar principle as SLS, but with metal powders. The minimal layer height is similar to SLS but the support structures are necessary and resulting surface roughness is rather high. Altogether these factors limit the application for turbomachinery in the as-printed state. On the other hand, majority of references have been found for this AM technology in the literature such as [174, 191]. The possibility to print cooling channels directly without a need of drilling has been successfully explored for high temperature turbochargers for automotive. [192, 193]

4.2.5 Post-processing of AM components

Almost any part produced by AM in its as-printed state is not fulfilling the requirements for turbomachinery operation. Post-processing is therefore an essential part of the manufacturing process and is the finishing operation with a goal to improve the quality of the part and to meet the design specifications. The printed part has to account for additional material that is removed during the post-processing, as most of the methods have effects on geometry.

Metal parts post-processing includes a heat treatment before the component is removed from the support plate, otherwise the part may get cracked or damaged. Heat treatment of the separate part is usually done before the machining or finishing process, which follows standardized procedures. [194] Alternative method is *Hot Isostatic Pressing* is often adopted in aerospace printed parts and whole metal turbine blades to reduce the porosity of the material and improve the fatigue resistance of the part. [195, 196, 197] Fatigue strength of AM parts is one of the main barriers that limits widespread use of AM also for critical parts of larger turbomachines. [198] The microstructure of the part is full of impurities and voids introduced during the layer-by-layer method and this may initiate a crack that leads to fatigue failure of the part. [199] Several methods might be adopted to increase fatigue strength of an AM part, e.g. shot, ultrasonic or laser peening or heat treatment for residual stress recovery. [198]

Another issue is the surface quality of the part in the as-printed state. The roughness is usually not sufficient and not suitable for turbomachine parts as it would lead to very high friction losses in the fluid flow channel. Hence, machining or polishing of the functional surfaces is very often applied. If very low surface roughness is to be obtained, it might be necessary to polish the blade surface using sand or bead blasting. *Electrochemical machining (ECM)*, *abrasive flow machining (AFM)* or a combination of these have been

successfully used as conventional methods [200] and now are recommended and explicitly configured for AM parts [201].

Additional heat treatment is not common for plastic parts as these are usually much less loaded then metal parts. [202, 203] Nevertheless, it still significantly improves the material properties, as has been shown for FDM parts in [204, 205]. Some improvements have been achieved also for nylon SLS parts. [206] SLA methods are usually post-cured by UV light rather than thermally treated. Surface quality treatment has similar possibilities as for metal AM parts. Additional option is using suitable solvent vapours and chemical treatment for smoothing of the surfaces with very little to negligible impact on the final geometry of the product. Also, typically for SLS, coating of the part can be applied. [207]

This work focuses however in exploring low cost and proof-of-concept possibilities. Heat treatment will not be applied as the loading stresses will be very low. Regarding the surface quality, for the low cost and in order to create a baseline, performance of the as-printed surface quality will be explored primarily. In several cases, effect of surface polishing by hand tools will be assessed. Turning on lathe will be however applied to achieve circular and cylindrical tolerances.

Chapter 5

Goals of the thesis

Bases on the thorough review, LiBr aqueous solution (and generally salt solutions) used typically in absorption chillers may hold a significant thermodynamic and technical potential for power production as the Kalina cycle has. Possibilities of these absorption power cycle (APC) systems with salt solution working fluids have in the past, however, been only rarely theoretically investigated. Furthermore, no experimental work has been found to explore the technical feasibility of such concept. The goals of the thesis can be therefore summarized as follows:

- Find theoretical benefits and range of prospective applications
- Upon the theoretical potential, prove technical feasibility of the APC by:
  - Designing and building APC as a proof-of-concept
  - Demonstration of operability of APC and its components, including turboexpander featuring additively manufactured components
  - Provide comparison between theoretical and real operation of key system's components, especially regarding temperature glide and expander feasibility
- Based on system operation, suggest actual range of applicability and

suggested heading of future salt solution APC development The first goal of the thesis lies in theoretical investigations to identify the application potential in two prospective fields, which are the waste heat recovery (WHR) and combined power and cooling. The potential is evaluated in comparison to other suitable benchmark technologies such as absorption systems with other working fluids (typical water-ammonia mixture from Kalina cycle) or organic Rankine cycle (ORC), an industrial standard in WHR and small externally heated power

producing systems. Clearly already from the literature review and parameter consideration, APC with salt solution might be feasible only in decentralize energy systems.

The second goal is to prove a technical feasibility of the APC and its components. Even though a single component of the system and related physical phenomena could be studied in detail, building and operation of the complete system to prove all components in operation together is seen as much more beneficial for research and development. APC with salt solution has not been to authors' knowledge successfully operated before. The system components can be to certain extent adopted from absorption chillers and from small power systems such as ORC. The goal of the system design is to have maximal benefits of the APC principles (such as temperature glide) but at the same time ensure components and system operability. Specific focus of this goal is in investigating possibilities of a cost-effective turboexpander. Possibilities of using plastic materials and additive manufacturing of the components is to be explored.

Based on the experience with operation and its analysis, another goal is to perform a comparison between the real component and system operation and the predicted performance. The crucial components and phenomena are cycle performance, i.e. cycle and utilization efficiency, temperature glide determining the extent of possible heat transfer from the heat source and performance of the expander. In summary an actual range of APC application feasibility and major issues for future research and development are to be concluded.

Chapter 6

Theoretical cycle investigations

An interesting possibility and many research gaps were identified in the literature review regarding the salt solution APC performance. This chapter therefore investigates the theoretical performance for specific application fields in greater detail. After description of the calculation methods, used models and description of performance indicators (different efficiencies can be defined) are presented the results. They start with an analysis of ideal cycles' potential, validation of APC models and illustrative presentation of the APC system and of working fluid parameters. Following is an analysis of performance potential for waste heat recovery, performed for a range of parameters and including a comparison to various alternatives or sensitivity of performance to cycle parameters. These results were published mainly in author's works [VN1, VN2]. Then, three case studies show the specific APC potential in selected applications including low temperature solar thermal system, application as a bottoming cycle or CCS systems waste heat recovery [VN3, VN4, VN5].

The second part of the chapter focuses on a concept of a combined power and cooling system with well controllable ratio between the two products. As such, it has not been considered with salt solution fluids until author's work [VN3] and then it has been in detail investigated in author's work [VN6] providing again cycle detailed parameters, sensitivity to main control parameters, comparison to benchmark combined system, comparison between multiple salts for aqueous solution. Finally, an analysis of performance against APC optimized for waste heat recovery points out a significant difference in cycle parameters between the two specific applications.

6.1 Models

Configurations of the thermodynamic cycles considered in this work are summarized here, while their choice is driven not just by the highest theoretical

parameters, but also technical feasibility. After their introduction, thermodynamic models are set up, together with specifics in calculation methods, arising mostly from employing specific working fluids and their formulations. The thermodynamic models are complemented by their input parameters and auxiliary models of other equipment of larger systems into which the cycles are applied in further investigations.

6.1.1 Cycle configurations

Many previous studies focused on potential of performance improvement by increasing complexity of the cycle configurations. This work aims at providing a thorough investigation of simple layouts that have a potential for actual applications, so that it can be later supported by an experimental study. The layout of baseline absorption power cycle is illustrated in Figure 2.1b. This layout is in principle the same as the basic one proposed by Ishida et al. [54, 55] and the one used in the work of Hernando-Garcia et al. [57]. The cycle consists of a pre-heater at the end of which (state 3) is saturated liquid, followed by a desorber-steam generator from which exits a mixture of steam and absorbent solution (state 4, in the figure as single exchanger). The liquid and vapour phases are split off in the separator. After separation, the steam (state 5) is in a superheated state due to the different liquid–vapour equilibrium temperatures of pure water and the solution. The separated rich solution (state 7) goes to the recuperator where its heat is transferred to the feed solution (state 1). Steam goes to the turbine, after which (state 6), at the beginning of absorber-condenser, it is adiabatically mixed with and absorbed into the LiBr-rich solution (state 9). Steam is absorbed until liquid–vapour equilibrium is established, resulting in a temperature increase while maintaining the same pressure (state 10). During absorption, this temperature glide is also present. As the liquid absorbent concentration gradually decreases, the (equilibrium) temperature decreases as well. The pressure of the liquid fluid after condensation (state 11) is then increased by the pump to state 1.

The absorber needs to be cooled to reject the heat. In this work the power requirement for heat rejection is evaluated as a major part of the parasitic load. The reason is, that for low temperature systems the related parasitic load can correspond to a significant share of produced work. Same might be the case for heat input when fan or pump is needed. The purpose of the studies performed here is usually a comparison to a chosen reference. The heat input mass flow rate remains in case of open loop heat source the same, while in the heat rejection, mass flow rate and outlet parameters of heat rejection fluid are a function of the cycle parameters. Therefore, only heat rejection will be considered in the analyses with open loop heat source. Three basic and somewhat simplified configurations of heat rejection systems are considered and described schematically in Figure 6.1. These are wet cooling tower (CT),

dry air cooler (DC) and direct air cooled condensation / absorption (ACC). The pressure drop of the air is considered for the analysed cases while in some the pressure drop at the water side is included as well, especially in case of wet cooling towers - CT. Dry cooling methods are based on pinch points, while the air leaving the wet cooling tower is assumed to be saturated with water [208]. The temperature of the cooled water is obtained using a chosen so called approach - the difference between the wet bulb temperatures of the air inlet and the temperature of the cold water outlet. All methods assume an induced draft configuration, so the air properties for the fan power are evaluated at the outlet.

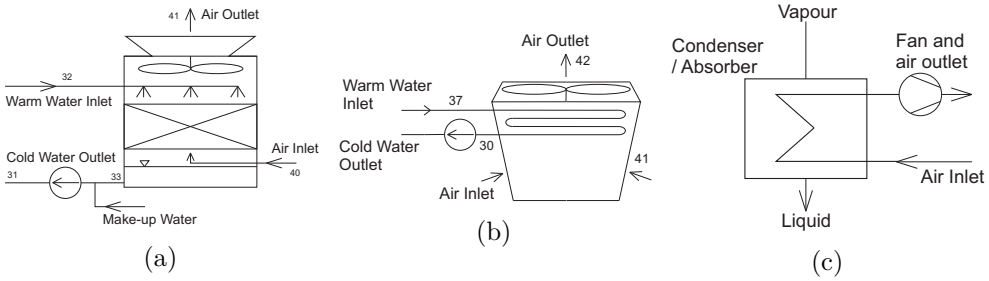

Figure 6.1: Scheme of the (a) wet cooling tower, (b) dry cooler and (c) direct air condensation/absorption used in the models

To assess the performance of the proposed APCs with various working fluids with respect to other options, several reference cycles are chosen and modelled. The cycles used for comparison are mostly based on the Rankine cycle as shown in either simple or recuperated configuration in Figure 6.2. A classical Rankine cycle using superheated water vapour is used only for a reference (RC1). The second (RC2) and third (RC3) configurations are Rankine cycles using various organic working fluids (also denoted by ORC and specific working fluid). For sake of a simple comparison, all ORC are expanding from saturated steam. The application of superheaters in small ORC units is limited by the additional complexity and cost, even though a small superheating of several K might be required. The difference between RC2 and RC3 is in the shape of the saturated vapour curve, as the expansion in RC2 typically ends in the wet steam region (uses so called wet fluids), and in RC3 in the superheated region (dry fluids, although specific cases may differ for the given operating conditions). These two cycles have identical schemes; both follow that shown in Figure 6.2a. In cases where the expansion results in superheated vapour at temperature more than pinch point above the pump outlet temperature, it is considered possible to use a recuperator according to Figure 6.2b, and these cases are presented as R-ORC or the working fluids are grouped under designation RC3R.

When the APCC is investigated, a schematic arrangement of the investigated configuration is represented in Figure 6.3. Two-branch arrangement of the

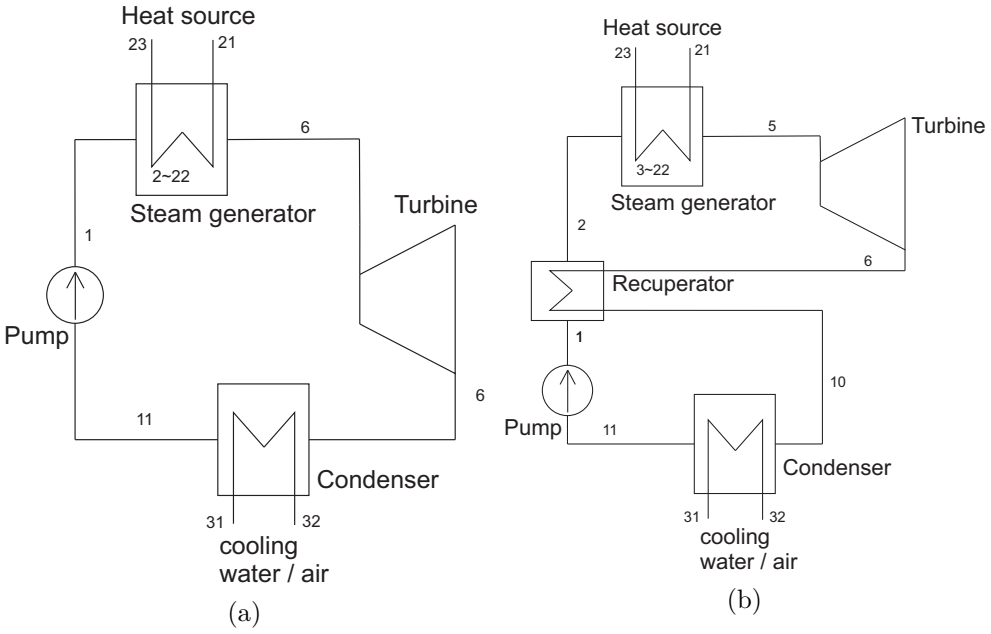

Figure 6.2: Scheme of the reference Rankine cycles in (a) simple and (b) recuperated configurations

cycle is characterized by a separate power branch which corresponds to states highlighted by bold in the cycle 1-2-3-4-5-**6-7**-12-16-17 and by a separate chiller branch that goes through states highlighted by bold in the cycle 1-2-3-4-5-**8-9-10-11**-12-16-17. Apart from this modification, the cycle includes the typical components of the absorption cycle, where the LiBr rich solution goes through a liquid loop 1-2-3-4-13-14-15-16-17. Note that the configuration is actually identical to absorption chillers, just with the power branch added.

The principle follows the APC, only a splitter divides the steam flow into the two branches based on the required ratio between power and cooling, defined as SR (splitting ratio). In the chiller loop, the vapour is first condensed (states 8 - 9), and the condensed water is throttled and evaporated in an evaporator while producing a cooling effect. The low-pressure steam then joins the flow from the turbine in state 12. This low-pressure steam is absorbed into a LiBr rich liquid from stream 15, first adiabatically (stream 16) and then with heat rejection in absorber until saturated liquid at state 17. Only single configuration regarding heat rejection is considered with the absorption and condensation heat being transferred to a water circuit passing through a dry cooling tower.

The reference ORC-VCC system is depicted in Figure 6.4. It consists of an organic Rankine cycle (states 1 to 8) and VCC (states 11-15). Points not shown in the diagrams correspond to pinch points within the heat exchangers. In order to allow the flexible ratio between produced work and chiller output,

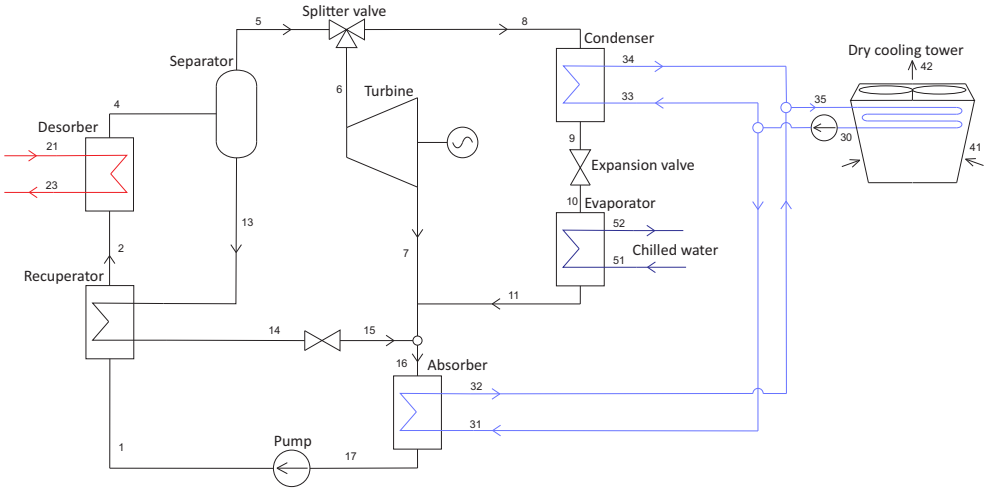

Figure 6.3: Schematic diagram of the proposed combined cooling and power cycle

the systems are entirely mechanically decoupled; ORC has a separate generator at the expander, and the vapour compression cycle has a separate motor for the compressor. The ORC here utilizes R245fa, a typical working fluid for low-temperature ORC. For the vapour compression cycle, R1234ze(e) was chosen as a typical refrigerant representing new, environmentally friendlier fluids.

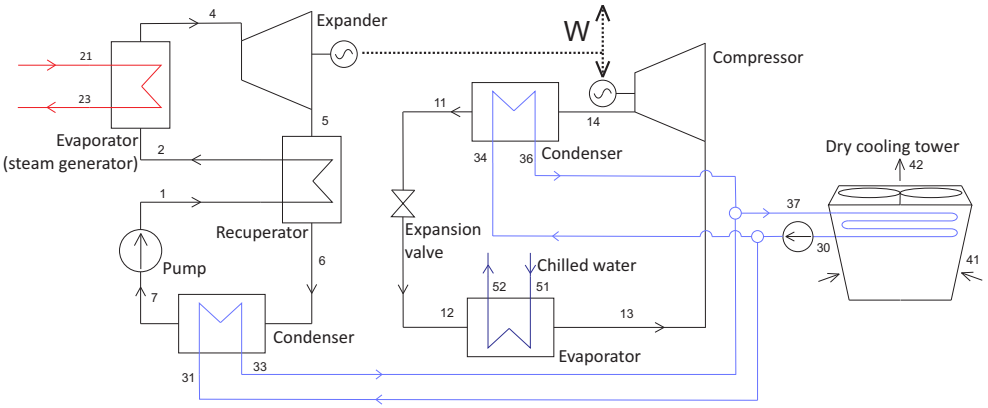

Figure 6.4: Schematic diagram of the reference combined cooling and power system – ORC and VCC

6.1.2 Thermodynamic models

Most of the theoretical investigations are based on pinch point analysis, which gives a limit to heat transfer in heat exchangers. There are rather typical assumptions, which are the following: steady-state operation with the fluid

in thermodynamic equilibrium in all nodes, constant isentropic efficiency of components, no heat losses of the components and no pressure losses (unless specifically mentioned for heat rejection fans and pumps), no subcooling is considered at the absorber and condenser outlet and an effect of varying fluid velocities is neglected. Additionally, electrical and mechanical efficiency are, for sake of clear comparison, neglected as well.

For the reference subcritical ORC, the maximal allowed pressure of the working fluid is additionally limited to 90% of the absolute critical pressure of the working fluid. Note that in some cases, the pinch point can shift between the point of saturated liquid and pump (or recuperator) outlet. Supercritical cycles are then considered for some comparisons as well, but are presented as a separate category (SC-ORC).

The system of balance equations of all the states accounting for every single component and including necessary fluid properties is developed. One of the most elementary principles used in modelling is the conservation of mass flow and energy for each of the component presented by Equations (6.1) and (6.2). The working fluid can be a mixture, thus ξ_{ji} represents the ratio of mass flow of fluid component j to total mass flow in the particular stream i. In the two-phase fluid, the components are evaluated separately for each phase.

$$\sum_i \sum_j \xi_{ji} \dot{m}_i = 0 \tag{6.1}$$

$$\sum h_i \dot{m}_i + \dot{Q} - \dot{W} = 0 \tag{6.2}$$

Rotating components as expanders, pumps, compressors or a fan for dry cooler are calculated using isentropic efficiency, Equations (6.3) and (6.4). Note that consumed work (pump, fan) has a negative sign in order to comply with Equation (6.2).

$$\dot{W}_{\text{exp}} = \dot{m} \left(h_{\text{in}} - h_{\text{out},is} \right) \eta_{is} \tag{6.3}$$

$$\dot{W}_{\text{pump / comp / fan}} = \dot{m} \left(h_{\text{in}} - h_{\text{out, is}} \right) / \eta_{\text{is}} \tag{6.4}$$

6.1.3 Calculation methods

As there are in many models present iteration loops and as optimization and sensitivity analyses are required, the models are built and solved using the software EES (Engineering Equation Solver). It is an engineering software

for solving large implicitly written systems of algebraic non-linear equations including a wide range of fluid property functions. After providing the mathematical model and guesses for the variables, solution is found using a specific variant of the Newton's method. Only in a case of fluid properties based on the Peng-Robinson equation of state is used a process engineering modelling software AspenPlus. It is used in cases, where a suitable mixture fluid property formulations are not present in the EES, nor are they available in the literature to additionally implement them. The range of automatic optimization and analyses is however limited. Results were transferred for final analyses and processing either to the EES or spreadsheets with also available fluid properties REFPROP.

The models of the cycles were mentioned to be based on equations of mass and energy conservation with positive heat going in the system and work out of the system, Equation (6.1) and (6.2), which were written for each apparatus or their parts, and also for fluid components (e.g. salt and water). In the two-phase region of the salt solution, the liquid content can be handled as a saturated liquid at a given pressure (or temperature) and concentration, while the vapour (pure water steam) properties are determined for a particular pressure and temperature as superheated steam. This is beneficial when fluid properties do not allow automatic evaluation of the two phase region properties, such as for the LiCl solution providing only vapour-liquid-equilibrium parameters. Also, when the required properties were not available, ideal properties, such as of incompressible fluid, were used.

All HXs are considered to have a counter flow configuration. Heat transfer takes place with defined pinch points in HXs. Partial evaporation and condensation processes in the mixtures, marked further as desorption and absorption, are assumed to occur at variable temperatures of the temperature glide as the concentration of the less volatile component changes in the liquid phase (increases in desorption). To determine the position of the pinch point and the shape of Q-t curves, HXs were discretized by the total heat transferred, which was divided in every element between heat for evaporation (or absorption), heat to warm up (cool down) the liquid solution, and heat to warm up (cool down) vapour content, according to Figure 6.5. The computational model was set-up using a step-by-step method starting at one side of the HX, with the equilibrium state of the phases solved in each step. Specific equations used are provided in Appendix A. With a constraint of a given pinch point in the HX and pairing the heat transfer with the secondary fluid, the heat exchanger model is fully defined. For better convergence, the calculation can be based on changes to elementary concentration instead of on elementary transferred heat. This is an issue especially with some salt solution fluid property formulations. The calculations have shown, that the absorber has its pinch point typically in the middle of the phase change process. The desorber typically has its

pinch point at the start of evaporation (desorption) and for maximal power output the minimal temperature difference can be applied also to the desorber outlet. The recuperator has a minimum temperature difference on the cold end, though onset of boiling in the recuperator is also possible with certain settings of the cycle parameters.

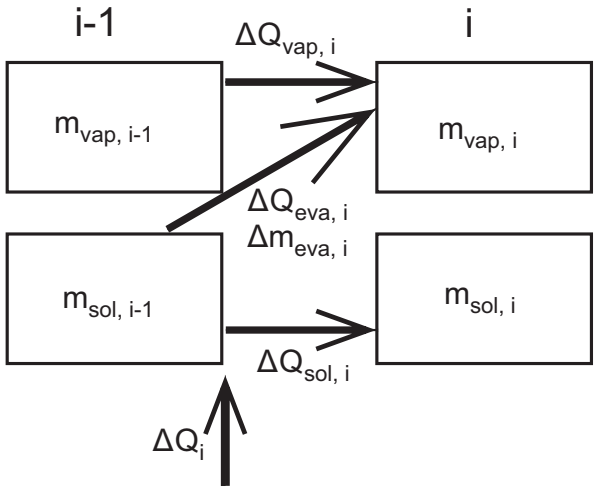

Figure 6.5: The process of heat and mass transfer during the desorption of a water from a salt solution between two HX elements.

Within the provided boundary conditions the Rankine cycles with a single component working fluid have two degrees of freedom. Typically, these are high and low pressure levels or, to better stay within the limits of thermodynamic boundaries, evaporation and condensation temperatures. Using a mixture working fluid adds one more degree of freedom by the solution concentration. In APC, evaporation (desorption) takes place only partially and thus its extend adds yet another degree of freedom. In the investigation of the APC was however found, that the maximum power is provided, when the two phase outlet of the desorber also observes the minimum temperature difference. By implementing this requirement, the resulting degree of freedom of APC is three. Within the investigation, the parameters selected as controlling ones are selected as either the high-pressure level in the system p_1, absorption pressure p_{11} and the initial concentration of LiBr ξ_1, or instead of the absorption pressure, final absorption temperature T_{11} can be used. Again using both temperature levels is suggested instead of both pressures, but with given solvers it caused issue with the calculation convergence. The thermodynamic model of APC then also serves as a frame for extension of components model into design (or eventually off-design) models used later in the thesis, especially for heat transfer design models for desorber and absorber.

6.1.4 General input parameters and boundary conditions

The input parameters and boundary condition of the various performed analyses differ in specific values, but the nature of them is generally the same. There is always a specification of the heat source by its fluid type and state, temperature of inlet, eventually limitation on the outlet. Similar is the case of the heat sink and chilled water in case of cooling. These heat transferring fluids might involve also a pressure drop that needs to be overcome by auxiliary equipment.

The second type of the boundary conditions is the limiting aspect of heat transfer in the heat exchangers. Typically, it is a specified minimal temperature difference, but other parameters as heat exchanger effectiveness or UA value can be used as well. Isentropic efficiency of components as pump, expander or fan are then used based on realistic values to correct the produced or required power compared to the ideal one. As the purpose of most of the analyses is to perform a comparison between various thermodynamic cycles, for simplicity of the results interpretation, mechanical and electrical efficiencies of the components are in these cases neglected.

6.1.5 Additional models

This work will evaluate also application to low temperature solar collectors as a heat source, specifically evacuated tube collectors ("low temperature" with respect to power cycle temperature levels). For the estimation of such systems' potential throughout various weather conditions, model of the collector and related solar model to process actual irradiation data must be established.

Solar model in this work follows a general model described for example by [209] and here will be described only briefly with details provided in Appendix B or in author's work [Sc16]. The model first describes geometry of Sun movement with respect to given position and surface on Earth with a normal irradiation determined from solar constant. Then a correlation [210] is used using sky clearness index relating solar irradiation out of the Earth's atmosphere and actual measured value G to obtain a diffuse light. Following that the diffuse radiation and direct radiation contents are evaluated. Finally, for a surface that is not horizontal, there is additional (though small) content of reflected light based on environment reflectivity ρ. In the model there are following inputs: day of the year, solar time ST, experimentally obtained solar irradiance to horizontal surface $G = f(ST)$ for each hour from above, collector slope β_{surf}, collector azimuth γ, location latitude ϕ.

The collector model provides a portion of irradiation absorbed by the collector, heat losses that are a function of ambient temperature and finally its output and efficiency. The inputs of the collector model are: irradiation per given surface (direct, diffuse and reflected components from the solar model), ambient

temperature T_{amb}, mean temperature of collector fluid. Additionally are used collector transversal incidence angle modifier (IAM) and a function of longitudinal incidence angle modifiers (IAM) obtained from reported parameters in the collector database as a 6th order polynomial fit with incidence angle. Diffuse and reflected light IAM are constant for single surface setting with respect to effective diffuse and reflected angles of incidence obtained from correlations [211]. For a given collector aperture area the energy input to the collector is expressed by the right hand side expression in Equation (6.5). The collector has thermal losses which are evaluated from reported efficiency curve coefficients a_1 and a_2, mean temperature of collector fluid and ambient temperature. These losses are described by the right hand side expression in Equation (6.6). Net collector output is the difference between the two and only positive output is accounted for (no operation assumed when the output would be negative). Collector output then relates to fluid mass flow rate based on inlet and outlet temperatures. The collector efficiency is defined by Equation (6.7) as a ratio of energy output in heat transfer fluid to irradiation energy of the collector aperture area.

$$\dot{Q}_{col} = m\left(h_{fl,out} - h_{fl,in}\right) \tag{6.5}$$

$$\begin{aligned}\dot{Q}_{col} = A_a\left[K_{\theta,b}G_{bT} + K_{\theta,d}G_{dT} + K_{\theta,r}G_{rT}\right]\eta_0 - \\ A_a\left[a_1\left(t_m - t_{amb}\right) + a_2\left(t_m - t_{amb}\right)^2\right]\end{aligned} \tag{6.6}$$

$$\eta_{col} = \frac{\dot{Q}_{col}}{\left(G_b + G_d + G_r\right)A_a} = \frac{\dot{Q}_{col}}{G_T A_a} \tag{6.7}$$

Photovoltaic module model is considered to provide a reference to the power cycles. In the model, reflectance ρ of the panels is obtained from estimated values of constants $\rho_{ref} = 0.05$ and $b_0 = 0.11$. PV module temperature is then estimated by Equation (6.8) or for the incidence angle θ larger than 85° considered as ambient to prevent numerical issues. This estimation neglects produced power in the balance equation, but given the efficiency, provides a reasonable accuracy for initial potential evaluation. The heat transfer coefficient α is based on a simple correlation with assumed average windspeed u of 2 m/s resulting in value 13.3 $W \cdot m^{-2} \cdot K^{-1}$. Efficiency of the module is then obtained from Equation (6.9). Two types of PV modules were considered, polycrystaline and amorphous silicon modules. Values of constants adopted in the PV model are summarized in Table 6.1.

Table 6.1: Boundary conditions and parameters of the PV modules models.

Cell type	η_{ref} (%)	β (% K^{-1})	ρ_{ref} (1)	b_0 (1)
polycrystalline	15	-0.4	0.05	0.121
amorphous	6	-0.2	0.05	0.110

$$T_{PV\ \text{panel}} = T_{amb} + \frac{(1-\rho)G_T}{\alpha} = T_{amb} + \frac{\left(1 - \left\{1 - (1-\rho_{\text{ref}})\left[1 - b_0\left(\frac{1}{\cos\theta} - 1\right)\right]\right\}\right) G_T}{\alpha} \tag{6.8}$$

$$\eta_{PV\text{panel}} = \eta_{\text{ref}}\ (1 + \beta\,(T_{PV\ \text{panel}} + 25))\left(1 + 0.03 \ln \frac{G_T}{1000}\right) \tag{6.9}$$

6.2 Performance indicators

In the waste heat recovery and generally with open loop heat sources, there is not important just a single efficiency parameter as the maximum cycle efficiency usually doesn't reflect the point of maximal power output. Furthermore for clear assessment of the performance, efficiency is calculated both according to the first law of thermodynamics (energy efficiency) and according to the second law (exergy efficiency). The efficiency is also calculated as gross (excluding heat rejection auxiliary power requirement – parasitic load) and net (including all parasitic loads). As the efficiency of the cycle does not directly correspond to the power output and as the optimum parameters for either are typically different, two types of efficiency references were considered.

First, the efficiency can be related solely to the heat input into the cycle. This option characterizes the cycle only and does reflect the amount of recoverable heat. It is valid in closed loop circuits and generally where the heat content of the source stream is not wasted after the heat transfer. It can be in the case of fluid circulating in solar panels, in cases where heat is required and utilized downstream of the heat transfer to the cycle with low potential (heating, drying etc.), or when additional heat cannot be extracted due to reasons as a precipitation risk in cold geothermal brines or dew point of acid flue gas. First-law efficiency is then defined by Equation (6.10) and (6.11), and second-law (exergy) efficiency by Equation(6.12) and(6.13), both for gross and net power respectively. The auxiliary power consumption accounts in this study for air fan and a cooling water pump (only with wet cooling tower) or heat source circulation pump (only with solar collector).

$$\eta_{1st,cycle,gross} = \frac{W_{\text{gros}}}{Q_{\text{in}}} = \frac{W_{\text{exp}} - W_{\text{pump}}}{m_{hs} \cdot (h_{hs,in} - h_{hs,out})} \tag{6.10}$$

$$\eta_{1st,cycle,net} = \frac{W_{net}}{Q_{in}} = \frac{W_{exp} - W_{pump} - W_{aux}}{m_{hs} \cdot (h_{hs,in} - h_{hs,out})} \tag{6.11}$$

$$\eta_{2d,cycle,\text{gross}} = \frac{W_{\text{gross}}}{Ex_{in}} = \frac{W_{exp} - W_{\text{pump}}}{m_{hs} \cdot [(h_{hs,\text{ in}} - h_{hs,\text{ out}}) - T_0 \cdot (s_{hs,\text{ in}} - s_{hs,\text{ out}})]} \tag{6.12}$$

$$\eta_{2d,cycle,net} = \frac{W_{net}}{Ex_{in}} = \frac{W_{\text{exp}} - W_{pump} - W_{aux}}{m_{hs} \cdot [(h_{hs,in} - h_{hs,out}) - T_0 \cdot (s_{hs,in} - s_{hs,out})]} \tag{6.13}$$

Second, there is the efficiency of heat source utilization, which represents maximum attainable work from given open-loop heat source. Here, the cycle output refers to the total heat content in the stream of the heat source with respect to ambient conditions. The reference, in this case, is the heat released when the heat source is cooled down to the ambient temperature. Therefore, it considers also the capability of the cycle to extract the heat from the heat source. This is particularly the area where the cycles with temperature glide should provide an advantage by better matching their Q-T profile to the heat source. [20, 21]. Values of heat source utilization efficiency are obtained from Equations (6.14) and (6.15) for first-law efficiency and Equations (6.16) and (6.17) for second-law efficiency, again with respect to gross and net power output. The ambient or "dead" state denoted by the subscript "0" represents the heat source cooled to dry bulb temperature except for using the wet cooling tower, where it corresponds to the wet bulb temperature

$$\eta_{1st,util,gross} = \frac{W_{gross}}{Q_{hs}} = \frac{W_{\text{exp}} - W_{pump}}{m_{hs} \cdot (h_{hs,in} - h_{hs,0})} \tag{6.14}$$

$$\eta_{1\text{st},util,net} = \frac{W_{\text{net}}}{Q_{hs}} = \frac{W_{\text{exp}} - W_{pump} - W_{aux}}{m_{hs} \cdot (h_{hs,in} - h_{hs,0})} \tag{6.15}$$

$$\eta_{2d,util,gross} = \frac{W_{\text{gross}}}{Ex_{hs}} = \frac{W_{exp} - W_{pump}}{m_{hs} \cdot [(h_{hs,in} - h_{hs,0}) - T_0 \cdot (s_{hs,in} - s_{hs,0})]} \tag{6.16}$$

$$\eta_{2d,util,net} = \frac{W_{net}}{Ex_{hs}} = \frac{W_{exp} - W_{pump} - W_{aux}}{m_{hs} \cdot [(h_{hs,in} - h_{hs,0}) - T_0 \cdot (s_{hs,in} - s_{hs,0})]} \tag{6.17}$$

It should be noted that maximization of cycle efficiency even cannot be applied to the reference Rankine cycles. Maximizing its efficiency would result in an increase in evaporation pressure and temperature (and pinch point temperature). In that case, even though cycle efficiency increases, the amount of heat transferred from the heat source into the cycle decreases. Heat source utilization efficiency is therefore a trade-off between the maximum heat transferred and the maximal cycle efficiency in converting it to work. Lastly, the investigated cycle can be just a one part of a more complex system with other equipment efficiencies (e.g. connection with solar collector converting irradiation to heat). Then the cycle efficiency becomes only one in a series to obtain a performance and efficiency of the entire system.

Considering the performance indicators of the cogeneration system, in literature they have been demonstrated to various degrees of complexity in energy and exergy analyses. One rather comprehensive approach is to account for primary energy conversion for the same power, heat and cold energy production from a global perspective. It includes the comparison with an average power production efficiency of the electricity obtained from the power grid and a coefficient of performance of a benchmark system, as proposed for CCP and CCHP cycles by Ayou et al. [41]. Author of this work, however, believes that in the current state of technology of APC systems, for a clear assessment of the parameters of the cycle, and from the viewpoint of potential users, manufacturers or operators, simpler and more straight-forward performance indicators are suitable and required.

The simple energy efficiency η_{cycle} is defined using Equation (6.18), where $\dot{W}_{cycle}$ is the net work of the cycle, $\dot{Q}_{chill}$ is the chiller output and $\dot{Q}_{in}$ is the total thermal input used from the heat source. It can be divided into the efficiency of power production $\eta_{(1st,cycle,pow)}$ and the COP of the chiller COP_{cycle}, which are defined in Equations (6.19) and (6.20), respectively. The power production efficiency may be negative when the cycle power production drops below zero ($W_{exp} < W_{pump}$) for a higher chiller output.

$$\eta_{1st,cycle} = \frac{\dot{W}_{cycle} + \dot{Q}_{chill}}{\dot{Q}_{in}} = \frac{\dot{W}_{exp} + \dot{W}_{pump} + \dot{Q}_{chill}}{\dot{Q}_{in}} \tag{6.18}$$

$$\eta_{\mathrm{1st,cycle,pow}} = \frac{\dot{W}_{\mathrm{cycle}}}{\dot{Q}_{in}} \tag{6.19}$$

$$\text{COP}_{\text{ cycle}} = \frac{\dot{Q}_{\text{chill}}}{\dot{Q}_{\text{in}}} \tag{6.20}$$

When the auxiliary power requirements are considered (here represented by fan power for heat rejection), the formula for power efficiency $\eta_{(1st,cycle,pow,net)}$ changes in its numerator according to Equation (6.21). The net overall efficiency or COP with respect to the overall energy input is not reported in such a manner because the gross and net power efficiencies already show the difference between the two.

$$\eta_{\text{1st,cycle,pow,net}} = \frac{\dot{W}_{\text{net}}}{\dot{Q}_{in}} = \frac{\dot{W}_{\text{cycle}} + \dot{W}_{\text{fan}}}{\dot{Q}_{\text{in}}} \tag{6.21}$$

Exergy efficiency is determined to assess the useful products, work, and cooling output from the perspective of the second law of thermodynamics. For the cycle itself, the exergy efficiency $\eta_{2nd,cycle}$ is defined by Equation (6.22), while the net exergy efficiency $\eta_{2nd,cycle,net}$, including that of auxiliary systems, is given by Equation (6.23). The change in exergy of the heat source $\Delta\dot{E}x_{hs}$ and chilling streams $\Delta\dot{E}x_{chill}$ is represented by Equations (6.24) and (6.25), with the states corresponding to Figures 6.3 and 6.4. State 0 corresponds to the ambient temperature (T_0 in K units); $\dot{m}_{cool}$ represents the mass flow rate of the coolant.

$$\eta_{2nd,cycle} = \frac{\dot{W}_{cycle} + \Delta\dot{E}x_{chill}}{\Delta\dot{E}x_{in}} \tag{6.22}$$

$$\eta_{2nd,cycle,net} = \frac{\dot{W}_{net} + \Delta\dot{E}x_{chill}}{\Delta\dot{E}x_{in}} \tag{6.23}$$

$$\Delta\dot{E}x_{\text{chill}} = \dot{E}x_{\text{cf,out}} - \dot{E}x_{\text{cf , in}} = \dot{m}_{\text{cool}}\left[(h_{52} - h_{51}) - T_0\,(s_{52} - s_{51})\right] \tag{6.24}$$

$$\Delta\dot{E}x_{hs} = \dot{E}x_{hs,in} - \dot{E}x_{hs,out} = \dot{m}_{hs}\left[(h_{21} - h_{23}) - T_0\,(s_{21} - s_{23})\right] \tag{6.25}$$

In applications with an open-loop heat source (such as WHR), utilisation efficiency ($\eta_{1st,util,net}$ for the 1^{st} law evaluation and $\eta_{2nd,util,net}$ for the 2^{nd} law evaluation) is again a more important parameter than cycle efficiency. The reference is the heat released when the heat source is cooled to the ambient temperature; the capability of the cycle to extract heat from the heat source is considered. Also for CCP cycles this is the area where the temperature glide

should provide an advantage by better matching the Q–T profile to the heat source [20, 21]. Efficiency functions, therefore, change the denominator term, as shown in Equations (6.26) and (6.27). The utilisation efficiency of power production and COP are analogous to Equations (6.19)–(6.21) with $\dot{Q}_{hs}$ in the denominator, and as such it is not necessary to repeat the equations.

$$\eta_{1\mathrm{st},util,net} = \frac{\dot{W}_{net} + \dot{Q}_{\mathrm{chill}}}{\dot{Q}_{hs}} = \frac{\dot{W}_{net} + \dot{Q}_{\mathrm{chill}}}{\dot{m}_{hs}\left(h_{21} - h_0\right)} \tag{6.26}$$

$$\eta_{2nd,util,net} = \frac{\dot{W}_{net} + \Delta\dot{E}x_{chill}}{\dot{E}x_{hs}} = \frac{\dot{W}_{net} + \Delta\dot{E}x_{chill}}{\dot{m}_{hs}\left[\left(h_{21} - h_0\right) - T_0\left(s_{21} - s_0\right)\right]} \tag{6.27}$$

6.3 Power cycle results

Various applications and case studies are proposed for the APC. First, there is however provided a general framework of thermodynamic limits with several ideal cycles, within which the benefit of APC utilizing salt solutions can be sought. Before main investigations is a suitable point to place comparison of the model results with prior works. An introduction to general cycle parameters and resulting peculiarities is followed by an analysis of heat source utilization potential, one of the main considered benefits of the proposed APC before the proposed APC is compared to other APCs (other working fluids). A sensitivity study of main APC parameters concludes the investigation of cycles. This section then outlines three further application possibilities for low temperature heat sources before concluding with a summary of the findings.

6.3.1 Thermodynamic limits and ideal cycles

Before analysing the results of the investigated proposed thermodynamic cycles with parameters corresponding to reference and state of the art systems, it is suitable to show what the thermodynamic limits of ideal cycles are. Simple set of boundary conditions for such a parametric study was chosen as is summarized in Table 6.2. Heat source and sink fluids were taken as ideal air. There is provided a temperature of a heat rejection fluid, taken as ambient and its temperature increase during heat rejection. Then, there is a minimal temperature difference between the heat source and the working fluid, which is the same also between the working fluid and the heat rejection fluid. Isentropic efficiencies of respective components are 100%. No power requirements for auxiliary equipment is considered here.

The cycles selected for comparison are trilateral cycle in several forms. First, to show a thermodynamic potential, trilateral cycle neglecting pinch point and

Table 6.2: Boundary conditions for analysis of ideal cycles' potential

ΔT_{amb} (°C)	ΔT_{hs} (°C)	ΔT_{min} (°C)	$\Delta T_{rej,rise}$ (°C)	ρ_{air} (kPa)
20	60-200	10	10	100

heat rejection fluid temperature rise (TC). Then, reflecting the temperature rise of heat rejection fluid but still neglecting minimal temperature differences is actually a limiting case of the Lorenz cycle, denoted as LC1. Limiting case, because there is no isentropic compression, the heat input and output curves intersect at the point of lowest cycle temperature. Lorenz cycle when the minimal temperature differences are respected, it is denoted as LC2. Efficiency of the Lorenz cycle is calculated according to Equation (6.28) [93] (with thermodynamic temperature in K and necessary assumption of constant heat capacity, which is practically valid in the investigated range of temperatures). For illustration is added a Carnot cycle (CC). To illustrate expectation of technically feasible cycles, ideal Rankine cycles with steam (RC) and two organic fluids are added as well. These are using isobutane for lower temperature range (ORC1) and MM for higher (ORC2). All Rankine cycles were considered without superheating. Figure 6.6 provides an illustration of the cycles in a TS diagram, which is similarly modified as was in Figure 1.1. The cases with CC, RC and ORC have their efficiency dependent on their temperature and pressure levels. The heat rejection is fixed through given pinch point and the rejection fluid temperature rise. On the high pressure levels these temperatures were optimized for each cycle to obtain maximal power output from given heat source (maximum utilization efficiency). The ORC is considered with a specific working fluid in this example only as long as the pinch point between the heat source and the working fluid is at the beginning of evaporation, therefore ORC1 has last point at 150°C, beyond which high pressure level gets too close to the critical point and pinch point would transfer to the cold end of the heat exchanger, later eventually the cycle would become transcritical.

$$\eta_{\mathrm{LorenzCycle}} = \frac{\bar{T}_{\mathrm{in}} - \bar{T}_{\mathrm{rej}}}{\bar{T}_{\mathrm{in}}} = \frac{(T_{\mathrm{rej,out}} - T_{\mathrm{rej,in}}) / \ln(T_{\mathrm{rej,out}} / T_{\mathrm{rej,in}})}{(T_{hs,in} - T_{hs,out}) / \ln(T_{hs,in} / T_{hs,out})} \quad (6.28)$$

As auxiliary power requirement is not considered, the resulting values can be considered as gross regarding the performance indicators. The efficiency values (of the optimized cycles) were plotted with respect to heat source temperature to give a clear comparison of the resulting parameters. First is provided a second law efficiency in Figure 6.7. Here, the exergy potential of the trilateral cycle corresponds to perfect heat source utilization, thus having efficiency of unity. Already introducing the heat sink temperature rise is notable efficiency

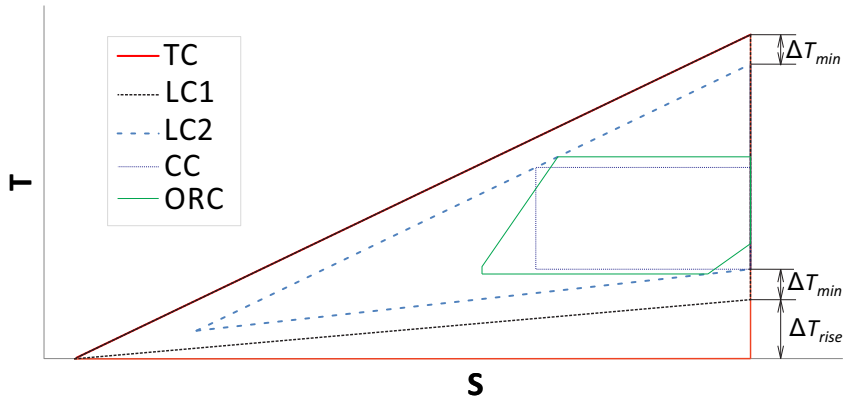

Figure 6.6: Illustrational TS diagram of several ideal cycles investigated for waste heat recovery

decrease, though major step is towards the ideal Lorenz cycle within given constraints of minimum temperature difference, LC2. Following cycles, though in ideal form, are another significant drop below this. Even though performance of the selected ones (and after optimization) does not differ so extensively, Carnot cycle is inferior to ORC. The RC, even though it can extract slightly more heat from the heat source than Carnot cycle, has its performance slightly below Carnot cycle as a result of real fluid properties. Note that below 50°C heat source the cycles considering pinch point cannot be working and therefore the efficiency is zero. Rising tendencies are therefore attributed largely to a decreasing relative effect of the pinch point and related losses (irreversibilities). For illustration are additionally plotted notably higher efficiencies considering only the cycle, not heat source utilization. These values are meaningful to closed loop heat source, for which the cycles are however not optimized. These values also illustrate the importance to distinguish between the utilization and cycle values.

Following Figure 6.8 shows, how the previously presented values translate into the values of the 1^{st} law efficiencies. Theoretical potential utilization efficiency is less than 12% for the 100°C heat source, but even ideal Lorenz cycle reflecting only minimal temperature difference causes a decrease to 7% efficiency and ORC reaches utilization efficiency of only 2.6% at the efficiency of standalone cycle around 7%. This highlights the importance of the 2^{nd} law analysis and points out at the issues within (very) low temperature waste heat recovery. Also this justifies 1^{st} law efficiency values in order of several percent or less, even though such values might at first appear as extremely low and unprospective. Additionally note, that even though cycle efficiency is the highest for the Carnot cycle, ORC can provide higher power output and thus utilization efficiency by extracting more heat from the heat source.

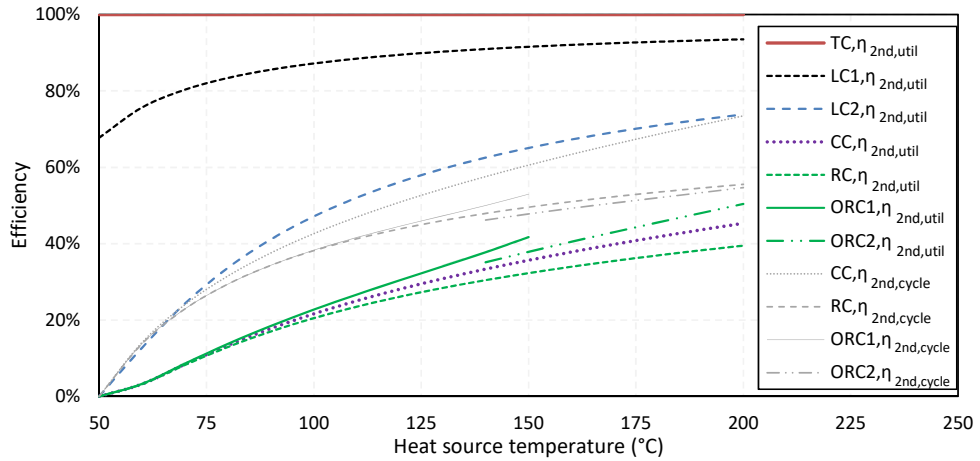

Figure 6.7: Exergy (2^{nd} law) efficiencies of ideal thermodynamic cycles in WHR application

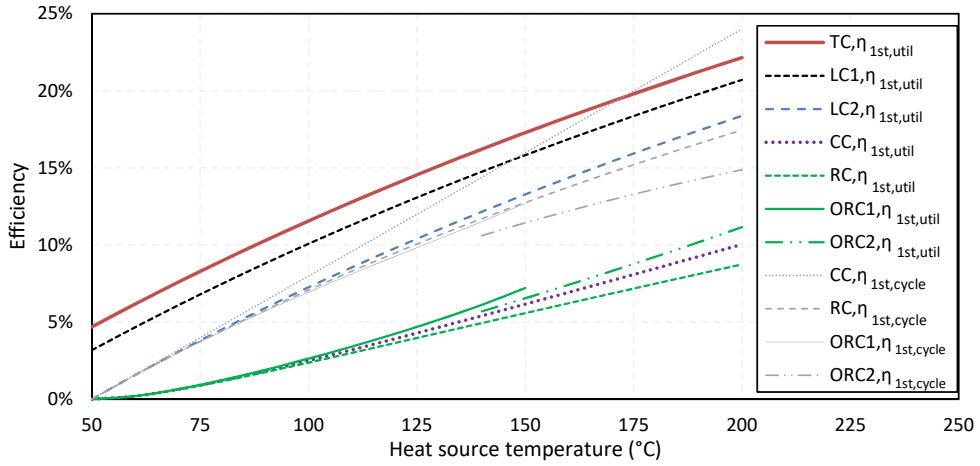

Figure 6.8: Energy (1^{st} law) efficiencies of ideal thermodynamic cycles in WHR application

As a conclusion from this short analysis regarding very low temperature heat sources can be concluded that application of conversion systems is intrinsically hindered by low energy efficiency potential, which gives limited space for power production. Currently used thermodynamic cycles are here at source temperatures of 100°C at about one third of the thermodynamic limit, but all the cycles provide similar performance. A detailed techno- and thermo-economic analysis is needed in search and selection of novel cycles that have the prospect for feasibility in these applications. Important aspects are namely complexity and cost of the system, even more important in decentralized applications where much of the unutilized heat sources are present. Therefore

much of the content is focused on practical prospects of a rather simple, though still novel, cycle, than on exploration of potentially more efficient but highly complex and unrealizable configurations.

6.3.2 Comparison with previous works and model validation

For the APC system, a comparison and validation of the model is at first presented with results provided for a LiBr-based cycle in references [57, 59], and between the properties of two formulations of a LiBr solution. The recuperative HX is solved based on its effectiveness, taken in accordance with [59] as 0.82 (considering the NTU method). Table 6.3 shows that the results are in fairly good agreement. Some discrepancies may be caused by divergence between details in the models and in the formulations of properties used in the previous studies. Although the study by Shokati et al. [59] is supposed to have been based on the same formulations as the first ones used in this work, it was not possible to obtain the same results for the pressure in the absorber, p_{11}. Additionally, the cycle efficiency is plotted as a function of the evaporator and absorber pressures, which is compared with those from [57] in Figure 6.9, showing a good agreement between the data.

Table 6.3: A comparison of LiBr-based cycle parameters from [57], [59], and the present paper using the property formulations by Pátek and Klomfar [127] (P) and Kim et al. [126] (K).

Parameter	**[57]**	**[59]**	**P**	**K**	**[57]**	**[59]**	**P**	**K**	**[57]**	**[59]**	**P**	**K**
T_S (°C)	140				120				100			
T_{11} (°C)	50				50				50			
p_5 (kPa)	106.4				60.4				31.1			
ξ_{11} (%)	47.5				47.5				47.5			
p_{11} (kPa)	4.2	4.4	4.27	4.22	4.2	4.4	4.27	4.22	4.2	4.4	4.27	4.22
$\Delta\xi$ (%)	5.5	5.73	5.39	5.55	4.1	4.33	4.09	4.25	3.2	3.39	3.20	3.34
$\dot{m}_6$ (kg/s)	2.33	2.36	2.33	2.33	2.85	2.9	2.86	2.85	3.83	3.91	3.84	3.82
$\eta_{1st,cycle}$ (%)	14.1	14.19	14.27	14.29	11.7	11.74	11.6	11.84	8.9	8.89	8.98	9.03
$\dot{Q}_{in}$ (MW)	7.089	7.045	7.008	6.997	8.576	8.521	8.480	8.447	11.276	11.244	11.131	11.078
$\dot{Q}_{out}$ (MW)	6.089	6.044	6.008	5.997	7.577	7.523	7.480	7.447	10.275	10.245	10.131	10.078
$\dot{W}_{turb}$ (MW)	1.002	1.002	1.002	1.002	1.002	1.001	1.002	1.002	1.001	1.001	1.002	1.002
$\dot{W}_{pump}$ (kW)	2.1	1.98	2.25	2.22	2.0	1.86	1.95	1.89	1.5	1.38	1.57	1.51

6.3.3 Detailed parameters of the cycles

The heat source for the detailed investigation has been designated as a liquid water (considered as pressurized at 8 bar to ensure its liquid phase for the analysis) with temperatures of 60–160°C, which can represent a stream of industrial waste heat, fluid from geothermal or low temperature solar sources. For setting up the model, the mass flow rate of the heat source fluid is fixed at 1 $kg \cdot s^{-1}$. Two methods of cooling are considered here, a wet cooling tower (CT) and an air cooled condenser/absorber (ACC), both with an induced fan to overcome the air pressure drop. Boundary conditions for the cycles are

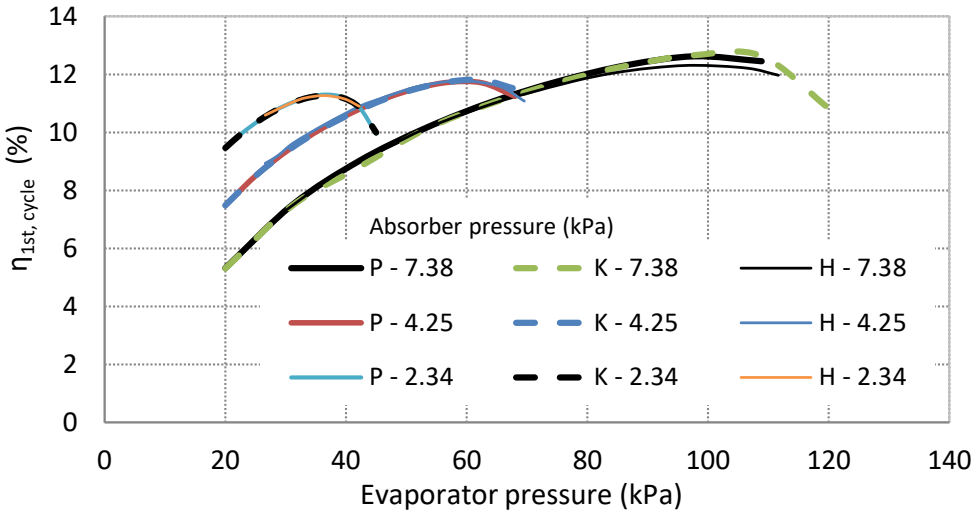

Figure 6.9: Energy efficiency of the cycle ($\eta_{1st;cycle}$) as a function of evaporator and absorber pressures for formulations of properties according to [127] (P) and [126] (K) in comparison with results by [57] (H) for a turbine inlet temperature of 120°C and a weak LiBr solution mass fraction of 47.5%.

Table 6.4: Boundary conditions for LiBr APC detailed parameters and a general study of salt APC prospects of heat source utilization

T_{DB}	T_{WB}	p_{amb}	RH_{air}	H_{eq}	η_{turb}	Approach	η_{pump}
(°C)	(°C)	(kPa)	(%)	(m)	(%)	(°C)	(%)
25	21	100	70	15	80	5	70
η_{fan}	Δp_{CT}	$RH_{CT,out}$	n	$\Delta T_{min,hot}$	Δp_{ACC}	$\Delta T_{min,cond}$	
(%)	(Pa)	(%)	(-)	(°C)	(Pa)	(°C)	
70	95	100	30	10	150	5	

summarized in Table 6.4. Pump efficiency is set to the same value for all pumps in the system. The pinch point for the recuperator is the same as for the heat input HX, $\Delta T_{min,hot}$. The pressure drop of the air in the CT, Δp_{CT}, is set with respect to the manufacturer's data from [212], and n is the number of segments for each HX discretization. Ambient conditions were set for a relatively warm climate or summer conditions.

The parameters in each node of the system for the LiBr cycle with a CT are listed in Table 6.5, and a temperature-entropy ($T-s$) diagram of this cycle appears in Figure 6.10. The $T-s$ diagram clearly shows the variable evaporation (desorption) and condensation (absorption) temperatures together with the temperature rise caused by adiabatic absorption in the beginning of the absorption-condensation process. A cycle with these parameters has also been drawn into the Dühring plot presented for illustration in earlier

section in Figure 2.6, where it is compared with a cooling cycle with the same maximum temperature of the working fluid in the steam generator (90°C). It can be seen that, compared to the cooling cycle, the APC optimized for utilization efficiency has the advantage of having the working fluid further from the crystallization barrier. Problems with crystallization, which are sometimes encountered in cooling machines, should not pose a problem in this APC. The potential issue of reaching the crystallization barrier was not encountered in the cycle under any of the modelled conditions. A major difference from previous studies [46, 57, 59], which focused more on cycle-only efficiency, was observed with respect to solution concentration. The weak solution concentration at the utilization-optimized parameters was significantly lower (approximately 30% of salt) and the change of concentration was also higher. The reason for such behaviour is found in the prioritizing higher temperature glide of the phase change over the highest mean heat-input temperature. This maximizes the heat transfer from the heat source to the cycle, which occurs at a relatively high mean temperature, and it also achieves a high outlet temperature of the heat rejection fluid while keeping a very low absorber pressure. A larger change in concentration also results in a smaller liquid flow through the recuperator and a smaller amount of recuperated heat.

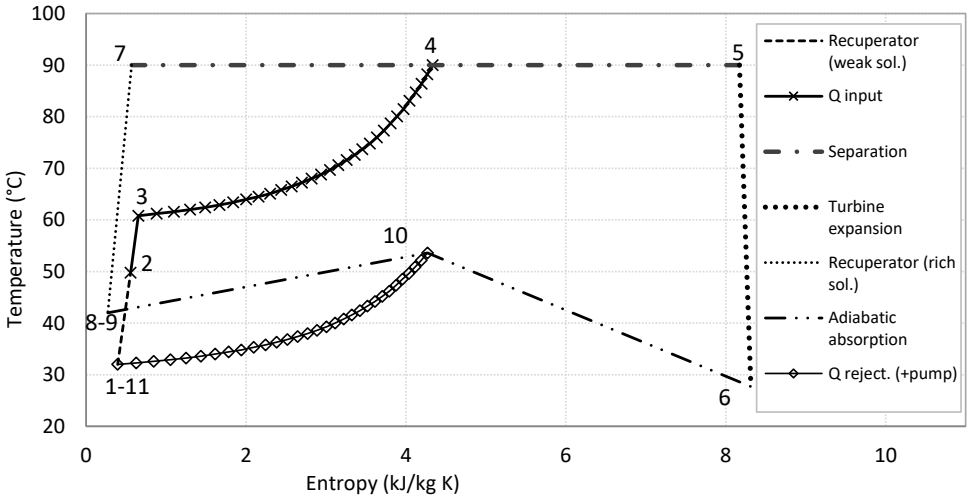

Figure 6.10: A temperature-entropy (T-s) diagram of the LiBr cycle at 100°C and cooling tower.

The Q-T curves, given in Figure 6.11, exhibit a good match of temperature profiles for the heat addition and heat rejection processes (boiling and condensation) in their respective HXs. The figure shows that the heat addition process has a pinch point when reaching a saturated liquid state of the working fluid. However, the shape of the curve for heat rejection, which is impacted by a decrease in LiBr liquid solution concentration, causes its pinch point to be

Table 6.5: Parameters in the nodes of the absorption power cycle working with a 100°C heat source and cooled by a wet cooling tower.

Node number	T_i (°C)	h_i (kJ kg^{-1})	m_i (kg s^{-1})	p_i (kPa)	s_i (kJ $kg^{-1} \cdot K^{-1}$)	ξ_i (kg kg^{-1})
1	32	79.2	0.97	16.3	0.394	0.272
2	49.8	130.1	0.97	16.3	0.557	0.272
3 (pinch p.)	60.8	162.2	0.97	16.3	0.654	0.272
4	90	1421	0.97	16.3	4.335	0.539
5	90	2668	0.48	16.3	8.171	0
6	27.7	2495	0.48	3.7	8.314	0
7	90	197.2	0.49	16.3	0.569	0.539
8	42	96.2	0.49	16.3	0.271	0.539
9	42	96.2	0.49	3.7	0.271	0.539
10	53.6	1285	0.97	3.7	4.268	0.514
11	32	79.2	0.97	3.7	0.394	0.272
21	100	419.7	10	800	1.307	
22	70.8	297.1	10	800		
23	70.1	294	10	800	0.956	
31	26	109.3	28.18	147.2		
32	36	150.9	28.18	147.2		
33	26	109.1	27.78	100		
40	25	61.3	26.65	100		

located within the phase change process, and its exact location depends on the ratio of cooling water and working fluid flowrates and their inlet temperatures.

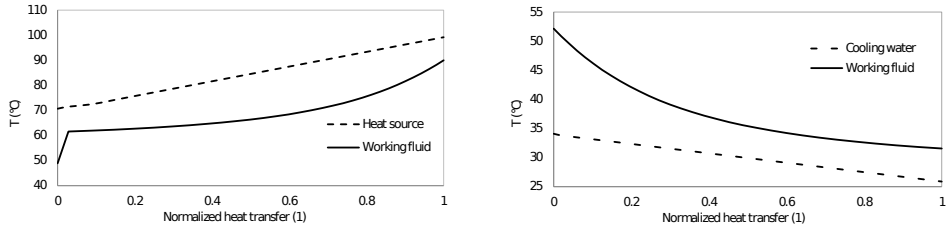

(a) (b)

Figure 6.11: Q-T curves of the normalized a) heat addition and b) heat rejection in the LiBr cycle with a cooling tower, a heat source at 100°C, and optimization for maximum heat source utilization.

6.3.4 Heat source utilization general analysis

Utilization efficiency corresponding to power output is the key performance indicator for open loop heat sources instead of only cycle efficiency (η_{cycle}).

Cycle-only efficiency has been studied and reported in the past for LiBr-water and water-ammonia based cycles. Utilization of the given heat source stream is however seen to hold a wider application potential. Therefore, maximal net energy efficiency of heat source utilization was searched for in the APC models at the given boundary conditions from Table 6.4. The optimization variables are the absorption temperature and pressure, T_{11} and p_{11}, which together define the concentration of the weak solution. Then high pressure in the system, p_1, together with temperature T_4, based on the temperature from the heat source, these define the concentration of the solution at the end of boiling (desorption). The efficiency of the reference cycles is optimized with respect to the evaporation temperature, T_3, and the condensing (absorber outlet) temperature, T_1. Cycles with recuperation are considered only in cases possible within the given boundaries (available heat for recuperation within the limits of the minimal temperature difference in recuperative HX). The working fluids chosen for explored cases are for RC2 water, R143a, R152a, methanol, ammonia, R290 and R1234yf; for RC3, these are isobutane, n-butane, cyclohexane, RC318, HFE7100, R245fa and MM.

The results for the maximized first-law net efficiency of heat source utilization ($\eta_{1st,util,net}$) for APCs and for the reference Rankine cycles (separately for maximal cases with and without heat recuperation) are shown in Figure 6.12. Alternatively, the results for the net second-law efficiency of heat source utilization ($\eta_{2nd,util,net}$) are shown in Figure 6.13. Tabulated results for cycle-only efficiency and both gross and net efficiencies are given in the Appendix C, tables C.1 and C.2 for first- and second-law efficiencies with CT heat rejection, and tables C.3 and C.4 for first- and second-law efficiencies with ACC heat rejection. Note that as the ambient (or "dead") state of utilization efficiency is different for the CT and the ACC, the second-law efficiency is fairly similar. However, this does not apply to absolute power output, which is lower in the case of the ACC. It is important to notice what effect the heat rejection auxiliaries' power requirement has on the cycle efficiency. Although gross efficiency may still be at reasonable levels, this parasitic load takes almost all of the power output of a 60°C heat source. The temperature glide of the APC during absorption decreases the amount of cooling fluid required (allows its higher outlet temperature) and decreases the parasitic load. This is one of the reasons why heat source temperatures below approx. 110-120°C appear as the prospective domain of APCs, as they can deliver more power than the Rankine cycles. At the same time, the power output provided by the water-ammonia (basic Kalina) APC is fairly comparable to the salt-based APCs. However, in the domain of main interest for APCs, that is, for heat source temperatures below 120°C, the water-ammonia cycle has the lowest efficiency among APCs. This changes as the temperature of the heat source rises above 130°C, where water-ammonia cycle has the highest efficiency of APCs.

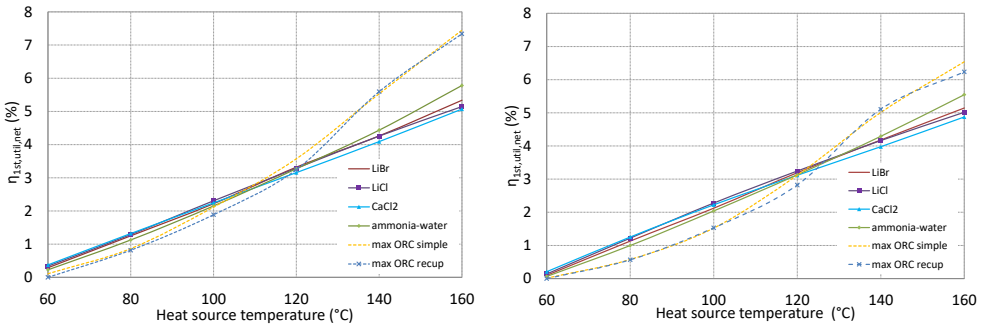

(a) cooling tower (b) air cooled condenser

Figure 6.12: Maximum net heat source utilization energy (first law) efficiency ($\eta_{1st,util,net}$) for the APCs and for the reference Rankine cycles with different heat rejection methods.

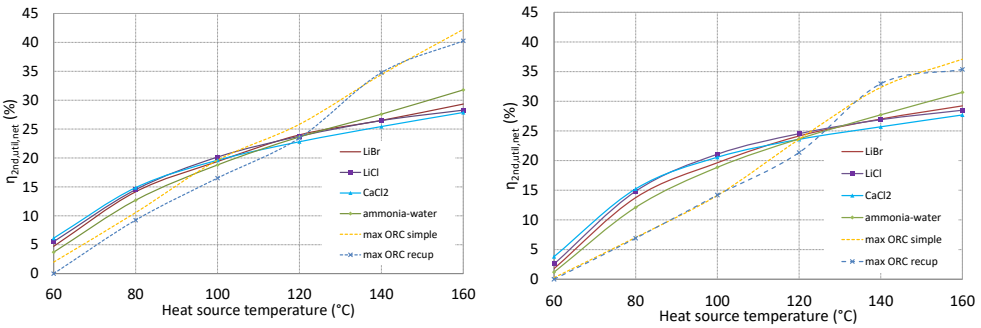

(a) cooling tower (b) air cooled condenser

Figure 6.13: Maximum net heat source utilization exergy (second law) efficiency ($\eta_{2nd,util,net}$) for the APCs and for the reference Rankine cycles with different heat rejection methods.

In order to highlight the difference between the gross and net efficiency, Figure 6.14 shows these two values, for clarity in only selected rows of data, which are the LiBr APC and the maximum ORC for the CT heat rejection. The difference is notably smaller for the APC provided by the aforementioned temperature glide during heat rejection, requiring less auxiliary power. Therefore note, that the gross efficiency of the two systems has its intersection at lower temperatures, around 90°C.

The difference between the maximums of the reference Rankine cycles and the APCs is larger for the ACC and so is the temperature range of the APC's highest efficiency. This indicates that the reference Rankine cycles are more susceptible to energy requirements for heat rejection; this shows a higher potential for applications with insufficient cooling water, where an ACC has to be used as the means of heat rejection. To better show the gain of the proposed

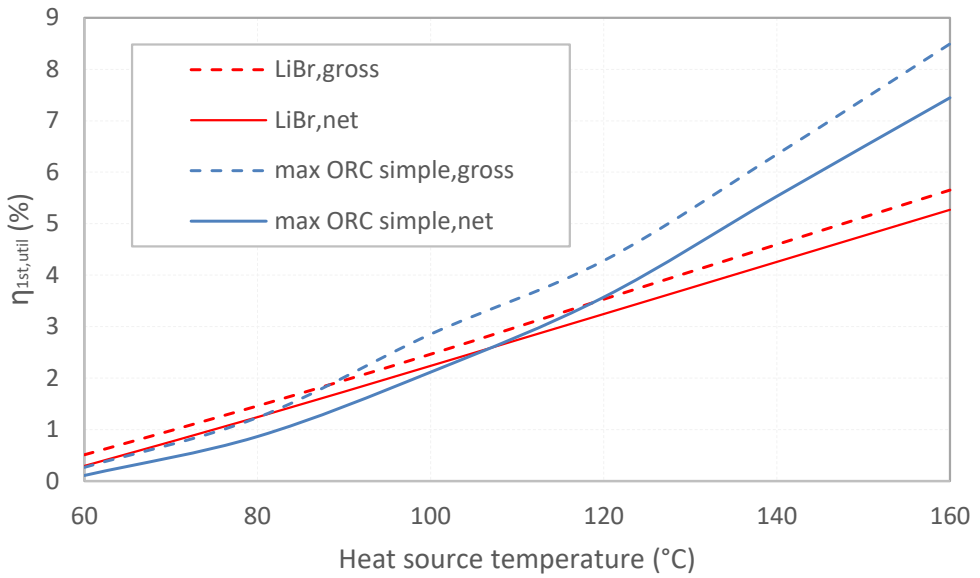

Figure 6.14: Gross and net heat source utilization energy (first law) efficiency ($\eta_{1st,util}$) for the APC and simple ORC.

cycle, the ratio of utilization efficiencies is plotted in Figure 6.15. The gain of APCs increases with decreasing heat source temperature. The figure shows that for temperatures below approximately 120°C, the APCs can deliver a power output higher than the maximum of investigated ORCs. Furthermore, despite very small first- and second-law efficiency at heat source temperatures below 80°C while using an ACC for heat rejection, the APCs are capable of delivering more than twice the power. For heat rejection using a CT with the same source temperature, the gain is not as significant, though it still exceeds 50%. When salt APCs are compared with water-ammonia APCs, a slight gain can be observed for source temperatures below approx. 130°C. The LiBr APC is presented separately, as it is believed to be the best option achievable in real device implementation.

To compare the results with others' results, the summary of various works on trilateral cycles, zeotropic working fluid cycles and supercritical ORC cycles in [27] gives at heat source temperatures around 100°C relative improvement in efficiency of heat source utilization generally between 4 and 60%, which is comparable with APC net efficiency improvement in range of source temperatures 80–120°C. It is although necessary to keep in mind different boundary conditions in each of the cases, which can have a significant impact on overall performance.

High and low pressure levels and the concentration of the salt (or ammonia) solution coming from the absorber and from the steam generator in the liquid

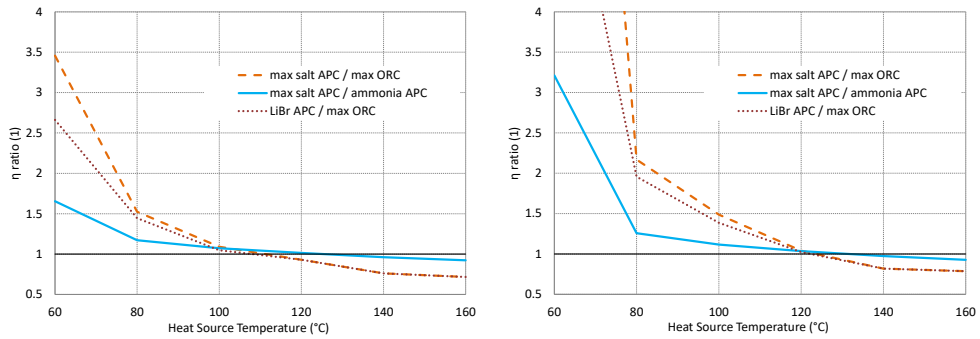

(a) cooling tower

(b) air cooled condenser

Figure 6.15: The efficiency ratios of the analysed cycles and the maximums of the reference cycles. The polylines are caused by combining results for discrete heat source temperatures.

phase are presented in Table 6.6 for the APCs with a CT and in Table 6.7 for the APCs with an ACC. The pressure in the Kalina cycle is typically relatively high; in the explored temperature range, boiling occurred at 1.2 to 5.1 MPa and absorption at 0.9 to 1.3 MPa. This may cause problems with turbine efficiency. Although by typical considerations, a very compact and seemingly cheap device would be obtained, it's very small size might contribute to large losses. The pressure of the LiCl and $CaCl_2$ and mostly also LiBr cycles is for low temperatures in a very deep vacuum, which may cause significant problems in design for air tightness. The results show that utilization efficiency for all APCs has maximal value for the lower concentration of salt in the weak solution and the change to a higher concentration. The change in concentration for maximizing power production gradually increases together with the increasing temperature of the heat source (i.e. the concentration gradient rises with the temperature gradient of the cycle). A summary of high and low pressures for all of the investigated cycles can be found in Appendix C tables C.5 and C.6 for CT and ACC, respectively.

Table 6.6: Pressure levels and solution concentration (of salt or ammonia) for APCs with a cooling tower where heat source utilization efficiency has been maximized.

T_{hs} (°C)	60		80		100		120		140		160	
p (kPa)	p_4	p_{10}	p_4	p_{10}	p_4	p_{10}	p_4	p_{10}	p_4	p_{10}	p_4	p_{10}
LiBr − P	4.2	2.5	7.2	2.6	12.5	2.8	24.1	3.6	38.3	3.9	58.7	4.3
LiBr − K	4.8	2.8	8.2	2.9	16.3	3.7	24.4	3.7	39.9	4.0	59.0	4.2
LiCl	2.2	1.3	5.4	1.9	12.1	2.6	22.6	3.3	43.9	4.0	85.4	4.6
CaCl2	1.4	0.8	4.2	1.4	11.3	2.4	24.0	3.5	42.9	4.5	67.0	5.1
NH3	1213	938	1639	978	2292	1091	3050	1174	3760	1159	5054	1289
ξ (kg/kg$_{sol}$)	ξ_1	ξ_7	ξ_1	ξ_7	ξ_1	ξ_7	ξ_1	ξ_7	ξ_1	ξ_7	ξ_1	ξ_7
LiBr − K	36.7	45.6	35.6	51.7	27.2	53.9	27.0	58.3	23.5	61.0	19.8	64.2
LiCl	35.4	42.4	30.1	44.4	24.4	54.1	19.1	53.1	13.7	51.5	8.7	51.4
CaCl2	53.6	62.0	44.7	61.6	35.7	61.3	24.9	63.0	14.6	66.4	8.0	71.4
NH3	76.0	65.7	79.0	59.1	86.0	55.8	92.0	52.6	91.0	48.4	98.0	48.2

Table 6.7: Pressure levels and solution concentration (of salt or ammonia) for APCs with an ACC where heat source utilization efficiency has been maximized.

T_{hs} (°C)	60		80		100		120		140		160	
p (kPa)	p_4	p_{10}	p_4	p_{10}	p_4	p_{10}	p_4	p_{10}	p_4	p_{10}	p_4	p_{10}
LiBr-P	5.2	3.0	7.2	2.4	12.5	2.8	21.2	2.9	34.8	3.4	57.6	4.0
LiBr-K	5.0	2.9	8.2		12.4	2.9	19.1	2.7	33.8	3.3	60.2	4.0
LiCl	1.7	0.9	3.7	1.2	9.6	1.9	21.3	2.8	44.1	3.9	85.4	4.2
$CaCl_2$	1.7	1.0	5.4	1.8	10.9	2.3	20.7	2.9	38.3	3.8	61.8	4.4
NH_3	1470	1112	1711	985.3	2113	989.3	2856	1074	3760	1148	4973	1286
ξ (kg/kg$_{sol}$)	ξ_1	ξ_7	ξ_1	ξ_7	ξ_1	ξ_7	ξ_1	ξ_7	ξ_1	ξ_7	ξ_1	ξ_7
LiBr-K	37.1	45.0	36.5	51.6	37.5	56.9	36.6	60.8	31.6	62.8	24.9	64.0
LiCl	38.6	45.7	35.4	50.0	28.9	52.9	22.7	52.3	15.0	51.9	11.7	51.5
$CaCl_2$	50.2	58.4	40.6	57.6	36.1	61.9	30.6	65.7	22.5	68.7	15.8	73.2
NH_3	84.8	73.8	79.2	60.5	80.0	53.4	85.0	50.7	90.0	48.4	97.0	47.7

6.3.5 Comparison with other APC, ORC zeotropic fluids and transcritical ORC

In order to compare other possible working fluids such as ionic liquids or potential of zeotropic ORCs, a shorter investigation presented also in author's work [VN2], has been performed with the heat source considered as a hot air at temperatures 100°C and 200°C and heat sink is assumed as air at 15°C. Heat rejection takes place in an air cooled condenser (requiring a fan). Values of the assumptions taken in this case model are summarized in Table 6.8. Note that the pressure of working fluids is here not limited by lower or upper bound as in some other works. Rather there will be a discussion of an impact of resulting pressure on an equipment design.

Working fluids considered in this analysis, are traditional ammonia-water mixture, from salt solutions is chosen water-LiBr as it has higher commercialization potential due to experience from absorption cooling, amyl acetate-

Table 6.8: Boundary conditions for the comparison study of salt APC with other APC and ORC zeotropic fluids

T_0 (°C)	p_0 (kPa)	η_{exp} (%)	η_{pump} (%)	η_{fan} (%)	$\Delta T_{eva,min}$ (°C)	$\Delta T_{cond,min}$ (°C)	Δp_{air} (Pa)
15	101.325	80	70	70	20	10	150

CO_2 mixture is chosen based on reference [65], methanol-heptanol is chosen as most perspective alcohol mixture [66]. Ionic liquids are included by 1-ethyl-3-methylimidazolium tetrafluoroborate with refrigerant R134a (R134a-[EMIM][BF4]) and with water (H_2O-[EMIM][BF4]), as suggested by decent COP performance in absorption cooling regime [122]. ORC is considered both sub-critical (denoted just as ORC) and supercritical (SC-ORC). Components for subcritical ORC are chosen as isobutane, hexamethyldisiloxane (MM), R245fa, R134a and for reference also water. The maximal pressure in subcritical operation is limited to 90% of absolute critical pressure and expansion takes place from the saturated vapour state (superheating doesn't bring thermodynamic benefit). Subcritical ORC is demonstrated as both, non-recuperated and recuperated (R-ORC) for reference (minimal benefit), supercritical only as non-recuperated. Supercritical ORC fluids are chosen specifically for each temperature. For 100°C is considered R143a, and R41 (azeotropic mixture), for 200°C R143a, R245fa and isobutane. ORC with zeotropic mixtures are represented by a mixture of n-pentane - cyclohexane based on Eller et al. [66]. A non-recuperated scheme according to the Figure 6.2a is adopted. At the same time a zeotropic mixture ORC is a limiting case for several APC fluids. Within APC performance optimization it is allowed for the mixture quality to reach 100% and thus behave as an ORC, unless it is salt solution. Expansion then takes place from the saturated vapour state, same as for regular ORC. Superheating in either does not bring any thermodynamic benefit as is also supported by the optimization results here.

Except for pinch point specification, the endpoint of heat addition in supercritical state is constrained by requirement that the expansion doesn't pass through the saturated vapour line more than once and outlet steam quality is more than 95%.

Performance of the cycles after optimization is summarized in Table 6.9 for 100°C heat source and in Table 6.10 for 200°C heat source. Inspecting the results, it is clear that same as for the previous analysis a simple Rankine cycle is better choice at higher temperatures while lower temperatures are a domain of cycles using working fluid mixtures. The best performance at low temperature has the water-LiBr APC, closely followed by the zeotropic ORC and methanol – heptanol APC. Traditional water-ammonia Kalina APC has performance behind these, but it is still better than single fluid ORC.

Table 6.9: Results of thermodynamic analysis for 100°C heat source

Cycle, fluid	$\eta_{1st,\ util,net}$ (%)	$\eta_{1st,\ util,gross}$ (%)	$\eta_{1st,\ cycle,gross}$ (%)	$\eta_{2nd,\ util,net}$ (%)	$\eta_{2nd,\ util,gross}$ (%)	Note
APC $NH_3 - H_2O$	1.4	1.7	5.5	11.3	13.8	$C_{NH_3} = 89\%$
APC H_2O-LiBr	1.6	2.0	6.1	13.2	15.8	$C_{H_3O} = 41\%$
APC Amyl-Acetate-CO_2	1.0	1.8	3.6	7.8	14.6	$C_{AA} = 11\%$
APC Imidazolium-R134a	0.9	1.5	8.7	7.3	11.8	$C_{\mathrm{R134a}} = 77\%$
APC Imidazolium -H_2O	1.0	1.4	6.8	8.1	11.7	$C_{H_3O} = 8\%$
APC MeOH-HepOH	1.5	2.0	6.5	12.2	15.8	$C_{MeOH} = 60\%$
ORC pentane-cyclohexane	1.6	2.0	7.1	12.9	16.5	$C_{Pentane} = 60\%$
RC H_2O	1.0	1.5	6.4	8.4	12.4	
ORC Isobutane	1.1	1.6	5.9	8.6	13.0	
ORC MM	1.0	1.5	5.5	8.0	12.1	
ORC R245fa	1.1	1.6	6.0	8.7	13.1	
R-ORC Isobutane	–	–	–	–	–	Opt. $Q_{\mathrm{rec}} = 0$
R-ORC MM	1.0	1.5	5.9	8.2	12.2	
R-ORC R245fa	–	–	–	–	–	Opt. $Q_{\mathrm{rec}} = 0$
SC-ORC R143a	0.8	1.1	6.2	6.2	8.7	
SC-ORC R41	1.2	2.0	4.6	9.6	16.0	

Performance of the selected ionic liquids is rather disappointing, performing worse than all ORC. On the other hand this shouldn't be generalized to all ionic liquids as a number of possible fluids and even absorbent-absorbate pairs are enormous. Similarly the performance of amyl acetate in comparison with other cycles is poor. Supercritical cycles do not bring any advantage for the higher temperatures and only a very small improvement against other cycles for R41 refrigerant for lower temperatures.

Results of gross cycle efficiency again demonstrate that in waste heat recovery applications cycles with high efficiency do not necessarily provide high utilization efficiency of the heat source (and thus absolute power output). Also a difference between gross and net efficiency shows how important it is at the low temperature, using even more than 30% of gross power output. Most obvious is a case of SC-ORC with R41 where gross 2.0% efficiency shrinks to only 1.2% net efficiency. Exergy efficiency further shows the share of parasitic load on the whole work potential by difference between gross and net values. Absolute values of exergy efficiency then point at the impact of pinch-point values relative to available temperature differences between the heat source and the heat sink, where at the 200°C heat source the values are above 40% while for the 100°C the best value just exceeds 13%, gain pointing out the issue the low temperature heat utilization.

Table 6.10: Results of thermodynamic analysis for 200°C heat source

Cycle, fluid	$\eta_{1st,util,net}$ (%)	$\eta_{1st,util,gross}$ (%)	$\eta_{1st,cycle,gross}$ (%)	$\eta_{2nd,util,net}$ (%)	$\eta_{2nd,util,gross}$ (%)	Note
APC$NH_3 - H_2O$	7.1	7.8	14.3	30.9	34.4	c_{NH_3} = 97%, RC mode
APCH_2O – LiBr	6.3	6.9	17.8	27.8	30.2	c_{H_2O} = 80%
APC Amyl-Acetate-CO_2	5.8	6.7	9.3	25.4	29.2	c_{NH_3} = 13%, RC mode
APC Imidazolium −R134a	5.7	6.1	15.7	25.1	26.7	c_{R134a} = 50%
APC Imidazolium $-H_2O$	5.0	5.6	12.3	21.9	24.7	c_{H_2O} = 9%
APCMeOH – HepOH	6.5	7.1	17.6	28.4	31.0	c_{MeOH}=65%, RC mode
ORC Pentane-cyclohexane	7.2	7.9	13.1	31.6	34.5	$c_{Pentane}$=60%
RCH2O	5.8	6.6	14.7	25.3	28.9	
ORC Isobutane	8.5	10.0	12.6	37.4	43.8	
ORCMM	6.7	7.8	11.8	29.4	34.3	
ORCR245fa	9.3	10.6	14.6	40.7	46.4	
R – ORC Isobutane	8.8	10.3	13.0	38.4	45.2	
R – ORCMM	7.0	8.0	14.9	30.6	34.9	
R – ORCR245fa	9.3	10.6	15.2	40.9	46.6	
SC – ORCR143a	6.3	7.4	9.7	27.6	32.6	
SC-ORC Isobutane	8.8	10.1	13.6	38.5	44.2	
SC-ORC R245fa	7.2	8.0	15.2	31.7	34.9	

Temperature glide effect is illustrated by Q-t curves of heat addition and heat rejection of selected fluids in Figure 6.16 for the 100°C heat source and Figure 6.17 for the 200°C heat source. Note that cooling air for heat rejection has different mass flow for each case and for lucidity it is not shown in the figures. The fluids with zeotropic mixtures or with a fluid in supercritical state can well follow the heat source as it cools down. Amyl acetate – CO_2 and ORC with supercritical or near-supercritical fluids have excellent pinch match at the heat source side. Net power production is however affected by another parameters. In this case lower enthalpy difference to be utilized by expander causes low power production. Excessive amount of the heat transferred to the working fluid then gets rejected which can further increase parasitic load. On the other hand APC with imidazolium – R134a achieves high cycle efficiency, but limited heat transferred to the cycle allows also only a limited power production.

For practical application of the power cycles are important further aspects as

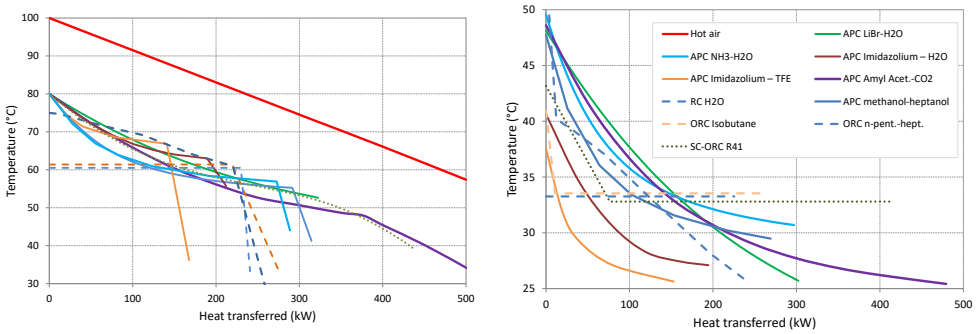

(a) (b)

Figure 6.16: Q-T curves for (a) heat addition and (b) heat rejection of cycles with mixture fluids, selected ORC and SC-ORC, for 100°C heat source (cooling air curves not shown as they would be different for each case)

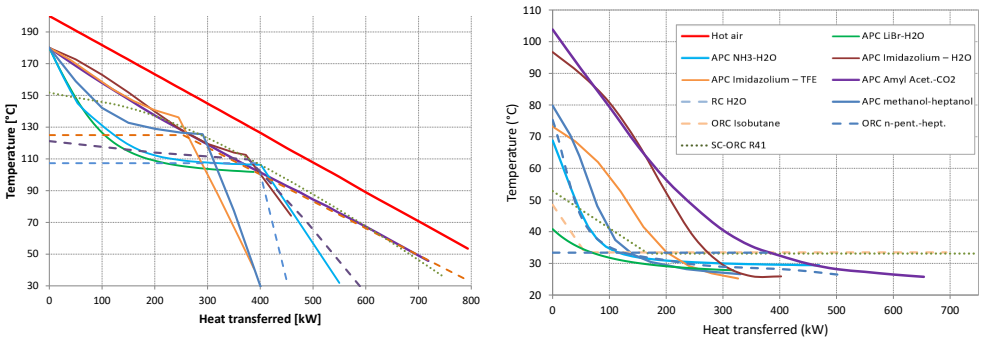

(a) (b)

Figure 6.17: Q-T curves for (a) heat addition and (b) heat rejection of cycles with mixture fluids, selected ORC and SC-ORC, for 200°C heat source (cooling air curves not shown as they would be different for each case)

pressures in the system or the vapour quality for expander design and reliable operation. These parameters are presented in Table **??**. The highest pressures are in amyl acetate – CO_2 APC and are in order of ten MPa, which can mean small device as many authors claim. However, necessity of thick walls and safety measures for high pressure vessels increases the cost and thus limits actual applicability. Smaller sized units in distributed generation would also suggest low efficiency of expanders due to relatively large leakages through necessary design clearances. Similar is the case of NH_3-H_2O APC, SC-ORC and some subcritical ORC with still very high pressures in order of MPa. APC using the alcohol mixture (methanol-heptanol) or ionic liquids have their vacuum much more moderate. From this point comes interesting the zeotropic ORC with n-pentane – cyclohexane as the high pressure is slightly above ambient while the low pressure is at moderate vacuum.

Table 6.11: Pressure levels and expander outlet quality for the investigated cycles

Cycle, fluid	100°C heat source			200°C heat source		
	p_{high} (bar)	p_{low} (bar)	x_e (%)	p_{high} (bar)	p_{low} (bar)	x_e (%)
APC NH_3-H_2O	20.70	10.67	98	68.80	11.13	96
APC H_2O-LiBr	0.06	0.01	98	0.94	0.03	95
APC Amyl-Acetate-CO_2	92.50	60.00	97	200.00	60.00	93
APC Imidazolium-R134a	0.60	0.10	99	4.90	0.08	100
APC Imidazolium-H_2O	0.90	0.33	94	4.70	0.31	100
APC MeOH-HepOH	0.63	0.18	95	6.50	0.16	97
ORC pentane- cyclohexane	1.40	0.43	100	5.50	0.52	100
RC H_2O	0.20	0.05	95	1.31	0.05	90
ORC Isobutane	8.97	4.46	100	30.91	4.46	100
ORC MM	0.28	0.09	100	1.56	0.09	100
ORC R245fa	4.79	2.00	100	32.86	2.00	100
R-ORC MM	0.28	0.09	100	1.57	0.09	100
SC-ORC R143a	39.00	16.25	100	–	–	–
SC-ORC R41	75.20	45.70	100	–	–	–
R-ORC Isobutane	–	–	–	30.91	4.41	100
R-ORC R245fa	–	–	–	32.86	1.99	100
SC-ORC R143a	–	–	–	50.00	14.97	100
SC-ORC Isobutane	–	–	–	45.00	4.41	100
SC-ORC R245fa	–	–	–	37.00	2.05	100

6.3.6 APC performance sensitivity analysis

The effects of the main salt APC thermodynamic parameters controlling the cycle performance are further revealed by a sensitivity analysis. For this purpose, the controlled variables are the high-pressure level in the system as p_1, condensing pressure p_{11} and the initial concentration of LiBr ξ_1. The pressure-level sensitivities of the net efficiencies both of resource utilization and of the cycle itself, for a heat source temperature of 100°C (with nominal conditions at maximal $\eta_{2nd,util}$) and other parameters from Table 6.4, are shown in Figure 6.18. Unlike in Figure 6.9 used in model validation and 1st law efficiency, the efficiency here is presented also with the parasitic load necessary for the heat rejection. Absorber pressure appears to be the same for maximal efficiency of both the cycle and the heat source utilization, where the maximum verges on the physical limits with respect to absorber pressure. Steam generator pressure for maximal cycle-only efficiency stays at relatively higher pressure levels and drops sharply after reaching the maximal point. This is caused by the decreasing concentration difference between the weak and rich solutions, thus resulting in a higher mean temperature of heat addition.

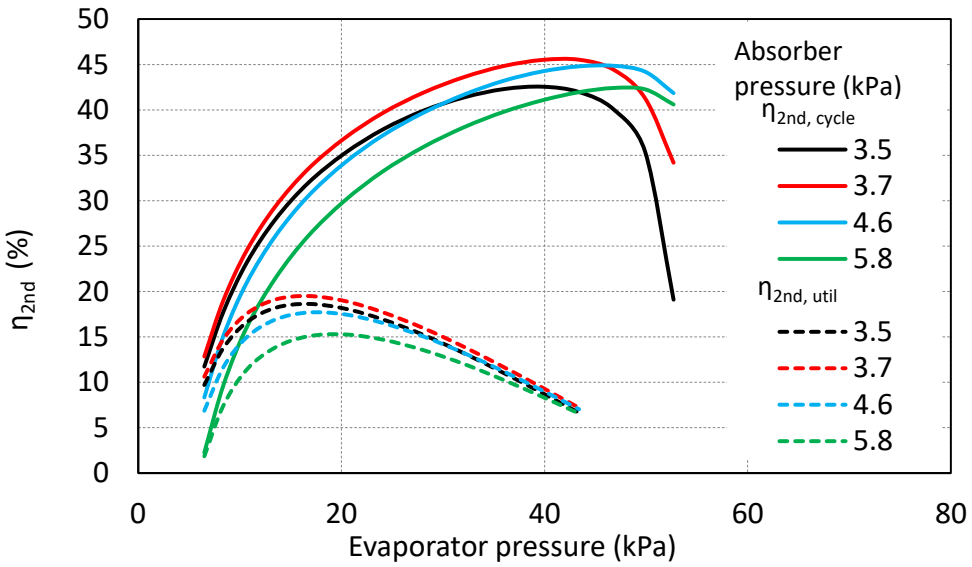

Figure 6.18: The sensitivity of the second law efficiency of the heat source utilization and of the cycle with respect to evaporator and absorber pressures for a LiBr cycle with a 100°C heat source and a cooling tower.

The effect of the LiBr concentration ξ_1 was further explored for two cases, assuming the same basic operating conditions as in the pressure sensitivity analysis. The first case was with fixed pressure levels in the cycle, and the second was with a fixed final temperature of absorption-condensation, T_{11}. The results of both are shown in Figure 6.19. In the first case of fixed pressure levels, the physically available range of concentrations was smaller within the boundaries of other parameters, and both its characteristics remained almost flat throughout the whole range, although heat source utilization efficiency was more sensitive and decreased more steeply as the concentration of the weak solution rose. When temperature T_{11} was fixed, the changing concentration ξ_1 also affected the pressure p_{11}. The maximum efficiency of heat source utilization was relatively flat when compared to the cycle efficiency, with a very deep fall once the point of maximal efficiency was exceeded.

6.3.7 Case study 1 - low temperature solar system

Following the general analyses, three case studies of more specific APC applications are presented here. The first one is focusing on solar thermal heat utilization. Small scale solar ORC plants were suggested and investigated both theoretically and experimentally, which can work with various types of solar collectors but most of the built units are for research and demonstration purposes only [213, 214, 215]. Given the potential of the APC with LiBr solution in waste heat recovery and given the presence of relatively cheap

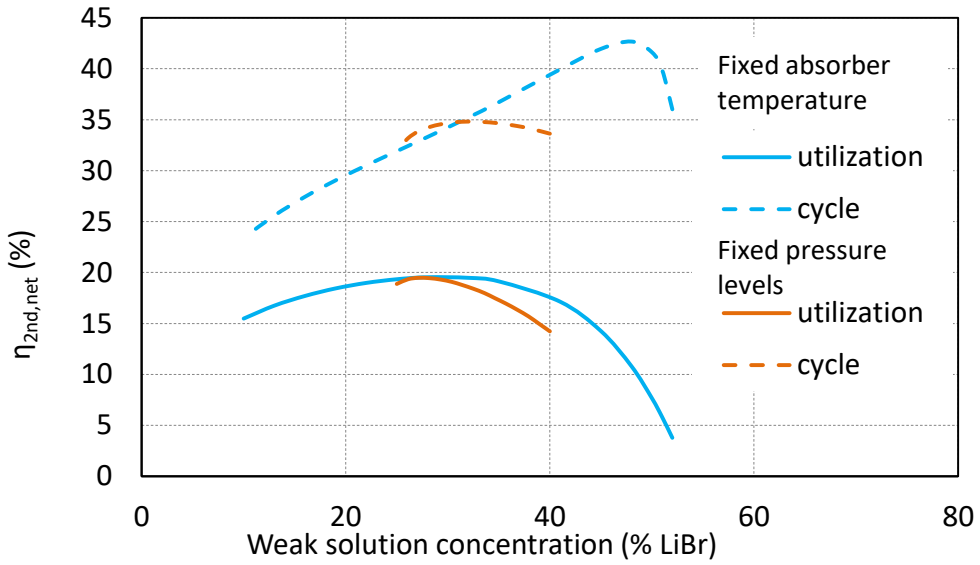

Figure 6.19: The sensitivity of the second law efficiency of the heat source utilization and of the cycle with respect to the weak-solution concentration of LiBr for a LiBr cycle with a 100°C heat source and a cooling tower.

solar collectors for heating on the market, a suggestion to combine these two systems emerges. Therefore this case study, in detail described in author's work [VN5, Sc16], is exploring the option of coupling the heat engines (ORC and APC) and solar collectors (evacuated tube type). Overall performance is then analysed, including a comparison with PV. Note that the power cycles in this case use closed loop heat source. Parameters of the collector however change with the operation temperature, where thermal losses are evaluated with respect to mean collector temperature.

A simple (non-recuperated) ORC is used as a benchmark cycle. Within the assumed minimum temperature difference constrains, the recuperated amount of heat would be very small or even none. The working fluid was chosen as R245fa as a standard fluid in ORC and in many studies and actual plants. Auxiliary systems necessary to operate the system are pumps for the heat transfer fluids which need to overcome mainly pressure losses. Heat rejection system power requirement is represented by a fan of a dry cooler. Overall configuration of both systems is in Figure 6.20. Pressurized water is assumed in the loop between the collector and the heat engine, which has pressure drop driven by quadratic law. Reference value for the entire loop is taken as 10 times value of collector itself, taken from datasheet[1]. Details of the solar and collector models and interconnection with the power cycle models is provided in Appendix B.

[1] http://www.eurosunsolar.de/en/sunstar-df-100/

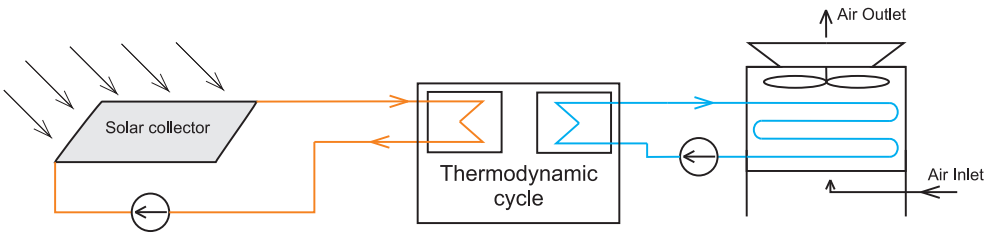

Figure 6.20: Configuration of power system using solar collectors.

Table 6.12: Boundary conditions and parameters of the solar systems case study.

p_{amb} (kPa)	RH_{amb} (%)	$\Delta T_{\text{min,liq-wf}}$ (°C)	$\Delta T_{\text{min,wf-wf}}$ (°C)	$\Delta T_{\text{min,DC}}$ (°C)	$\Delta p_{\text{cool loop}}$ (kPa)
101	70	5	5	10	80
Δp_{DC} (Pa)	η_{exp} (%)	η_{pump} (%)	η_{fan} (%)	β_{surf} (°)	γ (°)
200	80	70	70	30	0
ρ (1)	ϕ (°)	$\eta_{\text{col,ref}}$ (%)	a_1 ($Wm^{-2}K^{-1}$)	a_2 ($Wm^{-2}K^{-2}$)	A_a (m^2)
0.2	50	79.2	1.62	0.0021	1.114

The solar model uses experimental data of temperatures and solar irradiation of horizontal plane measured for Prague, Czechia. Heat loss and pressure drop is considered only where explicitly stated, otherwise neglected. Heat transfer is limited by constant minimal temperature differences (pinch points). The constant assumptions and boundary conditions are summarized in Table 6.12 (refer to the solar model description for specific symbols), where subscripts *amb* stand for ambient, *liq* stand for liquid phase of fluid, *wf* for working fluid, *DC* for dry cooler. Included are collector parameters ($\eta_{col,ref,a1,a2}$) obtained from the *Solar Keymark Database*[2] (selected Eurosun Sunstar DF 100/6 representing rather efficient evacuated vacuum tube collector).

The PV models can be directly coupled with the solar model and power produced is evaluated for a model in each time step and given the simplification of neglecting produced electricity in thermal energy balance, no iteration is needed. Power produced is simply evaluated from Equation (6.29) with surface area for further analyses taken as 1 m^2.

$$W_{PVnet} = \eta_{PV\ \text{panel}}\, G_T A \tag{6.29}$$

For the heat engines, net power is evaluated after obtaining expander power

[2]http://www.solarkeymark.dk/CollectorCertificates

Table 6.13: Parameters for chosen (reference / design) point at the time of the year 2919.5 h.

ST (h)	θ (°)	T_{amb} (°C)	G_{horiz} (Wm^{-2})
15.5	49.5	14.2	321
G_{bT} (Wm^{-2})	G_{dT} (Wm^{-2})	G_{rT} (Wm^{-2})	G_{Tsum} (Wm^{-2})
70.5	240.5	4.3	315.3

production and power consumption of all components. An input and control value of for the heat engine models are heat source inlet temperature, i.e. collector outlet temperature. Collector return temperature is thus a function of heat engine parameters. Mean collector temperature to evaluate its efficiency can be obtained only after the cycle parameters are given. Obtaining parameters of the heat engines with thermal collectors with operation limits imposed only by the pinch points would possess following issues. In winter months with very low temperature, the condensation (or absorption) pressure would enormously decrease but also the cooling circuit water could get below freezing point. To mitigate this issue, the operation of the heat engine was split into two regimes, first as defined above with pinch point limits which goes down to ambient air temperature of -5°C. For temperatures below this point, the condensation (absorption) pressure and the cooling circuit return temperature are kept constant. Details with example charts of this behaviour on the net cycle efficiency and collector mean temperature are in Appendix B (e.g. Figure A2.2).

At first the parameters of the ORC and APC cycles are presented. A starting reference point for the cycle parameters was taken from parameters of the cycles optimized for highest net electricity production with respect to conditions for 1st May around 3 pm (time=2919.46 h). Solar and ambient parameters for this point are summarized in Table 6.13.

Resulting parameters of the cycle for the boundary regimes of their operation, i.e. for the cases of ambient temperature 35°C and -5°C to -20°C are presented in Table 6.14 for the APC. Node numbers correspond to Figure 2.1b. In order to see a behaviour of different settings, effects of intensity of cooling (ΔT of cooling air) and case of fixed condensing temperature for different ambient temperatures are explored and depicted in Figure 6.21. An optimal point for the selected conditions is apparent. Also, it can be seen that operating the cycle with given pinch points even for different ΔT_{air} gives higher efficiency than keeping condensing (final absorption) temperature constant.

Providing more insight into the behaviour of the system, Figure 6.22 shows system efficiency under the considered mode of operation and collector efficiency

Table 6.14: Parameters of APC operating at limits of the regimes. (Node numbers – see figure 2.1b)

	(°C)	(kJ/kg)	(kg/s)	(bar)	(kJ/kgK)	(kg_{LiBr}/kg_{sol})
T_{amb} = 35°C						
1	52.3	115	1.70	0.25	0.49	0.378
2	75.4	175	1.70	0.25	0.66	0.378
3	77.3	180	1.70	0.25	0.68	0.378
4	91.4	762	1.70	0.25	2.31	0.378
5	91.4	2669	0.39	0.25	7.97	0.000
6	41.7	2531	0.39	0.08	8.08	0.000
7	91.4	197	1.31	0.25	0.63	0.490
8	57.3	121	1.31	0.25	0.41	0.490
9	57.3	121	1.31	0.08	0.41	0.490
10	64.1	672	1.70	0.08	2.17	0.476
11	52.3	115	1.70	0.08	0.49	0.378
T_{amb} = −5°C to −20°C						
1	14.0	20	1.62	0.25	0.17	0.378
2	63.4	144	1.62	0.25	0.57	0.378
3	77.3	180	1.62	0.25	0.68	0.378
4	91.4	763	1.62	0.25	2.31	0.378
5	91.4	2669	0.37	0.25	7.97	0.000
6	5.5	2310	0.37	0.01	8.29	0.000
7	91.4	198	1.25	0.25	0.63	0.490
8	19.0	37	1.25	0.25	0.14	0.490
9	19.0	37	1.25	0.01	0.14	0.490
10	23.1	557	1.62	0.01	2.02	0.476
11	14.0	20	1.62	0.01	0.17	0.378

for various cases of collector irradiation GT based on cases of total time of the experimental annual irradiation 2919 h (G_T =315 W/m2), 4355 h (G_T =725 W/m2), 5745 h (G_T =446 W/m2). Note that due to different ratios between direct, diffuse and reflected light and angle/azimuth of incidence, the results can't be entirely generalized as there are different IAMs. The collector efficiency difference between ORC and APC case is very small, as the mean temperature is has a similar value, only slightly higher temperature for ORC causes its slightly lower efficiency. The magnitude of coefficients a_1 and a_2 makes the collector efficiency trend to appear nearly linear. Cycle efficiency (same for different G_T as it is a function of temperature levels) is obviously increasing with available temperature difference according to the 2^{nd} law of thermodynamics and is noticeably higher for APC, causing higher net system efficiency. The trend of overall efficiency is dependent on the cycle and collector efficiency and a breaking point in operation regime below -5°C has a negative

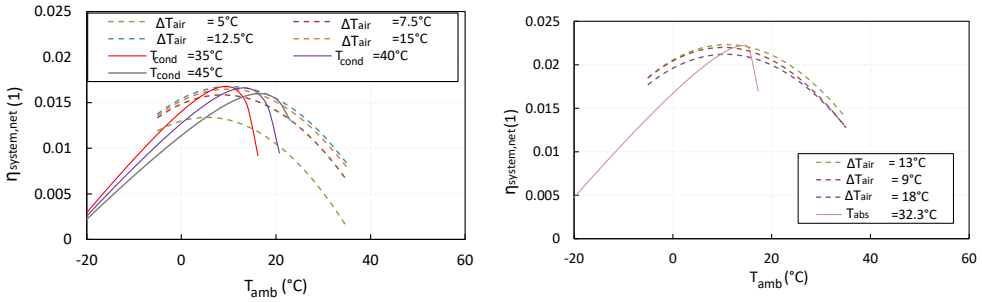

(a) (b)

Figure 6.21: Effect of ambient temperature and different types of condenser / absorber operation regime on net system efficiency with a) ORC and b) APC.

effect on this trend.

The most important result is however a net power production potential throughout the year. Figure 6.23 shows a cumulative power production per aperture area for the system with power cycles. The collector outlet temperature is varied while other parameters are fixed by the boundary conditions and described operating regime. For the ORC a 12 K temperature difference between evaporation temperature and collector outlet temperature is kept constant, according to the reference case. APC isn't limited by a pinch point within the exchanger, therefore the temperature difference comes directly from the boundary conditions, while the concentration change of the liquid LiBr solution in the evaporator is kept constant. Results show higher power production of the APC. Note that the maximum points still might not represent the most optimized situation allowing different operation regime, but they are fully sufficient for initial evaluation.

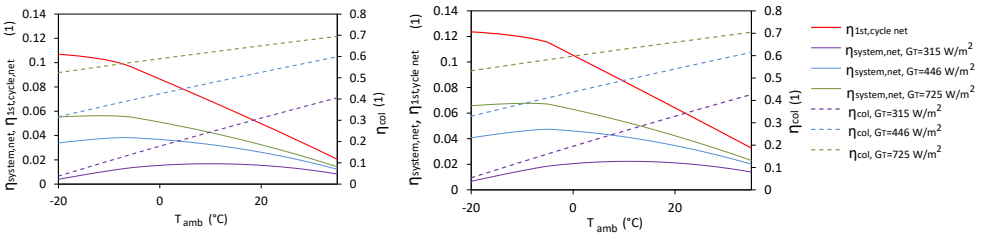

(a) (b)

Figure 6.22: Effect of ambient temperature and different irradiation (for total time 2919 h, G_T =315 W/m2; 4355 h, G_T =725 W/m2; 5745 h, G_T =446 W/m2) on collector and overall system efficiency for a) ORC and b) APC

Finally, a comparison of maximal power production values from the heat engines compared to the results of photovoltaic panels is in Table 6.15. These

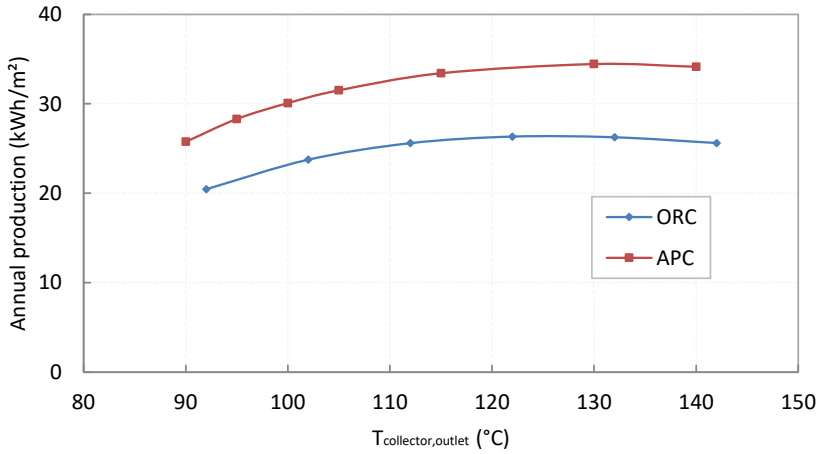

Figure 6.23: Annual potential of electricity production from ORC and APC.

values show nearly double potential of amorphous PV and about five times higher potential for polycrystaline PV systems which only hardly justifies direct application of heat engine systems in this configuration. There are however further considerations.

Table 6.15: Annual maximal expected power production potential for analyzed systems.

system	max ORC	max APC	$PV_{amorphous}$	$PV_{polycrystaline}$
kWh/(m^2 year)	26.3	34.4	61.8	153.8

The results for heat engines annual production has to be taken though as initial estimates with possibilities for some efficiency increase. These possibilities are in detailed optimization and controlling for adjustment to a maximal power point for each time period. However major power production increase (so that to surpass PV systems) is not expected anyway and fully off-design performance might also provide lower cycle performance. The results are preliminary, assuming design parameters at all times, i.e. constant minimum temperature differences in the heat exchangers, constant pressure drop on heat rejection side equipment and constant efficiency of pumps, expander and fan. For actual power production evaluation, a system of specific sizing of the equipment in a single operating mode would need to be made. Even though the results show lower overall efficiency and power production than for the photovoltaic modules, ORC and especially APC systems may find niche applications and have certain advantages. The first one is the possibility to integrate a thermal energy storage at rather low cost. Power production thus can have smooth supply and can be available when needed.

Table 6.16: The boundary conditions of the bottoming unit for a high temperature ORC.

T_{amb} (°C)	p_{amb} (kPa)	$\Delta T_{min,liq-wf}$ (°C)	$\Delta T_{min,gas-wf}$ (°C)	$\Delta T_{min,wf-wf}$ (°C)	$\Delta T_{min,DC/ACC}$ (°C)
15	101	5	20	5	10
η_{exp} (%)	η_{pump} (%)	η_{fan} (%)	$\Delta p_{H_2O\ loop}$ (kPa)	Δp_{ACC} (Pa)	Δp_{DC} (Pa)
75	75	70	80	150	200

6.3.8 Case study 2 – bottoming cycle to ORC

Use of the APC as a bottoming cycle directly connected to a high temperature ORC that has a condensation temperature well above ambient was investigated in author's work [VN3]. Example application might be a cogeneration ORC, however operated in summer at design conditions, when however there is no heat demand. Process configuration would be a second condenser of the ORC serving as a heat input HX into a bottoming cycle. This case is again compared with a low temperature ORC as a baseline, here with recuperation. R245fa is used as a standard low temperature ORC fluid. Boundary conditions are provided in Table 6.16.

If heat rejection process would be isothermal or close to isothermal, Rankine cycle as a bottoming unit would be in the pinch point analysis a logical choice. Heat rejected from ORC condensers comes often however from significantly superheated vapour and therefore this case is also analysed for APC. The specific heat source considered here is a condensing stream of vapour in experimental microcogeneration ORC operated at the UCEEB, Czech Technical University [6]. Particularly there is 130°C vapour of hexamethyldisiloxane (MM) condensing at 90°C (74 kPa), assumed 5°C subcooling and the heat transfer of 50 kW. Heat rejection is assumed by a dry cooler. Heat transfer to the cycles is schematically depicted by Q-T diagrams in Figure 6.24. It can be seen, that for the APC there is a pinch point within the evaporation of LiBr at the point of saturated MM vapour and an optimized concentration causes a rapid rise in temperature of the LiBr solution after this point. As a result we can see in overall a good match between heat source and working fluid one end, so it can be variably adjusted between parameters for the cycles given in Table 6.17, where the APC achieves 15% higher net power output. These results are however valid only within given assumptions such as un-recuperated topping cycle and no bottoming ORC expander inlet superheat; the theoretical evaporation curve might in practice also pose some difficulties.

Table 6.17: Resulting parameters of the cycles as bottoming units for ORC condensing at 90°C transferring 50kW of heat.

	W_{cycle} (kW)	W_{net} (kW)	$\eta_{1st,\text{ cycle,gross}}$ (%)	$\eta_{1st,\text{ cycle,net}}$ (%)	$p_{\text{cycle,high}}$ (kPa)	$p_{\text{cycle,low}}$ (kPa)
ORC	4.8	4.0	9.5	8.0	895	205
APC	5.2	4.6	10.4	9.2	51	5

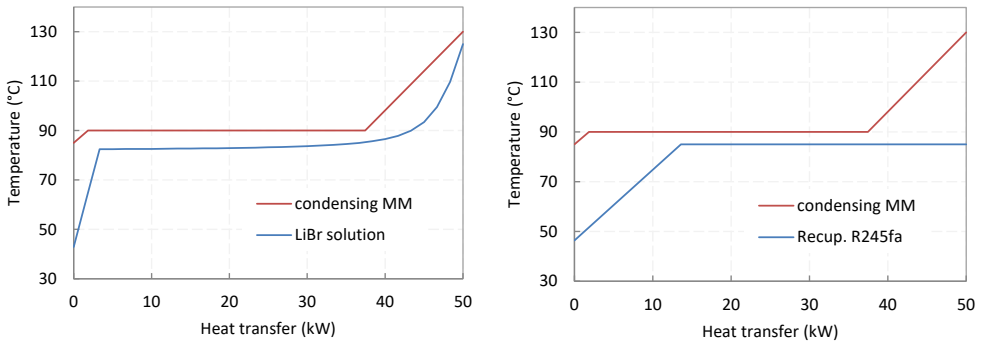

(a) (b)

Figure 6.24: Q-T diagrams of heat transfer to (a) the ORC and (b) the APC when used on condensing MM as a heat source.

6.3.9 Case study 3 – waste heat utilization in CCS systems

In this case study, described in detail in author's work [VN4], the LiBr APC has been considered along with ORCs for waste heat recovery from waste heat in several Carbon Capture and Storage (CCS) technologies to improve efficiency of the entire system. This option has been explored instead of attempts to utilize the heat back within the system as complex heat recovery systems could hinder flexibility of the system. Rather here is considered just a standalone WHR system that doesn't affect the original technology. Three CCS plant options have been explored, post-combustion capture, oxy-combustion and finally pre-combustion in Integrated Gasification Combined Cycle (IGCC) plant. Summary of the considered waste heat streams and their potential power production with respect to the plant fuel input are in Table 6.18. It shows additionally saved cooling thermal duty as some of the technologies would require cooling anyway and WHR technology takes care of a part of it.

Results of application of proposed WHR units into the plants are summarized in Table 6.19. The effect on post-combustion plant is almost negligible. Oxyfuel and pre-combustion CCS have very similar efficiency but when WHR systems are applied the difference is 3 p.p. better for the pre-combustion from relatively large number of utilizable waste heat streams. WHR can be applied also to the

Table 6.18: Waste heat recovery options for the CCS plants.

Waste heat stream	Temperature (°C)	Heat flow (% of LHV input)	WHR unit type	Power increase (% of LHV input)
Post-combustion system:				
CO_2 compression IC/AC	102 (cooling fluid)	1.3	LiBr APC	0.03
Desorber heating outlet	115	2.3	Isohexane ORC	0.05
Saved cooling duty	–	1.2	–	0.001
Oxyfuel CCS plant:				
ASU air compressors IC/AC	234 (cooling fluid)	9.0		
CO_2 compression IC/AC	105 (cooling fluid)	7.1	Isohexane ORC	1.13
Saved cooling duty	–	10.5	LiBr APC	0.17
IGCC plant (with and without CCS):				0.01
ASU air compressors IC/AC	234 (cooling fluid)	3.2		
Gasifier O_2 compressors IC/AC	246 (cooling fluid)	1.1	Isohexane ORC	0.40
Gasifier N_2 compressors IC/AC	201 (cooling fluid)	0.3	Isohexane ORC	0.12
Coal dryer outlet vapours	110	3.3	Isohexane ORC	0.02
Syngas cooling (CCS/no CCS)	252 / 125	13.2 / 2.6	LiBr APC	0.14
CO_2 compression IC/AC (CCS only)	113 (cooling fluid)	3.8	LiBr APC	0.09
Flue gas aftercooler (CCS/no CCS)	110 / 110	6.0 / 7.3	LiBr APC	0.18 / 0.20
Saved cooling duty (CCS/no CCS)	–	31.9 / 10.6	–	0.03 / 0.01

(IC = intercooler, AC = aftercooler)

Table 6.19: Results of application of proposed WHR units into the plants.

	PC Plant	PC plant - Oxyfuel	PC plant - post comb.	IGCC	IGCC - CCS
Original efficiency (%)	38.99	31.13	28.12	43.18	31.27
Efficiency with WHR (%)	38.99	32.44	28.20	44.18	35.45
Efficiency increase (p.p.)	0	1.31	0.08	1.10	4.18

base case IGCC adding over 1 p.p. in efficiency. In case of often start-ups and shut-downs the proposed solution brings another benefit increased flexibility from decoupling of the power cycle from syngas production and processing. The APC systems are always providing rather marginal benefit, however it is in accord with feasibility for rather smaller systems.

6.3.10 Discussion and summary and of the power cycle theoretical investigations

Absorption power cycles (APC) based on aqueous salt solutions of LiBr, LiCl, and $CaCl_2$ were investigated base on pinch point analysis for primarily waste heat recovery applications in comparison with various alternative cycles. Among them were considered steam Rankine cycle for a reference, ORC with various working fluids (subcritical as well in some cases supercritical, with working fluid mixtures, simple and recuperated) and several other APC working fluid options (water – ammonia as Kalina cycle, amyl acetate – CO_2, methanol – heptanol, selected ionic liquid with water or refrigerant). For heat rejection were considered wet cooling tower, air cooled condenser (absorber) or dry cooler. Very important aspect is a consideration of a parasitic load of heat

rejection (fans, pumps) as the power requirement can be of a similar order of magnitude as the turbine power output. The cycles were optimized for maximal net power output, typically represented by utilization efficiency. At the point of maximal utilization efficiency, the cycle efficiency is often rather comparable for many of the cycles. The amount of heat that can be transferred to the cycle, combined with the effect of lower heat rejection power requirements due to fans and pumps, favours APC in the domain of very low temperatures. Generally higher benefit was shown for applications with higher cooling power demand. Absorption power cycles begin to have a thermodynamic benefit over Rankine cycles for heat source temperatures below approximately 120°C (exactly depends on many parameters and boundary conditions). The relative efficiency improvement rises over 150% for heat source temperatures below 80°C. The reason is the aforementioned high power demands of the heat rejection. The highest efficiency of heat source utilization (and power output) was delivered by the $CaCl_2$- and LiCl-based cycles, followed by the LiBr-based cycle. The difference between different salt solution systems is however very small. Comparable performance was also achieved with alternative mixture of methanol-heptanol. The ammonia-water mixture absorption cycle has the lowest efficiency of APCs in this low temperature domain.

In the comparison with ORC for waste heat recovery it is important to note, that recuperation for ORC has minimal effect in waste heat recovery applications for sensible heat source without restrains on its outlet temperature. Reason is it doesn't increase gross power production as was also noted in the literature [20, 21], but increases system complexity, in real devices it increases turbine backpressure and there is minimal effect on net utilization efficiency. In APC however, the recuperator serves to lower the liquid absorbent temperature, improving the absorption process itself. Compared to ORC, the pressure loss also does not play a crucial role in this case as both fluids are liquid. Effect of recuperation on utilization efficiency is also a reason why more complex schemes are not considered in this investigation, even though such approach is quite common in some scientific literature that is decoupled from practical implementation. A presentation of three case studies shows, that waste heat recovery doesn't not need to be the only field of APC prospective application. Low temperature solar system investigation has shown a superior performance compared to ORC (though inferior to photovoltaic, prospective for purposefully thermal systems). Similar results were obtained for bottoming cycle of ORC at the temperatures suitable otherwise for heating systems (if there is no demand). Here might specifically combined power and cooling system find an interesting potential. Lastly the waste heat does not need to come from the industry, but even certain power plants systems, such as ones with CCS.

All salt-based absorption cycles operate in a vacuum (including high pressure level) in the entire investigated range of heat source temperatures, with the

deepest vacuum present in $CaCl_2$- and LiCl-based cycles. The absolute pressures are in order of kPa. The water-ammonia combination, due to its typically high pressures, provides the potential for a very compact turbine; however, for small power outputs the very low volumetric flow could result in a very inefficient device (and/or high rotational speed), not to mention corrosion problems from ammonia. Salt solution are corrosive as well, inhibitors are typically in place but turbine should operate in a clean vapour. Either way, a vacuum in the cycle requires a fully airtight mechanical design. The LiBr solution seems to provide a trade-off between acceptable vacuum, high cycle efficiency and there is wide experience of this fluid from absorption chillers. Interesting aspect further affecting the design is low pressure water vapour, where the large volumetric flow results in bulky device but provides potential for design of a highly efficient turbine at low to moderate speed (investigated in following sections). These APC are therefore more suitable for small distributed energy systems rather than large scale system. Low temperatures then suggest use of low cost materials, even, as author investigates later on, polymeric 3D printed materials.

Application of cycles with mixed working fluids might come across further issues from actual kinetics, two phase flow pattern (homogeneity) and heat transfer coefficients. This affects the design of the two-phase heat exchangers. Current literature doesn't successfully report actual temperature glide in Kalina cycles even though demonstration units have been built and other works report only cases of very small temperature glide designs for LiBr absorption systems [150]. Actual phase change behaviour and performance of the prospective APC mixtures water-LiBr and methanol-heptanol as well as ORC mixture n-pentane – cyclohexane should be investigated in greater detail. Environmental impact and toxicity of working fluids is recently getting also much more attention. LiBr perfectly fulfils these requirements among APC. Ammonia and methanol do have some, though limited, toxicity, and imidazolium ionic liquids and amyl acetate have their toxicity higher.

Even though further investigations could cover more complex, exergy and economic theoretical analyses etc., major unknowns are observed in verification of the cycle operation according to the provided assumptions. Therefore, after theoretical investigation of obvious APC use for combined power and cooling in the next subsection, the key aspects of technical feasibility of the APC is investigated experimentally.

6.4 Combined absorption power and cooling cycle

The absorption power and cooling combined cycle (APCC) comes as a logical application of the APC concept into the existing technology. In the study of the APCC, first, overall parameters of the system are reported with the most

Table 6.20: Boundary conditions of the combined cooling and power cycle models.

T_{amb} (°C)	p_{amb} (kPa)	RH_{amb} (%)	T_{hs} (°C)	T_{eva} (°C)	T_{51} (°C)	$\Delta T_{\min,HX}$ (°C)
25	101.325	70	95	5	15	5
m_{hs} (kgs^{-1})	p_{hs} (kPa)	p_{cw} (kPa)	Δp_{DC} (kPa)	η_{is} (%)	$\xi_{sol,1}$ (%)	$T_{hs,out}$ (°C)
2.5	8000	200	0.15	80	56	85

typical working fluid, LiBr solution. The reference ORC-VCC system is shown alongside. The boundary conditions input parameters of the models in this analysis are summarised in Table 6.20. The values are taken to reflect similar actual systems of absorption chillers [36]. The expander efficiency is taken as a state of the art from micro turboexpander experimental investigations [179, 215]. For simplicity of the results interpretation, electrical and mechanical efficiencies are not considered separately; it would however only disadvantage the benchmark ORC-VCC system in cold energy production.

A sensitivity analysis following detailed illustration of cycle parameters at selected operating point shows the performance with respect to the major inputs. The effect of auxiliary equipment consumption on the net performance is shown as well as the difference of results for constant heat input and for an open-loop heat source. Lastly is presented a comparison of the APCC parameters with optimal parameters of absorption power-only cycles and a comparison of different working fluids. The controlled variables in sensitivity analysis are the temperatures of the heat source fluid T_{hs} (mass flow fixed for all cases) and of ambient air T_{amb}, which provide cooling water from the dry cooler after rejecting heat. A higher pressure is used for the heat source water so that it remains liquid for sensitivity analysis with respect to higher heat source temperatures.

6.4.1 Baseline APCC and comparison with VCC-ORC

The parameters of the cycles for the baseline condition, when the heat source outlet temperature is fixed at 85 °C, and the splitting ratio SR has a value of 0.5, are shown in Table 6.21. Moreover, Tables D.1 and D.2 in Appendix D list the reported thermodynamic parameters in all the system nodes, where the controlling parameters of the cycles are highlighted in bold. The parameters as solution concentrations were chosen as typical for absorption chillers and were the baseline parameters for further analyses.

The cycle efficiency is mainly affected by the cooling output, while the exergy efficiency is affected by the power output. This is further demonstrated in the

Table 6.21: Main resulting parameters of the APCC and ORC–VCC at baseline conditions with SR 0.5.

Parameter	Unit	APCC	ORC-VCC
$\eta_{1\text{ st,cycle}}$	%	43.5	24.8
$\eta_{1\text{ st,cycle,pow}}$	%	4.24	3.81
$\text{COP}_{\text{ cycle}}$	1	0.39	0.21
$\eta_{1\text{ st,cycle,pow,net}}$	%	1.88	1.51
$\eta_{2\text{ nd,cycle}}$	%	33.3	26.4
$\eta_{2\text{ nd,cycle,net}}$	%	20.1	13.6
$\dot{Q}_{\text{chill}}$	kW	41.3	22.0
$\dot{Q}_{\text{hs,used}}$	kW	105.1	105.1
$\dot{Q}_{\text{rej}}$	kW	141.9	123.1
$\dot{Q}_{\text{rec}}$	kW	43.3	3.0
$\dot{W}_{\text{exp}}$	kW	4.46	8.58
$\dot{W}_{\text{pump}}$	kW	−0.003	−0.29
$\dot{W}_{\text{comp}}$	kW	0	−4.29
$\dot{W}_{\text{fan}}$	kW	−2.48	−2.42
$\dot{W}_{\text{net}}$	kW	1.98	1.58

sensitivity analysis. The APCC, in comparison with the ORC–VCC system, provides nearly double chiller capacity while having at the same time an approximately 25% higher net power output. The power requirement of the auxiliary equipment ($\dot{W}_{fan}$) is similar for both cases.

Figure 6.25 shows T–s and T–S diagrams (with specific and absolute entropy) of the APCC to provide a clear idea of the processes occurring in the cycle. It can be seen that the recuperated heat as a sensible heat input to the solution is rather large compared with the heat input and heat added for the phase change process. This is caused by a small concentration difference in the solution, which is common for absorption chillers. This is different from the situation of the APC optimised for waste heat recovery, where the concentration difference must be significantly larger to obtain a larger temperature glide. As the pressure difference in the absorption cycle is low, the entropy change during throttling or expansion in the diagrams is also considerably small.

6.4.2 Sensitivity analysis of APCC and ORC-VCC cycle parameters

The sensitivity analysis is performed first for the parameters from the cycle perspective (situations with constant heat input and closed-loop heat source). Following is the analysis performed for operation in open loop such as waste heat recovery applications, where the goal is a maximization of the utilization efficiency (regardless of cycle efficiency and amount of heat extracted from the

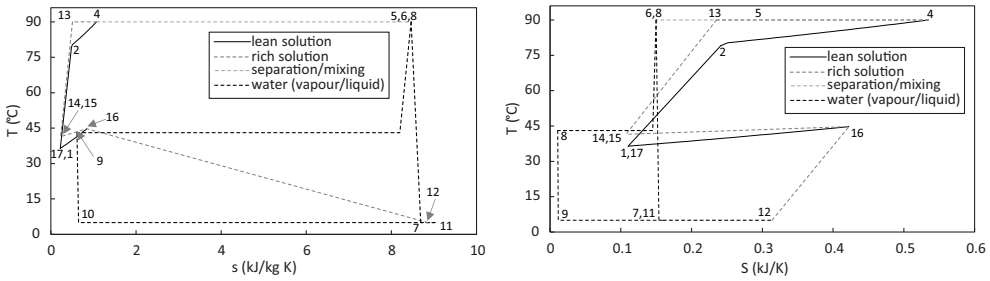

(a) (b)

Figure 6.25: Temperature entropy diagrams of the combined cycle for the baseline conditions for specific entropy (a) and absolute entropy (b) of the working fluid.

heat source).

The APCC and ORC–VCC are proposed for flexible operation with variation between power and cooling output defined by the splitting ratio SR, so its impact on the performance indicators is significant and is shown in Figure 6.26. As expected from the SR definition, all the considered parameters depend linearly on the splitting ratio. However, the results clearly illustrate the disproportion between the quantity and quality of the products—cooling output and electricity. The energy efficiency is largely affected by the cooling output because the absolute value of the electrical output is low. The situation is nearly the opposite for the exergy efficiency. As the exergy of chilled water is rather low, the exergy efficiency is highest when only electricity is produced. The net efficiencies then show the extent of power needed to run the fans. In the regime for the maximum cooling load (SR = 0), the negative net electrical efficiency represents the power consumption of all auxiliary systems. The absolute value of power input is more than half the positive net power production in the purely power-producing regime (SR = 1). The disproportion between the low exergy of the chilled water output and the high exergy of the electrical output then causes low exergy efficiency for the chiller operation. It can even result in negative exergy efficiency values for SR between 0 and approximately 0.2. The exergy output of chilled water is, in this case, lower than the required electricity (pure exergy) input.

In the power-only production regime, the absorption cycle has only slightly better performance than the ORC (gross and net power efficiencies of 8.5% and 6.9% for APC against 7.9% and 6.1% for ORC). However, a large difference is observed for the chiller regime with a COP of 0.79 for the absorption system and 0.42 for the ORC–VCC, respectively, while the net power efficiency is nearly the same (-3.2% versus -3.1%). A clear advantage of the absorption system for the combined cooling and power system is shown.

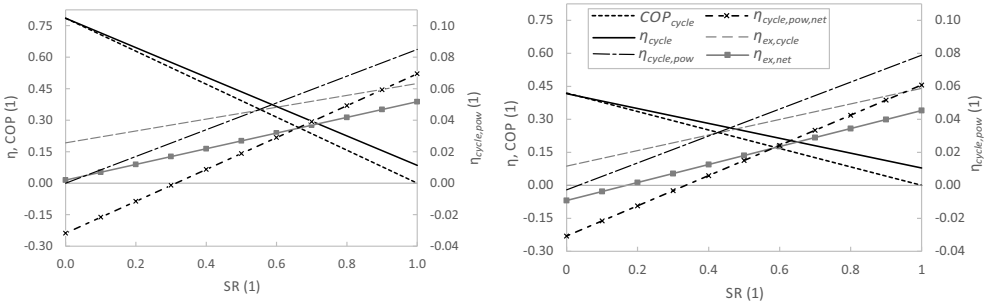

(a) (b)

Figure 6.26: Sensitivity analysis of cycles' performance with respect to the splitting ratio, for APCC (a) and ORC-VCC (b).

The difference in the lean and rich concentrations is among the most important controlling parameters of the absorption cycles. Figure 6.27 shows its impact when the heat source temperature is kept constant, and the concentration difference $\Delta\xi$ is used as an input in the model instead of the outlet temperature of the heat source. As $\Delta\xi$ increases at a nearly constant desorber temperature, the pressure drops. A limit for the high $\Delta\xi$ is the pressure in the condenser so that the condensation temperature is sufficiently high for heat rejection to the ambient. Under the pinch point constraints, a low condenser pressure causes the cooling water and air mass flow rates to increase, and so does the parasitic load. As a result, a sharp decline in the net power efficiency can be seen when the chiller branch is in operation, whereas only a moderate decrease is observed for producing only power. The gross power efficiency has a maximum at a very low $\Delta\xi$, where the cycle extracts only a small amount of heat from the heat source at high temperature. The net efficiency maximum is at higher values before it declines owing to the low-temperature difference in the condenser and absorber and the associated high parasitic load. The COP increase with $\Delta\xi$ is only moderate, while there is a sharp drop in the net power efficiency after its optimum.

Sensitivity analyses of heat source temperature (two operating regimes) as well as ambient and evaporator temperatures are in agreement with the typical behaviour of absorption chillers or power cycles. For comprehensive information, they can be found in the Appendix D in Figures D.1 and D.2.

6.4.3 Sensitivity analysis of utilization parameters

To maximise the utilisation of a heat source, fixing its outlet temperature is not suitable. Searching for the optimum is straightforward by varying the specified boiling temperature of the ORC, maximising the net power output of the cycle. The VCC is independent of the ORC. For the APCC, the net power and COP work against each other. The approach adopted in the optimisation

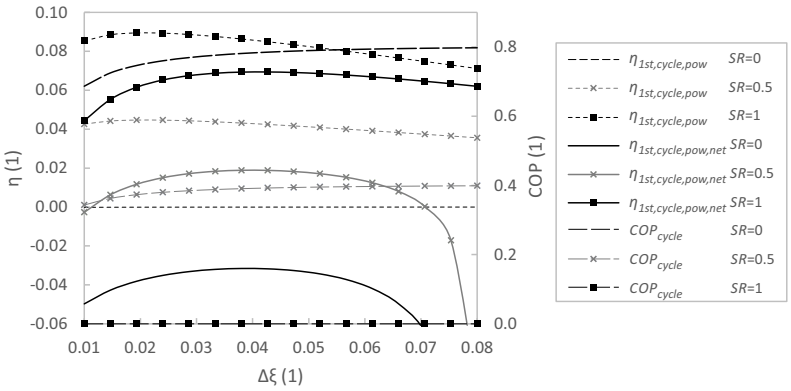

Figure 6.27: COP, gross and net APCC system efficiency at varied concentration difference

is to search for a concentration difference $\Delta\xi$ and lean solution concentration ξ_1 which together provide maximal net power output at SR = 0.5. The resulting parameters for each node for both systems are presented in Tables D.3 and D.4 (in Appendix D).

The values of utilisation efficiency and COP are shown for both systems in Figure 6.28. The trends are similar to that of the efficiency with respect to the transferred heat, but the values are significantly lower because the cycles can utilise only a small portion of the heat from the heat source. The APCC again provides a significantly higher COP in the pure chiller regime. The overall exergy efficiency is approximately zero for the APCC (parasitic load corresponds to power input), whereas it attains negative values for the ORC–VCC owing to the low exergy of the cooling output. The point where the net utilisation efficiency and COP intersect is the point at which the net power output is zero. When the system is used only for power production, the ORC-VCC has a higher efficiency, although only by 0.1%.

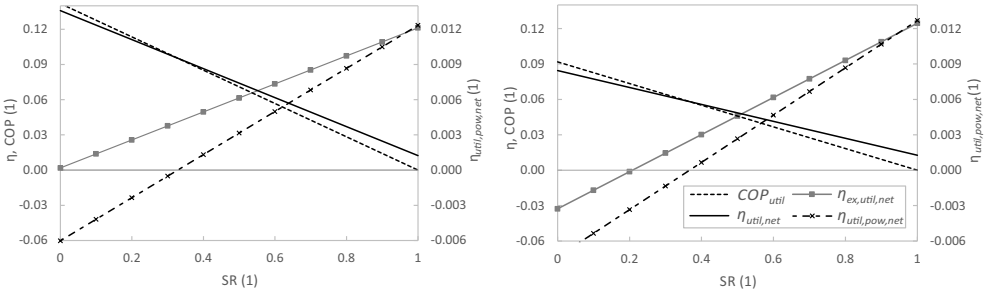

(a) (b)

Figure 6.28: Energy and exergy efficiency and COP for heat source utilization with respect to the splitting ratio, for APCC (a) and ORC-VCC (b).

Figure 6.29 shows the impact of the heat source temperature and concentration difference on the utilisation parameters. As it is fairly common for absorption chillers, increasing the heat source temperature results in a notable decrease in the COP, but a higher cooling capacity from the same heat source mass flow rate. For the power production, the efficiency with the temperature difference increases. The sharp decrease in the net power efficiency at low temperatures is caused by the decreased temperature difference for heat rejection, mainly from the condenser. Therefore, this drop is not observed in the power-only production regime. While varying the concentration difference, the maximum efficiency point of the power-only production lies beyond the displayed region. This is explored further in section 6.4.5 on the comparison of APCC with APC for power-only production. A higher concentration difference, however, causes a decrease in the desorber and condenser pressure and, thus, the condensing temperature. It limits the operational possibility of the APCC and increases the parasitic load, regardless of an increase in the COP. Therefore, for specific applications, optimisation with respect to the required power and cooling output can be performed.

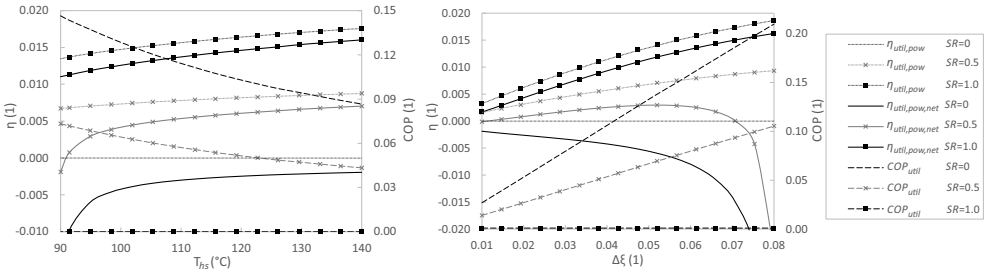

(a) (b)

Figure 6.29: Utilization COP, gross and net APCC system efficiency at varied heat source temperature (a) and varied concentration difference (b).

6.4.4 Comparison of working fluids for APCC

To compare the results with the possibilities of other working fluids, an investigation was conducted to include also an ammonia–water mixture and alternative aqueous solutions with LiCl and $CaCl_2$, which are also considered for absorption chillers. With ammonia, the combined system has been in previous literature considered with and without a rectifier, where the rectifier would increase the ammonia concentration from the separator outlet. To provide coherent work with the same layout and system complexity, the basic configuration without the rectifier is considered. The water–ammonia system has a vapour quality at an evaporator outlet lower than one and corresponds to the fluid temperature limit provided by the minimum required temperature difference. The reason is the temperature glide, and the excessively high

Table 6.22: Main resulting cycle parameters of the different working fluids – salt solutions and water-ammonia mixture

	ξ_1	ξ_2	p_1	p_2	SR	COP_{cycle}	$\eta_{1st,cycle,pow}$	$\eta_{1st,cycle,pow,net}$	$\eta_{2nd,cycle,gross}$	$\eta_{2nd,cycle,net}$
	(1)	(1)	(kPa)	(kPa)	(1)	(1)	(%)	(%)	(%)	(%)
$H_2O - LiBr$	0.56	0.60	8.7	0.87	0	0.79	0.0	−3.2	19.2	1.5
					0.5	0.39	4.2	1.9	33.3	20.1
					1	0.00	8.5	6.9	47.4	38.8
$H_2O - LiCl$	0.44	0.52	9.1	0.87	0	0.79	0.0	−3.1	19.3	2.2
					0.5	0.40	4.4	2.0	34.0	21.0
					1	0.00	8.7	7.1	48.7	39.7
$H_2O - CaCl_2$	0.56	0.68	7.7	0.87	0	0.74	0.0	−3.3	18.2	−0.3
					0.5	0.37	3.8	1.6	30.4	17.9
					1	0.00	7.6	6.5	42.6	36.3
$NH_3 - H_2O$	0.50	0.45	1512.2	458.6	0	0.56	−0.9	−3.6	8.3	−6.3
					0.5	0.28	3.1	1.0	23.9	12.2
					1	0.00	7.1	5.5	39.6	30.7

mixture evaporation temperature after the most of the ammonia is already in a vapour form.

The parameters of the concentrations were chosen to agree with the typical values and to provide a reasonable trade-off in performance between the auxiliary (fan) consumption and the cycle performance. The same issue has already been discussed for the LiBr APCC. Table 6.22 lists the results for the major cycle parameters. The performances of the cycles with a salt solution are quite similar. The best chiller performance is achieved using the LiCl solution. The COP is 0.79, which is the same as that of the LiBr solution, which had a slightly higher net power consumption. The highest power production resulted from the LiCl solution. The water–ammonia working fluid provided the poorest performance with an approximately 30% lower COP in chiller operation and 20% lower net power output. Note that the water-ammonia system COP could be partially improved by adding the rectifier, but it would not improve the power output.

Table 6.23 lists the results of the heat source utilisation parameters. The pressures and concentrations were optimised in the same way as described in the previous section. There is a small difference in the cycle parameters, regardless of the optimisation for heat source utilisation. This is discussed in the section 6.4.5. The LiCl and LiBr solutions again exhibited the best chiller performance, followed by the water–ammonia and $CaCl_2$ solutions. The LiBr and LiCl solutions also provided the highest power production efficiency. The best performance of these two salts was also observed in the exergy efficiency of heat source utilisation. The NH_3–H_2O mixture again proved to have the lowest chiller performance (even negative exergy efficiency) with the highest power requirement and lowest COP. However, in power production, it surpasses the $CaCl_2$ solution.

Table 6.23: Main resulting utilization parameters of the different working fluids – salt solutions and water-ammonia mixture

	ξ_1	ξ_2	p_1	p_2	SR	COP $_{util}$	$\eta_{1st,util,pow}$	$\eta_{1st,util,pow,net}$	$\eta_{1st,util,gross}$	$\eta_{1st,util,net}$	$\eta_{2nd,util,net}$
	(1)	(1)	(kPa)	(kPa)	(1)	(1)	(%)	(%)	(%)	(%)	(%)
H_2O-LiBr	0.56	0.61	8.1	0.87	0	0.14	0.0	-0.6	14.2	13.6	0.2
					0.5	0.07	0.7	0.3	7.8	7.4	6.2
					1	0.00	1.5	1.2	1.5	1.2	12.1
H_2O-LiCl	0.43	0.52	9.2	0.87	0	0.13	0.0	-0.5	12.5	13	0.7
					0.5	0.07	0.7	0.3	6.9	7.2	6.2
					1	0.00	1.4	1.2	1.2	1.4	11.7
H_2O-$CaCl_2$	0.55	0.67	8.0	0.87	0	0.10	0.0	-0.5	10.6	11.0	0
					0.5	0.05	0.6	0.2	5.8	6.1	4.7
					1	0.00	1.1	1.0	1.0	1.1	9.4
NH_3-H_2O	0.51	0.43	1417.7	455.1	0	0.11	-0.1	-0.7	10.5	10.0	-2
					0.5	0.05	0.6	0.2	6.0	5.5	4.4
					1	0.00	1.4	1.1	1.4	1.1	10.9

Clearly, the LiBr and LiCl solutions provide the best performance for both the closed-loop and open-loop heat source utilisation. Because LiBr is the most commonly applied salt in absorption chillers, it appears to be the best candidate for the application of the proposed system.

6.4.5 Comparison of APCC with APC for waste heat recovery

Because APC has been proposed for power production with the same range of working fluids, there is an opportunity for comparison. APC showed a thermodynamic benefit for low-temperature heat utilisation and waste heat recovery [57, 59] (and author's work). The operating conditions of APCC and APC for waste heat recovery, however, differ significantly, especially regarding the optimal concentration level and concentration difference in operation. This is because of the fixed concentration of the APCC lean solution given by the heat rejection temperature from the absorber and the absorber pressure given by the required evaporator temperature. Figure 6.30 shows the effect of the concentration difference in the power cycle (SR = 1) when the rich solution concentration and absorber outlet temperature are constant (heat source outlet temperature and absorber pressure are no longer fixed). The cycle efficiency has a maximum point at a low concentration difference near the APCC nominal point. The utilisation efficiency has a maximum as well, but at much higher concentration differences. This is partly because of the heat source outlet temperature, which indicates the amount of heat recovered by the cycle from the heat source. The evaporator temperature rises with the concentration difference, which is the reason this regime is suitable for power production, but not very suitable for the chiller regime.

These results show that the absorption chiller regime can utilise only a small fraction of energy from the heat source. APC is commonly deemed more suitable for waste heat recovery because it does not have the limitation of

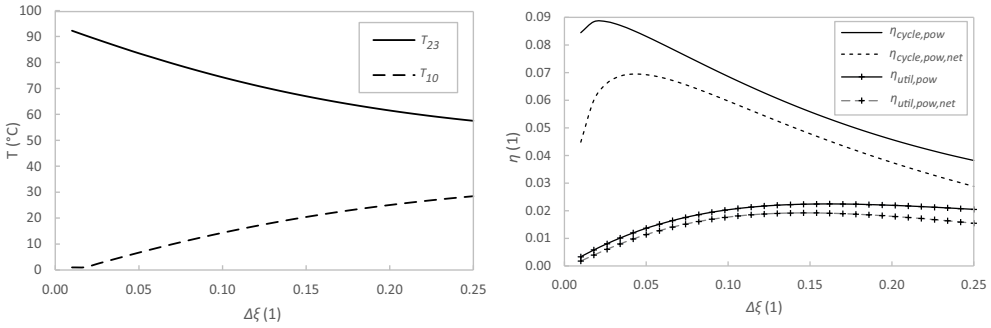

(a) (b)

Figure 6.30: APC system (SR=1) parameters at varied concentration difference for higher heat recovery from the heat source: cycle and utilization efficiency (a) and heat source outlet and evaporator temperature (b).

the evaporator (absorber) pressure to ensure the evaporator temperature. By changing the concentration difference by approximately threefold under the same other boundary conditions, the utilisation efficiency can almost be doubled. This provides a prospect for a real system, where the charge of the working fluid with a lower concentration could be used for long-term power-only operation. An example could be winter operation when the cooling production is not required.

6.4.6 Summary of combined power and cooling cycle

The concept of a combined cooling and power absorption cycle operating with aqueous solutions of salts (such as LiBr) was investigated. The configuration of the cycle was purposely kept in its simplest form to ensure that a real-life application could be feasible for such a system. The system can be gradually adjusted between the power and chiller operation regimes according to a demand. The application field is identical to that in cases where absorption chillers are already considered, in terms of both heat source temperatures and sizes. The added flexibility can thus improve the capacity factor of the installed unit or ensure better utilisation of the waste heat stream, thereby changing the economics in favour of the installation of the absorption systems.

The proposed system is compared with an organic Rankine cycle coupled with a vapour compression cycle as a benchmark. The models are based on pinch point analysis and include parasitic loads related to heat rejection, an important parameter for small-scale low-temperature systems. Two operation cases are analysed: a closed-loop heat source, when the cycle parameters are of the interest, and an open-loop heat source, where utilisation efficiency is essential. With a 95°C water heat source and LiBr solution working fluid, the proposed absorption system shows superior performance for all the parameters

but the pure net power production efficiency with respect to heat source utilisation, where the values were around 1.2% (exergy efficiency around 12%), nearly the same as those of the benchmark system. For thermally activated cooling without power production, the absorption system on a closed-loop heat source between 95°C and 85°C provides a roughly COP of 0.79, while power the consumption is maintained at similar or better values. For heat source utilisation, the COP (0.14) is higher by more than one-third. In the power-only production regime, the absorption cycle with a closed loop heat source has still a better performance with gross and net power efficiencies of 8.5% and 6.9%, though the difference against ORC is less than one percentage point. The exergy efficiency is highest in the power only regime with values of 47% and 39% (gross and net), while in the chiller regime the net value approaches zero due to parasitic load.

A comparison of several salt solutions and water–ammonia mixture showed the best performance of LiBr and LiCl, but all salt solutions exhibited rather similar efficiency as well as COP. The water–ammonia mixture showed the worst performance in all but heat source utilisation efficiency of power production.

When the maximum utilisation of the heat source is preferred, the absorption chiller regime can utilise only a small fraction of the energy from the heat source owing to the limitation in cycle parameters so that the evaporator temperature can be kept sufficiently low. In this regime, the cycle efficiency is near its maximum (gross 9%), but the utilisation efficiency is low, net around 0.68%. However, for periods of prolonged power-only operation, the utilisation efficiency can be improved over to 1.9% by changing the cycle parameters by charging the cycle with a lower concentration of the solution working fluid. At such conditions the cycle can extract more heat from the heat source.

For low-temperature heat sources, the proposed absorption system is a suitable choice from a thermodynamic standpoint, as well as the system complexity and technical feasibility. The LiBr solution appears to be the most promising working fluid because of its good performance, and it is the most common fluid in current absorption chillers. Other benefits are identical to those of salt solution APC.

Chapter 7

Experimental development of the absorption power system

In this section there are described considerations and subsequent design of two experimental systems of APC with salt solution working fluid. As the performance difference between different salts is minimal and as majority of the systems worldwide using LiBr solution, this was the working fluid of choice also here. The first developed test rig was made primarily to test flow boiling with temperature glide during the phase change. Its design and operation led to several dead-ends. The second test rig was built as an entire LiBr solution APC with expected nominal power output around 300 W. Commencement and operation experience of both units is described followed by an analysis of the obtained experimental results, primarily from the second one – whole APC unit.

The questions to be answered were actual feasibility of the salt solution APC concept as well as of its components, such as verification of actual and usable temperature glide in the heat exchangers to allow their high exergy efficiency and possibility of providing a cost-effective expander solution, as it is typically a costly component in nearly every heat engine.

Before the experimental systems design, first sizing considerations of the author described in [VN8] has shown a preliminary technical feasibility of design of two sizes of an APC system, 20 kW and 500 kW nominal power output. The systems were designed in configuration with a flow boiling shell & tube desorber followed by a separator derived from geothermal applications. Turbine model used 1D loss models for large steam turbines, and the absorber assumed average mass transfer coefficient based on experimental results from the literature. Except for physical size, very important result is that at moderate rotational speed (3 000 or 9 000 rpm) the turbine model with three stages provided isentropic efficiency

of 80% and higher with full admission and notably standard blade heights (36-430 mm). This is caused by the high volumetric flowrate, even though for rather low power output levels. Based on these results, turboexpanders are investigated in the next chapter with focus on low cost rapid manufacturing concept, i.e. additive manufacturing including polymer materials.

7.1 Configuration and design of the 1^{st} testrig

The section shows at first the testrig concept based on the objectives to be measured and intended system variability. The second part outlines the components and system design. As only limited results were achieved with this system, it serves mainly as a reference.

7.1.1 Overall concept

A concept of the first test rig has been proposed by author in [VN9] and then is described in actual configuration with obtained results in [VN10]. The fundamental objective was an experimental verification of the temperature profile (glide) along the desorber and absorber length during the phase change along with observation of related flow boiling two phase flow. As the flow boiling pattern highly depends on buoyancy effects, one design request is a variable angle of the desorber. Additionally, visualization of the two-phase flow is required as well.

Schematic design of the originally intended and of actually built configuration is given in Figure 7.1. A configuration of the rig has been developed with capability of measuring required properties and parameters and also modularity for running only its part or for changing the equipment. In the figure the collection tank d contains the solution of low LiBr concentration. As a result of operation where mixing releasing heat may take place within this tank, it needs to be cooled. The LiBr solution is pumped through the cycle by a pump e to the desorber *a*. The two-phase mixture at the desorber outlet is separated to a liquid and vapour phase in separator *b*. The liquid phase goes through heat exchanger *c* to adjust the temperature either directly into the collection tank or into the absorber *h*. Vapour is either condensed in condenser *f*, where conductivity measurement can take place, and routed to the collection tank or after pressure adjustment in a valve and temperature adjustment in heat exchanger *g* (expander emulator) routed into the top of absorber *h*. Alternatively actual expander *i* was intended for another parallel branch. The low LiBr concentration solution exiting the absorber is collected back into the tank. The desorber, separator and absorber were intended as exchangeable for different designs of the equipment. Absorber branch was expected to be added after the first desorber and separator tests. Evacuation system (not drawn) is necessary to get into the operating pressure in vacuum as is expected in

application of these absorption power cycles. To tackle the corrosion issues while device is filled with the potentially corrosive working fluid and not in use, a nitrogen purge system is employed.

In the scheme in Figure 7.1 are the expected measurements given in the circles, where p stands for pressure, T for temperature, $\dot{m}$ for mass flow rate (calculated from volumetric flowrate) flow σ for conductivity intended to obtain LiBr concentration or purity of separated steam. Sight glasses were designed to be used in several pieces of the equipment for optical inspection, specifically in desorber (flow boiling regime) and on vapour line (visually check for quality regarding droplets).

7.1.2 Design of components and resulting system

Since subsequent tests have shown only a limited feasibility of the approach adopted for this first testrig, the design details are provided only for the reference in Appendix E, here it is described only briefly. It is also largely similar to the approach in the preliminary system sizing work [VN8] described earlier. Sizing has been performed nominally for about 13 kW of heat input, operation at pressure down to 20 kPa (higher eventually for comfort of operation) and temperature at the desorber outlet at 155°C. Assumed liquid concentration change was from 30 to 60% (wt) and basic (lean) solution mass flow rate 7 $g \cdot s^{-1}$. The desorber is conceptually designed as three segments of a modified tube in tube heat exchanger (solution inside) with sight glasses in between. Thermocouple measurements are distributed along the length to monitor temperature development of both fluids. Important feature is a variable angle of the desorber. Whole desorber is on a frame hinged at one end, so it can be variably adjusted between horizontal and vertical position (anywhere between them, the top is held by a crane hook). Design of the two phase fluid separator is again based on geothermal centrifugal type. Condenser is of a shell & tube type using a coil of CATS tubes. A magnetically driven micropump is used as a feeding pump. Thermal oil electric boiler is designed and oil is then circulated by an off the shelf hydraulic gear pump with modified seals to sustain higher temperatures. The rig has been built in the laboratories of the Department of Energy Engineering, Faculty of Mechanical Engineering, Czech Technical University in Prague and it is shown in Figure 7.2, as a model in vertical position of the desorber and two photographs after assembly. Operation and results, which have shown major issues in this desorber concept for APC, are described in section 7.3.

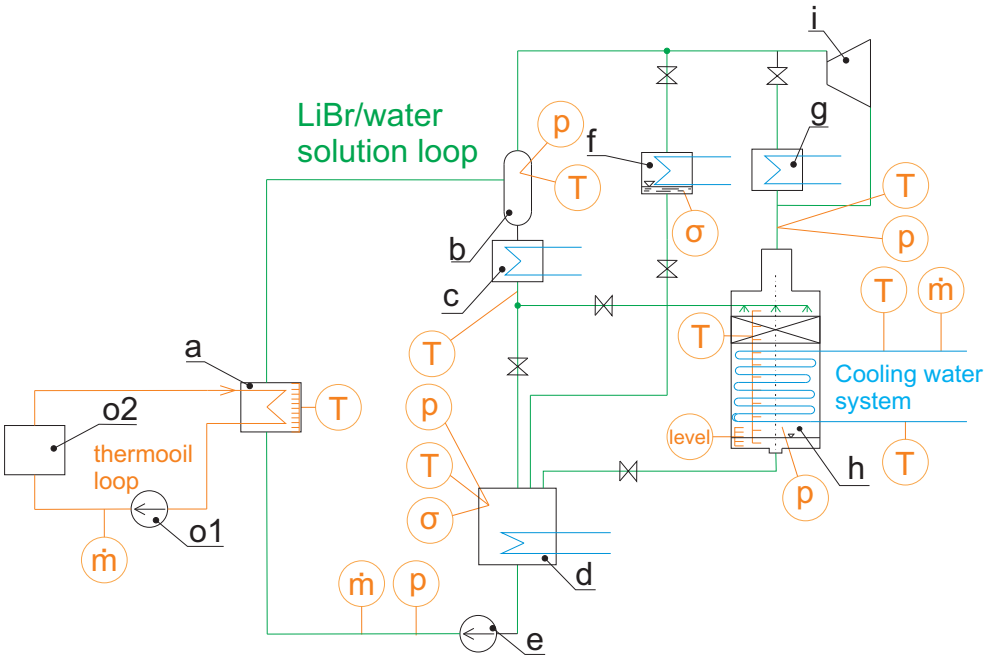

(a)

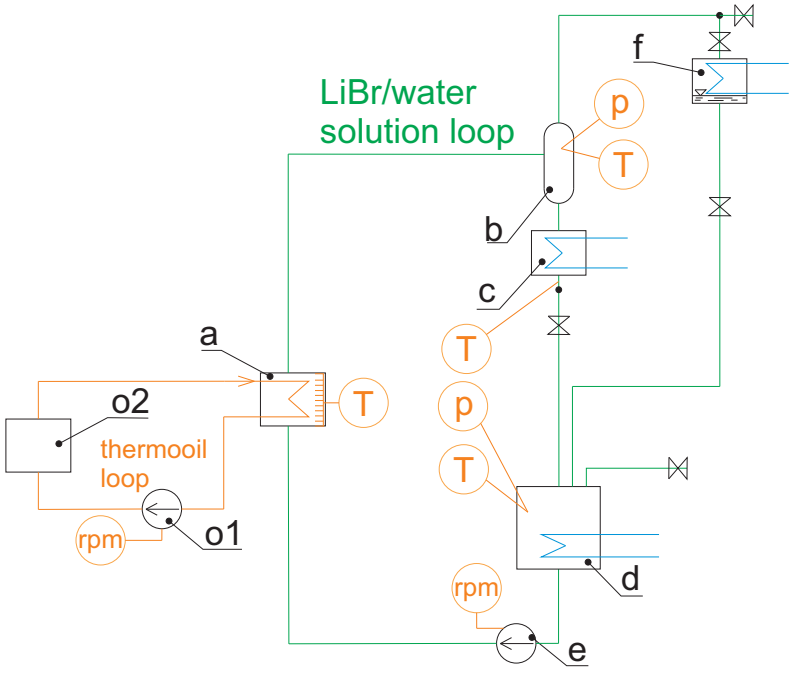

(b)

Figure 7.1: Schematic design of the first experimental rig, original intent (a) and actually built one (b)

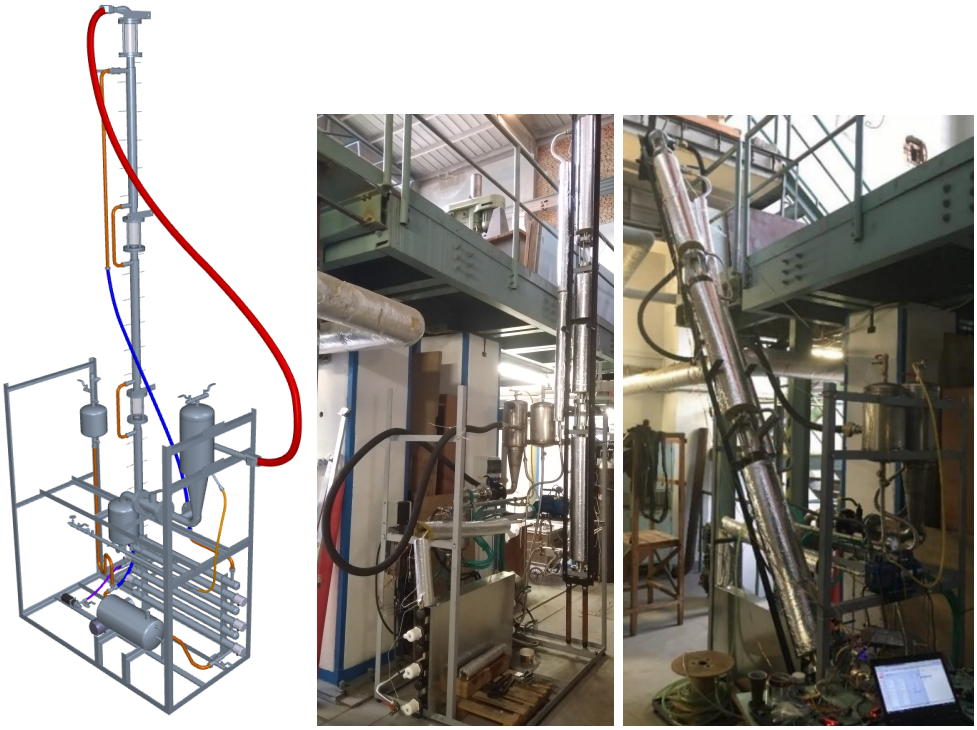

Figure 7.2: A 3D model and photography of the first test rig in vertical position and a photography at 60° angle

7.2 Configuration and design of the proof of concept APC unit (2^{nd} testrig)

After only limited success with the first test rig (detailed further on), leaving the technical feasibility of LiBr APC as even more pressing question, it was decided as more important to address this point even if the design performance does not follow thermodynamically optimized parameters. A new system was designed, description of which is in this section and follows the same logic as for the first testrig, starting with the overall concept. The system is configured as a full APC unit and more technically feasible approach to its components was taken. Following is the detailed description of the design of the components as well as the whole unit.

7.2.1 Overall concept

A new experimental system was proposed as a fully operational APC unit, according to the schematic in Figure 7.3a. Its design, described in detail in author's work [VN11], is to serve as a proof of the whole concept as well as of specific components (e.g. 3D printed turboexpander). Therefore, the

parameters were selected conservatively and partly similar to ones of absorption chillers, rather than according to theoretical results for the most efficient WHR system. It is expected, that the design can be later improved for increased efficiency, power output, reduction of components size and cost etc. The nominal condition is selected as 20 kW_{th} of heat input with expected generator power output in hundreds of watts. The designed mass concentration difference was limited with respect to expected sub-optimal performance of the temperature glide in heat exchangers and their limited size (cost). A summary of the main design parameters and expected performance is provided in Table 7.1.

Design model of the cycle is based on the thermodynamic model described previously, extended by the heat transfer and sizing calculations. It has prescribed pinch points (12 K, 5 K and 10 K for desorber, recuperator and absorber respectively). Isentropic efficiency of the expander and pump has been preliminarily selected on the conservative values of 40 % and 20 % respectively. Main resulting parameters are given in Table 7.2 and a $T - s$ diagram for illustration of the processes is in Figure 7.3b. The utilization efficiency is, to evaluate also later performance of the cycle rather than heat rejection system, referenced to cooling water inlet temperature.

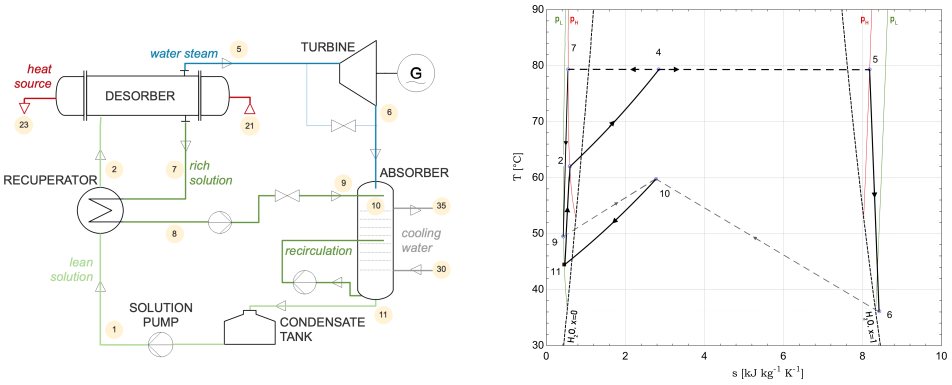

(a) (b)

Figure 7.3: APC experimental rig, (a) schematic diagram, (b) Ts diagram of the designed cycle extended to saturation vapour and liquid lines of LiBr solution at high and low system pressure and of water

7.2.2 Design of components

The components of APC are rather specific and thus this section describes a chosen methodology and considerations foregoing the design. Due to its importance and specific undergone development, the issue of the expander is addressed in detail in a separate chapter.

Table 7.1: Main design parameters of the experimental APC unit

Heat source	Topping ORC with hot water circuit		
Heat source inlet temperature	T_{hs}	90	°C
Heat input	$\dot{Q}_{\text{in}}$	20	kW
Working pair	$H_2O - LiBr$		
Concentration of the lean solution	ξ_{lean}	35	% LiBr (mass)
Concentration of the rich solution	ξ_{rich}	50	% LiBr (mass)
Turbine design power output	$\dot{W}_{\text{gross}}$	$0.3 - 0.5$	kW
Heat sink	Cooling water closed circuit with dry cooler		
Cooling water inlet temperature	T_{rej}	30	°C

Table 7.2: Main resulting parameters of the unit from a design model

Total LiBr mass flow	$\dot{m}_{LiBr}$	0.0913	kg/s
Total water mass flow	$\dot{m}_{H_2O}$	0.0167	kg/s
High admission pressure	p_{HP}	13.38	kPa
Low emission pressure	p_{LP}	5.99	kPa
Heat source outlet temperature	$T_{hs,\text{ out}}$	81.8	°C
Heat transferred in desorber	$\dot{Q}_{in}$	20	kW
Heat transferred in recuperator	$\dot{Q}_{\text{rec}}$	1.15	kW
Heat transferred in absorber	$\dot{Q}_{abs}$	19.63	kW
Turbine power output	$\dot{W}_{\text{gross}}$	0.37	kW
Required solution pump power	$\dot{W}_{\text{pump}}$	0.7	W
Required cooling water pump power	$\dot{W}_{\text{cw;pump}}$	42.1	W
Required cooling fan power	$\dot{W}_{\text{fan}}$	73.4	W
Net Plant power output	$\dot{W}_{\text{net}}$	0.26	kW
1^{st} law efficiency of the cycle	$\eta_{1st,cycle,gross}$	1.9	%
Net 1^{st} law efficiency of the plant	$\eta_{1st,cycle,net}$	1.3	%
Net exergy efficiency of the plant	$\eta_{2nd,util,net}$	2.0	%

Desorber and separator: Originally two conceptual configurations were considered. The first one was a plate heat exchanger with a vapour separator downstream and the second one was a single component heat exchanger of the shell & tube configuration (large volume, LiBr solution in the shell with specified liquid level), which is common to absorption chillers. Uncertainties linked to the actual operation of plate exchangers, risk of too high pressure drop, the fact that the solution is only partly evaporated and an unknown regime of two-phase flow occurring in the heat exchanger causes the latter concept to be adapted for this experimental unit. In the calculations, it is still expected that the exchanger will behave in a counter-flow configuration with the goal to gradually increase the LiBr concentration of the solution and its temperature from the inlet to outlet. In order to approach this behaviour, a

conceptual design of a single passage of both fluids in the exchanger is adopted.

For computational purposes, the exchanger has been discretized into 30 elements (each marked as i in the equations presented) of identical heat transfer. In each of these elements, the temperature difference between the heating water and the solution, variation in the properties of the fluid and the UA value are calculated. This way, the heat transfer coefficients are evaluated separately in each element as well. On the heating fluid side (water), standard Gnielinski correlation (presented for example in Equation (E.1)) is used for the heat transfer coefficient evaluation.

LiBr solution is in a saturated and nearly quiescent (very small velocity of flow) state along the entire exchanger. Very small portion of sensible heat after the recuperator to reach the saturation is neglected. The boiling and evaporation take place at the submerged conditions, in the liquid solution. Pool boiling correlation shown in Equation (7.1) is adopted from [216] to obtain the heat flux $\dot{q}_i$ iteratively with respect to the temperature difference between a hot wall surface and working fluid and then used to obtain the boiling heat transfer coefficient $\alpha_{boil,i}$ by combining with Equation (7.2) via the surface temperature $T_{surf,i}$ in the model. These equations are provided and solved for each element. Conduction in pipes is included in overall heat resistance as well, although for simplicity of calculation, only as conduction through a flat plate (radial effects neglected).

$$\frac{c_{p,l,i}}{h_{fg,i}} \cdot (T_{surf,i} - T_i) = 0.0136 \cdot \left[\frac{\dot{q}_i \cdot 10^{-3}}{\nu_{l,i} \cdot h_{fg,i}} \cdot \left[\frac{\sigma_{LiBr}}{g \cdot (\rho_{l,i} - \rho_{v,i})} \right]^{0.5} \right]^{0.34} \cdot \mathrm{Pr}_{l,i}^{0.85} \tag{7.1}$$

$$\dot{q}_i = \alpha_{\mathrm{boil},i} \left(T_{\mathrm{surf},i} - T_i \right) \tag{7.2}$$

The total area needed for desorption is calculated with given number of tubes and their diameters at given heat transfer coefficients. In order to get a technically suitable combination of tube diameter, number and length, a sensitivity analysis was performed, results of which are in Figure 7.4. The selected design point is also highlighted.

Following the described methodology, the resulting heat exchanger has a heat transfer surface area of 3.1 m2, consisting of 70 tubes DN8 (13.5 x 2.35 mm) with a functional length of 1.035 m. This value was then increased to 1.15 m for technological reasons and as the inlet and outlet are not entirely at the tube endpoints. Arrangement of the tubes is in a way, so that a liquid

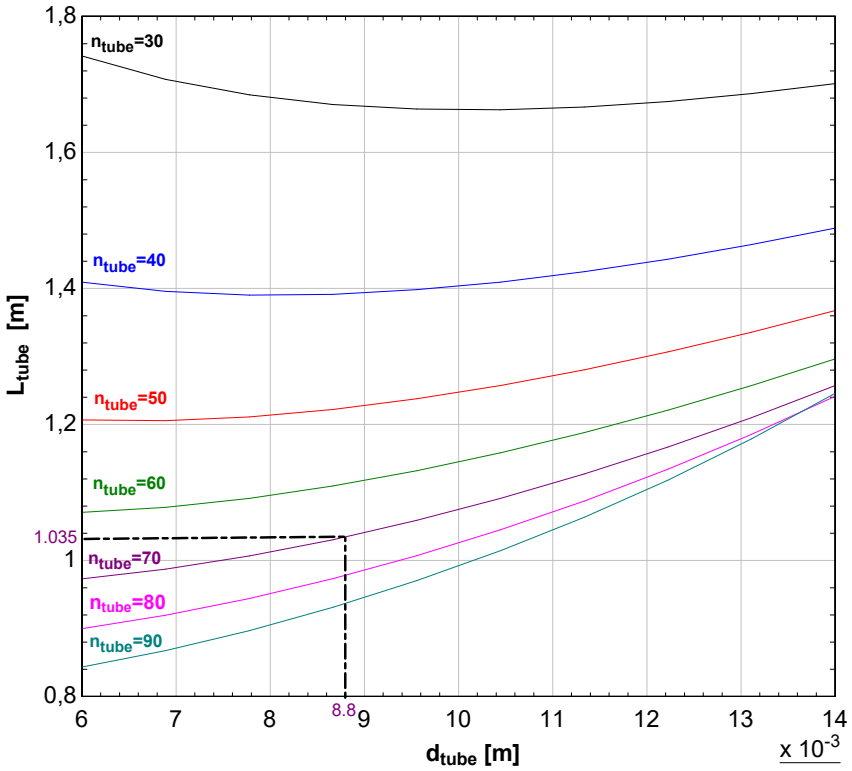

Figure 7.4: Sensitivity analysis of the total length of tubes in the desorber as a function of the inner diameter of tubes and their number

level above them has a sufficient margin to the top of the shell. Temperature sensors along the shell length are incorporated to provide information on the actual temperature glide in this type of exchanger. Design details are shown in Appendix F along with calculated profiles along the length of the temperature, mass flow rate of liquid and vapour and distribution of heat transfer coefficient/heat flux. General overview of the final design of the desorber is shown in Figure 7.6a.

Absorber: Experimental works have shown a large uncertainty in the absorption rate in comparison with the theoretical and often very complex predictions. Furthermore, the absorber of the APC works at different conditions (higher turbine outlet pressure, higher temperatures and different concentrations), than it is typical for the chiller cycle. For the efficient APC concept, a counter-flow absorber configuration is required. Therefore, a rather simple methodology with subsequent oversizing and available means of absorption improvements are adopted. The sizing is based on heat and mass transfer taking place according to Figure 7.5. A convective mass transfer coefficient between the vapour and the liquid solution, as described in Equation (7.3), in which $\dot{m}_{H_2O}$ is vapour

mass absorbed, k_l is mass transfer coefficient (ms^{-1}), ρ_l is liquid density, $\Delta\xi_{H_2O}$ is difference in concentration between saturated solution at given temperature and pressure and actual concentration of subcooled solution in the liquid film. Due to the nature of numerical calculation, in each HX element is then used expression in Equation (7.4) providing the required surface area of each HX element. The liquid film is here expected to be present on all the heat transfer area A of the absorber. Heat transfer coefficient between the film and tube surface is obtained based on Equations (7.5), (7.6) and (7.7) from [217], where $\dot{q}_i$ is the element's heat flux, and Rei is the Reynolds number of the falling film, Γ_i is mass flow of the working fluid per averaged circumference of the coils in the direction of flow O_{coil} and $\mu_{l,i}$,i is dynamic viscosity of the liquid film fluid. Similarly as for the desorber, Appendix F provides a distribution of key parameters along the desorber surface area (height).

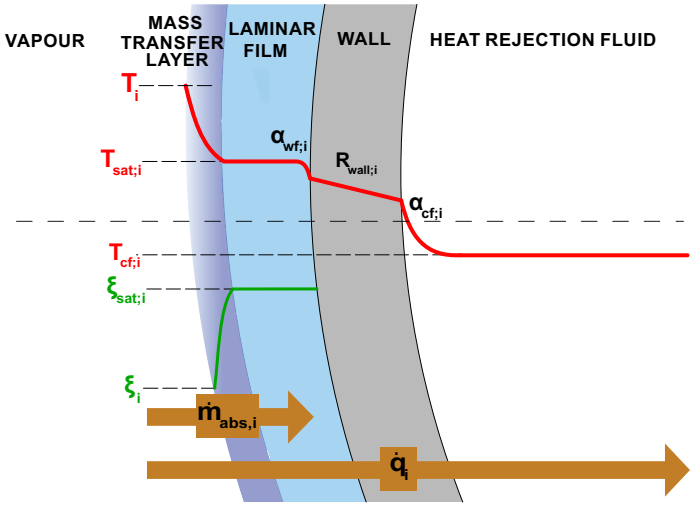

Figure 7.5: Schematic representation of the heat and mass transfer to the falling film in the absorber model

$$d\dot{m}_{H_2O} = k_l \rho_l \Delta\xi_{H_2O} dA \tag{7.3}$$

$$\dot{m}_{H_2O,abs,i} = k_l \rho_{l,i} \left(\xi_{1,sat,i} - \xi_{1,i}\right) A_i \tag{7.4}$$

$$\alpha_{wf,i} = 129.7712 \xi_{l,i}^{-0.8058} \dot{q}_i^{0.2422} Re_i^{-0.0856} \tag{7.5}$$

$$Re_i = \frac{4\Gamma_i}{\mu_{l,i}} \tag{7.6}$$

$$\Gamma_i = \frac{\dot{m}_{l,i}}{2O_{\text{coil}}} \tag{7.7}$$

In order to ensure operation in the case of lower absorption rate, the surface area is oversized, and an additional recirculation of the solution is implemented. In order to keep as much as possible of the counterflow principle, to be able to assess the operation of this part as well as the performance extent of the recirculation, a second (lower) segment of the cooling coils is added underneath within the same absorber. Recirculation nozzles are placed into the middle of the entire absorber height in between the two cooling coil segments of nearly the same surface area. This modification multiplies the total surface area of the cooling coils needed by 1.9 in comparison to the theoretical model. Besides having covered an off-design operation, this enlargement of the area secures the uncertainty of the theoretical mass and heat transfer model.

The modelled absorber thus consists of two coil sections with parallel connection of cooling water. The section is designed with four DN15 (21.3 x 2.0 mm) stainless pipes coiled at different diameters, each measuring about 20 metres in length. Temperature sensors are added along the height to measure the temperature profile within the absorber. The resulting design is presented in Figure 7.6b.

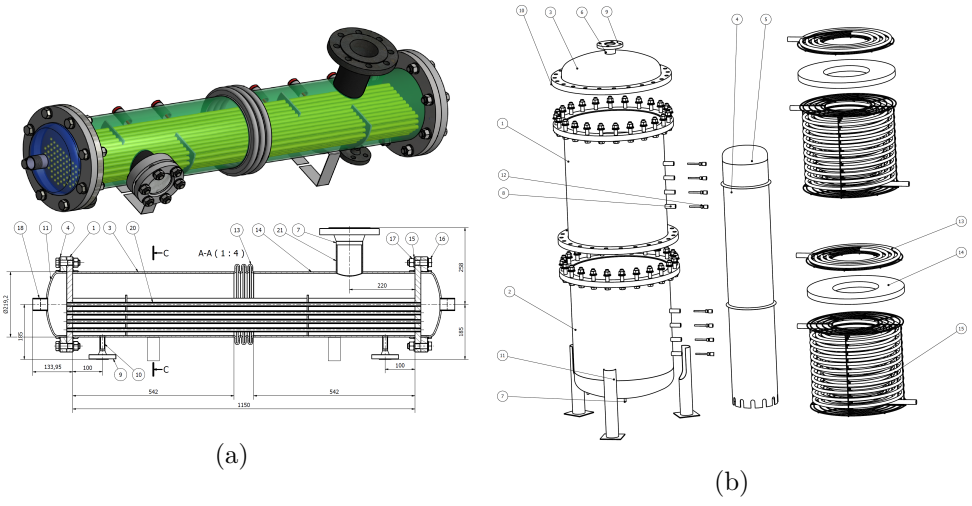

(a) (b)

Figure 7.6: (a) Design of the desorber and (b) design of the absorber

Recuperator: There are no special requirements for the recuperator, which has liquid phase fluid on both sides. Thanks to a booster pump in the LiBr rich solution branch the pressure drop is not a major issue either. A flat plate exchanger is used, specifically, SWEP heat exchanger B5T with a size designed via manufacturer-provided sizing tool based on proprietary correlations.

Expander is described separately in a following chapter. It has been designed to fit between flanges with only electrical wires passing through the hermetic containment of the APC.

Solution pumps: Requirements for the pump are hermetic design, low required NPSH, corrosion resistance and very small volumetric flowrates in order of a few dozen ml s^{-1}. A micro gear pump driven via a magnetic coupling has been chosen as it seems to fulfil these requirements, particularly Topsflo MG213. The same micro gear pump is used as well for the booster pump on the rich solution and as the absorber recirculation pump.

Other components and considerations: A solution tank is added downstream from the absorber, mainly to provide storage of the solution for both maintenance and operation with varying solution volumetric flow at different experimental regimes. The solution tank is equipped with an additional cooling coil in case of an insufficient NPSH and a sight glass.

Besides having designed all the crucial components separately, thorough care needs to be taken regarding the interconnection of the whole system. The performance of the absorption process is heavily dependent on the interaction of the absorbent (lithium bromide solution) and the absorbate (water) in the components. In order to keep the low pressure needed in the whole system, a series of arrangements are taken into consideration. An air-tight quality welding is used in the manufacturing of components. In case of the interconnection of components, high-quality sealing (mostly Teflon or silicone based) is chosen on flanges on vapour side and NPT threads are used on other piping connections.

Another reason that raises the importance of a well-sealed system is the high risk of corrosion in case of oxygen intrusion. The water-LiBr solution is highly corrosive if it gets in contact with oxygen. For this reason, stainless steel is used as a material for all of the components. Although copper or carbon steel are common in absorption devices, it is not recommended for an experimental unit as oxygen intrusion and improper inhibitor choice might occur in higher frequency. Inhibitors that are added to the solution are typically lithium salts of chrome, molybdates and nitrates, where the nitrates specifically are used here. During commissioning, the working space needs to be evacuated prior to charging the working fluid. For the same reason, during the long-term outages, nitrogen is introduced to protect the components from oxidation/corrosion processes.

7.2.3 Resulting system

The resulting main dimensions and parameters of the components are summarized in Table 7.3. Design of the overall system is then depicted in Figure 7.7, and the system was built at the University Centre for Energy Efficient

Buildings of the Czech Technical University in Prague. It is apparent that oversized experimental absorber, where maximal counter-flow temperature profile is intended, is by far the largest and the tallest of the components. A turbine is placed upstream, right above the absorber's inlet. The highest point is thus 4.3 m above the ground.

Design methods theoretically described in available literature mainly for desorber and absorber yield physically large components for this low-temperature heat source of 90°C. This is due to low operating pressures that accounts for large volumetric flows, small mass flow rates, and also due to the factor of design safety margin. Out of 20 kW of thermal heat input in the heating water, there is 0.37 kW expected to be converted to power with the rest being rejected in the absorber. Net designed power output respecting the own power consumption in the system is 0.26 kW. This yields a 1^{st} law efficiency of the cycle of 1.3% (net utilization 1^{st} law efficiency 0.12%). Although the system is thermodynamically partly optimized, this number might be somewhat reduced due process and design uncertainties and aspects unforeseen omitted in the calculation.

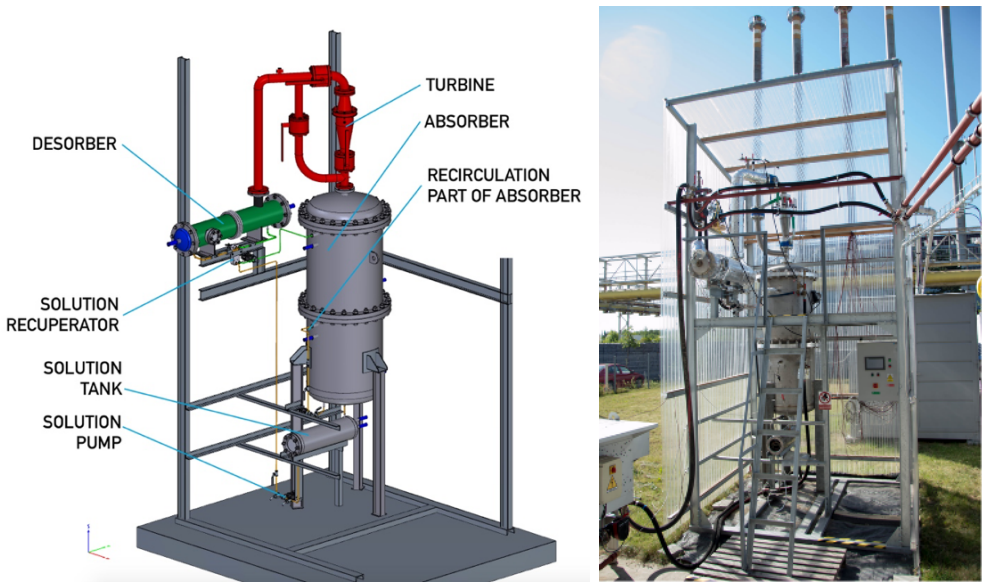

Figure 7.7: Overall design of the experimental APC unit (Red coloured components are for vapour branch, green for LiBr rich solution piping and light brown colour for LiBr lean solution piping)

The power output of a few hundreds of watts is a result of a small pressure difference and low mass flow rate of the steam for the given heat input. These parameters, however, can be also altered with a change in the concentration difference. The design is performed for a conservative concentration difference

Table 7.3: Resulting parameters of the components of the unit

Component	Design	Dimensions	Performance
Desorber	Single pass Shell & Tube, LiBr in shell and heating water in tubes	70 pipes of DN8 (13.5 x 2.35) with a length of 1.15 m; liquid volume of 14.4 l	Heat load=20 kW; min ΔT= 12 K; $\dot{m}_{HS}$=0.58 kgs^{-1}; $\dot{m}_{des,in}$=26 gs^{-1}
Absorber	Spiral heat exchanger of two sections of cooling coils with distribution nozzles and packing; cooling water in tubes	4 spiral pipes of 20 m in length each in one coil section; section height: 0.86 m;	Heat rejection: 19.6 kW
Recuperator	Flat plate SWEP B5T	Specified by manufacturer	Heat load: 1.15 kW
Expander	3D printed (SLS, Polyamide PA 2200) axial single stage turbine with permanent magnet generator, design between flanges	D_{mean} = 120 mm	Nominal power 360 W, η_{is} = 44% (15 000 rpm)
Pumps	Three identical pumps TOPSFLO MG213XK/DC24WI on lean solution feeding branch, on absorber recirculation and on rich solution branch	Specified by manufacturer	Flow range: 300 – 3500 ml/s; power: max 70 W

between lean and rich solution, but its impact on the cycle efficiency as well as the potential utilization efficiency of potential open loop (waste heat) has significant effect as was seen already in the theoretical calculation sensitivity analyses. The theoretical results suggested high utilization efficiency for large concentration difference (and thus temperature glide). Operation with a large temperature glide, on the other hand, has not been reliably reported for absorption systems, adding on the possible negative aspects. Finally, the performance can be also significantly improved in case of higher expander efficiency (here designed at suboptimal velocity ratio as will be seen further).

Instrumentation: Due to the fact that the proposed apparatus is an experimental unit, it is equipped with measuring components. These include pressure, temperature and volumetric flow sensors on the branches downstream and upstream the crucial components. As described before, temperature sensors

are also installed within the desorber and absorber.

In the APC rig, most of the measurements are taken and recorded via PLC system AS332T-A with measuring cards for RTD temperature sensors, voltage and current input. Additional temperature sensors for temperature glide are measured via Labview (cRio module). The turbine load is controlled via an in-house built DC load (output current is rectified first) system, which includes a PID regulator to keep the required rotational speed. This system also records the voltage and current along with rotational speed based on produced AC current frequency. Some details about this method can be found, for example, in [VN12].

Figure 7.8 shows a simplified PFID of the APC rig and the position and types of measurements within the system. It also shows design thermodynamic properties in respective streams. The details of the sensors for the measured variables are summarised in Table 7.4.

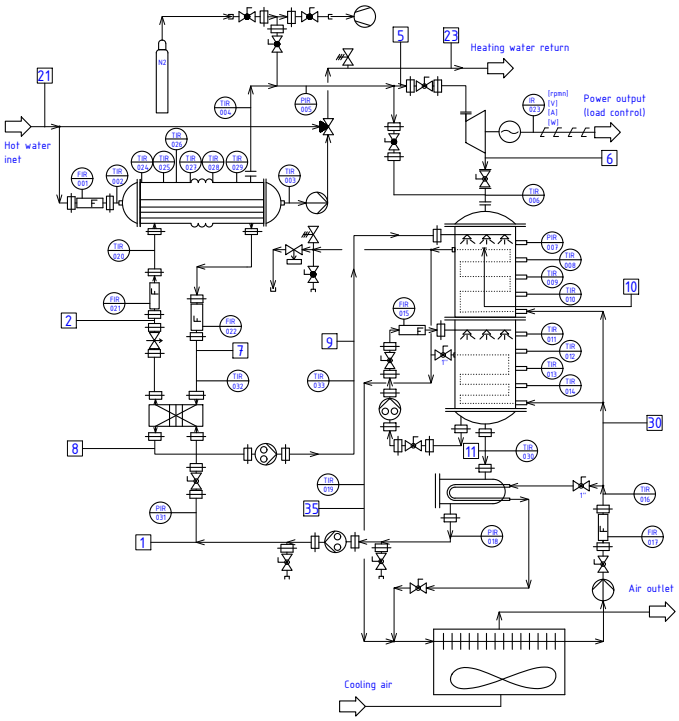

Stream overview			
Stream	T [°C]	p [bar]	m [kg/s]
1	44.51	0.134	0.02609
2	60.78	0.134	0.02609
5	78.00	0.134	0.007826
6	36.14	0.05993	0.007826
7	78.00	0.134	0.01826
8	49.51	0.134	0.01826
9	49.51	0.05993	0.01826
10	59.81	0.05993	0.02609
11	44.51	0.05993	0.02609
21	90.00	2	0.5790
23	81.78	2	0.5790
30	30.00	2	0.2622
35	47.90	2	0.2622

Figure 7.8: APC experimental rig simplified PFID

Table 7.4: Test rig sensors and transducers

Parameter	Type	Range	Error
p (kPa)	Ceramic capacitive DMP331	$0-200$ or 400 kPa	0.10%FS, 0.35% FS
T (°C)	Pt100 RTD (4 wire)	-50°C $-$ 200°C	$0.5\% + 0.3$°C
$\dot{V}$ (l min^{-1})	Vortex LIQUI-VIEW Base LVB	$0.5-10$, $3.5-50$, $5-85$ l min^{-1}	$< 1\%$ FS
U (V)	Voltage divider +Arduino A/D	$0-60$ V	$2\% + 0.03$ V
I (A)	U drop (Arduino A/D, 1 block)	$0-30$ A	$2\% + 0.02$ A
n (RPM)	El. freq. (Arduino A/D)	2k $-$ 100k	~ 20 rpm(@$10k$ rpm)

7.3 Commissioning and operation of the experimental rigs

During the commissioning the advantage of APC in very low pressures, allowing in theory for efficient low power low speed turboexpander, has turned out to be also a significant operation issue. Unresolved sealing of the system was also one reason why the works on the 1^{st} testrig were eventually discontinued after only preliminary tests. It however provided useful information for the second test rig concept.

7.3.1 1^{st} testrig

The experiments turned out to serve as a verification whether a suitable flow pattern in the designed desorber can be achieved. The experience from the operation is also provided in author's work [VN10]. As the system was not completely air tight, in order to prevent corrosion, experimental campaigns were performed with demineralized water at decreased pressure (about 5- 20 kPa before start up, though it increased during operation) instead of LiBr solution, which was planned to be introduced later after the initial operation. The goal was to find a two phase flow pattern with as much homogeneous flow of vapour and liquid as possible, which would correspond to the common assumption in the theoretical models. That means, that the liquid and vapour would be in a thermodynamic equilibrium and traveling by the same speed through the desorber towards its outlet and the separator. As the LiBr solution flows through the desorber, temperature glide should achieve gradual increase in the (boiling) temperature, vapour content and thus also velocity.

Since the nature of the experiments was preliminary, the testrig was commissioned without originally intended flowmeters (also limited funding) and the flowrate was estimated from the speed of the volumetric pumps and their chamber volume or characteristics. Measurement of conductivity was not needed because of using only water, but also detailed electronics design of the sensor has, compared to expectations, proven to pose many issues. Among

them can be mentioned the need of using (safe voltage) AC current to prevent solution electrolysis or need of detailed calibration and evaluation method taking into account the change of the conductivity with solution temperature. Extent of such work would exceed the scope of the thesis to achieve required goals.

The tests have been done in the range of the desorber angle between zero and 90° (vertical). As predicted by flow pattern maps in the literature, horizontal position results in a stratified flow, completely unsuitable for this concept and design. Since the liquid stays in the bottom part of the exchanger and does not flow to the outlet, in case of LiBr solution the liquid would increase in concentration and subsequently fill the entire volume, for which this once through heat exchanger is not designed for. Low angles result in a periodic plug flow which breaks along the desorber length. At angles around 30° is the flow pattern transforming to plug-bubble and slug-churn flow with improving homogeneity. The periodic nature however does not completely disappear (frequency still around 1 Hz). Figure 7.9 shows these three flow patterns form desorber sight glasses.

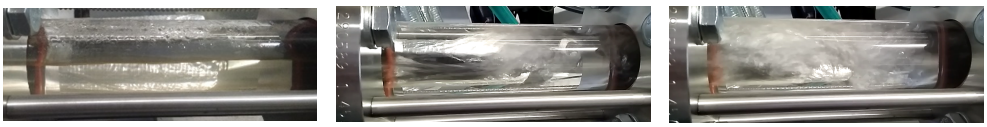

(a) (b) (c)

Figure 7.9: Photography of the flow patterns with water tests under (a) horizontal position, (b) 15° and (c) 30° angle

In vertical position (and generally at high angles) the flow pattern significantly differed along the height. Specific recorded cases for low, medium and high positions of the sight glasses are in Figure 7.10. At the lowest sight glass the flow pattern was always free of any oscillations and in form of bubbly flow (figure shows at rather low heat flux). Intermediate height shows a transition between slug and churn while some oscillations seemingly occurred, although with rather higher frequencies (around 4 Hz). The column that was oscillating was in order of hundreds millimetres so this flow pattern might be theoretically suitable for gradual increase of boiling temperature in LiBr solution. At the highest position, however, only occasionally appeared a slug of two phase mixture (period of seconds to dozens seconds) which discontinuously transferred certain amount of two phase mixture towards the separator. Figure catches a moment when the slug is in the middle of the sight glass. Continuous non-oscillatory outflow from the heat exchanger has not been achieved. Another issue is that actually a temperature glide was recorded, but with a negative trend. The reason is clearly in a pressure difference in case of present liquid column (full vertical desorber corresponds to more than 40 kPa), which is obviously too

much for a cycle with high pressures around 10 kPa.

(a) (b) (c)

Figure 7.10: Photography of the flow patterns with vertical position at, from left to right, low, middle and upper sight glass.

This investigation shows already at the commissioning phase that the APC's desorber concept as a once-through heat exchanger (with relatively high flow area cross section) might provide significant issues due to non-steady flow regime and possibly high pressure drop. This phenomenon shows that a search for a suitable configuration of the flow boiling exchanger poses many further challenges. Together with the literature data on pressure drop when using plate heat exchanger, it was found out that a different approach needs to be adopted. The obtained results further increased the uncertainty of APC technical applicability. The test rig had further issue from leaks that were not managed to be detected, making any operation with LiBr solution problematic due to the risk of high speed of corrosion and as a result also contamination of LiBr solution. Therefore it was decided to build the 2^{nd} testrig, in design partly close to a traditional configuration of LiBr chillers, which would serve as a proof of concept APC.

7.3.2 2^{nd} testrig

Operation of the 2^{nd} testrig was successful, with the first results provided in [VN13] and more detailed analysis of the results being in [VN14, VN15]. Before each test campaign, the system was evacuated, and after it, the rig was filled with nitrogen slightly above ambient pressure to prevent oxygen intrusion and potential corrosion. The tests were performed for ranges of

charged solution concentration of 54% (as purchased), then 50%, 45% and 40% (changed by adding respective mass of demineralized water into the system) and additionally during commissioning with pure demineralized water. During the experimental tests, controlling parameters of the cycle were set. The cycle operating with the turbine has two degrees of freedom, speed of the main pump and the rich solution pump. In addition, when the bypass valve is used instead of the turbine, its opening simulates the turbine's swallowing capacity, thus providing another degree of freedom. The pumps were operated so that the recirculation pump was set to run at a certain constant speed, while the lean solution pump was (manually) controlled to provide a constant liquid level in the desorber. The opposite method of control has proven to be unreliable. At certain states, the liquid solution stopped returning to the storage tank. One suspected reason is crystallisation, though there should have been a margin from the limiting concentration. This phenomenon might deserve deeper focus in the future. In addition, the pump's control and long time constant of the system sometimes caused notable departures from the steady-state liquid flows. At least partial correction for these discrepancies is provided in the next chapter.

The heat source was a hot water taken as part of the heating output of biomass-fired ORC micro-cogeneration units, either a 50 kW version described in [6] or a scaled-up 120 kWth version. Due to the internal settings of the ORC units and partly heat losses in the heat input pipes, the heat source temperature was typically between 75 and 85°C, while it could be further decreased by a three-way valve mixing in the return water. Thus, the range of the explored heat source temperature was 67-88°C. The heat sink was provided by a cooling water loop which rejected the heat into the air in a dry cooler, and its temperature depends on ambient conditions. The range of the explored cooling water temperatures was 11-46°C. The range of temperature difference between heat source inlet and cooling water inlet was 38-71K, but bear in mind that the mass flow rates differed as well, between 0.15-0.87 kg/s at the heat source side and 0.27-0.47 kg/s at the cooling water. The experimental campaigns with LiBr solution were performed in total in 9 days between June and November 2020. A sample of recording of the selected data from the operation is in Figure 7.11, with a distinct period of turbine operation, while the bypass was operated at the rest of the time. The selected operation data of the steady state periods are summing up for about 20 hours (excluding transition states) out of which the turbine was in operation for more than 6 hours.

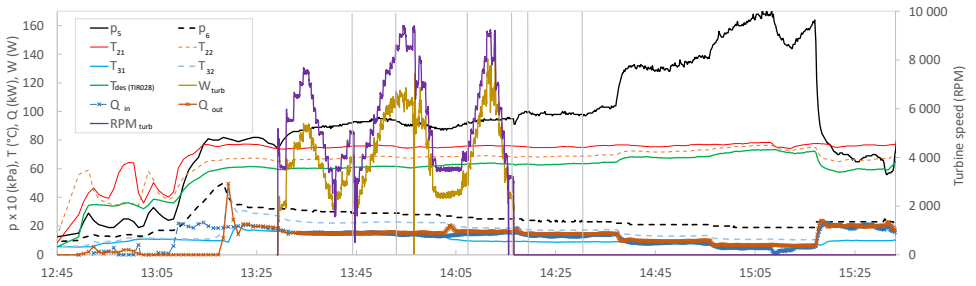

Figure 7.11: Example of the record of selected parameters from the APC operation with an indication of the selected steady-state periods with and without turbine operation (numbers correspond to the PFID)

7.4 Data Evaluation Methods

From the recoded data are selected periods of relatively constant operation, evaluated primarily by the steadiness of the pressure levels. An example of such states selection is in Figure 7.11. For further evaluation, the average values from these selected periods were obtained, and each value was treated as an operational state.

7.4.1 Working fluid mass flow rate issue

The mass flow rate cannot be directly evaluated from the volumetric flow rate of the liquid streams. The reason is that the density is a function of LiBr concentration, which is not directly measured. Therefore, the desorber's mass and energy balance equations are used with the inputs, outputs, and measuring points according to Figure 7.12a and respective set of equations are simultaneously solved in EES. The assumption is that the rich solution leaving the absorber is at the saturated rich solution temperature; thus, its concentration is given. As the solution is boiling within the desorber, this assumption should be accurate. Two approaches were explored. The first one considered solution of equation system involving both measured volumetric flowrates, fluid densities and mass balance of both the solution and one fluid component (LiBr or water). A second approach uses the energy balance instead of one (e.g. liquid output) mass-density relationship. Using the energy balance also helps to smoothen and lower the impact of transient effects affecting the flow rate during cycle control (rising or falling of desorber liquid level) and volumetric flow rate measurement inaccuracies. In ideal conditions with fully steady state conditions and accurate measurements the values should be the same. This difference is also associated with a slight mismatch in either the mass or energy balance of the system. Except for solving the mass flow rate, the solution concentrations are also obtained in this calculation. A further slight difference in results is obtained if mass balance is applied to whole

desorber or, e.g. to energy balance of separation (from calculated 2 phase fluid quality). Fluid properties are evaluated from the REFPROP database for water and from a formulation in [126] for the LiBr solution.

The resulting graph in Figure 7.12b shows the discrepancy between the steam mass flow rates obtained from the approach using the energy balance and from the mass balance based the difference of the two measured volumetric flow rates. In order to select data with higher quality, values with relative difference smaller than 40% or absolute difference smaller than 0.0015 kg/s were selected.

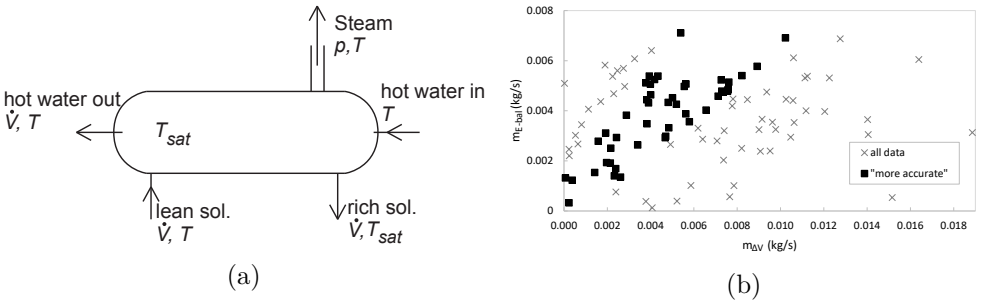

(a) (b)

Figure 7.12: Schematic diagram of desorber parameters used in the evaluation of steam mass flow rate (a) and graph of steam mass flow rate obtained by the difference in measured volumetric flow and from the energy balance (b)

One another approach has been previously explored to evaluate the mass flow rate. The first point of the temperature measurement along the desorber length was considered to be the point of reaching the saturation of the lean solution. This approach would explain the low temperature glide via small concentration difference of the solution. But it has a substantial deviation in mass flow rates. The steam mass flow rate from the evaluated mass balance is more than three times lower than obtained from the energy equation. When concentration data are inserted into the cycle model, lean and rich solution mass flow rates need to be about three times higher than measured. Thus the actual concentration change needs to be higher, and this approach was disregarded.

7.4.2 Cycle parameters and potential

The turbine isentropic efficiency evaluation is described separately in the respective chapter. For the system itself, the important parameter is not just cycle efficiency (specified in Equation (7.8)), but also a utilization efficiency (with respect to heat source heat content). Reference for the utilization efficiency was taken as cooling water inlet temperature $T_{cw,in}$ as shown in Equation (7.9). Only the gross efficiency (excluding all parasitic load and also cycle pumps) was evaluated at this point. The APC was in most of the time operated with the bypass valve, simulating a general turbine. In order to assess the potential of the cycle in general, a hypothetically achievable

expander efficiency η_{turb} of 65% has been assumed as safely realistic for such small systems based on [179, 218]. The cycle parameters are then calculated with this expander efficiency value.

When the turbine was in operation the system produced an actual power output. This DC (after rectification) power output, i.e. including turbine isentropic efficiency, generator efficiency and rectifier diode efficiency (voltage drop), is then used to evaluate actual system efficiency as shown in the second expressions in Equations (7.8) and (7.9). The number of operating points with turbine is lower with one reason being the given turbine's swallowing capacity, limiting the range of cycle states.

$$\eta_c = \frac{W_{turb}}{\dot{Q}_{in}} = \left. \frac{\dot{m}_{\text{steam}} \cdot (h_{turb,in} - h_{turb,out,is}) \cdot \eta_{turb}}{\dot{m}_{hs} \cdot (h_{hs,in} - h_{hs,out})} \right|_{\eta_{turb}=65\%}$$
$$\text{OR } \eta_c = \frac{\dot{W}_{\text{turb , el,measured}}}{\dot{Q}_{\text{in}}} \tag{7.8}$$

$$\eta_u = \frac{W_{\text{turb}}}{\dot{Q}_{\text{source}}} = \left. \frac{\dot{m}_{\text{steam}} \cdot (h_{\text{turb,in}} - h_{\text{turb,out,is}}) \cdot \eta_{\text{turb}}}{\dot{m}_{hs} \cdot (h_{hs,in} - h_{hs}(T = T_{cw,in}))} \right|_{\eta_{turb}=65\%}$$
$$\text{OR } \eta_c = \frac{\dot{W}_{\text{turb , el,measured}}}{\dot{Q}_{\text{source}}} \tag{7.9}$$

7.4.3 Uncertainty analysis

Uncertainty analysis of the systematic error is performed for the cycle parameters. Partial derivatives of the resulting parameters are substituted by differences with a specified step from the measured value. Since the measured temperature and pressure differences are rather small and the method of obtaining turbine mass flow rate and solution concentration are not direct measurements, evaluated uncertainties are in the order of often dozens percent of the reported value, with the median of the uncertainty (including possible outliers) of the main parameters reported in Table 7.5. This highlights the fact that the results need to be taken primarily as the report of the first proof of concept operation. For higher accuracy a different approach to the instrumentation can be taken in the future. Note the specifically low uncertainty value for rich solution concentration as the solution at the desorber outlet is saturated and only one pressure and temperature affect the resulting value. Similarly, the measured utilization efficiency is calculated from higher temperature difference and from directly measured power output, even though the overall values are low.

Table 7.5: Median uncertainties of major cycle parameters

Parameter	Uncertainty (%)	Parameter	Uncertainty (%)
Cycle efficiency (η_{turb}=65%)	17.8	Steam mass flow rate	35.9
Utilization efficiency (η_{turb}=65%)	39.9	Solution flowrate	25.9
Cycle efficiency (measured $\dot{W}_{\mathrm{turb,el}}$)	22.0	Rich solution concentration	1.3
Utilization efficiency (meas. $\dot{W}_{\mathrm{turb,el}}$)	7.2	Lean solution concentration	6.3
Pressure ratio	20.4	Concentration change	34.6

7.5 Experimental Results and Discussion

The experimental performance has been explored mainly from three points of view, regarding parameters of the cycle, the performance of the plastic 3D printed turbo-expand, and actual temperature profiles during the phase change with the temperature glide.

7.5.1 Cycle parameters

The cycle and utilisation efficiency for all selected and analysed steady states and assumed expander efficiency of 65% (or rather efficiency potential) are plotted in Figure 7.13a as a function of the cycle pressure ratio (PR) and distributed according to the charged LiBr concentration (40-54%). The operation states recorded as more accurate are highlighted here with rich colour. The second graph (Figure 7.13b) shows the same parameters but for actual expander electrical power output when the turbine was operated. In these graphs are shown the uncertainties values (in Figure 7.13a only for the more accurate states). They however serve primarily for illustration that the results are mostly illustrational rather than highly precise. Full uncertainty graphs of all cycle results are provided in Appendix G.

The operation points are recorded over a range of heat source and heat sink temperatures and mass flow rates. To partially generalise the data concerning the temperature potential between the heat source and heat sink, Figure 7.14a shows the efficiency data points plotted as a function of a temperature difference between the heat source and heat sink inlets. It is not an exhaustive range of possible operation states, but the general trend is that the maximum cycle efficiency is independent of the charged fluid concentration. However, the highest utilisation efficiency is a domain of the lowest explored charged concentration. This can be explained that the low charged concentration offers a higher space for the concentration change between the lean and rich solution, thus higher heat input.

Multiple efficiency values for the same temperature difference (e.g. around 67°C, cycle efficiency, 40% charged solution concentration) are partly caused by the high uncertainty, partly the temperatures of heat source and sink can

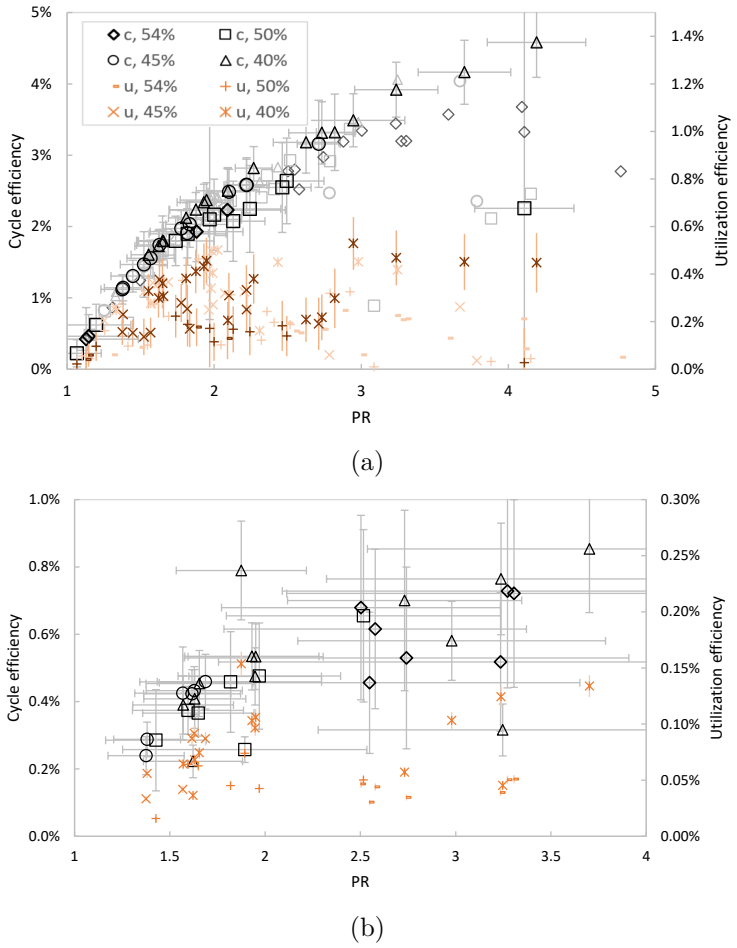

Figure 7.13: Cycle and utilisation efficiencies as a function of cycle pressure ratio and charged LiBr concentration, (a) with the hypothetical 65% expander efficiency, higher accuracy states in bold and (b) measured parameters with the plastic turbine

differ. Another cause is in different cycle efficiency at different pressure ratios and steam mass flow rate, i.e. bypass valve opening. Lastly there can be a different ratio between the lean and rich solution flowrate (another degree of freedom for the APC control). This fact suggests that the optimal control strategy is also not as straight forward as for simple cycles such as ORC.

The concentration change is furthermore used for plotting the data in Figure 7.14b. Here we can see a confirmation of the thermodynamic models that the highest cycle efficiency is associated with lower values of concentration change. Only few data points at the lowest concentration change below 2% suggest, that at this region it does not need to apply absolutely. On the other hand, the utilisation efficiency increases with the concentration change with

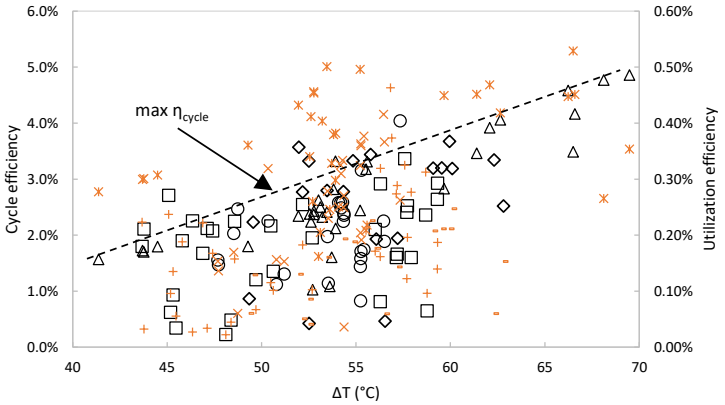

(a)

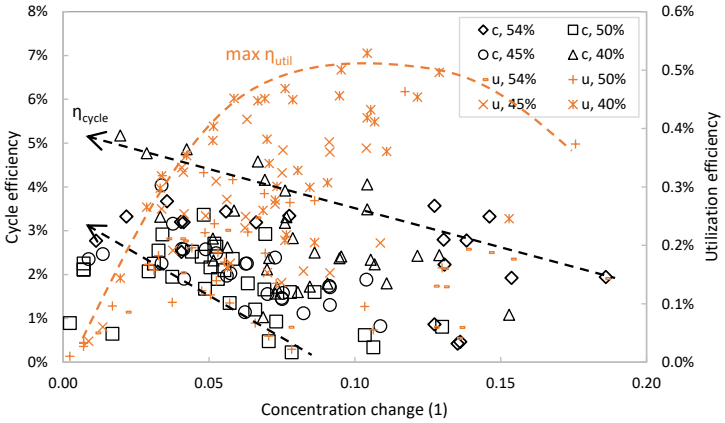

(b)

Figure 7.14: Cycle and utilisation efficiencies as a function of charged LiBr concentration and temperature difference between the heat source and heat sink (a) and of a concentration difference (b), all with the hypothetical 65% expander efficiency

a possible optimum at somewhat higher values. Thus, a drop in utilisation efficiency might come with a further increase in the concentration difference (if the operating conditions allow such a state), but not that many data at that region were obtained. This behaviour is further seen in detail for 40% LiBr charge concentration in Figure 7.15, where cases with a low variation between the heat source and sink inlet temperatures and flowrates were selected.

7.5.2 Temperature glide measurements

One of the objectives of the experiments was to evaluate the actual temperature glide during the non-isothermal phase change during desorption and absorption, as high temperature glide was suggested in the past as suitable for waste heat

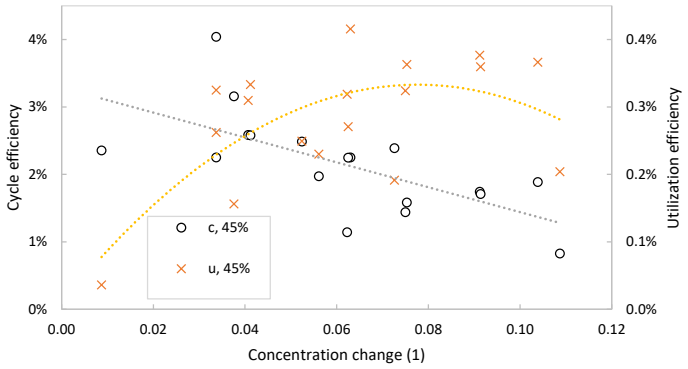

Figure 7.15: Detail of cycle and utilisation efficiencies as a function of the solution concentration difference for cases with low heat source and sink inlet temperature and mass flow rate variation

recovery. This glide for several selected operation states is shown for both desorber and absorber in Figure 7.16. The measured temperature in the desorber corresponds to the boiling solution as the probes are placed under the liquid level. The recorded glide is significantly lower than predicted yet still measurable. A certain decrease of the glide was expected due to the large volume shell & tube exchanger with a nearly quiescent pool of the boiling solution in the shell. Interestingly, the glide doesn't differ significantly between the operation states with various solution charge LiBr concentration. However, such a result is in accord with Figure 7.14b, where no clear relation between concentration difference and charge solution concentration has been found. The lowest absolute values for the 40% concentration are caused only by the fact that the ambient conditions allowed lower temperatures at these tests. Also note, that the uncertainty of the glide measurement is around 1.2K, though as a difference between values from the same series of sensors and the same measurement system, this uncertainty should practically be smaller.

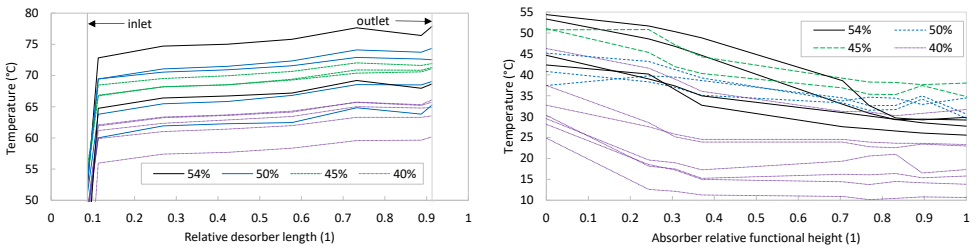

(a) (b)

Figure 7.16: Measured temperature glide profiles in desorber and absorber (absorber 0 corresponds to top part with vapour inlet)

In most cases, the absorber had operational only the upper half as the lower

half was designed only as a backup if the absorption rate is insufficient. The measured values however show often a gradual temperature decrease, even if cooling water was not flowing in the lower set of coils. The measured temperature might correspond to the low-pressure water vapour as the temperature probes were not always fitted exactly between the cooling coils. Therefore, it is hard to estimate how the sensors are wetted with the liquid solution, and the results need to be taken as possible for either vapour or liquid, which do not need to be at the same temperature. The first temperature (inlet at height 0) shown is the turbine outlet vapour, while the next point of measurement is after a packing (for adiabatic absorption) and a small portion of cooling coils. Adiabatic absorption may explain the temperature increase in some cases between the inlet and the first measurement. An increase in temperature in the bottom part may be associated with improper wetting by the solution, while the steam has a higher temperature. The last value corresponds to the solution outlet temperature.

The extent of the temperature glide is in theoretical models associated with the concentration change of the solution. Also, the concentration change and temperature glide are related to the cycle PR. These two relationships are shown in Figure 7.17. In the first graph, the general trend of increasing PR with a decrease in concentration change is observed. Several lines can be identified in the trends, each corresponding to the similar heat source and heat sink conditions. The second graph also shows a general trend of increased temperature glide with increased concentration change. However, at any given concentration change, the spread of the glide values is very high. Note the much higher absolute values of measured glide in the absorber, partly associated with measurement of the vapour phase and partly from a better counter-flow operation.

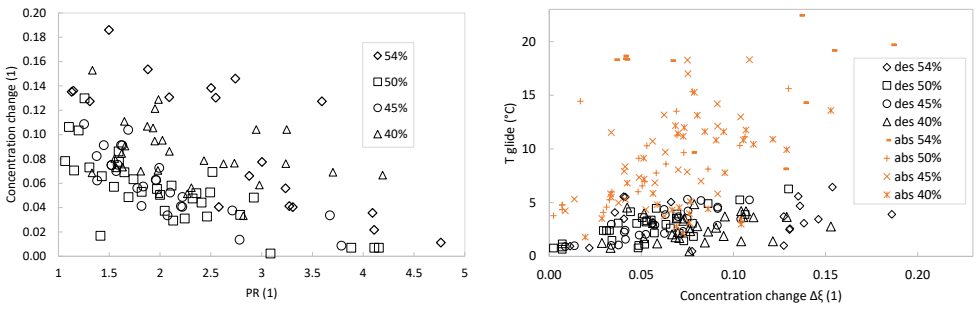

(a) (b)

Figure 7.17: Concentration change as a function of pressure ratio and temperature glide as a function of concentration change for all measured states

7.5.3 Comparison with the design models

For a selected case out of the "more accurate" states, an analysis of parameters and comparison with design models, when the operation parameters are fitted back into it, is performed. The design model doesn't work for fully off-design calculation, but it can provide an insight of a performance comparison between design and actual. Desorber analysis and measured data are used to obtain the heat source and heat sink outlet parameters, turbine inlet pressure, lean solution concentration and mass flow rate and absorber outlet temperature. Then, the design model is adjusted, with one input being the actual size of the heat exchangers. A comparison of the main cycle parameters from the design model and measured data is shown in Table 7.6.

Interestingly, at these boundary conditions, the desorber, according to the design model, has worse heat transfer performance than in reality. Even though the actual LiBr concentration difference and temperature glide are smaller, the cycle can in reality extract more energy from the heat source. Moreover, the improved heat transfer is regardless of a very tranquil boiling process observed on smooth stainless tubes. On the other hand, the absorber performs worse where the model predicts notably lower pressure and, as a result, a better cycle and utilisation efficiency.

In order to better compare other measured cycle parameters with the modelled ones, a correction factor *CorrF* to the overall heat flux in desorber and mass transfer coefficient in absorber has been determined. Additionally, the concentration and pressure in the absorber do not correspond to the outlet temperature, so the model was extended to solution subcooling at the absorber outlet.

An essential parameter in the theoretical studies determining the performance in waste heat recovery is the Q-T diagram of the heat input. Furthermore, for heat rejection, the shape of the Q-T diagram and the related mass flow rate of the cooling fluid relates to the parasitic load. Figure 7.18 compares the measured Q-T diagrams to the ones from the corrected model. From this comparison, we can see that regardless of baffles for working fluid meandering in the desorber, the solution temperature rises much faster than required. The remaining temperature glide during the phase change is only moderate. The pinch point then shifts to the point of saturated lean solution from the design point at the heat source inlet.

In the absorber, the vapour temperature corresponds to the saturated solution, while the solution itself on the tube surface is subcooled. The measured temperature profile corresponds to the inlet vapour temperature (lower than theoretical after adiabatic absorption), followed by probably measured vapour temperature before accurately following the modelled liquid solution tempera-

Table 7.6: Comparison between modelled and measured parameters

Parameter	Unit	design model	corrected model	measured
ξ_{rich}	%LiBr	45.0	47.5	47.5
ξ_{lean}	%LiBr	37.6	37.6	37.6
p_{des}	kPa	9.2	9.2	9.2
p_{abs}	kPa	3.2	4.8	4.8
$CorrF_{\text{des}}$	1	0	1.59	n.a.
$CorrF_{\text{abs}}$	1	0	0.30	n.a.
ΔT_{des}	K	17.1	13.8	9.5
$\Delta T_{\text{abs,vap-water}}$	K	6.0	13.4	n.a.
$\Delta T_{\text{abs,liq-water}}$	K	2.2	2.4	3.9
$\dot{Q}_{\text{in}}$	kW	11.1	13.5	13.5
$\dot{W}_{\text{turb, calc}}$	W	395	317	317
η_{cycle}	%	3.56	2.30	2.30
η_{util}	%	0.54	0.43	0.43

ture. This result suggests that the outlet solution is subcooled as it just follows the course of the liquid phase. The actual process doesn't allow the return of the bulk solution temperature back to the saturation temperature, even though such it can be found in many theoretical studies (also previous author's).

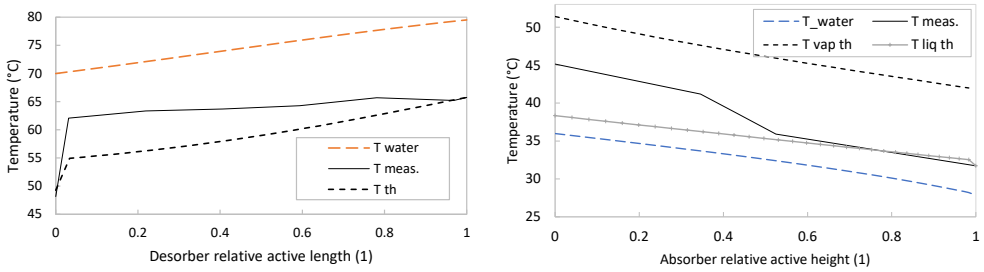

(a) (b)

Figure 7.18: Comparison of measured temperature glide profiles in desorber and absorber with the corrected model

Another deviation from the cycle models is a lower measured vapour temperature exiting the steam generator than corresponds to the saturated mixture temperature (identified by outlet liquid solution). This is illustrated in Figure 7.19, where the theoretical values of pure vapour superheat (saturated solution temperature minus saturated steam temperature at corresponding pressure) are shown with respect to the calculated rich solution concentration. The superheat based on the measured steam temperature is on average 7 K lower, with the spread of the difference in values between 0.5 K and 19 K. Part of the lower temperature can be caused by thermal loss between the desorber and

measuring point 1200 mm away. The loss should be nearly constant regardless of the steam mass flow rate, but the data says this is not the case. Adding the spread of the values and mostly constant temperature difference between the actual and the theoretical values suggests another phenomenon that causes departure from the thermal equilibrium. Generation of vapour at a part of the heat exchanger closer to solution inlet, where boiling solution temperature is lower, can have only partial effect as the measured desorber temperature glide is on average less than 3K. One suggestion is, that the generated vapour is immediately not in the thermal equilibrium with the solution, but further investigation would be required to confirm this.

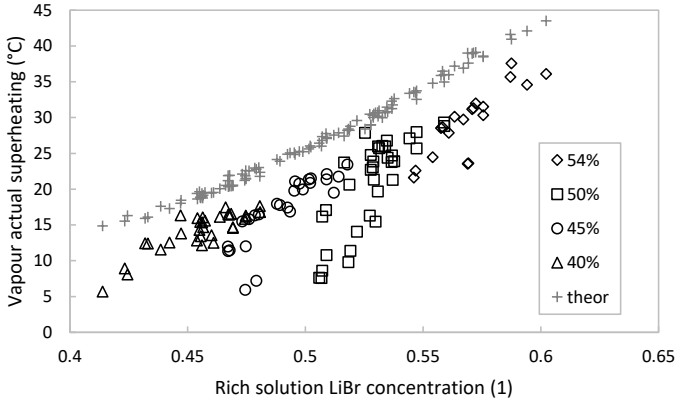

Figure 7.19: Measured and predicted superheat at the desorber outlet

7.6 Summary of APC experimental development

A first experimental step performed was a design and construction of a test rig for measurement of the temperature glide and visualisation of the two phase flow during desorption. In preliminary tests with low pressure water, it however turned out unsuccessful as the flow regime was oscillating, suffering pressure losses, thus unsuitable for the salt APC. Additionally, many sealing issues in the test rig were present.

Following on that, a proof of concept absorption power cycle unit with LiBr solution working fluid has been designed and built, using some design features from absorption chillers to ensure a successful operation. Experimental performance and results have shown the overall technical feasibility of the concept. This is the first reported operation of a power cycle with a salt solution to the author's knowledge. A 3D printed plastic turbine has been operated in the system, but it is described in detail in following chapter. Hypothetical performance achievable with an expander of 65% isentropic efficiency was analysed. With the heat source temperature below 90°C, the maximum gross electrical cycle efficiency obtained with current turbine reached 0.8% and about 150 W.

However, with a state of the art turbo-expander with 65% isentropic efficiency, there is a potential for maximal cycle efficiencies of almost 5% and heat source utilisation efficiencies around 0.5%, which are values rather comparable to the ideal ORC systems.

Even though many of the experimental data are encumbered by high measurement uncertainty, actual behaviour and parameters have shown several important aspects to consider when designing APC systems with LiBr solution. First, the temperature glide in the desorber has been achieved only at a much smaller extent than it was designed. This is regardless of achieving a large concentration difference of the working fluid. The performance of the desorber regarding heat transfer turned out however better than according to the heat transfer model. The opposite was though the case of the absorber. Further improvement for desorber heat transfer could be in having higher roughness of the heat transfer surface. Still, the applied design of desorber has limited feasibility for the waste heat recovery applications where large temperature glide is essential.

Since the unit has been built in a way to ensure some successful performance, rather than the best thermodynamically possible performance, there are many aspects that can be improved now, once the concept has been proven. Among them can be mainly features as improving "counter-flow-ness" of the desorber or better turboexpander engineering design (discussed later). In order to improve data accuracy, flow-meter on the vapour line or dedicated absolute pressure sensors specifically for vacuum (though has potential issues with pressurized sealing tests) and long term operation tests should be used.

Chapter 8

Experimental development of expanders

Expander was already described as the essential component of the power cycle that greatly affects its performance, but also cost. The low pressures and related high volumetric flow of the steam in salt solution APC suggests turbine as the obvious choice of the expander. Low temperatures then suggest application of even plastic materials. Lastly the complex shapes of turbine flow paths raise a question whether additive manufacturing can be utilized. Due to the expander's significance and special attention to manufacturing by additive technologies a separate chapter is dedicated to this component. A review of additive manufacturing in turbomachinery with further details from section 4.2 can be found in author's work [VN16]. First there were developed several air turbines, which served as the initial proof of concept of the adopted approach in turbine development and manufacturing. Following the air tests, the same concept of the turbine has been used for the experimental APC.

8.1 Turboexpander concept

The selection of the turbo-expander configuration was focused mainly on simplicity, low cost and prospect of a decent performance. At the same time, modularity and uniformity of general turbine design together with customization to specific needs at the level of blading modifications was required in the experimental system. A single stage turbine was considered. The following standard configurations were at first considered:

- Radial inflow, axial outflow, reaction – common, higher efficiency but requires very high speed.

- Radial inflow (impulse) – provides a balance between rpm and performance if designed well [219].
- Axial (impulse) – less common in micro applications, though sometimes favoured [172, 178, 219, 218]; allows more compact design; allows lowest rpm with decent efficiency.

Even though radial reaction turbine is commonly favoured for micro-applications such as in [173, 174, 175, 176, 177, 25], impulse turbine (primarily axial), considered for example in [172, 178, 219, 218] has important benefits such as:

- Rather low rotational speed with decent efficiency
- Partial admission allows easy scaling up or down for different power outputs
- Lower sensitivity to larger clearances (better for low manufacturing tolerances)
- Availability of loss correlations and 1D models
- Robustness of blade shape design without detailed CFD optimization

Therefore this impulse (mainly axial) type of turbine became the focus of further investigations. At first, the main goal of the experiments performed within the scope of this thesis was to verify a proof-of-concept additive manufactured micro scale turboexpander that can be safely operated with cold air and easily transported with a possibility of quick replacements of the flow components. Experiences from these experiments and cold aerodynamic tests were intended be utilized for the design and future operation of the turbine with other working fluids. A secondary objective was to test various additive manufacturing methods and their feasibility for turbomachinery, respectively how their accuracy of the prints, mechanical properties and the surface roughness affect the overall isentropic efficiency of the machine.

Many turbine designs find increasingly more attractive possibilities of permanent magnet generators due to many of their advantages. For the experimental and demonstration system, the choice went to conversion of an aeromodelling BLDC (brushless direct current) motor into such generator. Owing to the robust construction of these motors, they are adopted to be also a support of the rotor. Thus no other bearings are necessary. The rotor is then fitted to the shaft via collet. A specific method of measuring and control of the power is described later with the whole test rig. The design of the first turbine and a photograph of the assembled central part for axial air experimental turbine are

shown in Figure 8.1, but the general concept is with small subsequent improvements kept across all so far experimentally investigated turbines. Important aspect of this design is the possibility to quickly change nozzle and rotor components, so that various configurations and components manufactured by different technologies can be tested. Regardless of this simplified mechanical design, the resulting performance and mainly comparison of performance between various components and technologies can be later applied to the other designed turbines.

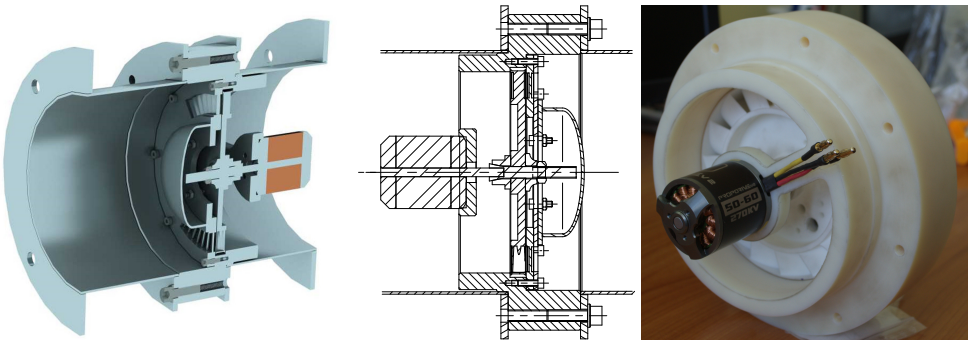

Figure 8.1: Design of the air turbine for tests of AM components and photograph of its assembled central

8.2 Turbine design

Three impulse turbine configurations are designed within this work. The first is an axial air turbine, a baseline and most flexible solution for testing various geometries or components made by various AM technologies. The second configuration is a radial cantilever, serving for a comparison. Lastly, based on both measured performance and technical complexity in achieving a hermetic design, the APC turbine is designed also in axial configuration.

8.2.1 Axial air turbines' design

Boundary conditions: The sizing of the turboexpander follows the requirement of the least number of parts (e.g. single print for rotor wheel). The size is also limited by the size of considered 3D printers – by the working area. The enthalpy drop was chosen rather low to keep the nozzles subsonic. Baseline and nominal parameters of the testing turboexpander were selected as:

- Working fluid – pressurised, considered heated air at 100°C
- Outlet pressure – ambient (1.01 bar)
- Enthalpy drop 30 kJ/kg (i.e. inlet pressure 1.357 bar)

- Rotor speed 10 000 rpm
- Isenthalpic power output 4 kW
- Mean blade D 120 mm (reasonable for 3D printing)

Model: The design is based on typical designs of single stage of expander as described in [218, 220, 221] and modified for small dimensions and technology of 3D printing. The mathematical model of the turbine is based on a 1D design utilizing Euler equation and a loss model accounting for major pressure and energy losses. The principle of calculation follows a traditional methodology developed by the turbine manufacturer, Skoda Power company, and in detail described by Kadrnozka [220] or Ambroz [221]. The mathematical model was built in the EES, in which also the sensitivity analysis and optimization with respect to its parameters took place. The main constraints include a limit in low angles of the physical blade due to manufacturing by 3D printing. Other limitations included considerations to be reasonably close to the loss correlations area of validity, if possible. Summary of the design equations and parameters is in Appendix H.

The design was adopted for simplicity and maximal modularity in case of components replacement. This one is true especially for stator vanes and rotor blades, which are designed to be printed as entire wheels instead of single blades that would be assembled. Blade shapes were selected from the blades catalogue [222] for suitable conditions and selected chord lengths.

Results of the 1D model and construction design: The resulting parameters are summarized in Table 8.1. The selected blades are S-90-12A for stator vanes and R-26-17A for the rotor from a blade catalogue [222] (depicted in Figure 8.2). The relative pitch was chosen to be in the recommended region, namely between 0.6 and 0.9. Outlet angle of the stator vanes is a compromise between maximum performance from the 1D model and maximal angle in 3D printing manufacturability. Two stators and rotors geometries were built with different chord lengths and numbers of blades. Due to the expected potential issues in operation, nominal rotational speed was chosen sub-optimal at 10 000 rpm.

The nominal performance parameters are summarized in Table 8.2. The expected efficiency is rather low. However, it is rather typical value in micro system as this. The portion of delivered power output and specific losses as a result of the 1D model are shown in Figure 8.3. The most significant loss is by far the outlet velocity loss as for given diameter the optimal speed would be significantly higher (highly suboptimal velocity ratio). The ratio of losses due to secondary flow due to end-walls and partial admission is the result of optimization concerning blade length and partial admission degree. A

Table 8.1: Resulting design parameters of the turbine

Parameter	Value	Units	Parameter	Value	Units
Vanes outlet α_1	14.3	°	Number of stator blades z_1 (for full admission)	60/15*	1
Buckets inlet β_1	19.2	°	Number of rotor blades z_2	55/15*	1
Buckets outlet β_2	19.1	°	Partial admission e	34	%
Chord angle α_y	35	°	Partial ad. segments i	2	1
Chord angle β_y	82.8	°	Mean diameter d	120	mm
Stator chord b_1	8.1/32.2*	mm	Blade length l_1	17.2	mm
Rotor chord b_2	9.8/38.5*	mm	Blade length l_2	18.2	mm

* (short / long chord blades version)

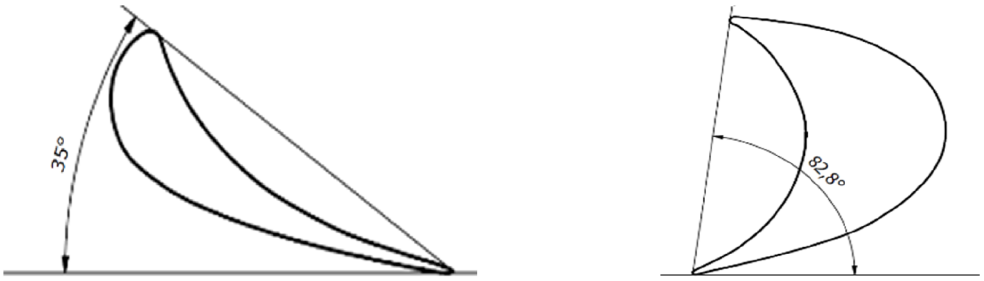

Figure 8.2: Stator (left) and rotor (right) blades for the axial turbine (modified from [222])

sensitivity analysis of the main design parameters in the design are in Appendix H, Figure H.1.

Note however, that due to limits identified later in testing phase on multiple components, the actual experimental tests were performed at much lower degree of admission, particularly 6.67% corresponding to one nozzle in the long chord version and three in the short chord version. Additionally for a reference was measured one configuration with double admission, where another roughly 180° shifted nozzle(s) was used as well (nozzles were manufactured as full wheels and a covering disc with a sealing was used to define the admission). The temperature was near the ambient. The reason for this were later discovered issues with the heating system, capacity of the compressor and limitation in the developed electronics for a power output load management. Therefore, design model was recalculated with same isentropic drop (same velocity angles) and the new partial admission with the results provided also in Table 8.2 and Figure 8.3.

The assembled turbine segment was shown previously in Figure 8.1. Two stator frames were manufactured, one from nylon (simpler, lighter, appeared still suitable for desired stress and temperatures) and one from aluminium

Table 8.2: Nominal design turbine performance parameters

Partial admission, inlet T	**6.7%** , **20°C**	**34%**, **100°C**	
Inlet air pressure p_0	147.6	135.7	kPa
Air mass flow rate	0.034	0.034	kg/s
η excl. addit. losses	69	69	%
η_{is} (excl. mech. loss)	33.6	54.5	%
$\dot{W}_{shaft}$ (excl. mech. loss)	0.34	2.18	kW
Outlet temperature	10	84	°C

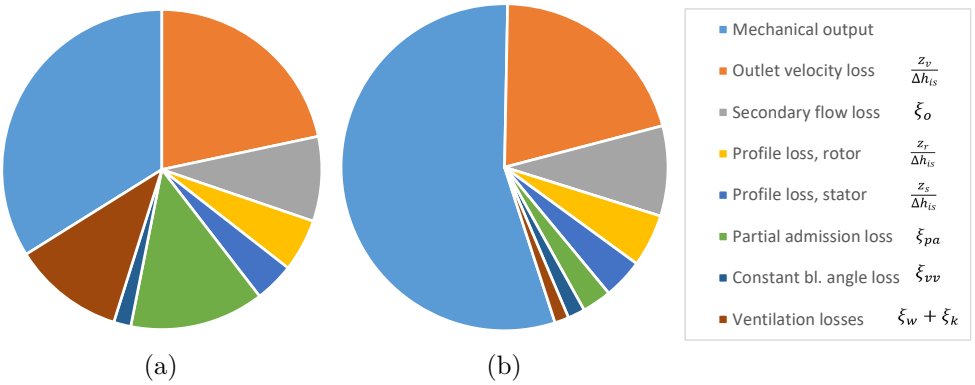

(a) (b)

Figure 8.3: Distribution of isentropic power to delivered power and specified losses for (a) actually operated admission 6.7% and (b) original design admission 34%

alloy. Turnigy SK3-6364-245 aeromodelling BLDC motor was used with the aluminium stator frame and most experimental data were measured with it, Turnigy NTM PropDrive v2 5060-270 was used in the nylon frame for the rest of the experiments.

The stator and rotor wheels were manufactured by various additive technologies (FDM, SLS, DMLS) allowing various combinations and comparison of the suitability of specific technologies. These AM technologies differ in the resulting surface roughness, geometrical precision and strength of the material, and the goal was to evaluate these effects on the overall efficiency of the turbomachine. In Figure 8.4 are shown the details of the stator wheels' blading. The values of surface roughness of the blades are summarized in Table 8.3. The surface roughness measurements were performed inside the channel on the pressure side of the blade in the fluid flow direction, and the total values were averaged from five measurements with the lowest and the highest values of Ra left out. The accuracy of the roughness meter is declared as 10% of the measured Ra value.

The wheels are without any post processing, and the same goes for the stators

Table 8.3: The surface roughness of the first-generation stator blades, measured inside the channel in the fluid flow direction

AM technology	Value	Units
Selective Laser Sintering (SLS, nylon)	5	μm
Fused Filament Extrusion (FDM, ABS)	7.1	μm
Laser Powder Bed Fusion (DMLS, stainless steel) - as printed	20	μm

as well as the rotors. The printed components have faces adjusted on lathe and rotor wheels are dynamically balanced, but the nozzle and rotor blade surfaces are without any surface treatment, i.e. in the as-printed state. Especially in case of DMLS, the surface roughness in locations printed as overhanging is very poor.

(a) (b) (c) (d)

Figure 8.4: Investigated axial air turbine stator wheels, (a) DMLS as-printed short chord, (b) SLS long chord, (c) SLS short chord, (d) FDM long chord

8.2.2 Radial cantilever air expander design

The radial cantilever impulse turbine design was developed for a comparison as an alternative design configuration. It is based on a 1D design utilizing Euler equation and a loss model, which has been in detail described in [VN17] and has

Table 8.4: Boundary conditions for the radial turboexpander design

Design parameter	Value	Units	Design parameter	Value	Units
Working fluid	Air	–	Mass flow rate	0.03	kg/s
Inlet pressure	1.4	bar	Design δh_{is}	27	kJ/kg
Outlet pressure	1	bar	Midspan diameter	110	mm
Inlet temperature	20	°C	Design rotational speed	12000	rpm

Table 8.5: Resulting design parameters of the radial turboexpander

Nozzle outlet angle α_1	15	°	Rotor blade height (inlet)	18.4	mm
Rotor bl. inl. angle β_1	22.8	°	Rotor blade height (outlet)	12.2	mm
Rotor bl. out. angle β_2	22.7	°	Number of nozzles z_1	2	1
Nozzle length b_1	5	mm	Number of rotor blades z_2	42	1
Nozzle height h_1	12	mm	Nozzle outlet Mach no.	0.66	1
Rotor chord b_2	10	mm	Isentropic efficiency	60	%
Partial admission	10	%	Mechanical output	530	W

been successfully applied to supersonic micro turbo-expanders. It is different from the axial air turbine, was not available to the author at the time of the axial turbine design and thus the results can serve also partly for a comparison between the two approaches. The same reference then discusses also the shape of flow paths and the choice of some boundary conditions, which are often given by the engineering constraints. They are summarised along with selected ones in Table 8.4. Proof-of-concept micro-scale radial impulse turboexpander was designed to operate with air and 27 kJ/kg isentropic enthalpy head and the design pressure ratio of 1.4, as comparable parameters to the axial design. The rest of the design is as well the same with the previous turbine. For the sake of safe operation of the machine, the design was again constrained not to run into high rotational speed and fluid speeds respectively.

Some design parameters, such as the number of blades and partial admission with the blade height, had been optimized to provide the maximum isentropic efficiency within the given limits. Other design parameters such as chord to pitch ratio were chosen by previously proven rules of thumb. Resulting parameters such as power, efficiency, resulting partial admission or blade height are along with major geometrical parameters presented in Table 8.5. To provide a better idea of the rotor blade shape, its cross-section is further illustrated in Figure 8.5.

Mechanical design of this turbine was further simplified with primary purpose of air tests and, unlike previous, it cannot be adopted in hermetic systems without any modifications. The design however even better allows the turbine to be easily transported, assembled and disassembled (or changed components)

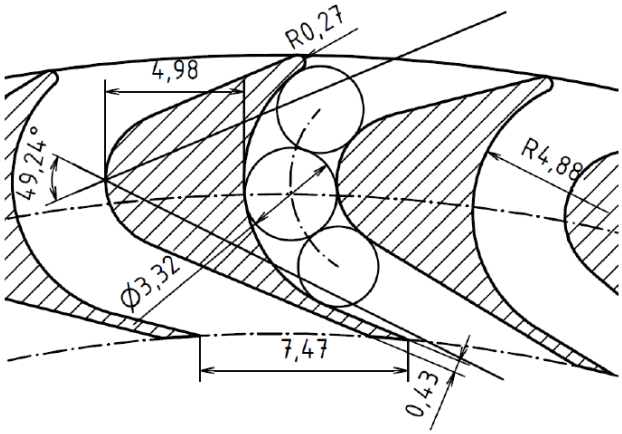

Figure 8.5: Buckets geometry design; based on the original geometrical model from [223, 224]

with the "plug & play" concept. The generator, stator nozzle segments and additional covering parts of the un-admitted rotor are all fitted to a base plate laser-cut from a stainless steel sheet. To limit parasitic airflow, the additional lid was added on top of the assembly with an opening for the axial outflow of the working fluid. In its photograph in Figure 8.6 can also be seen the pressure taps to measure inlet pressure at the nozzle entry. Turnigy Aerodrive SK3-5065-236KV BLDC motor was used as a generator.

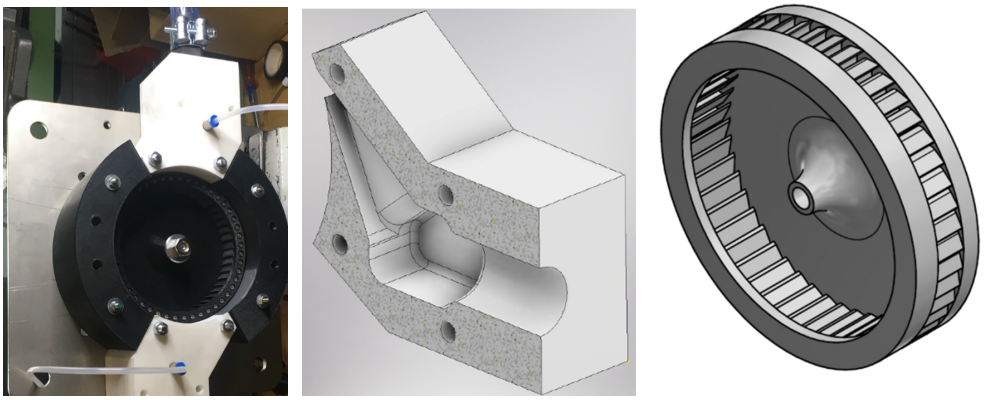

(a) (b) (c)

Figure 8.6: A photograph of the (a) assembled radial turbine; for the sake of clarity, without the lid, (b) the turbine nozzle cutaway and (c) the turbine rotor; both parts 3D printed

As the primary purpose of this expander is to test the possibilities of the 3D printed plastic components for turbomachinery applications. The nozzles

Table 8.6: The surface roughness of the rotor blades, measured in the fluid flow direction

AM technology	Value	Units
Stereolithography (SLA resin)	Ra 3.0	μm
Selective Laser Sintering (SLS nylon)	Ra 5.07	μm
Fused Filament Extrusion (FDM disc & shroud)	Ra 2.3	μm

and rotor, in detail in Figure 8.6b and 8.6c, were manufactured by additive technologies. The nozzles were made from nylon by SLS. The rotor was made in two versions, one version was also SLS, while the other had the blades manufactures by stereolithography (SLA) from a resin, which tends to have better surface quality. The disc and shroud of the other rotor wheel were then made from ABS by FDM technology and each blade was screwed in from the bottom and the top. The surface roughness of the flow components has also been investigated, and it is summarised in Table 8.6.

8.2.3 APC expander design

The working fluid in the expander is a pure water steam (theoretically, no crossover of liquid droplets with LiBr should take place) which is after the separation supposed to be in a superheated state at the same temperature as the boiling solution, which is 78°C at the design point. The design pressure ratio (PR) is 2.2, thus slightly supersonic. Regardless the very low mass flow rate, the isentropic volumetric flow after the expansion is about 0.2 $m^3 s^{-1}$, which justifies use of dynamic expander. When choosing the turboexpander type, axial impulse type with concept similar to the first air expanders was adopted. Among advantages of this design is that the expander is inserted between flanges into the piping in a simple hermetic design.

Major boundary conditions and geometrical parameters were chosen with respect of previously explored air micro turboexpanders. These include mean diameter of around 120 mm, nozzle outlet absolute angle 15° and sub-optimal design rotational speed of 15 000 rpm (optimal is according to 1D model about 30 000 rpm) due to the risk of resonance and excessive vibrations. The partial admission, respectively blade height, is then a result of optimization. For the performance calculations were used several versions of loss models for larger steam turbines from [220] and described in Appendix H. Even though the correlations are valid primarily for much larger turbines, it gives still a first estimate for this proof-of-concept system. Air turbines show a good match, as will be shown among the results. But it might not be the case here in slightly supersonic conditions. Parameters as the chord length or pitch to chord ratio were again selected based on recommended values and rules of thumb such as in [220, 222]. Six nozzles were then placed in two groups across the centre of

Table 8.7: Boundary conditions and results of the APC turbine design

Turbine inlet T_{TI}	78	°C	Partial admission e	36	%
Turbine inlet p_{TI}	13.38	kPa	Blade height*	15/16	mm
Pressure ratio PR	2.23	1	Chord length* b	50/24	mm
Enthalpy drop Δh_{is}	119.2	kJ·kg^{-1}	Nozzles count	6	1
Design speed	15000	rpm	Rotor bl. count Z_r	20	1
Mean diameter	117	mm	Expected η_{is}	$35.8 - 46.9$	%
Nozzle divergence	6	°	Expected $\dot{W}_{\text{mech}}$	$332 - 435$	W

*nozzles / rotor

the turbine disc. Summary of the boundary conditions, optimized parameters and expected performance is summarized in Table 8.7. Note however, that for optimal rotational speed around 30 000 rpm, the 1D models provide isentropic efficiency of up to 68%. The high spread of the design efficiency values only points at the fact, that the adopted 1D models results are only for preliminary application and more detailed engineering needs to be performed for actual applications in the future.

Mechanical design and manufacturing technologies were largely adopted from the air axial turboexpander, while certain aspects were partially improved such as limitation of potential internal leakage issues. Turnigy PROPDRIVE V2 4258 500KV BLDC motor was selected as a permanent magnet generator, with higher "KV" value (rpm/V) in expectation of higher speeds. This configuration has advantage of all rotational parts being hermetically enclosed within the working fluid area, while the output of the system is a three phase current, from which all required parameters (rotational speed, voltage, and current) can be determined. It is only the three cables, which need to be sealed. For the given experimental purposes, no additional bearings are necessary as the generator has its own and the rotor is fitted to the shaft simply with a collet. All other components of the turbine were manufactured from polyamide (nylon) based on the previous experience with air turbines. Nylon provided the best results regarding performance as well as cost effectiveness and manufacturing speed and as the loading of the stages and operating temperatures are low, its application in this type of heat engine appears especially suitable. Components were manufactured again either by additive manufacturing (stator with nozzles, rotor, front lid) or by traditional machining (stator flange in which all the components are placed). The additively manufactured components are utilized in the as-printed state of the flow components i.e. no additional polishing or surface treatment was applied. Only modifications performed was lathe machining the rotor faces to ensure cylindrical and concentric shape and drilling of balancing holes in the dynamic balancing process. The design schematics and the components of the turbine are depicted in Figure 8.7.

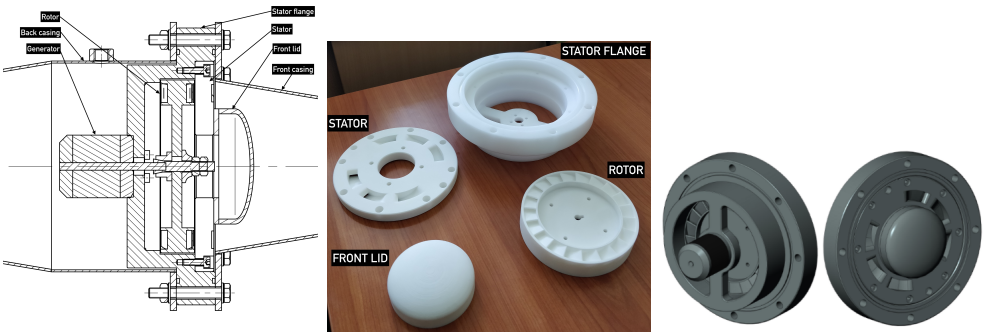

(a) (b) (c)

Figure 8.7: Designed turboexpander for the APC, (a) cross section of the assembly, (b) manufactured plastic turbine components, (c) a 3d model of the turbine

8.3 Testing and evaluation methods

Turbine testing took place on an air testrig and for the APC turbine in the experimental APC unit. Each of them has its specifics, so the measurement methods are described separately. Once the turbine performance and working fluid parameters are known, described data processing and performance evaluation are identical, regardless of applied turbine type or the testrig.

8.3.1 Air expander test-rigs

The air expanders were tested at two compressed air test rigs shown in Figure 8.8. The first rig was built at CTU in Prague and served mainly for preliminary measurements and set-up of system operation. The inlet pressure is obtained by controlling compressor together with regulation and a bypass valves for fine adjustments. The second one is a test rig is present at the PDLT laboratory of Strömungsmaschinen & Thermische Maschinen, Drucklufttechnik, Fakultät Maschinenbau / Umwelttechnik at Ostbayerische Technische Hochschule Amberg-Weiden in Amberg (OTH Amberg-Weiden), where more accurate testing took place regarding the system for constant pressure control and precise volumetric flow measurements.

Turbine rotor is directly connected to the generator. The generator speed and electrical parameters are measured and recorded. The rotational speed is obtained from the generated phase-voltage frequency which is directly proportional to generator rpm by fixed periods per revolution given by a number of rotor magnets and stator coils (synchronous generator). Additionally optical speed measurement was implemented for validation. A simple method for control of the turbine and for measurement of the produced power is a proposed load unit. An electrical connection of this system is in Figure 8.9. The

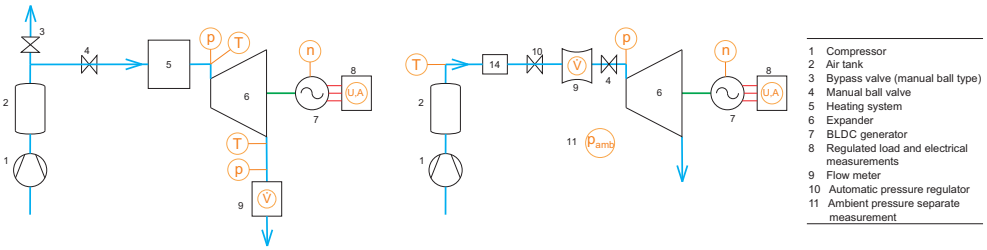

Figure 8.8: Test rigs configuration, left – purpose built rig at CTU in Prague, right – test rig PDLT at OTH Amberg-Weiden

generator produces three-phase alternating current. After rectification, overall voltage is measured, and a calibrated resistor is used for current measurement via a voltage drop. Rectifier has a nearly constant voltage drop which is added to the calculation of overall generator voltage. A load is controlled by opening the transistors in their linear regions. A control, provided by Arduino Uno, is designed to offer constant current regime between zero load to fully open transistors and a regime of controlled RPM, where the load is controlled by a PID regulator.

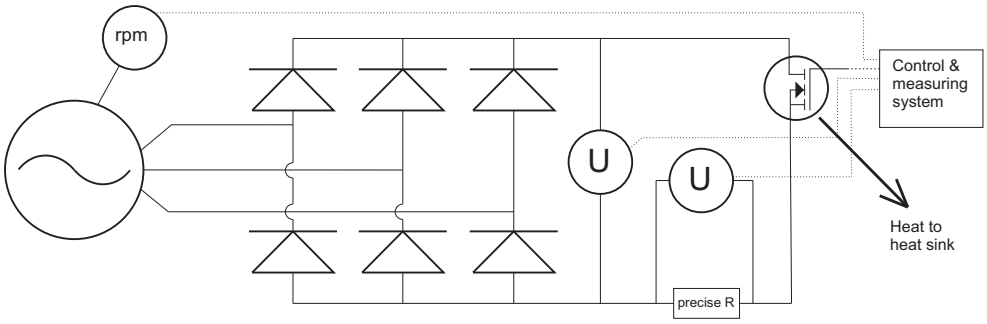

Figure 8.9: Electrical connection of power measurement and dissipation system.

Instruments and their parameters are summarized in Table 8.8. Note that certain further inaccuracy might come from consideration of a constant voltage drop across the rectifying diodes. The design considers for higher power output multiple parallel rectifiers and up to four transistors per each rectifier. Various forced convection heat sinks were explored including repurposed CPU PC coolers. All the electrical components were fitted into a frame which is easily transportable and mobile.

Temperature, pressure and the volumetric flow rate is logged into the laboratory LabView system. Other parameters – rotational speed, voltage and current are gathered by Arduino, which then through USB connection sends the information into a PC. Ambient pressure is measured on a separate device and

Table 8.8: List of measurement devices used during the experiments

Sensor	Measured quantity	Signal	Range	Error
OTH Amberg rig				
IFM PG 2453	Pressure	4–20 mA	−1–25 bar(g)	0.5%
Postberg cp104s	Vol. flow	0–10 V	2.26–462 Nm^3/h	±3%
Sitrans PN150	Δp	4–20 mA	0–60 mbar	0.2%
CTU Prague rig				
PXM309-3.5A10V	p_{in}	0–10 V	0–3.5 bar	1%
PXM309-002A10V	p_{out}	0–10 V	0–2 bar	1%
Float flowmeter LBZ-80	Vol. flow	visual	80–400 m^3/h	1.5%
K thermocouple KMQSS-125G-6 + USB-TC01	T	mV	−100–1400°C	0.7°C
Power Load unit				
AC frequency	RPM	(el. freq.)	500k rpm	∼2 rpm (@10k rpm)
IR sensor TCRT5000	RPM (aux.)	3.3–5 V	500k rpm	∼20 rpm (@10k rpm)
Arduino A/D (+Volt. div.)	Voltage	0–60 V	0–60 V	2% + 0.03 V
Arduino A/D (U drop)	Current	0–15 A	0–15 A(1 block)	2% + 0.02 A

logged manually.

8.3.2 APC turbine test-rig

The APC turbine has been after initial tests verifying its operation installed and tested within the APC proof-of-concept unit described above. The load control and measurement system is in its design identical with the one for the air test rigs. Data processing and performance evaluation thus follows also a methodology described below. The only difference is the working fluid (real water steam) and method for obtaining steam mass flow rate as described in respective chapter on APC experimental system.

8.3.3 Data processing and performance evaluation

The raw dataset of power, rotational speed, voltage, electrical current and inlet pressure is displayed for illustration in Figure 8.10 and Figure 8.11. The system was controlled in a constant rpm regime with the distinct steps in the turbine speed. The transfer between each speed has a breaking period with certain overshoot in the increase of the speed and decreased load period

in decreasing speed due to the nature of the controller (non-linear system, PID constants need to give decent results in large range of system conditions). Maximal obtained speed (and highest voltage, lowest current) is seen to be beyond the maximal power output.

The steady states were manually selected from the data with the corresponding timestamps and the quantities during the steady-state operation of the turbomachine were averaged. The averaged quantities are then evaluated with an objective to obtain the mechanical power output (on the shaft) and isentropic efficiency of the turbine at each state.

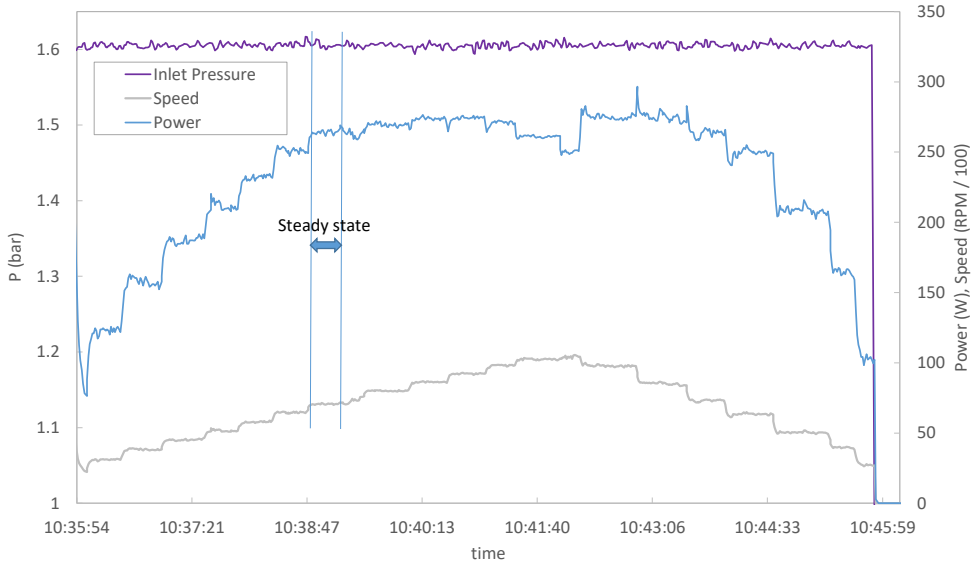

Figure 8.10: Raw dataset from the experimental campaign for one pressure ratio – inlet pressure, speed and electrical power output

Isentropic efficiency is evaluated from the theoretical power output in isentropic expansion and from known generator efficiency. As the generator choice or even design can be in the future precisely selected, this work focused primarily on the performance from fluid dynamic point of view. Therefore, even though electrical power output was of course calculated as well, it is not primarily reported in this work. The method is in detail described in Appendix I.

The mass flow rate of working fluid in case of air tests and APC commissioning with pure water is obtained from measured volumetric flowrate. In the APC experiments with the LiBr solution, the mass flow rate is obtained based on the aforementioned method of desorber mass and energy balance in cycle investigation. Except for that the evaluation methodology is identical for all expanders.

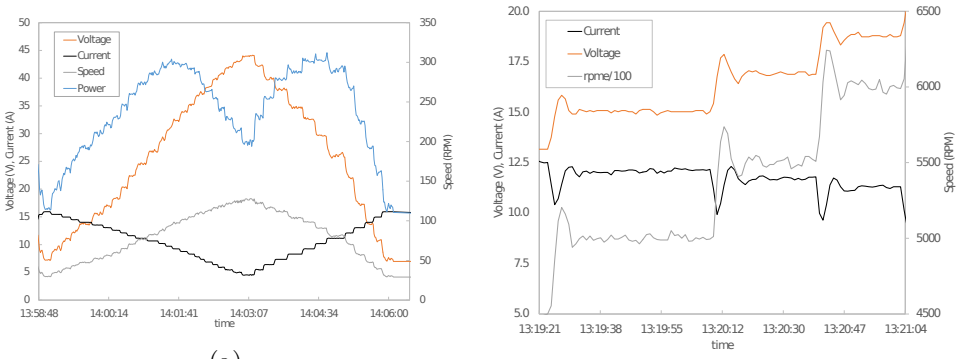

(a) (b)

Figure 8.11: (a) Raw dataset from the experimental campaign for one pressure ratio - voltage, current, speed and power, (b) A detailed sample of the recorded speed data - regulation for constant rpm

8.4 Expander performance results

Performance results are organized according to the turbine configurations, axial air turbine, radial air turbine and APC turbine. Most of the experimental analyses were performed with the axial air turbine, while the radial air turbine serves as a reference for an alternative approach to the configuration and the APC turbine performance is then reported as part of the APC unit operation with low-pressure steam and achieved parameters as temperatures around 70°C and absolute pressures in the order of kPa.

8.4.1 Axial air expanders results

Main results of the axial air turboexpanders, reported in detail in author's works [VN17, Sc5], are presented here. Since there were many variations of the tested configurations regarding the three 3D printing technologies (SLS, FDM, and metal DMLS) and two chord-length configurations, a summary provided in Table 8.9 provides for orientation in the presented results.

Example of a typical turbine characteristics for several PR that was obtained, specifically with SLSl/SLSl configuration, is shown in Figure 8.12. The very first measured efficiency values had maximum around 10%. The figure shows for illustration single such characteristics designated as "old". The poor performance was caused by an insufficient sealing of the surroundings of stator nozzles, particularly between main stator frame and stator blades wheel and between the stator wheel and a disc defining the partial admission. A major loss was therefore caused by internal leakages. Once this issue had been overcome,

Table 8.9: Summary of tested axial air turbine configurations

Designation	Stator (technology / material / chord length)	Rotor (technology / material / chord length)
SLSI/SLSI	SLS / nylon / 32.2 mm	SLS / nylon / 38.5 mm
SLSI/ SLSs	SLS / nylon / 32.2 mm	SLS / nylon / 9.8 mm
SLSs/ SLSs	SLS / nylon / 8.1mm	SLS / nylon / 9.8 mm
FDMI/SLSI	FDM / ABS / 32.2 mm	SLS / nylon / 38.5 mm
FDMI/SLSs	FDM / ABS / 32.2 mm	SLS / nylon / 9.8 mm
DMLSs/DMLSs	DMLS / steel 316L / 8.1 mm	DMLS / steel 316L / 9.8 mm

the efficiency improved here towards 20%. This is below design point (34% for PR around 1.4 and 10 000 rpm) and the difference is discussed below.

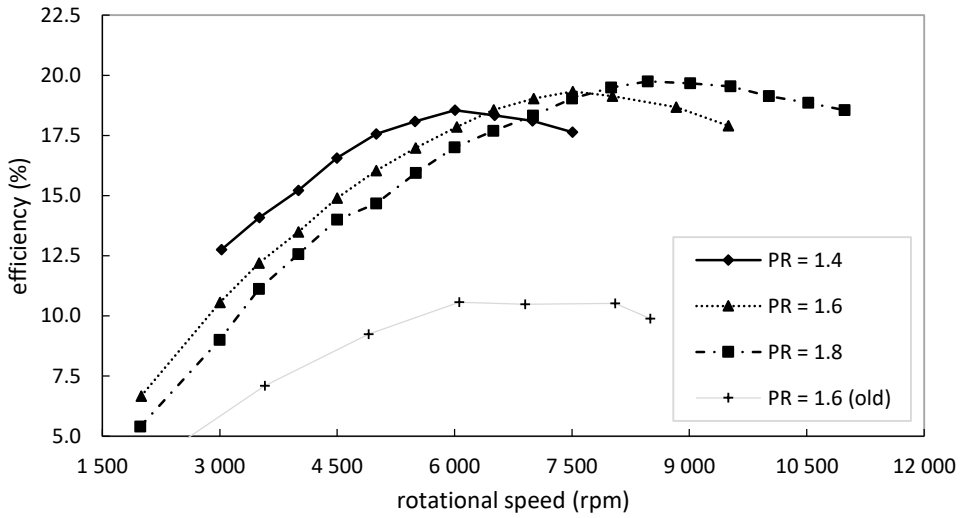

Figure 8.12: Experimentally determined isentropic total-to-static efficiency of the "SLSl/SLSl" turbine

In order to compare the performance of wheels of different configurations and made by different technologies, Figure 8.13 provides isentropic efficiency curves for a pressure ratio about 1.6. For the SLS components, clearly the worst performance is obtained by the SLSs/SLSs configuration. It is slightly surpassed by the SLSl/SLSl and the best performance has the SLSl/SLSs. It appears, that the combination of larger nozzles and smaller rotor buckets is the best combination. An interesting feature is the similarity between performance of SLS and FDM nozzles. The FDM technology leaves typical notches on the surface, perpendicular to the air flow. Regardless, the performance is same or slightly better than for the SLS with much better surface quality. The combination of short chord for both rotor and stator however turned out rather well for the metal parts made by DMLS, regardless of their very poor surface

quality. The maximal speed differs for each configuration and marks the last achieved point in the operation. Beyond this, vibrations of the system did not allow to reach higher speed or the power quickly dropped to idle (probable contact between rotor and stator would dissipate all energy) and the turbine was operated at such speed for very short time to prevent damage.

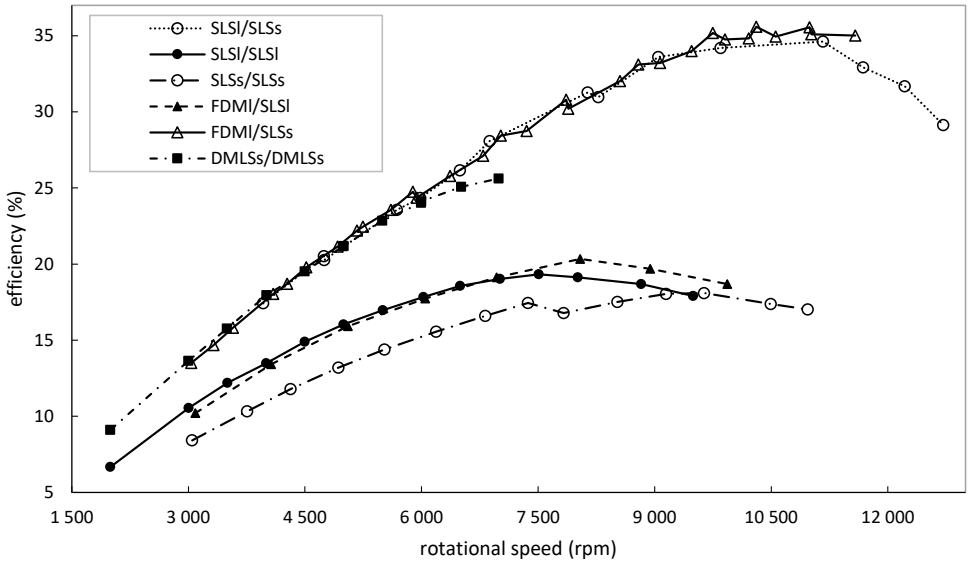

Figure 8.13: Comparison of experimentally obtained efficiency curves at PR about 1.6 for air turbine with components manufactured in several configurations and technologies.

Finally, for the best configuration SLSl/SLSs, a trial run with double admission (two nozzles, about 180° apart) has been performed and the experimental performance was compared to the design model. The results are in Figure 8.14. Here it is very interesting, that the design model fairly accurately predicts the performance. The higher admission provides higher efficiency and has the maximum at higher speed as related losses become relatively smaller. In order to further verify the accuracy of models for specific losses, hypothetical performance of fully admitted wheel is further calculated from the results. In the first attempt, denoted "wov" as without ventilation, it was argued that ventilation losses as applied in similar size turbines from model described in [VN17] make for all the difference to the fully admitted turbine performance. This correlation works well for similar size and power supersonic turbines working with air or organic fluid. As the "wov" curves do not however match, it is not the case in here. Then, the ventilation (windage) and partial admission losses were evaluated for the experimental datapoints and denoted "wopa" as without partial admission. Since more detailed turbine performance parameters were required, a simplified off design model with constant rotor relative speed

angle β_2 was assumed. When these two losses are added to the efficiency values, there is a very good match for the most of the turbine speed range.

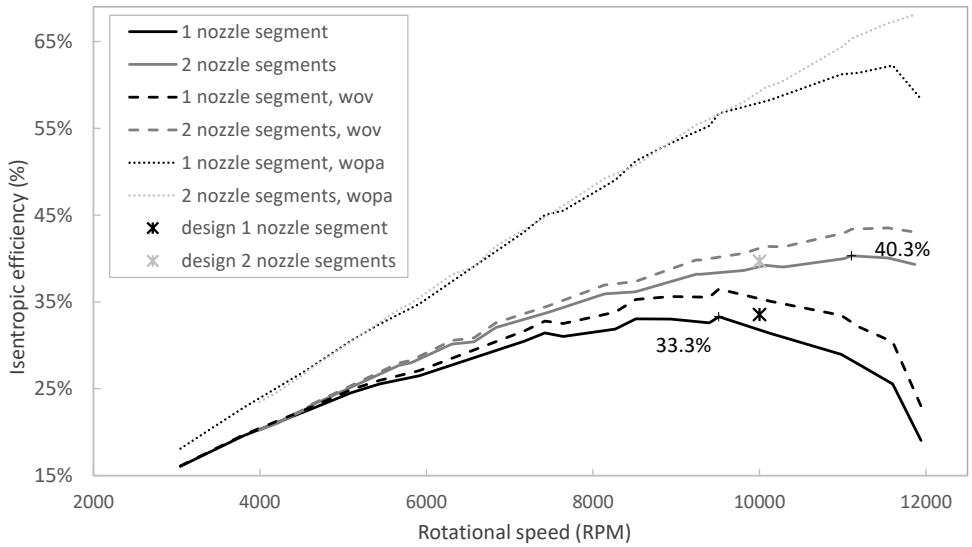

Figure 8.14: Effect of the partial admission, comparison with design model and comparison of related loss models for PR about 1.4 and configuration SLSl/SLSs.

These results are actually very surprising as the loss models are for much larger steam turbines. It appears, that for sub-sonic air flow they work very well. The rather good performance of poor surface quality blades also suggests, that at these speeds and particular Reynolds numbers, due to specific boundary effects, the rough surface might not be disadvantageous. The mass flow rate also corresponded to about 91% of the design mass flow rate, therefore no major effective decrease in the cross section area is present either. Note also that no CFD optimization has been performed and relatively large clearances between rotor and stator were present. This surely provides space for further performance improvement in the future works.

8.4.2 Radial cantilever expander results

The results of the radial cantilever air turbine, described in detail in author's work [VN12], are presented on the efficiency curves below. Two assemblies were investigated, one with the rotor manufactured by SLS from nylon and the other one with the rotor made by a combination of FDM (ABS filament, disc and shroud) and SLA (resin, blades). The originally expected behaviour would be that the assembly with blades manufactured with higher precision and lower surface roughness (FDM+SLA wheel) would yield higher isentropic efficiencies due to the lower friction losses and better geometrical accuracy of the fluid flow path.

In Figure 8.15a the measured turboexpander efficiency curves for pressure ratios of 1.46, 1.56 and 1.66 of the assembly with the SLS rotor are displayed. The rotational speed of the rotor was controlled by varying the load of the generator in the region of 2 500 up to 11 000 rpm. Nominal rotational speed was not reached due to the resonance vibrations of the rotor and a risk of damage. The highest isentropic efficiency observed was 36% at 10 500 rpm. If the rotor was better dynamically balanced, it would be probably possible to yield higher results of the efficiency, as the maximum of the parabolic efficiency curve was not yet met and would reach the maximum at around 40%. The design point is though at 60% isentropic efficiency at 12 000 rpm, which was not achieved in either of the two experimental set-ups.

In Figure 8.15b, the measured turboexpander efficiency curves for pressure ratios of 1.45, 1.55 and 1.65 of the assembly with SLA rotor are displayed. The rotational speed of the rotor was measured from 2 500 up to 12 000 rpm. Higher speed was probably reached as a result of lighter rotor, prone to excessive vibrations at higher speeds. The highest isentropic efficiency observed was 29.2% at 10 700 rpm. Again the design point of 60% isentropic efficiency at the nominal rotational speed was not achieved by an even larger margin. The SLA set-up was 6.8 percentage points of isentropic efficiency behind the SLS rotor assembly, although the resulting surface roughness of the SLA blades measured in Ra was almost half of the roughness of the SLS rotor. The maximum efficiency point was again measured for the pressure ratio of 1.5 in contrast to the design pressure ratio of 1.4. Note that at the nearly design pressure ratio, the maximum of the efficiency is around 8 000 rpm, i.e. at 66% of the design speed. This indicates additional losses relating to the air flow, which were not considered and accounted for in this design.

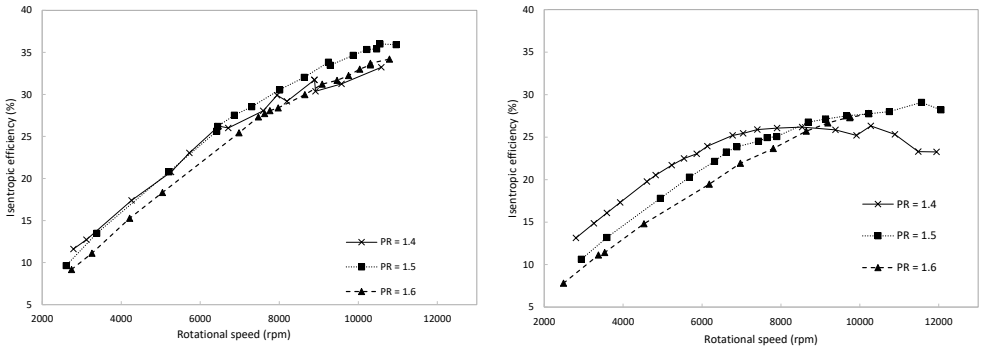

(a) (b)

Figure 8.15: Turbine efficiency curves for three different pressure ratios; set-up with SLS nylon rotor (a) and SLA resin rotor (b)

The reasons for not achieving the design values of isentropic efficiency from the 1-D tool may be of several different natures. A severe issue observed was

the insufficient sealing of the surroundings of stator nozzles. A major loss was, therefore caused by leakages where some of the air did not enter the rotor and bypassed it. A detailed CFD analysis of the flow components is absent as well. Optimized shapes of the nozzles and buckets would potentially increase the efficiency of the turbine (this time they were not selected from a catalogue). An issue that may negatively affect the low experimental values of isentropic efficiency is the design of the rotor blades, where the blade height at the inlet is identical to the blade height of the nozzle at the outlet. A small increment in the rotor blade height at the inlet may positively improve the fluid flow behaviour at the rotor inlet and thus improve the efficiency. The last factor is suitability of the design loss models as they are valid for highly supersonic micro turboexpanders with higher degree of admission and smooth surfaces. This is contrary to the previous results with surprising good match with design correlations for large steam turbines.

8.4.3 APC demonstrator expander results

APC expander was first operated with deionized water during commissioning, which provided some first results. Later it was operated with the LiBr solution as described before in the cycle operation, analysis and results. The results are reported in author's work [VN13, VN15]. Unlike in air turbines, here was highly varied both the turbine inlet pressure as well as the outlet pressure. Summary of all obtained experimental efficiency characteristics is in Figure 8.16 and power output in Figure 8.17. During the operation, a resonance frequency and related vibrations caused that the maximal turbine speed was around 8000-9000 rpm, right above half of the nominal speed. Even with the poor surface quality, the efficiency is mostly within boundaries provided by different loss models. This shows a high prospect of the plastic 3D printed concept with better engineering than was adopted for this proof of concept. Furthermore, inspection after about a year in the environment with LiBr and more than 6 hours of total operation, nor the turbine, nor the generator showed any signs of damage or corrosion (except for surface corrosion of several steel bolts holding the generator, which did not have any, even zinc, surface treatment).

The detail of turbo-expander operation for only the states selected as more accurate is shown in Figure 8.18. Both figures confirm that the generally expected trend of decreasing efficiency with increasing the pressure ratio is valid. Furthermore, even with the poor surface quality of the flow sections, the efficiency is mostly within boundaries provided by the applied loss models.

Uncertainty analysis was performed also regarding the APC turbine performance (except for RC regime in commissioning) in the same manner as was the case for the cycle operation. The median of isentropic efficiency uncertainty is 3.4 percentage points. Appendix G provides the turbine characteristics with

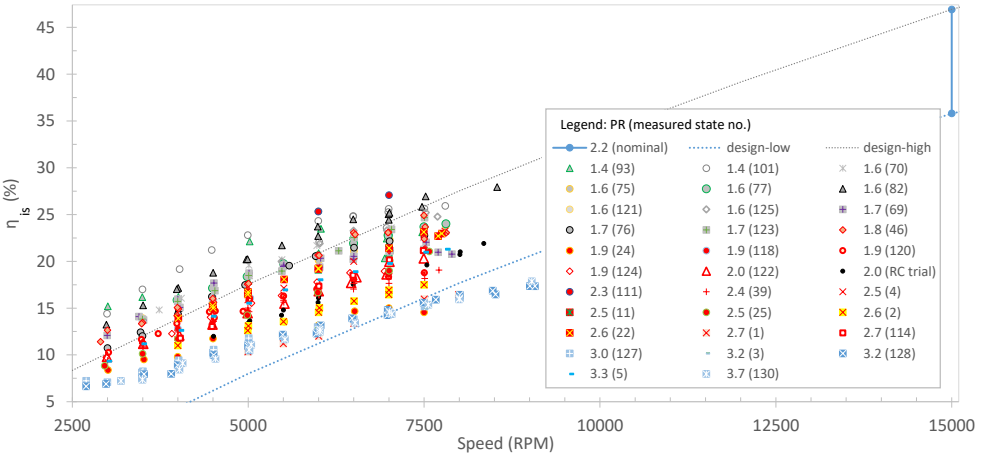

Figure 8.16: Measured turbine efficiency characteristics from APC operation and comparison with design

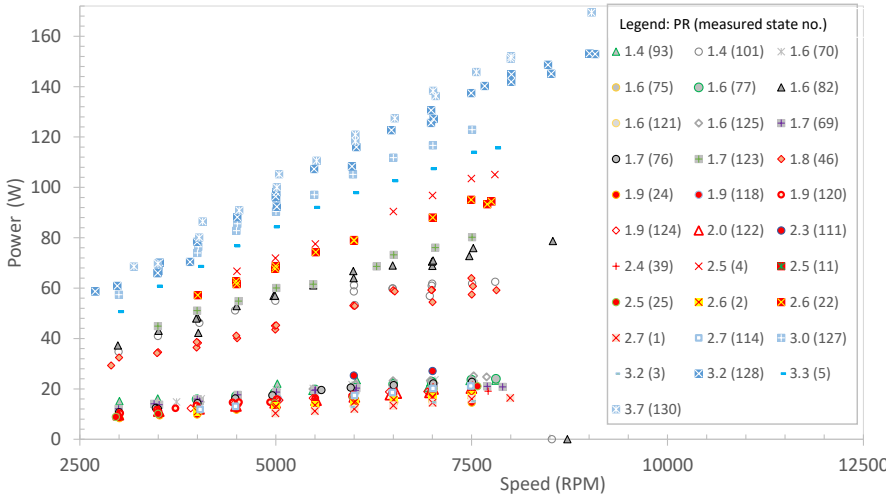

Figure 8.17: Measured turbine characteristics of mechanical output against speed from APC operation

the plotted uncertainty values for the more accurate states. Here it was not included in the figure to increase its readability. As the large share of the uncertainty value comes from the power load system, the uncertainty increases with the power output within single PR dataset. On the other hand, very low turbine outlet pressures cause high uncertainties for a given dataset as the pressure is closer to zero and thus the least accurate range of the sensor.

To summarize the performance, there are several reasons behind the very low efficiency of the tested turbine. One is surely the poor surface quality of the flow sections as for these first trials, no post-processing was applied and the

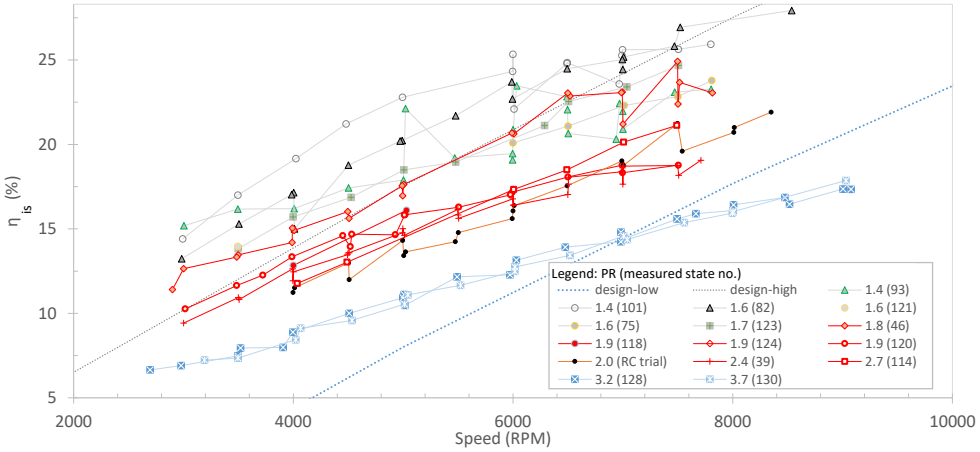

Figure 8.18: Measured turbine characteristics from APC operation for states with higher accuracy

surface is in the as-printed state and the steam velocity is high. Even though the performance matches design models well with the air expanders, here at near sonic or slightly supersonic flow, there is no physical possibility that the impact would be other than detrimental. Second reason is the low velocity ratio, as it can be seen already from the design point at unreached 15 000 rpm and the theoretical optimum being around 30 000 rpm. Lastly, design was performed with loss models adopted from large steam turbines and no CFD optimization of the geometry has been performed. This shows a high prospect of the plastic 3D printed concept, especially with more advanced design engineering than was adopted for this first proof of concept.

8.5 Summary of turbo-expander development

Presented work with the air turbo-expanders with the 3D printed and plastic components and BLDC motor as a permanent magnet generator has been among the first experimental verifications of feasibility of such a concept. It has shown to be a very cost effective and quick method to build turboexpanders in case of both axial and radial cantilever impulse turbines. This method is especially suited for proof of concept applications. The obtained efficiency reaching maximum range of only 35-40%, especially for sub-sonic stages, is indeed rather low.

On the other hand, in case of axial turbine in suitable geometrical configuration of investigated nozzles and rotor chord lengths, performance surprisingly well follows the design model, using loss correlations from MW scale steam turbines. The surface quality of the flow channels has not shown for the tested sub-sonic

air turbines to be the limitation, which points out to specific boundary layer effects at given Reynolds numbers.

In the APC operation with water steam, the nylon axial turbo-expander with the generator have shown over the experimental campaigns no damage both for the nylon components and the generator connected directly to the rotor with the low-pressure steam flowing around. Due to the high volumetric flow rates, it has been proven that the turbine is a suitable expander for APC with LiBr solution, even at very low power outputs. Lower than expected isentropic efficiency reaching about 25% can be significantly improved in future designs. Note that custom buckets for rotor and nozzle shapes were applied here unlike catalogue selected for the axial air turbine, which might further hinder the performance.

All the axial turbines were operated at sub-optimal design of the 1D models (either regarding partial admission or speed), no CFD optimization has been performed for geometry optimization while mechanical vibration issues limited operation at higher speed. With better design in future works, there is therefore a high potential of this novel 3D printed turbo-expander approach as a cost-effective solution.

Chapter 9

Conclusion

This thesis investigates the topic of absorption power cycles (APC) with aqueous salt (such as LiBr) solution as a working fluid. It starts from the review of this specific concept, goes to investigation of a theoretical potential of standalone APC or as an absorption power and cooling combined cycle (APCC) and continues to proof of concept experiments, performing world's first reported operation of the APC with salt solution. The thesis goals were achieved as the theoretical range of feasible application was found in utilization of very low temperature (below about 120°C) heat sources, primarily in waste heat recovery or as part of a APCC system. Low pressures and large vapour volumetric flowrates predestine the application for small distributed energy systems (kW to dozens kW output). The goal of proving technical feasibility was achieved as the APC unit with LiBr was built and successfully operated. Specifically, a goal of measuring the temperature glide was considered in the design, so that actual temperature profiles were obtained in measurements and compared to predicted ones. A turboexpander system using polymer based additively manufactured components and converted permanent magnet motor as a generator was developed as a cost-effective solution. The goal of identifying actual range of applicability has shown, that actual temperature profiles and heat transfer might somewhat lower APC feasibility for waste heat recovery, however the solution with cost effective turboexpander remains feasible for combined power and cooling systems.

APC were extensively studied in the past only with water-ammonia mixture, i.e. Kalina cycle and as such were even partly commercialized. Further research at certain point started to focus on potential of highly complex layouts where prospects of commercialization are rather low. Experimental, pilot and first commercial systems with Kalina cycle show, that system needs to be simple and still it is prone to many issues. It is unlikely that for high temperature and high power output region Kalina cycle would squeeze out current mature systems

based on Rankine or even Brayton cycle. By the potential of exergy efficiency, it however holds potential to low temperature and waste heat recovery (WHR) in applications, where even organic Rankine cycle (ORC) is not feasible. This is seen also in the more recent development of the Kalina cycle systems applied to waste heat or geothermal resource with power output range of 50 kW to 5 MW.

Regarding alternative working fluids the range of previous research is much less extensive. Several alternatives to the water-ammonia mixture have been proposed in theoretical studies. Specifically, interesting is use of alcohol mixtures or salt aqueous solutions and among them solution of LiBr. The LiBr solution is a working fluid applied in many commercial absorption chillers but only several studies considered it for power production. Applications for WHR or similar open loop and low temperature heat source with stress on utilization efficiency have however not been previously comprehensively analysed. Low pressures (vacuum, order of kPa, max dozens kPa in high pressure part) in all nodes of the cycle determine that LiBr solution can never be a competition in field of large power output systems, however it can be beneficial in small distributed systems due to less strict legal requirements on pressure systems or possibility of designing efficient turboexpander with feasible size and speed for very small mass flow rates, but large volumetric flow rates. Note that Kalina cycle provides the opposite characterisation with high system pressures.

Therefore, a theoretical investigation was focusing on a comparison of thermodynamic model results for the proposed APC (primarily aqueous salt solutions of LiBr, LiCl, and $CaCl_2$) against alternatives as ORC in various configuration (recuperation does not bring however purely thermodynamic benefit in WHR) and several other APC working fluid options including typical water-ammonia mixture. For this method of screening a pinch point analysis was chosen as the most suitable. Very important aspect is a consideration of a parasitic load of heat rejection (fans, pumps) as the power requirement can be of a similar order of magnitude as the turbine power output. The cycles were optimized for maximal net power output, typically represented by utilization efficiency. The region of salt solution APC superiority was found for very low heat source temperatures and applications with higher cooling power demand. Absorption power cycles begin to have a thermodynamic benefit over organic Rankine cycles for heat source temperatures below approximately 120°C (exactly depends on many parameters and boundary conditions). The difference between different salt solution systems is very small and is also comparable to methanol-heptanol mixture. In the low temperature region, the salt APC is followed by Kalina cycle and after that are ORC systems.

To provide some numbers, the cycle efficiency of optimized salt APC ranges from 2% (gross) and 0.5% (net) for 60°C heat source over 8.5% (gross) and

7.5% (net) for the breaking point of 120°C to 13% (gross) and 12% (net) for 160°C heat source. The utilization efficiency, more important for WHR, ranges from 0.5% (gross) and 0.1% (net) for 60°C heat source over 3.6% (gross) and 3.2% (net) for 120°C to 6% (gross) and 5% (net) for 160°C heat source. The values might appear very low, but it is caused by the low temperature with low thermodynamic potential. To better evaluate how the thermal potential is used, exergy efficiency or 2^{nd} law (of thermodynamics) efficiency can be used. For heat source utilization the efficiency is in range from 10% (gross) and 2% (net) at 60°C heat source to 33% (gross) and 29% (net) at 160°C heat source.

APC can find its application also as a bottoming cycle or in low temperature solar thermal systems where the performance was found significantly better than alternative ORC, as it was shown in performed case studies.

The review shows also prospects of combined systems of power and cold energy production. Applications based on water-ammonia chillers have not been seen in reality probably due to the environmental, material and regulatory issues or due to low flexibility of cooling output in case of experimentally explored Goswami cycle. Due to the extent of LiBr chillers, this working fluid also offers a large potential for combined heat and power systems. For proper classification, there was documented a large range of principles and configurations of the combined power and cooling systems, which were by the author classified into the four major groups:

a Separate thermodynamic cycles coupled by heat

b Separate thermodynamic cycles coupled by work

c Single branch thermodynamic cycle for both power and thermally activated cooling

d Branched thermodynamic cycle for either power or thermally activated cooling

Systems coupled by heat refer primarily to utilization of thermally activated chiller as the bottoming cycle. Coupling by work (mechanical or electricity) means in principle two completely standalone systems (some components can be shared though), where a portion of the work produced by a power subsystem is immediately consumed by the chiller. The temperature and pressure potential of the expander or condenser, throttling valve and evaporator can be used also in a serial configuration in single branch systems. However, it typically provides a trade-off between cooling and power production. Specific case resulting of a thermodynamic peculiarity of absorption systems is a Goswami cycle, using sub-ambient temperature of expanded ammonia rich vapour to get

some cooling effect (LiBr system could work similarly, but preliminary results have shown too little potential). The last configuration is the domain of the absorption systems, where either a very flexible system can smoothly switch the evaporated refrigerant vapour between expander and the chiller branch, or a system can utilize the rich liquid solution from the desorber for power production in various methods (with or without additional heat input) but the flexibility is sacrificed.

Regardless of this wide range of systems and extensive research in each of them, it appears that the works of the author are the first to propose a simple, thus technically feasible, configuration of an absorption system with a parallel chiller loop in one branch and an expander loop in another using LiBr solution (or any aqueous salt solution). This configuration was therefore selected for a detailed analysis of its potential for both closed loop (e.g. solar thermal systems) and open loop (waste heat recovery) systems and compared with an organic Rankine cycle coupled with a vapour compression cycle as a benchmark. With a 95°C water heat source and LiBr solution working fluid, the proposed absorption system shows superior performance for all the parameters but the net power production efficiency with respect to heat source utilisation in power only regime, where the values were around 1.2% (exergy efficiency around 12%) and are nearly the same as the benchmark. Absorption cooling-only system on a closed-loop heat source between 95°C and 85°C provides a roughly double COP (0.79), while power consumption is maintained at similar or better values. Optimizing for heat source utilisation, the COP (0.14) was higher by more than one-third. In the power-only production regime, the absorption cycle has still a better performance with gross and net power efficiencies of 8.5% and 6.9%, though the difference against ORC is less than one percentage point. The exergy cycle efficiency is the highest in the power only regime with values of 47% and 39% (gross and net), while in the chiller regime the net value approaches zero due to parasitic load. The absorption chiller regime can, when compared to APC, utilise only a small fraction of the energy from the heat source owing to the limitation in cycle parameters such as evaporator temperature. The cycle efficiency is near its maximum (gross 9%), but the net utilisation efficiency is only around 0.68%.

A comparison of several salt solutions and water–ammonia mixture showed the best performance of LiBr and LiCl, but again, all salt solutions exhibited rather similar efficiency as well as COP. The water–ammonia mixture showed the worst performance in all but heat source utilisation efficiency of power production.

Lastly the power cycle with LiBr (and generally any salt solution) has, based on available literature, never been experimentally explored. This is regardless rather small difference from absorption chillers and in overall seemingly techni-

cally feasible and not too complicated configuration. Insufficient attention in the literature is also paid to the experimental investigation of the temperature glide in absorption systems' heat exchangers. First experimental verification of this concept would serve to verify theoretically predicted benefits of this concept and show potentially yet unforeseen obstacles. Therefore, an experimental study is performed in the second part of the thesis to better clarify application potential of this system.

Before the experimental works, a review is focused first on experimental and commercial Kalina cycle and related APC systems. One of the main conclusions is that plate heat exchangers are used for the components with supposed temperature glide phase change. Corrosion and sealing has shown to be one of major issues in long term operation of these system though. Review of components of absorption chillers, primarily with LiBr solution, shows, that the potential of temperature glide is often not pursued. Several unorthodox approaches exist such as use of vapour permeable membranes or flat plate heat exchanger desorber. Issues such as pressure drop limit currently its application and thus for the first proof of concept system such approach was disregarded. Special part of the review is focusing on additive technologies for turboexpanders. The reason is, that especially in case of low pressure water vapour and low temperatures, polymer materials with cost effective manufacturing technology can hold a key for efficient and cheap turbine, typically one of the costliest power cycle components.

Two experimental systems were designed and subsequently constructed for validation of LiBr APC concept. The first one was intended primarily for visualisation of two phase flow regime and measurement of the temperature glide during desorption (boiling). In preliminary tests with low pressure water, it has however shown that the flow regime was unsuitable for the salt APC and many sealing issues in the test rig were present. Following on that, a proof of concept APC unit has been designed and built, following some design features from absorption chillers to ensure successful operation. This is the first reported operation of a power cycle with a salt solution to the authors' knowledge. Experimental performance and results have shown the overall technical feasibility of the concept. With the heat source temperature below 90°C, the maximum gross electrical cycle efficiency reached 0.8% and about 150 W. However, with a state of the art turbo-expander, there is a potential for maximal cycle efficiencies of almost 5% and heat source utilisation efficiencies around 0.5% at the explored operating conditions. These values are rather comparable to ideal Rankine cycles analysed at the introduction of APC theoretical results.

A 3D printed plastic turbine has been operated in the system. Actual behaviour and parameters have shown several important aspects to consider

when designing APC systems with salt solution. The temperature glide in desorber has been achieved only at a much smaller extent than it was designed. Larger one was present in the absorber, but along with requirement of a significant subcooling of the liquid solution. This is regardless of achieving a large concentration difference of the working fluid. Desorber performance turned out better than predicted regarding heat transfer. The opposite was though the case of the absorber. Still, the desorber design has limited feasibility for WHR, where high temperature glide is required.

The development of the turboexpanders is documented in the last part of the thesis. Additive manufacturing (3D printing) can in conjunction with brushless motors as generators provide a very cost-effective solution. Here, by using this approach, the reported results are also among the first experimental verification of such concept's feasibility, which was applied to single stage impulse axial and radial turbines. A single stage axial air subsonic expander with the best geometrical configuration and using plastic flow path components of stator and rotor in as-printed state reached maximum efficiency of 35-40%. This is not very high, but follows well 1D design model, while providing large space for future optimization. This is as even the 1D design model was originally optimized for different configuration than finally investigated; future CFD optimization can reveal further possible improvements and so can do mechanical design improvements allowing higher rotational speeds.

In the APC operation with water low temperature superheated steam, the nylon expander with the generator have shown no damage to the components from the operation. It has been proven that the turbine is a suitable expander for APC with LiBr solution at very low power outputs. Lower than expected isentropic efficiency reaching about 25% can be significantly improved in future designs as perhaps less suitable flow section geometry and surface in as-printed state in high fluid velocities are among the reason for such performance. Significant improvement in performance can be also obtained with design allowing higher turbine speed, as vibrations prevented the APC expander to operate beyond 9 000 rpm, well below optimal velocity ratio (design point 15 000 rpm, theoretical optimum 30 000 rpm).

In summary, the concept of APC with salt solutions as LiBr was found to be until author's works aside of many researchers' interest, even though it provides many opportunities. Comprehensive theoretical investigation based mostly on pinch point analysis found its potential as superior for low temperature and distributed applications. Following on that, it has been proven experimentally as technically feasible in form of the world's first LiBr APC unit operating at the Czech Technical University in Prague. The theoretically most prospective application, WHR, proved however to underperform compared to the expectations with smaller and less suitable temperature glide. This is contrary to

common assumption in many theoretical studies and should be taken into account. Possibility of cost effective polymer additively manufactured turboexpanders has been suggested and also proven as technically feasible. Further engineering optimization beyond the presented proof of concept system gives potential for its high efficiency. The most feasible application now appears as turbine integration into LiBr absorption chillers for cogeneration APCC systems, analysed theoretically also in this thesis. Since the presented unit and its components have been built in a way to ensure successful operation, rather than the thermodynamically best possible performance, there are many aspects that can be improved now. For such tasks, this thesis can serve as starting point with solid fundamentals in field of salt solution APC, APCC as well as 3D printed turboexpanders for small distributed energy systems.

List of Figures

List of Tables

Bibliography

[1] M. Son, V. Novotny, H. Choi, Thin-film nanocomposite membrane with vertically embedded carbon nanotube for forward osmosis, Desalination and Water Treatment 57 (55) (2016) 26670–26679. doi:10.1080/19443994.2016.1190110.

[2] V. Novotný, J. Maščuch, Model of small family house with micro cogeneration unit, Vytapeni, Vetrani, Instalace 25 (1) (2016).

[3] J. Mascuch, V. Novotny, M. Tobias, Economic aspects of micro-cogeneration systems — Insight into investors' approaches, in: 2018 Smart City Symposium Prague (SCSP), IEEE, Prague, 2018, pp. 1–5. doi:10.1109/SCSP.2018.8402654.

[4] J. Mascuch, V. Novotny, V. Vodicka, Z. Zeleny, Towards development of 1-10 kW pilot ORC units operating with hexamethyldisiloxane and using rotary vane expander, Energy Procedia 129 (2017) 826–833. doi:10.1016/j.egypro.2017.09.196.

[5] J. Mascuch, V. Novotny, J. Spale, V. Vodicka, Z. Zeleny, Experience from set-up and pilot operation of an in-house developed biomass-fired ORC microcogeneration unit, Renewable Energy 165 (2021) 251–260. doi:10.1016/j.renene.2020.11.021.

[6] J. Mascuch, V. Novotny, V. Vodicka, J. Spale, Z. Zeleny, Experimental development of a kilowatt-scale biomass fired micro – CHP unit based on ORC with rotary vane expander, Renewable Energy 2882–2895doi:10.1016/j.renene.2018.08.113.

[7] V. Vodicka, V. Novotny, Z. Zeleny, J. Mascuch, M. Kolovratnik, Theoretical and experimental investigations on the radial and axial leakages within a rotary vane expander, Energy 189 (2019) 116097. doi:10.1016/J.ENERGY.2019.116097.

[8] V. Vodicka, V. Novotny, J. Mascuch, M. Kolovratnik, Impact of major leakages on characteristics of a rotary vane expander for ORC, Energy Procedia 129 (2017) 387–394. doi:10.1016/j.egypro.2017.09.249.

[9] V. Novotny, J. Spale, D. J. Szucs, H.-Y. Tsai, M. Kolovratnik, Direct integration of an organic rankine cycle into an internal combustion engine cooling system for comprehensive and simplified waste heat recovery, Energy Reports 7 (2021) 644–656, technologies and Materials for Renewable Energy, Environment and Sustainability. doi:https://doi.org/10.1016/j.egyr.2021.07.088.

[10] L. Vesely, V. Dostal, O. Bartos, V. Novotny, Pinch point analysis of heat exchangers for supercritical carbon dioxide with gaseous admixtures in CCS systems, Energy Procedia 86 (2016) 489–499. doi:10.1016/j.egypro.2016.01.050.

[11] V. Novotný, M. Vitvarová, Effect of different configurations of physical solvent based acid gas removal and CO2 capture for IGCC CCS power plants, in: M. Vesely, Z. Hrdlicka, J. Hanika, J. Lubojacky (Eds.), 4th International Conference on Chemical Technology, Mikulov, Czech Republic, Czech soc industrial chemistry, Mikulov, Czechia, 2016, pp. 308–314.

[12] S. Roussanaly, M. Vitvarova, R. Anantharaman, D. Berstad, B. Hagen, J. Jakobsen, V. Novotny, G. Skaugen, Techno-economic comparison of three technologies for pre-combustion CO 2 capture from a lignite-fired IGCC, Frontiers of Chemical Science and Engineering 14 (3) (2020) 436–452. doi:10.1007/s11705-019-1870-8.

[13] V. Novotny, V. Basta, P. Smola, J. Spale, Review of carnot battery technology commercial development, Energies 15 (2) (2022). doi:10.3390/en15020647.

[14] Vaclav Novotny, Miroslav Rathan, Jan Špale, Martin Hofman, Vít Bašta, Carnot Battery for industrial waste heat recovery application - case study, comprehensive modelling and considerations for a pilot installation, in: International Workshop on Carnot Batteries, Stuttgart, 2020.
URL https://www.researchgate.net/publication/344557176_Carnot_Battery_for_industrial_waste_heat_recovery_application_-_case_study_comprehensive_modelling_and_considerations_for_a_pilot_installation

[15] V. Novotny, Combined heat and power coal fired plants – the best choice of early grid-scale Carnot batteries applications, in: Enerstock 2021, Ljubljana, Slovenia, 2021.

[16] I. Johnson, T. William, W. T. Choate, A. Amber Davidson, BCS Inc., Waste Heat Recovery: Technology and Opportunities in U.S. Industry, U.S.

Department of Energy - Industrial Technologies Program (2008) 1–112. URL http://www1.eere.energy.gov/manufacturing/intensiveprocesses/pdfs/waste_heat_recovery.pdf

[17] U. Department of Energy, Chapter 6: Innovating Clean Energy Technologies in Advanced Manufacturing Technology Assessments Waste Heat Recovery Systems, Tech. rep., U.S. Department of Energy, Washington, DC, USA (2015).

[18] S. Brückner, S. Liu, L. Miró, M. Radspieler, L. F. Cabeza, E. Lävemann, Industrial waste heat recovery technologies: An economic analysis of heat transformation technologies, Applied Energy 151 (2015) 157–167. doi:10.1016/j.apenergy.2015.01.147.

[19] B. K. Saha, B. Chakraborty, R. Dutta, Estimation of waste heat and its recovery potential from energy-intensive industries, Clean Technologies and Environmental Policy 1 (2020) 3. doi:10.1007/s10098-020-01919-7.

[20] R. DiPippo, Geothermal power plants: principles, applications, case studies, and environmental impact, Butterworth-Heinemann, Oxford, UK, 2012.

[21] H. Zhai, Q. An, L. Shi, V. Lemort, S. Quoilin, Categorization and analysis of heat sources for organic rankine cycle systems, Renewable and Sustainable Energy Reviews 64 (2016) 790–805. doi:https://doi.org/10.1016/j.rser.2016.06.076.

[22] M. Yu, M. S. Gudjonsdottir, P. Valdimarsson, G. Saevarsdottir, Waste heat recovery from aluminum production, in: Minerals, Metals and Materials Series, Vol. Part F6, Springer International Publishing, 2018, pp. 165–178. doi:10.1007/978-3-319-72362-4_14.

[23] M. Nikolaisen, T. Andresen, System impact of heat exchanger pressure loss in ORCs for smelter off-gas waste heat recovery, Energy 215 (2021) 118956. doi:10.1016/j.energy.2020.118956.

[24] D. Ziviani, A. Beyene, M. Venturini, Advances and challenges in ORC systems modeling for low grade thermal energy recovery, Applied Energy 121 (2014) 79–95. doi:10.1016/j.apenergy.2014.01.074.

[25] E. Macchi, M. Astolfi, Organic Rankine Cycle (ORC) Power Systems: Technologies and Applications, Woodhead Publishing, 2016.

[26] T. Tartière, M. Astolfi, A World Overview of the Organic Rankine Cycle Market, Energy Procedia 129 (2017) 2–9. doi:10.1016/j.egypro.2017.09.159.

[27] C. W. Chan, J. Ling-Chin, A. P. Roskilly, A review of chemical heat pumps, thermodynamic cycles and thermal energy storage technologies for low grade heat utilisation, Applied thermal engineering 50 (1) (2013) 1257–1273. doi:10.1016/j.applthermaleng.2012.06.041.

[28] N. Rossi, Testing of a new supercritical ORC technology for efficient power generation from geothermal low temperature resources, in: ASME ORC 2013 Conference, ASME ORC Conference 2013, Rotterdam, Netherlands, 2013.
URL http://hdl.handle.net/11311/1048794

[29] F. Campana, M. Bianchi, L. Branchini, A. De Pascale, A. Peretto, M. Baresi, A. Fermi, N. Rossetti, R. Vescovo, ORC waste heat recovery in European energy intensive industries: Energy and GHG savings, Energy Conversion and Management 76 (2013) 244–252. doi:10.1016/j.enconman.2013.07.041.

[30] K. Bennett, Power Generation Potential from Coproduced Fluids i the Los Angeles Basin, Ph.D. thesis, Stanford University (2012).

[31] Department of Energy and Ormat Join to Validate Electricity Generation from Oil Field Heat, http://www.ormat.com/news/department-energy-and-ormat-join-validate-electricity-generation-oil-field-heat, accessed on 2015-09-24 (2007).
URL http://www.ormat.com/news/department-energy-and-ormat-join-validate-electricity-generation-oil-field-heat

[32] L. Pierobon, F. Haglind, Design and optimization of air bottoming cycles for waste heat recovery in off-shore platforms, Applied Energy 118 (2014) 156–165. doi:https://doi.org/10.1016/j.apenergy.2013.12.026.

[33] M. Bianchi, A. De Pascale, Bottoming cycles for electric energy generation: parametric investigation of available and innovative solutions for the exploitation of low and medium temperature heat sources, Applied Energy 88 (5) (2011) 1500–1509. doi:10.1016/j.apenergy.2010.11.013.

[34] D. Thombare, S. Verma, Technological development in the Stirling cycle engines, Renewable and Sustainable Energy Reviews 12 (1) (2008) 1–38. doi:10.1016/j.rser.2006.07.001.

[35] M. A. Iqbal, S. Rana, M. Ahmadi, A. Date, A. Akbarzadeh, Experimental study on the prospect of low-temperature heat to power generation using Trilateral Flash Cycle (TFC), Applied Thermal Engineering 172 (2020) 115139. doi:10.1016/j.applthermaleng.2020.115139.

[36] K. E. Herold, R. Radermacher, S. A. Klein, Absorption chillers and heat pumps, CRC press, 1996.

[37] J. Deng, R. Wang, G. Han, A review of thermally activated cooling technologies for combined cooling, heating and power systems, Progress in Energy and Combustion Science 37 (2) (2011) 172–203. doi:10.1016/j.pecs.2010.05.003.

[38] G. Demirkaya, Theoretical and experimental analysis of power and cooling cogeneration utilizing low temperature heat sources, Ph.D. thesis, University of South Florida, (2011).
URL http://scholarcommons.usf.edu/etd/3069/

[39] K. Yang, H. Zhang, Z. Wang, J. Zhang, F. Yang, E. Wang, B. Yao, Study of zeotropic mixtures of ORC (organic Rankine cycle) under engine various operating conditions, Energy 58 (2013) 494–510. doi:10.1016/j.energy.2013.04.074.

[40] J. D. Maloney, R. C. Robertson, Thermodynamic study of ammonia-water heat power cycles, Tech. rep., National Laboratory, Oak Ridge (1953).

[41] D. S. Ayou, J. C. Bruno, R. Saravanan, A. Coronas, An overview of combined absorption power and cooling cycles, Renewable and Sustainable Energy Reviews 21 (2013) 728–748. doi:10.1016/j.rser.2012.12.068.

[42] A. I. Kalina, Generation of energy by means of a working fluid, and regeneration of a working fluid (EU Patent, EP0065042A1, Nov 1982).
URL https://www.google.com/patents/EP0065042A1?cl=en

[43] A. I. Kalina, Method of generating energy (US Patent, US4548043A, Oct 1985).
URL https://patents.google.com/patent/US4548043A/en

[44] Global Geothermal, Advanced Waste Heat Engineering, Global Geothermal Limited, 2014, accessed on 2015-01-27.
URL http://www.wasabienergy.com/,http://www.globalgeothermal.com/

[45] X. Zhang, M. He, Y. Zhang, A review of research on the Kalina cycle, Renewable and Sustainable Energy Reviews 16 (7) (2012) 5309–5318. doi:10.1016/j.rser.2012.05.040.

[46] E. Rogdakis, P. Lolos, Kalina Cycles for Power Generation, in: Handbook of Clean Energy Systems, John Wiley & Sons, Ltd, Chichester, UK, 2015, pp. 1–25. doi:10.1002/9781118991978.hces014.

[47] O. M. Ibrahim, S. A. Klein, Absorption power cycles, Energy 21 (1) (1996) 21–27. doi:10.1016/0360-5442(95)00083-6.

[48] R. Shankar, T. Srinivas, Options In Kalina Cycle Systems, Energy Procedia 90 (2016) 260–266. doi:10.1016/j.egypro.2016.11.193.

[49] M. Jonsson, Advanced power cycles with mixture as the working fluid, Doctoral thesis (2003).

[50] Wasabi Energy, Corporate Overview & Update, Tech. Rep. June, accessed on 2015-09-24 (2011).
URL http://www.wasabienergy.com/Downloads/\WAS%20Corp%20pres%20June%202011.pdf

[51] Z. Guzović, B. Majcen, S. Cvetković, Possibilities of electricity generation in the Republic of Croatia from medium-temperature geothermal sources, Applied energy 98 (2012) 404–414. doi:10.1016/j.apenergy.2012.03.064.

[52] Z. Guzović, D. Lončar, N. Ferdelji, Possibilities of electricity generation in the Republic of Croatia by means of geothermal energy, Energy 35 (8) (2010) 3429–3440. doi:10.1016/j.energy.2010.04.036.

[53] S. E. Aly, A theoretical analysis of a solar-fuel assisted absorption power cycle (SFAPC), Heat Recovery Systems and CHP 8 (2) (1988) 149–156. doi:10.1016/0890-4332(88)90007-5.

[54] T. Ishida, S. Kawano, I. Kohtaka, K. Yamada, H. Kaku, T. Narita, Hybrid Rankine cycle system (US Patent, US5007240A, Apr 1991).
URL https://patents.google.com/patent/US5007240A/

[55] T. Ishida, S. Kawano, I. Kohtaka, K. Yamada, H. Kaku, T. Narita, Hybrid Rankine cycle system (EU Patent, EP0328103A1, Aug 1989).
URL https://patents.google.com/patent/EP0328103A1/

[56] V. E. Styliaras, A mixed cycle for converting heat to mechanical work, Heat Recovery Systems and CHP 15 (8) (1995) 749–753. doi:10.1016/0890-4332(94)00083-W.

[57] N. Garcia-Hernando, M. de Vega, A. Soria-Verdugo, S. Sanchez-Delgado, Energy and exergy analysis of an absorption power cycle, Applied Thermal Engineering 55 (1) (2013) 69–77. doi:10.1016/j.applthermaleng.2013.02.044.

[58] M. De Vega, J. A. Almendros-Ibáñez, G. Ruiz, Performance of a LiBr-water absorption chiller operating with plate heat exchangers, Energy conversion and management 47 (18) (2006) 3393–3407. doi:10.1016/j.enconman.2006.01.005.

[59] N. Shokati, F. Ranjbar, M. Yari, A comparative analysis of rankine and absorption power cycles from exergoeconomic viewpoint, Energy Conversion and Management 88 (2014) 657–668. doi:10.1016/j.enconman.2014.09.015.

[60] J. Mascuch, Economic perspectives of connecting microcogeneration nad plug-in hybrids in Czech household [Ekonomicke perspektivy spojeni mikrokogenerace a plug-in hybridu v ceske domacnosti], in: 11th conference on Power System Engineering, Thermodynamics & Fluid Flow - ES 2012, Srni, Czech Republic, 2012.

[61] R. S. Patil, S. S. Bhagwat, Thermodynamic analysis and optimisation of double effect absorption type combined power and cooling cycle using LiBr-water as working fluid, International Journal of Exergy 34 (2) (2021) 159–178. doi:10.1504/IJEX.2021.113003.

[62] S. Yosaf, H. Ozcan, Exergoeconomic investigation of flue gas driven ejector absorption power system integrated with PEM electrolyser for hydrogen generation, Energy 163 (2018) 88–99. doi:10.1016/j.energy.2018.08.033.

[63] H. Ozcan, S. Yosaf, Energy and exergy analysis of advanced absorption power cycles using salt-water mixtures as working fluids, Article in International Journal of Exergy 25 (3) (2018) 187–202. doi:10.1504/IJEX.2018.10011561.

[64] X. Li, D. Zheng, M. Zhang, L. Dong, Vapor–liquid equilibrium measurement of 1, 1, 1, 3, 3-pentafluoropropane+ N, N-dimethylformamide/diethylene glycol dimethyl ether/N-methyl-2-pyrrolidone working fluids for absorption power cycle, Fluid Phase Equilibria 366 (2014) 1–8. doi:10.1016/j.fluid.2014.01.007.

[65] T. Robbins, S. Garimella, Low-Grade Waste Heat Recovery for Power Production using an Absorption-Rankine Cycle, in: International Refrigeration and Air Conditioning Conference, no. Paper 1157, Purdue, USA, 2010.
URL https://docs.lib.purdue.edu/iracc/1157/

[66] T. Eller, F. Heberle, D. Brüggemann, Second law analysis of novel working fluid pairs for waste heat recovery by the Kalina cycle, Energy 119 (2017) 188–198. doi:10.1016/j.energy.2016.12.081.

[67] D. W. Wu, R. Z. Wang, Combined cooling, heating and power: A review, Progress in Energy and Combustion Science 32 (5-6) (2006) 459–495. doi:10.1016/j.pecs.2006.02.001.

[68] J. Wang, Z. Han, Z. Guan, Hybrid solar-assisted combined cooling, heating, and power systems: A review (nov 2020). doi:10.1016/j.rser.2020.110256.

[69] M. Wegener, A. Malmquist, A. Isalgué, A. Martin, Biomass-fired combined cooling, heating and power for small scale applications – A review (nov 2018). doi:10.1016/j.rser.2018.07.044.

[70] D. S. Ayou, J. C. Bruno, A. Coronas, Combined absorption power and refrigeration cycles using low- and mid-grade heat sources, Science and Technology for the Built Environment 21 (7) (2015) 934–943. doi:10.1080/23744731.2015.1025681.

[71] G. Demirkaya, R. V. Padilla, D. Y. Goswami, A review of combined power and cooling cycles, Wiley Interdisciplinary Reviews: Energy and Environment 2 (5) (2013) 534–547. doi:10.1002/wene.75.

[72] J. Demierre, D. Favrat, J. Schiffmann, J. Wegele, Experimental investigation of a Thermally Driven Heat Pump based on a double Organic Rankine Cycle and an oil-free Compressor-Turbine Unit, International Journal of Refrigeration 44 (2014) 91–100. doi:10.1016/j.ijrefrig.2014.04.024.

[73] J. Rashidi, P. Ifaei, I. J. Esfahani, A. Ataei, C. K. Yoo, Thermodynamic and economic studies of two new high efficient power-cooling cogeneration systems based on Kalina and absorption refrigeration cycles, Energy Conversion and Management 127 (2016) 170–186. doi:10.1016/J.ENCONMAN.2016.09.014.

[74] A. C. Oliveira, C. Afonso, J. Matos, S. Riffat, M. Nguyen, P. Doherty, A combined heat and power system for buildings driven by solar energy and gas, Applied Thermal Engineering 22 (6) (2002) 587–593. doi:10.1016/S1359-4311(01)00110-7.

[75] H. Cho, A. D. Smith, P. Mago, Combined cooling, heating and power: A review of performance improvement and optimization, Applied Energy 136 (2014) 168–185. doi:10.1016/j.apenergy.2014.08.107.

[76] P. Ahmadi, I. Dincer, M. A. Rosen, Exergo-environmental analysis of an integrated organic Rankine cycle for trigeneration, Energy Conversion and Management 64 (2012) 447–453. doi:10.1016/j.enconman.2012.06.001.

[77] N. Chaiyat, T. Kiatsiriroat, Analysis of combined cooling heating and power generation from organic Rankine cycle and absorption system, Energy 91 (2015) 363–370. doi:10.1016/j.energy.2015.08.057.

[78] P. Kumar, O. Singh, Thermoeconomic analysis of SOFC-GT-VARS-ORC combined power and cooling system, International Journal of Hydrogen Energy 44 (50) (2019) 27575–27586. doi:10.1016/j.ijhydene.2019.08.198.

[79] J. Rashidi, C. K. Yoo, Exergetic and exergoeconomic studies of two highly efficient power-cooling cogeneration systems based on the Kalina and absorption refrigeration cycles, Applied Thermal Engineering 124 (2017) 1023–1037. doi:10.1016/J.APPLTHERMALENG.2017.05.195.

[80] D. Prigmore, R. Barber, Cooling with the sun's heat Design considerations and test data for a Rankine Cycle prototype, Solar Energy 17 (3) (1975) 185–192. doi:10.1016/0038-092X(75)90058-4.

[81] H. Wang, R. Peterson, K. Harada, E. Miller, R. Ingram-Goble, L. Fisher, J. Yih, C. Ward, Performance of a combined organic Rankine cycle and vapor compression cycle for heat activated cooling, Energy 36 (1) (2011) 447–458. doi:10.1016/j.energy.2010.10.020.

[82] B. Patel, N. B. Desai, S. S. Kachhwaha, V. Jain, N. Hadia, Thermo-economic analysis of a novel organic Rankine cycle integrated cascaded vapor compression–absorption system, Journal of Cleaner Production 154 (2017) 26–40. doi:10.1016/j.jclepro.2017.03.220.

[83] C. Kutlu, M. T. Erdinc, J. Li, Y. Wang, Y. Su, A study on heat storage sizing and flow control for a domestic scale solar-powered organic Rankine cycle-vapour compression refrigeration system, Renewable Energy 143 (2019) 301–312. doi:10.1016/j.renene.2019.05.017.

[84] S. Aphornratana, T. Sriveerakul, Analysis of a combined Rankine-vapour-compression refrigeration cycle, Energy Conversion and Management 51 (12) (2010) 2557–2564. doi:10.1016/j.enconman.2010.04.016.

[85] J. Wang, Y. Dai, Z. Sun, A theoretical study on a novel combined power and ejector refrigeration cycle, International Journal of Refrigeration 32 (6) (2009) 1186–1194. doi:10.1016/j.ijrefrig.2009.01.021.

[86] A. Habibzadeh, M. M. Rashidi, N. Galanis, Analysis of a combined power and ejector-refrigeration cycle using low temperature heat, Energy Conversion and Management 65 (2013) 381–391. doi:10.1016/j.enconman.2012.08.020.

[87] X. Yang, L. Zhao, H. Li, Z. Yu, Theoretical analysis of a combined power and ejector refrigeration cycle using zeotropic mixture, Applied Energy 160 (2015) 912–919. doi:10.1016/j.apenergy.2015.05.001.

[88] X. Yang, N. Zheng, L. Zhao, S. Deng, H. Li, Z. Yu, Analysis of a novel combined power and ejector-refrigeration cycle, Energy Conversion and Management 108 (2016) 266–274. doi:10.1016/j.enconman.2015.11.019.

[89] M. Sadeghi, M. Yari, S. M. Mahmoudi, M. Jafari, Thermodynamic analysis and optimization of a novel combined power and ejector refrigeration cycle – Desalination system, Applied Energy 208 (2017) 239–251. doi:10.1016/j.apenergy.2017.10.047.

[90] H. Ghaebi, H. Rostamzadeh, P. S. Matin, Performance evaluation of ejector expansion combined cooling and power cycles, Heat and Mass

Transfer/Waerme- und Stoffuebertragung 53 (9) (2017) 2915–2931. doi:10.1007/s00231-017-2034-3.

[91] F. Xu, D. Yogi Goswami, S. S. Bhagwat, A combined power/cooling cycle, Energy 25 (3) (2000) 233–246. doi:10.1016/S0360-5442(99)00071-7.

[92] G. Demirkaya, R. Padilla, A. Fontalvo, M. Lake, Y. Lim, Thermal and Exergetic Analysis of the Goswami Cycle Integrated with Mid-Grade Heat Sources, Entropy 19 (8) (2017) 416. doi:10.3390/e19080416.

[93] A. A. Hasan, D. Y. Goswami, S. Vijayaraghavan, First and second law analysis of a new power and refrigeration thermodynamic cycle using a solar heat source, Solar Energy 73 (5) (2002) 385–393. doi:10.1016/S0038-092X(02)00113-5.

[94] Rankine Engine, MicroCHP, accessed on 2015-04-08.
URL http://microchap.info/rankine%5C_engine.htmhttp://microchap.info/rankine_engine.htm

[95] C. Martin, D. Y. Goswami, Effectiveness of cooling production with a combined power and cooling thermodynamic cycle, Applied Thermal Engineering 26 (5-6) (2006) 576–582. doi:10.1016/j.applthermaleng.2005.07.007.

[96] A. Fontalvo, H. Pinzon, J. Duarte, A. Bula, A. G. Quiroga, R. V. Padilla, Exergy analysis of a combined power and cooling cycle, Applied Thermal Engineering 60 (1-2) (2013) 164–171. doi:10.1016/j.applthermaleng.2013.06.034.

[97] R. V. Padilla, G. Demirkaya, D. Y. Goswami, E. Stefanakos, M. M. Rahman, Analysis of power and cooling cogeneration using ammonia-water mixture, Energy 35 (12) (2010) 4649–4657. doi:10.1016/j.energy.2010.09.042.

[98] G. Demirkaya, R. Vasquez Padilla, D. Y. Goswami, E. Stefanakos, M. M. Rahman, Analysis of a combined power and cooling cycle for low-grade heat sources, International Journal of Energy Research 35 (13) (2011) 1145–1157. doi:10.1002/er.1750.

[99] S. Vijayaraghavan, D. Y. Goswami, A combined power and cooling cycle modified to improve resource utilization efficiency using a distillation stage, Energy 31 (8) (2006) 1177–1196. doi:10.1016/j.energy.2005.04.014.

[100] S. M. Sadrameli, D. Y. Goswami, Optimum operating conditions for a combined power and cooling thermodynamic cycle, Applied Energy 84 (3) (2007) 254–265. doi:10.1016/j.apenergy.2006.08.003.

[101] H. Chen, D. Y. Goswami, Simulation of a Thermodynamic Cycle with Organic Absorbents and CO2 as a Working Fluid, in: The 2008 AIChE Annual Meeting, Philadelphia, PA, USA.
URL https://folk.ntnu.no/skoge/prost/proceedings/aiche-2008/data/papers/P135631

[102] S. Vijayaraghavan, D. Y. Goswami, Organic working fluids for a combined power and cooling cycle, Journal of Energy Resources Technology 127 (2) (2005) 125–130. doi:10.1115/1.1885039.

[103] G. Demirkaya, R. V. Padilla, A. Fontalvo, A. Bula, D. Y. Goswami, Experimental and Theoretical Analysis of the Goswami Cycle Operating at Low Temperature Heat Sources, Journal of Energy Resources Technology 140 (7) (2018) 072005. doi:10.1115/1.4039376.

[104] G. Tamm, D. Y. Goswami, Novel combined power and cooling thermodynamic cycle for low temperature heat sources, part II: Experimental investigation, Journal of Solar Energy Engineering, Transactions of the ASME 125 (2) (2003) 223–229. doi:10.1115/1.1564080.

[105] J. Muye, D. S. Ayou, R. Saravanan, A. Coronas, Performance study of a solar absorption power-cooling system, Applied Thermal Engineering 97 (2016) 59–67. doi:10.1016/j.applthermaleng.2015.09.034.

[106] R. Shankar, T. Srinivas, Performance investigation of Kalina cooling cogeneration cycles, International Journal of Refrigeration 86 (2018) 163–185. doi:10.1016/J.IJREFRIG.2017.11.019.

[107] R. Shankar, T. Srinivas, Development and analysis of a new integrated power and cooling plant using LiBr–H2O mixture, Sadhana - Academy Proceedings in Engineering Sciences 39 (6) (2014) 1547–1562. doi:10.1007/s12046-014-0277-y.

[108] W. Rivera, K. Sánchez-Sánchez, J. A. Hernández-Magallanes, J. C. Jiménez-García, A. Pacheco, Modeling of Novel Thermodynamic Cycles to Produce Power and Cooling Simultaneously, Processes 8 (3) (2020) 320. doi:10.3390/pr8030320.

[109] D. C. Erickson, G. Anand, I. Kyung, Heat-Activated Dual-Function Absorption Cycle, ASHRAE Transactions: Symposia 110 (1) (2004) 515–524.

[110] C. P. Jawahar, R. Saravanan, J. C. Bruno, A. Coronas, Simulation studies on gax based Kalina cycle for both power and cooling applications, in: Applied Thermal Engineering, Vol. 50, Pergamon, 2013, pp. 1522–1529. doi:10.1016/j.applthermaleng.2011.11.004.

[111] G. Praveen Kumar, R. Saravanan, A. Coronas, Experimental studies on combined cooling and power system driven by low-grade heat sources, Energy 128 (2017) 801–812. doi:10.1016/j.energy.2017.04.066.

[112] J. López-Villada, D. S. Ayou, J. C. Bruno, A. Coronas, Modelling, simulation and analysis of solar absorption power-cooling systems, International Journal of Refrigeration 39 (2014) 125–136. doi:10.1016/j.ijrefrig.2013.11.004.

[113] C. F. Okwose, M. Abid, T. A. Ratlamwala, Performance analysis of compressor-assisted two-stage triple effect absorption refrigeration cycle for power and cooling, Energy Conversion and Management 227 (2021) 113547. doi:10.1016/j.enconman.2020.113547.

[114] N. Shokati, F. Ranjbar, M. Yari, A comprehensive exergoeconomic analysis of absorption power and cooling cogeneration cycles based on Kalina, part 1: Simulation, Energy Conversion and Management 158 (2018) 437–459. doi:10.1016/J.ENCONMAN.2017.12.086.

[115] R. Ventas, A. Lecuona, C. Vereda, M. Rodriguez-Hidalgo, Performance analysis of an absorption double-effect cycle for power and cold generation using ammonia/lithium nitrate, Applied Thermal Engineering 115 (2017) 256–266. doi:10.1016/J.APPLTHERMALENG.2016.12.102.

[116] J. Wang, Y. Dai, L. Gao, Parametric analysis and optimization for a combined power and refrigeration cycle, Applied Energy 85 (11) (2008) 1071–1085. doi:10.1016/j.apenergy.2008.02.014.

[117] N. Zhang, R. Cai, N. Lior, A Novel Ammonia-Water Cycle for Power and Refrigeration Cogeneration, in: Advanced Energy Systems, Vol. 2004, ASME, 2004, pp. 183–196. doi:10.1115/IMECE2004-60692.

[118] N. Zhang, N. Lior, Methodology for thermal design of novel combined refrigeration/power binary fluid systems, International Journal of Refrigeration 30 (6) (2007) 1072–1085. doi:10.1016/j.ijrefrig.2006.12.005.

[119] T. Parikhani, H. Ghaebi, H. Rostamzadeh, A novel geothermal combined cooling and power cycle based on the absorption power cycle: Energy, exergy and exergoeconomic analysis, Energy 153 (2018) 265–277. doi:10.1016/j.energy.2018.01.153.

[120] R. Younès, H. Zeidan, H. Harb, A. Ghaddar, Optimal design and economical study for solar air-conditioning by absorption chillers, in: International IIR Conference on Latest Development in Refrigerated Storage, Transportation and Display of Food Products, 2005.

[121] W. Weiss, M. Spörk-Dür, Solar Heat Worldwide. Global Market Development and Trends in 2018. Detailed Market Figures 2017., AEE–Institute for Sustainable Technologies, Gleisdorf, Austria (2019).
URL https://www.iea-shc.org/Data/Sites/1/publications/Solar-Heat-Worldwide-2019.pdf

[122] D. Zheng, L. Dong, W. Huang, X. Wu, N. Nie, A review of imidazolium ionic liquids research and development towards working pair of absorption cycle, Renewable and Sustainable Energy Reviews 37 (2014) 47–68. doi:10.1016/j.rser.2014.04.046.

[123] O. M. Ibrahim, S. A. Klein, Thermodynamic properties of ammonia-water mixtures, Transactions-American Society of Heating Refrigerating and Air Conditioning Engineers 99 (1993) 1495.

[124] R. Tillner-Roth, D. G. Friend, Survey and assessment of available measurements on thermodynamic properties of the mixture water+ ammonia, Journal of physical and chemical reference data 27 (1) (1998) 45–61. doi:10.1063/1.556014.

[125] E. J. Roehl, Applications of Dühring's Rule, Industrial & Engineering Chemistry 30 (11) (1938) 1320–1322.

[126] D. S. Kim, C. A. I. Ferreira, A Gibbs Energy Equation for LiBr/H2O Solutions, in: Proceedings of the 6th IIR Gustav Lorentzen Conference on Natural Working Fluids, Glasgow (UK), 2004.

[127] J. Patek, J. Klomfar, A computationally effective formulation of the thermodynamic properties of LiBr–H2O solutions from 273 to 500K over full composition range, International Journal of Refrigeration 29 (4) (2006) 566–578. doi:10.1016/j.ijrefrig.2005.10.007.

[128] H.-J. Kretzschmar, I. Stoecker, M. Kunick, S. Hasch, Property Library for Mixtures of Water/Lithium Bromide FluidEES with LibWaLi for Engineering Equation Solver (2011).
URL http://thermodynamik.hszigr.de/cmsfg/_data/FluidEES_LibWaLi_Docu_Eng.pdf

[129] Z. Yuan, K. E. Herold, Thermodynamic properties of aqueous lithium bromide using a multiproperty free energy correlation, HVAC&R Research 11 (3) (2005) 377–393. doi:10.1080/10789669.2005.10391144.

[130] W. Rivera, R. J. Romero, M. J. Cardoso, J. Aguillón, R. Best, Theoretical and experimental comparison of the performance of a single-stage heat transformer operating with water/lithium bromide and water/Carrol, International journal of energy research 26 (8) (2002) 747–762. doi:doi.org/10.1002/er.813.

[131] J. Pátek, J. Klomfar, Thermodynamic properties of the LiCl-H2O system at vapor-liquid equilibrium from 273K to 400K, international journal of refrigeration 31 (2) (2008) 287–303. doi:10.1016/j.ijrefrig.2007.05.003.

[132] M. R. Conde, Properties of aqueous solutions of lithium and calcium chlorides: formulations for use in air conditioning equipment design, International Journal of Thermal Sciences 43 (4) (2004) 367–382.

[133] X. Li, D. Zheng, Y. Shen, X. Meng, B. Li, Vapor–liquid equilibria of difluoromethane+ N, N-dimethylacetamide, difluoromethane+ dimethylether diethylene glycol and 1, 1-difluoroethane+ dimethylether diethylene glycol systems, Fluid Phase Equilibria 347 (2013) 15–21. doi:10.1016/j.fluid.2013.03.009.

[134] J. O. Valderrama, P. A. Robles, Critical properties, normal boiling temperatures, and acentric factors of fifty ionic liquids, Industrial and Engineering Chemistry Research 46 (4) (2007) 1338–1344. doi:10.1021/ie0603058.

[135] M. Seiler, C. Jork, W. Schneider, W. Arlt, Ionic liquids and hyperbranched polymers–Promissing new classes of selective entrainers for extractive distillation, in: International Conference on Distillation & Absorption, Dusseldorf, Germany, 2002.

[136] D. Mirolli, Kalina cycle power systems in waste heat recovery applications, Global Cement Magazine (2012).

[137] Wasabi Energy Limited, ASX Announcement - Wasabi Energy Achieves Start-Up of First Kalina Cycle AcoGen Unit at a Japanese Hot Spring, Tech. rep., accessed on 2015-09-24 (2012).
URL https://www.yumpu.com/en/document/read/4665733/announcement-wasabi-energy

[138] H. Leibowitz, M. Mirolli, First Kalina combined-cycle, Power Engineering, accessed on 2021-12-05 (1997).
URL https://www.power-eng.com/coal/first-kalina-combined-cycle/#gref

[139] S. Macwan, THE KALINA CYCLE® A Major Breakthrough in Efficient Heat to Power Generation, in: CHP2013 & WHP2013 Conference and Trade Show, 2013, accessed on 2021-12-05.
URL https://docplayer.net/50320875-The-kalina-cycle-a-major-breakthrough-in-efficient-heat-to-power-generation-presented-by-sunil-macwan.html

[140] H. Mlcak, M. Mirolli, H. Hjartarson, M. Ralph, Notes from the North: a Report on the Debut Year of the 2 MW Kalina Cycle® Geothermal

Power Plant in Húsavík, Iceland, TRANSACTIONS-GEOTHERMAL RESOURCES COUNCIL (2002) 715–718.

[141] R. Maack, P. Valdimarsson, Operating experience with Kalina power plants, VDI BERICHTE 1703 (2002) 107–116.

[142] P. Whittaker, Corrosion in the Kalina cycle An investigation into corrosion problems at the Kalina cycle geothermal power plant in Húsavík, Iceland, Ph.D. thesis, University of Iceland & the University of Akureyri (2009).
URL https://skemman.is/bitstream/1946/7042/1/Peter_Whittaker.pdf

[143] Tender sale of up to 3.4 MWe Kalina geothermal power plant technology of Unterhaching — ThinkGeoEnergy - Geothermal Energy News.
URL https://www.thinkgeoenergy.com/tender-sale-of-up-to-3-4-mwe-kalina-geothermal-power-plant-technology-of-unterhaching/

[144] Api schmidt bretten - plate heat exchangers, accessed on 2015-12-23.
URL http://www.powertechnology.com/contractors/cooling/api-schmidt-bretten/

[145] KALINA, Electricity from heat, Technology, accessed on 2016-04-24.
URL http://www.kalinapower.com/technology/

[146] Wasabi Energy Limited, ASX Announcement - Wasabi Energy Provides Update on Significant Kalina Cycle Related Activities &Development from Asia, Tech. rep., Melbourne, Australia, accessed on 2015-09-24 (2011).
URL https://www.asx.com.au/asxpdf/20110415/pdf/41y27tgxz9nlcv.pdf

[147] G. O. Tamm, Experimental investigation of an ammonia-based combined power and cooling cycle, Ph.D. thesis, UNIVERSITY OF FLORIDA (2003).

[148] C. Martin, Study of cooling production with a combined power and cooling thermodynamic cycle, Ph.D. thesis, University of Florida (2004).

[149] J. Ibarra-Bahena, R. J. Romero, Performance of Different Experimental Absorber Designs in Absorption Heat Pump Cycle Technologies: A Review, Energies 7 (2) (2014) 751–766. doi:10.3390/en7020751.

[150] W. A. Miller, The Experimental Analysis of Aqueous Lithium Bromide Vertical Film Absorption, Ph.D. thesis, The University of Tennessee, Knoxville (1998).
URL http://trace.tennessee.edu/utk_graddiss/1606

[151] F. Ragazzi, C. O. Pedersen, Thermodynamic optimization of evaporators with zeotropic refrigerant mixtures, in: 1996 annual meeting of the ASHRAE, San Antonio, TX (United States), 22-26 Jun 1996; Part Of ASHRAE transactions 1996: Volume 102, Part 2; PB: 836 p., no. April, Air Conditioning and Refrigeration Center. College of Engineering. University of Illinois at Urbana-Champaign., Atlanta, GA (United States), 1995.

[152] L. Zhao, Y. Zhu, X. Wang, J. Han, Heat transfer pinch point of zeotropic refrigerants in condenser with air-conditioning operation, Journal of chemical industry and engineering-China 58 (10) (2007) 2450.

[153] W. Mulroy, P. A. Domanski, D. Didion, Glide matching with binary and ternary zeotropic refrigerant mixtures Part 1. An experimental study, International Journal of Refrigeration 17 (4) (1994) 220–225. doi:10.1016/0140-7007(94)90037-X.

[154] M. Belghazi, A. Bontemps, J. C. Signe, C. Marvillet, Condensation heat transfer of a pure fluid and binary mixture outside a bundle of smooth horizontal tubes. Comparison of experimental results and a classical model, International journal of refrigeration 24 (8) (2001) 841–855. doi:10.1016/S0140-7007(00)00037-2.

[155] J. H. Kim, J. M. Cho, M. S. Kim, Cooling performance of several CO2/propane mixtures and glide matching with secondary heat transfer fluid, International Journal of Refrigeration 31 (5) (2008) 800–806. doi:10.1016/j.ijrefrig.2007.11.009.

[156] H. Khemani, Water-Lithium Bromide Vapor Absorption Refrigeration System, accessed on 2021-12-05 (2014).
URL http://www.brighthubengineering.com/hvac/66301-water-lithium-bromide-vapor-absorption-refrigeration-system/

[157] R. Nasr Isfahani, S. Moghaddam, R. N. Isfahani, S. Moghaddam, R. Nasr Isfahani, S. Moghaddam, Absorption characteristics of lithium bromide (LiBr) solution constrained by superhydrophobic nanofibrous structures, International Journal of Heat and Mass Transfer 63 (2013) 82–90. doi:10.1016/j.ijheatmasstransfer.2013.03.053.

[158] B. Michel, N. Le Pierrès, B. Stutz, Performances of grooved plates falling film absorber, Energy 138 (2017) 103–117. doi:10.1016/j.energy.2017.07.026.

[159] M. Mortazavi, R. Nasr Isfahani, S. Bigham, S. Moghaddam, Absorption characteristics of falling film LiBr (lithium bromide) solution over a finned structure, Energy 87 (2015) 270–278. doi:10.1016/J.ENERGY.2015.04.074.

[160] J. Olarte-Cortés, J. Torres-Merino, J. Siqueiros, Experimental study of a graphite disks absorber couple to a heat transformer, Experimental Thermal and Fluid Science 46 (2013) 29–36. doi:10.1016/j.expthermflusci.2012.11.013.

[161] N. García-Hernando, J. A. Almendros-Ibáñez, G. Ruiz, M. de Vega, On the pressure drop in Plate Heat Exchangers used as desorbers in absorption chillers, Energy Conversion and Management 52 (2) (2011) 1520–1525. doi:10.1016/J.ENCONMAN.2010.10.020.

[162] J. D. Marcos, M. Izquierdo, R. Lizarte, E. Palacios, C. A. Infante Ferreira, Experimental boiling heat transfer coefficients in the high temperature generator of a double effect absorption machine for the lithium bromide/water mixture, International Journal of Refrigeration 32 (4) (2009) 627–637. doi:10.1016/j.ijrefrig.2009.02.003.

[163] A. H. H. Ali, P. Schwerdt, Characteristics of the membrane utilized in a compact absorber for lithium bromide–water absorption chillers, International Journal of Refrigeration 32 (8) (2009) 1886–1896. doi:10.1016/j.ijrefrig.2009.07.009.

[164] R. Nasr Isfahani, A. Fazeli, S. Bigham, S. Moghaddam, R. N. Isfahani, A. Fazeli, S. Bigham, S. Moghaddam, Physics of lithium bromide (LiBr) solution dewatering through vapor venting membranes, International Journal of Multiphase Flow 58 (2014) 27–38. doi:10.1016/j.ijmultiphaseflow.2013.08.005.

[165] N. Garcia-Hernando, M. de Vega, M. Venegas, U. Ruiz-Rivas, Microabsorption chiller components based on membrane technology, in: Energy & Materials Research Conference - EMR2015, 2015.

[166] Project completion summary, Cooler homes from solar powered mini-chillers, accessed on 2016-06-30.
URL https://www.eon.com/content/dam/eon-com/ueber-uns/innovation/research_initiatives/SolarCool_PCS_EIRI_12458_131205.pdf

[167] R. Nasr Isfahani, K. Sampath, S. Moghaddam, R. N. Isfahani, K. Sampath, S. Moghaddam, Nanofibrous membrane-based absorption refrigeration system, International Journal of Refrigeration 36 (8) (2013) 2297–2307. doi:10.1016/j.ijrefrig.2013.07.019.

[168] H. Lazalde-Crabtree, Design approach of steam-water separators and steam dryers for geothermal applications, Geothermal Resource Concil Bulletin 13 (8) (1984) 11–20.

[169] Z. Zeleny, V. Vodicka, V. Novotny, J. Mascuch, Gear pump for low power output ORC – an efficiency analysis, Energy Procedia 129 (2017) 1002–1009. doi:10.1016/j.egypro.2017.09.227.

[170] M. Imran, M. Usman, B.-S. Park, D.-H. Lee, Volumetric expanders for low grade heat and waste heat recovery applications, Renewable and Sustainable Energy Reviews 57 (2016) 1090–1109. doi:10.1016/J.RSER.2015.12.139.

[171] S. Quoilin, M. V. D. Broek, S. Declaye, P. Dewallef, V. Lemort, Techno-economic survey of Organic Rankine Cycle (ORC) systems, Renewable and Sustainable Energy Reviews 22 (2013) 168–186. doi:10.1016/j.rser.2013.01.028.

[172] A. P. Weiß, Volumetric Expander Versus Turbine – Which Is the Better Choice for Small Orc Plants, in: 3rd International Seminar on ORC Power Systems, October 12-14, 2015, Brussels, Belgium, 2015, pp. 1–10.

[173] S. H. Kang, Design and experimental study of ORC (organic Rankine cycle) and radial turbine using R245fa working fluid, Energy 41 (1) (2012) 514–524. doi:10.1016/j.energy.2012.02.035.

[174] M. Pini, C. De Servi, M. Burigana, S. Bahamonde, A. Rubino, S. Vitale, P. Colonna, Fluid-dynamic design and characterization of a mini-ORC turbine for laboratory experiments, Energy Procedia 129 (2017) 1141–1148. doi:10.1016/J.EGYPRO.2017.09.186.

[175] D. Fiaschi, G. Manfrida, F. Maraschiello, Thermo-fluid dynamics preliminary design of turbo-expanders for ORC cycles, Applied Energy 97 (2012) 601–608. doi:10.1016/J.APENERGY.2012.02.033.

[176] D. Fiaschi, G. Manfrida, F. Maraschiello, Design and performance prediction of radial ORC turboexpanders, Applied Energy 138 (2015) 517–532. doi:10.1016/J.APENERGY.2014.10.052.

[177] F. Alshammari, A. Karvountzis-Kontakiotis, A. Pesiridis, T. Minton, Radial Expander Design for an Engine Organic Rankine Cycle Waste Heat Recovery System, Energy Procedia 129 (2017) 285–292. doi:10.1016/J.EGYPRO.2017.09.155.

[178] A. P. Weiss, G. Zinn, Micro Turbine Generators For Waste Heat Recovery And Compressed Air Energy Storage, in: 15th conference on Power System Engineering, Thermodynamics & Fluid Flow - ES 2016, Pilsen, 2016, pp. 1–9.

[179] A. P. Weiß., T. Popp, G. Zinn, M. Preißinger, D. Brüggemann, A Micro-Turbine-Generator-Construction-Kit (MTG-c-kit) for Small-Scale Waste Heat Recovery ORC-plants, in: Heat Power Cycles Conference, University of Bayreuth, 2018.

[180] G. Żywica, T. Kaczmarczyk, E. Ihnatowicz, P. Bagiński, A. Andrearczyk, Design and manufacturing of micro-turbomachinery components with application of heat resistant plastics, Mechanics and Mechanical Engineering Vol. 22 (nr 2) (2018). doi:10.2478/mme-2018-0051.

[181] G. Zywica, T. Z. Kaczmarczyk, E. Ihnatowicz, P. Baginski, A. Andrearczyk, APPLICATION OF A HEAT RESISTANT PLASTIC IN A HIGH-SPEED MICROTURBINE DESIGNED FOR THE DOMESTIC ORC SYSTEM, in: 5th International Seminar on ORC Power Systems, 2019.

[182] J. R. Tumbleston, D. Shirvanyants, N. Ermoshkin, R. Janusziewicz, A. R. Johnson, D. Kelly, K. Chen, R. Pinschmidt, J. P. Rolland, A. Ermoshkin, E. T. Samulski, J. M. DeSimone, Continuous liquid interface production of 3D objects, Science 347 (6228) (2015) 1349–1352. doi:10.1126/science.aaa2397.

[183] R. Janusziewicz, J. R. Tumbleston, A. L. Quintanilla, S. J. Mecham, J. M. DeSimone, Layerless fabrication with continuous liquid interface production., Proceedings of the National Academy of Sciences of the United States of America 113 (42) (2016) 11703–11708. doi:10.1073/pnas.1605271113.

[184] K. Rahbar, S. Mahmoud, R. K. Al-Dadah, N. Moazami, S. A. Mirhadizadeh, Development and experimental study of a small-scale compressed air radial inflow turbine for distributed power generation, Applied Thermal Engineering 116 (2017) 549–583. doi:10.1016/j.applthermaleng.2017.01.100.

[185] M. Meier, W. Gooding, J. Fabian, N. L. Key, Considerations for Using Additive Manufacturing Technology in Centrifugal Compressor Research, Journal of Engineering for Gas Turbines and Power (2019) 1–10doi:10.1115/1.4044937.

[186] I. Hernandez-Carrillo, C. Wood, H. Liu, Development of a 1000 W organic Rankine cycle micro-turbine-generator using polymeric structural materials and its performance test with compressed air, Energy Conversion and Management 190 (2019) 105–120. doi:10.1016/j.enconman.2019.03.092.

[187] I. Hernandez-Carrillo, C. J. Wood, H. Liu, Advanced materials for the impeller in an ORC radial microturbine, Energy Procedia 129 (2017) 1047–1054. doi:10.1016/j.egypro.2017.09.241.

[188] I. Hernandez, H. Liu, C. Wood, Advanced Materials for the Impeller in an ORC radial micro-turbine (presentation), in: ORC 2017, Milano, 2017. URL http://www.orc2017.com/uploads/File/Presentations/11.pdf

[189] J. E. Grady, W. J. Haller, P. E. Poinsatte, M. C. Halbig, S. L. Schnulo, D. Weir, N. Wali, M. Vinup, M. G. Jones, C. Patterson, T. Santelle, J. Mehl, A Fully Nonmetallic Gas Turbine Engine Enabled by Additive Manufacturing Part I : System Analysis , Component Identifi cation , Additive Manufacturing , and Testing of Polymer Composites, Tech. Rep. May, National Aeronautics and Space Administration, Glenn Research Center Cleveland, Ohio 44135 (2015). doi:NASA/TMâĂŤ2015-218748.

[190] K. C. Chuang, J. E. Grady, S. M. Arnold, R. D. Draper, E. Shin, C. Patterson, T. Santelle, R. Prototyping+manufacturing, C. Lao, M. Rhein, J. Mehl, A Fully Nonmetallic Gas Turbine Engine Enabled by Additive Manufacturing Part II: Additive Manufacturing and Characterization of Polymer Composites, Tech. rep., National Aeronautics and Space Administration, Glenn Research Center Cleveland, Ohio 44135 (2015).
URL https://core.ac.uk/download/pdf/42708657.pdf

[191] M. Arifin, B. Wahono, E. Junianto, A. D. Pasek, Process manufacture rotor radial turbo-expander for small scale organic Rankine cycles using selective laser melting machine, Energy Procedia 68 (2015) 305–310. doi:10.1016/j.egypro.2015.03.260.

[192] Y. Zhang, T. Duda, J. A. Scobie, C. M. Sangan, C. D. Copeland, A. Redwood, Design of an Air-Cooled Radial Turbine: Part 1 — Computational Modelling, in: Volume 8: Microturbines, Turbochargers, and Small Turbomachines; Steam Turbines, ASME, 2018, p. V008T26A013. doi:10.1115/GT2018-76378.

[193] Y. Zhang, T. Duda, J. A. Scobie, C. M. Sangan, C. D. Copeland, A. Redwood, Design of an Air-Cooled Radial Turbine: Part 2 — Experimental Measurements of Heat Transfer, in: Volume 8: Microturbines, Turbochargers, and Small Turbomachines; Steam Turbines, ASME, 2018, p. V008T26A014. doi:10.1115/GT2018-76384.

[194] P. ASTM International, West Conshohocken, Standard for Additive Manufacturing – Post Processing Methods – Standard Specification for Thermal Post-Processing Metal Parts Made Via Powder Bed Fusion, ASTM F3301-18a (2018).

[195] M. H. Bocanegra-Bernal, Hot Isostatic Pressing (HIP) technology and its applications to metals and ceramics, Journal of Materials Science 39 (21) (2004) 6399–6420, accessed on 2021-12-05. doi:10.1023/B:JMSC.0000044878.11441.90.

[196] B. Chmiela, B. Koscielniak, J. Cwajna, Effect of hot isostatic pressing on the microstructure of turbine blade airfoil made of nickel-base superalloy, Archives of Metallurgy and Materials 62 (1) (2017) 241–245. doi:10.1515/amm-2017-0036.

[197] Quintus Technologies, Hot Isostatic Pressing Supporting Additive Manufacturing Industry.
URL https://www2.quintustechnologies.com/HIP_Supporting_AM_Industry_Brochure_English

[198] L. Hackel, J. R. Rankin, A. Rubenchik, W. E. King, M. Matthews, Laser peening: A tool for additive manufacturing post-processing, Additive Manufacturing 24 (May) (2018) 67–75. doi:10.1016/j.addma.2018.09.013.

[199] Additive Manufacturing Standardization Collaborative, Standardization Roadmap for Additive Manufacturing, version 2 (June) (2018) 269.

[200] Y. Fu, X. Wang, H. Gao, H. Wei, S. Li, Blade surface uniformity of blisk finished by abrasive flow machining, The International Journal of Advanced Manufacturing Technology 84 (5-8) (2016) 1725–1735. doi:10.1007/s00170-015-8270-0.

[201] ©2013-2016 Extrude Hone, AFM: High-Quality Finishing for Industrial 3D Printing - Extrude Hone, accessed on 2019-01-10 (2016).
URL https://extrudehone.com/afm-high-quality-finishing-industrial-3d-printing

[202] C. Yang, X. Tian, D. Li, Y. Cao, F. Zhao, C. Shi, Influence of thermal processing conditions in 3D printing on the crystallinity and mechanical properties of PEEK material, Journal of Materials Processing Technology 248 (2017) 1–7. doi:10.1016/J.JMATPROTEC.2017.04.027.

[203] W. Jo, O.-C. Kwon, M.-W. Moon, Investigation of influence of heat treatment on mechanical strength of FDM printed 3D objects, Rapid Prototyping Journal 24 (3) (2018) 637–644. doi:10.1108/RPJ-06-2017-0131.

[204] V. Slavković, N. Grujović, A. Disic, A. Dišić, A. Radovanović, Influence of Annealing and Printing Directions on Mechanical Properties of PLA Shape Memory Polymer Produced by Fused Deposition Modeling, in: 6th International Congress of Serbian Society of Mechanics, Mountain Tara, Serbia, 2017.
URL https://www.researchgate.net/publication/317617713

[205] P. Parandoush, D. Lin, A review on additive manufacturing of polymer-fiber composites, Composite Structures 182 (2017) 36–53. doi:10.1016/j.compstruct.2017.08.088.

[206] A. Kamil, Post Processing for Nylon 12 Laser Sintered Components, Ph.D. thesis, Newcastle University (2016).
URL https://theses.ncl.ac.uk/dspace/bitstream/10443/3480/1/Kamil%2CA.2016.pdf

[207] A. Garg, A. Bhattacharya, A. Batish, On Surface Finish and Dimensional Accuracy of FDM Parts after Cold Vapor Treatment, Materials and Manufacturing Processes 31 (4) (2016) 522–529. doi:10.1080/10426914.2015.1070425.

[208] J. C. Kloppers, D. G. Kröger, A critical investigation into the heat and mass transfer analysis of counterflow wet-cooling towers, International Journal of Heat and Mass Transfer 48 (3) (2005) 765–777. doi:10.1016/j.ijheatmasstransfer.2004.09.004.

[209] J. Cihelka, Solar thermal technology [Solární tepelná technika], Malina, Praha, 1994.

[210] J. Orgill, K. Hollands, Correlation equation for hourly diffuse radiation on a horizontal surface, Solar Energy 19 (4) (1977) 357–359. doi:10.1016/0038-092X(77)90006-8.

[211] M. Brandemuehl, W. Beckman, Transmission of diffuse radiation through CPC and flat plate collector glazings, Solar Energy 24 (5) (1980) 511–513. doi:10.1016/0038-092X(80)90320-5.

[212] Cooling Tower Calculator (online tool), accesed on 2015-01-27.
URL http://www.gea-energytechnology.com/opencms/opencms/gas/en/calculators/CT_Calculator.htm

[213] R. Dickes, Solar-based ORC power systems, in: ORC-PLUS Workshop, Casablanca, 2016.
URL https://orbi.uliege.be/bitstream/2268/197155/1/Presentation_RDickes_ORC-Plus_workshop_OSV.pdf

[214] O. Aboelwafa, S.-E. E. K. Fateen, A. Soliman, I. M. Ismail, A review on solar Rankine cycles: Working fluids, applications, and cycle modifications, Renewable and Sustainable Energy Reviews 82 (2018) 868–885. doi:10.1016/j.rser.2017.09.097.

[215] A. Modi, F. Bühler, J. G. Andreasen, F. Haglind, A review of solar energy based heat and power generation systems, Renewable and Sustainable Energy Reviews 67 (2017) 1047–1064. doi:10.1016/J.RSER.2016.09.075.

[216] W. W. Charters, V. R. Megler, W. D. Chen, Y. F. Wang, Atmospheric and sub-atmospheric boiling of H2O and LiBr/H2O solutions, International Journal of Refrigeration 5 (2) (1982) 107–114. doi:10.1016/0140-7007(82)90085-8.

[217] C. Shi, Q. Chen, T.-C. Jen, W. Yang, Heat transfer performance of lithium bromide solution in falling film generator, International Journal of Heat and Mass Transfer 53 (2010) 3372–3376. doi:10.1016/j.ijheatmasstransfer.2010.02.051.

[218] A. P. Weiss, J. Hauer, T. Popp, M. Preissinger, EXPERIMENTAL INVESTIGATION OF A SUPERSONIC MICRO TURBINE RUNNING WITH HEXAMETHYLDISILOXANE, in: 36th Meeting of Departments of Fluid Mechanics and Thermodynamics, 16th conference on Power System Engineering, Thermodynamics & Fluid Flow - PSE 2017, 2017.

[219] A. P. Weiß, T. Popp, J. Müller, J. Hauer, D. Brüggemann, M. Preißinger, Experimental characterization and comparison of an axial and a cantilever micro-turbine for small-scale Organic Rankine Cycle, Applied Thermal Engineering 140 (2018) 235–244. doi:10.1016/J.APPLTHERMALENG.2018.05.033.

[220] J. Kadrnožka, Tepelné turbíny a turbokompresory: Základy teorie a výpočtů [Thermal turbines and turbocompressors: Basics of theory and calculations], CERM, Brno, 2004.

[221] J. Ambroz, Parní turbíny a kondenzace [Steam turbines and condensation], CTU in Prague, Prague, 1984.

[222] M. Y. Deych, G. A. Philipp, L. Y. Lazarev, Atlas of the Cascade Profiles of Axial-Flows Turbine, Tech. rep., Foreign Technology Div Wright-Patterson AFB Ohio (1976).

[223] C. Schieder, Weiterentwicklung eines Tools zur Auslegung von ORC-Turbinen [Further development of a tool for the design of ORC turbines], Master's thesis, Hochschule Amberg – Weiden (2013).

[224] J. Hauer, Analytische Studie zur optimierten Turbinenauslegung [Analytical study for optimised turbine design], Master's thesis, Hochschule Amberg – Weiden (2011).

[225] F. P. Incropera, A. S. Lavine, T. L. Bergman, D. P. Dewitt, Introduction to heat transfer, Wiley, 2007.

Author's publications related to the thesis

[VN1] V. Novotny, M. Kolovratnik, Absorption power cycles for low-temperature heat sources using aqueous salt solutions as working fluids, International Journal of Energy Research 41 (7) (2017) 952–975. doi:10.1002/er.3671.

[VN2] V. Novotny, M. Vitvarova, M. Kolovratnik, Absorption power cycles with various working fluids for exergy-efficient low-temperature waste heat recovery, in: S. Nižetić, A. Papadopoulos (Eds.), The Role of Exergy in Energy and the Environment, Springer, Cham, 2018, Ch. Energy Sys, pp. 99–111. doi:10.1007/978-3-319-89845-2_8.

[VN3] V. Novotny, V. Vodicka, J. Mascuch, M. Kolovratnik, Possibilities of water-lithium bromide absorption power cycles for low temperature, low power and combined power and cooling systems, Energy Procedia 129 (September) (2017) 818–825. doi:10.1016/J.EGYPRO.2017.09.104.

[VN4] V. Novotny, M. Vitvarova, M. Kolovratnik, Z. Hrdina, Minimizing the Energy and Economic Penalty of CCS Power Plants Through Waste Heat Recovery Systems, Energy Procedia 108 (2017) 10–17. doi:10.1016/j.egypro.2016.12.184.

[VN5] V. Novotny, D. Szucs, M. Kolovratnik, T. Matuska, Simulation of absorption power cycle and organic Rankine cycle using evacuated tube solar collectors., IIR Rankine Conference 2020. 2020-July (2020) 600–607. doi:10.18462/IIR.RANKINE.2020.1227.

[VN6] V. Novotny, D. J. Szucs, J. Špale, H.-Y. Tsai, M. Kolovratnik, Absorption Power and Cooling Combined Cycle with an Aqueous Salt

Solution as a Working Fluid and a Technically Feasible Configuration, Energies 2021, Vol. 14, Page 3715 14 (12) (2021) 3715. doi:10.3390/EN14123715.

[VN7] V. Novotny, D. Szűcs, M. Kolovratnik, T. Matuska, Simulation of solar collectors with two low temperature heat engines for buildings applications, in: 10th International Conference on System Simulation in Buildings, University of Liege, Liege, 2018.

[VN8] V. Novotný, M. Vitvarová, J. P. Jakobsen, M. Kolovratník, Analysis and Design of Novel Absorption Power Cycle Plants, in: ASME 2016 10th International Conference on Energy Sustainability, ES 2016, collocated with the ASME 2016 Power Conference and the ASME 2016 14th International Conference on Fuel Cell Science, Engineering and Technology, Vol. 1, American Society of Mechanical Engineers, ASME, Charlotte, 2016, p. V001T13A005. doi:10.1115/ES2016-59272.

[VN9] V. Novotny, J. Mascuch, H.-Y. Tsai, M. Kolovratnik, Design of Experimental Rig for Validation of Absorption Power Cycle Concept, Energy Procedia 105 (2017) 4990–4996. doi:10.1016/j.egypro.2017.03.998.

[VN10] V. Novotny, D. Suchna, M. Kolovratnik, Experimental rig for LiBr-water absorption power cycle - Design and first experimental results, in: AIP Conference Proceedings, Vol. 2047, 2018, p. 020013. doi:10.1063/1.5081646.

[VN11] V. Novotný, D. J. Szucs, J. Spale, V. Vodicka, J. Mascuch, M. Kolovratník, Absorption power cycle with LiBr solution working fluid-design of the proof-of-concept unit, in: 5 th International Seminar on ORC Power Systems, Athens, 2019.
URL https://www.orc2019.com/online/proceedings/documents/61.pdf

[VN12] J. Spale, V. Novotny, V. Mares, A. P. Weiß, 3D printed radial impulse cantilever micro-turboexpander for preliminary air testing, in: AIP Conference Proceedings, Vol. 2323, AIP Publishing LLC AIP Publishing, Pilsen, Czechia, 2021, p. 070002. doi:10.1063/5.0041433.

[VN13] V. Novotny, J. Spale, D. Suchna, J. Pavlicko, M. Kolovratnik, A. P. Weiß, Absorption power cycle with a 3D-printed plastic micro turboexpander - Considerations, design and first experimental results, in: AIP Conference Proceedings, Vol. 2323, American Institute of Physics Inc., 2021, p. 070003. doi:10.1063/5.0041429.

[VN14] V. Novotny, J. Spale, J. Pavlicko, M. Kolovratnik, Experimental investigation of a kw scale absorption power cycle with libr solution, in:

T. U. of Munich (Ed.), Proceedings of the 6th International Seminar on ORC Power Systems, Technical University of Munich, Technical University of Munich, 2021. doi:10.14459/2021mp1632900.

[VN15] V. Novotny, J. Spale, J. Pavlicko, J. Novotny, D. J. Szucs, M. Kolovratnik, Experience from the operation of an absorption power cycle with LiBr working fluid and its prospects for future, in: Heat Powered Cycles 2021, Bilbao, Spain, 2022, p. (accepted manuscript).

[VN16] V. Novotny, J. Spale, B. B. Stunova, M. Kolovratnik, M. Vitvarova, P. Zikmund, 3D Printing in Turbomachinery: Overview of Technologies, Applications and Possibilities for Industry 4.0, in: ASME Turbo Expo 2019: Turbomachinery Technical Conference and Exposition, Vol. 6, ASME International, Phoenix, 2019, p. V006T24A021. doi:10.1115/gt2019-91849.

[VN17] A. P. Weiß, V. Novotný, T. Popp, P. Streit, J. Špale, G. Zinn, M. Kolovratník, Customized ORC micro turbo-expanders - From 1D design to modular construction kit and prospects of additive manufacturing, Energy 209 (2020) 118407. doi:10.1016/j.energy.2020.118407.

[VN18] J. Spale, V. Novotny, J. Novotny, A. P. Weiß, M. Kolovratnik, Experimental Development of Additively Manufactured Turboexpanders towards an Application in the ORC, in: Heat Powered Cycles 2021, Bilbao, Spain, 2022, p. (accepted manuscrit).

[VN19] V. Novotny, M. Vitvarova, M. Kolovratnik, B. B. Stunova, V. Vodicka, J. Spale, P. Zikmund, M. Drasnar, E. Schastlivtseva, Design and Manufacturing of a Metal 3D Printed kW Scale Axial Turboexpander, in: ASME Turbo Expo 2019: Turbomachinery Technical Conference and Exposition, Vol. 8, ASME International, Phoenix, 2019, p. V008T26A023. doi:10.1115/gt2019-91822.

Nomenclature

Symbols

A	Surface area	(m^2)
a	Solar collector loss coefficients	(W m^{-2} K^{-1}),(W m^{-2} K^{-2})
b	Turbine blade chord length	(m)
b_0	PV panel reflectance coefficient	(1)
c	Absolute velocity	(m s^{-1})
C	Constant	(1)
$CorrF$	Correction factor	(1)
c_p	Specific isobaric heat capacity	(J kg^{-1} K^{-1}) or (kJ kg^{-1} K^{-1})
D	Diameter	(m)
e	Partial admission	(1)
Ex	Exergy flux	(kJ s^{-1})
f	Friction coefficient	(1)
Fr	Froude number	(1)
g	Gravity acceleration	(m s^{-2})
G	Irradiation (solar)	(W m^{-2})
G_{sc}	Solar constant	(W m^{-2})
G_{sf}	Surface-fluid combination parameter	(1)
h	Specific enthalpy, sun elevation angle	(kJ kg^{-1}), (°)
h'_{fg}	Modified latent heat of vaporization	(J kg^{-1})
H_{eq}	Equivalent pumping head	(m)
i	Partial admission number of segments	(1)
I	Current	(A)
K	Incidence angle modifier, turbine disc friction coefficient	(1), (1)
k	Heat conductivity	(W m^{-1} K^{-1})
k_l	Mass transfer coefficient	(m s^{-1})
k_T	Sky clearness index	(1)
l	Length, height	(m)
m	Mass	(kg)
m''	Mass flux	(kg m^{-2} s^{-1})
$\dot{m}$	Mass flow rate	(kg s^{-1})
n	Surface-fluid combination exponent, rotational speed	(1), (rpm)
Nu	Nusselt number	(1)

O	Perimeter	(m)
p	Pressure	(kPa or bar)
Pr	Prandtl number	(1)
Q	Heat	(kJ)
$q"_s$	Nucleate boiling heat flux, Heat flux for saturated boiling	(W m^2)
$\dot{Q}$	Heat flow	(kW)
$\dot{q}$	Heat flux	(kW m^{-2} or W m^{-2})
R	Turbine reaction	(1)
Re	Reynolds number	(1)
RH	Relative humidity	(%)
S	Entropy	(kJ K)$^{-1}$
s	Specific entropy	(kJ kg^{-1} K^{-1})
SR	Splitting ratio	(1)
ST	Solar time	(h)
T	Temperature, Torque	(°C or K), (Nm)
u	Peripheral velocity	(m s^{-1})
U	Voltage	(V)
v	Unit volume	(m^3 kg^{-1})
w	Relative velocity	(m s^{-1})
W_{dot}	Power	(kW or W)
x	Steam quality	(1)
z	Turbine primary loss, number of blades	(kJ kg^{-1}), (1)

Greek letters

α	Velocity angle, convection heat transfer coefficient	$(^\circ)$, $\left(\mathrm{Wm^{-2}\ K^{-1}}\right)$
β	Velocity angle, collector slope, PV temperature coef.	$(^\circ)$, $(^\circ)$, $(\mathrm{K^{-1}})$
γ	Collector azimuth	$(^\circ)$
Γ	Mass flow per length	$(\mathrm{kg\ s^{-1}\ m^{-1}})$
Δ	Difference	(1)
ζ	Turbine secondary loss factor	(1)
η	Efficiency	(1)
ν	Kinematic viscosity	$(m^2\ s^{-1})$
θ	Solar incidence angle	$(^\circ)$
μ	Dynamic viscosity, turbine flow constriction coefficient	(Pa s), (1)
ξ	Concentration	(1)
ρ	Reflectivity, Density	(1), $(\mathrm{kg\ m^{-3}})$
σ	Electrical conductivity, surface tension	$(\mathrm{S\ m^{-1}})$, $(\mathrm{Nm^{-1}})$
ϕ	Location latitude	$(^\circ)$
φ	Velocity coefficient (stator)	(1)
ψ	Velocity coefficient (rotor)	(1)
ω	Rotational speed	$(\mathrm{rad\ s^{-1}})$

Acronyms

ACC	Air cooled condenser
AM	Additive manufacturing
APC	Absorption power cycle
APCC	Absorption power and cooling cycle
BLDC	Brushless DC (motor)
$CaCl_2$	Calcium chloride
CCP	Combined cooling and power
CCHP	Combined cooling, heat and power
CHP	Combined heating and power
CO_2	Carbon dioxide
COP	Coefficient of performance
CT	Cooling tower
DC	Direct current, dry cooler
DMLS	Direct metal laser sintering
EBM	Electron beam melting
FDM	Fused deposition modelling
GAX	generator-absorber-exchanger
H_2O	Water
HX	Heat Exchanger
IAM	Incidence angle modifier
LiBr	Lithium Bromide
LiCl	Lithium chloride
$LiNO_3$	Lithium nitrate
MJF	Multi Jet Fusion
MM	Hexamethyldisiloxane
NaSCN	Sodium thiocyanate
NH_3	Ammonia
ORC	Organic Rankine cycle
PV	Photovoltaic
RC	Rankine cycle
SC	Supercritical
SLA	Stereolithography
SLS	Selective laser sintering

Subscripts

0	Dead state (efficiency) or reference
1st	1st law of thermodynamics
2nd	2nd law of thermodynamics
a	Aperture (solar collector)
abs	Absorption, absorber
amb	Ambient
aux	Auxiliary
b	Beam (direct irradiation)
boil	Boiling
c	Cycle
cf	Cooling (heat rejection) fluid
chill	Chiller, cold production
col	Collector
cond	Condensation, condenser
cw	Cooling (heat rejection) water
d	Diffuse (irradiation)
des	Desorber
el	Electrical
eva	Evaporated
exp	Expander
fg	Latent (enthalpy)
fl	Fluid
fluid2	Secondary fluid
g	Generator
horiz	On horizontal surface
HP	High pressure
hs	Heat source
i, j	Element/node, specie
is	Isentropic
k	Disc friction
liq, l	Liquid
LP	Low pressure
m	Mean
max	Maximal
meas	Measured
mech	Mechanical
min	Minimal
o	Finite blade length
pa	Partial admission
pow	Power

r	Reflected, rotor
rec	Recuperator / recuperated
rect	Rectified
ref	Reference
rej	Rejected, rejection (heat)
s	Stator
sat	Saturated
sol	Solution
surf	Surface (of wall in heat transfer or of collector)
T	Normal (irradiation)
th	Thermal, theoretical
TI	Turbine inlet
tot	Total
turb	Turbine
u	Primary turbine efficiency
u, util	Utilization
v	Outlet (turbine loss)
v, vap	Vapour
vv	Variable velocity profile across blade height
w	Windage (ventilation)
wf	Working fluid

Appendix **A**

Details of numerical APC heat exchangers calculation

These are equation of species balance, Equation (A.1), mass balance overall and of vapour, Equation (A.2) and (A.3), elementary heat transfer, Equation (A.4)) to (A.9) and finally determination of pinch point value, Equation (A.10) (then in the program iteratively changed to prescribed value).

$$\xi_i = \xi_{i-1} + \Delta\xi_i \tag{A.1}$$

$$m_{vap,i} = m_{tot} - m_{sol,i} \tag{A.2}$$

$$m_{\mathrm{eva},i} = m_{\mathrm{vap},i} - m_{\mathrm{vap},i-1} \tag{A.3}$$

$$\Delta Q_{\mathrm{eva},i} = m_{\mathrm{eva},i} \cdot (h_{\mathrm{vap},i} - h_{\mathrm{sol},i-1}) \tag{A.4}$$

$$\Delta Q_{\mathrm{sol},i} = m_{\mathrm{sol},i} \cdot (h_{\mathrm{sol},i} - h_{\mathrm{sol},i-1}) \tag{A.5}$$

$$\Delta Q_{\mathrm{vap},i} = m_{\mathrm{vap},i-1} \cdot (h_{\mathrm{vap},i} - h_{\mathrm{vap},i-1}) \tag{A.6}$$

$$\Delta Q_i = \Delta Q_{\mathrm{eva},i} + \Delta Q_{\mathrm{sol},i} + \Delta Q_{\mathrm{vap},i} \tag{A.7}$$

$$Q_{tot,i} = Q_{tot,i-1} + \Delta Q_i \tag{A.8}$$

$$h_{\text{fluid2},i} - h_{f\text{fluid2},i-1} = \frac{\Delta Q_i}{m_{\text{fluid 2}}} \tag{A.9}$$

$$\text{PinchPoint } = \min\left(T_{\text{fluid2},i} - T_i\right) \tag{A.10}$$

Appendix B

Solar and collector models and their coupling to cycle models

B.1 Solar model

Solar model follows a general model described for example by [209] and here will be described only briefly. In the model there are following inputs:

- Day of the year
- Solar time ST (1 hour resolution, adjusted to measured data from UCEEB, CTU in Prague)
- Experimental solar irradiance to horizontal surface *G=f(ST)* for each hour from above
- Collector slope
- Collector azimuth
- Location latitude

The output of the solar model is then irradiance of a specified surface with its distribution to direct, diffuse and reflected light. The model first describes geometry of Sun movement with respect to given position and surface on Earth with horizontal irradiation determined from solar constant G_{sc} from Equation (B.1). Then is used a correlation [210] using sky clearness index relating solar irradiation out of the Earth's atmosphere G_0 and measured value G to obtain diffuse light, Equation (B.2). Following that is evaluated the diffuse radiation and direct radiation contents. Finally, for a surface that is not horizontal there is additional (though small) content of reflected light.

$$G_0 = G_{sc}\left(1 + 0.033 \cdot \cos\frac{360 \cdot DR}{365}\right)\sin h \tag{B.1}$$

$$k_T = \frac{G}{G_0} \approx \frac{G_d}{G} = \begin{cases} 1.0 - 0.249k_T & \text{for } k_T < 0.35 \\ 1.557 - 1.84k_T & \text{for } 0.35 < k_T < 0.75 \\ 0.177 & \text{for } k_T > 0.75 \end{cases} \tag{B.2}$$

Irradiation of specific surface is then determined by trigonometric functions. Note that the trigonometric functions in the relations might cause incorrect values near incidence angles very close to and above 90°. Therefore, the irradiance values are limited to incidence angles only to 85° (actual power obtainable between 85°and 90° is anyway negligible and below the model accuracy).

Also note that the solar time provided with experimental data has to be adjusted to fit the actual longitude. It can be done either knowing a time zone and time of measurement. Other option (useful when these data are not available) is to plot the average irradiation and find the time of solar noon as a maximum of the smooth curve running through these points.

B.2 Collector model

The collector model provides a portion of irradiation that is absorbed by the collector, heat losses that are a function of ambient temperature and finally its output and efficiency. The inputs of the collector model are following:

- Irradiation per given surface (from solar model in direct, diffuse and reflected components)
- Ambient temperature T_{amb}
- Collector transversal and longitudinal incidence angle modifiers (IAM) from reported measurements
- Collector mean fluid temperature

A 6th order polynomial fit using MS Excel function *LINEST* is applied to the IAM so that these can be used later as a function. Subsequently is obtained transversal, longitudinal direction and overall IAM for direct irradiation (changing with each value), diffuse and reflected light. Note that the diffuse and reflected light IAM are constant for single surface setting with respect to effective diffuse and reflected angles of incidence obtained from correlations [211] in Equations (B.3) and (B.4).

$$\theta_d = 59.7 - 0.1388\beta + 0.001497\beta^2 \tag{B.3}$$

$$\theta_r = 90 - 0.5788\beta + 0.002693\beta^2 \tag{B.4}$$

Finally, for a given collector aperture area the energy input to the collector is expressed by Equation (B.5). The collector has thermal losses which are evaluated from reported efficiency curve coefficients a1 and a2, mean temperature of collector medium and ambient temperature. These losses are described by Equation (B.6). Net collector output is obviously a difference between the two heats and taken are only cases of positive output. When the output would be negative, no operation is assumed. Collector output then relates to fluid mass flow rate based on inlet and outlet temperatures according to Equation (B.7). Note that the mass flow rate is a function of input parameters.

$$\dot{Q}_{col,in} = A_a \left[K_{\theta,b} G_{bT} + K_{\theta,d} G_{dT} + K_{\theta,r} G_{rT}\right] \eta_{ref} \tag{B.5}$$

$$\dot{Q}_{col,loss} = A_a \left[a_1 \left(t_m - t_{amb}\right) + a_2 \left(t_m - t_{amb}\right)^2\right] \tag{B.6}$$

$$\dot{Q}_{\text{col,net}} = \dot{Q}_{\text{col,in}} - \dot{Q}_{\text{col,loss}} = \dot{m} \left(h_{\text{fluid,out}} - h_{\text{fluid,in}}\right) \tag{B.7}$$

B.3 Collector efficiency

The collector efficiency is defined by Equation (B.8) and it is just a ratio of energy output in heat transfer fluid to irradiation of collector aperture area. Obviously, it is a function of efficiency characteristics, ambient temperature, effective angles (through IAM) and energy incident to the collector aperture area in one of the three forms.

$$\eta_{col} = \frac{\dot{Q}_{col,net}}{\left(G_b + G_d + G_r\right) A_a} = \frac{\dot{Q}_{col,net}}{G_T A_a} \tag{B.8}$$

B.4 Models interconnection

The PV models can be directly coupled with the solar model and power produced is evaluated for model each time step and given the simplification of neglecting produced electricity in thermal energy balance, no iteration is

needed. Power produced is simply evaluated from Equation (B.9) with surface area for further analyses taken as 1 m^2.

$$\dot{W}_{PV,\,\mathrm{net}} = \eta_{PV,\,\mathrm{module}}\, G_T A \tag{B.9}$$

For the heat engines, net power is evaluated after obtaining expander power production and power consumption of all components. Obtaining parameters of the heat engines with thermal collectors is not so straight forward. Disregarding eventual iteration loops in the heat engines themselves (non-regenerated ORC has almost no issues but APC is computationally more demanding). There are also imposed additional limits as following only the pinch points, in winter months with very low temperature the condensation (or absorption) pressure would enormously decrease but also the cooling circuit water could get below freezing point. In order to mitigate this issue, the operation of the heat engine was split into two regimes, first as defined above with pinch point limits which goes down to ambient air temperature of -5°C (cooling water return temperature +5°C). For temperatures below this point is condensation (absorption) pressure and thus condenser (absorber) outlet temperature and the cooling circuit return temperature are further kept constant.

An input and control value of for the heat engine models are heat source inlet temperature. Outlet temperature is a function of heat engine parameters, thus the mean temperature to evaluate collector efficiency can be obtained only after the cycle parameters are given. The calculation methods used in the presented analyses are for clarity schematically shown in Figure B.1. The reason of creating the intermediate functions representing the heat engine in issues of model convergence with the entire inputs array as an input in the EES.

An approach taken is to obtain a net efficiency of the power cycle and collector mean temperature (change of mean temperature can be rather small) as a function of ambient temperature with other parameters of the cycle fixed. This is done by fitting a suitable polynomial in MS excel using a LINEST function on the data from the EES models. Example of the net cycle efficiency and temperature functions are in Figure B.2. Note that the change of the mean collector temperature is very small, in case of APC less than 0.5 K, in case of ORC is this change several degrees. Using these functions for heat engine simplification, performance can be easily evaluated and the power production potential can be estimated for the system in each time step of the model.

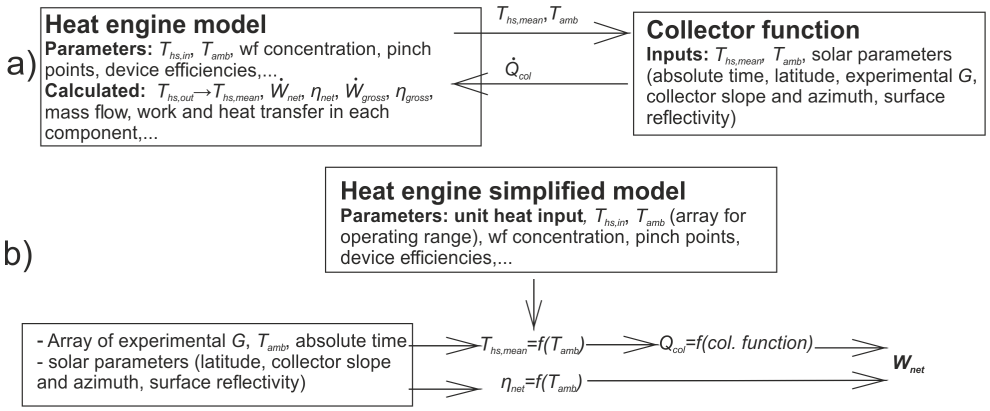

Figure B.1: Diagram of principle of the two calculation procedures used, a) completely in EES, b) in MS Excel based on functions of heat engine operation obtained from heat engine models in EES.

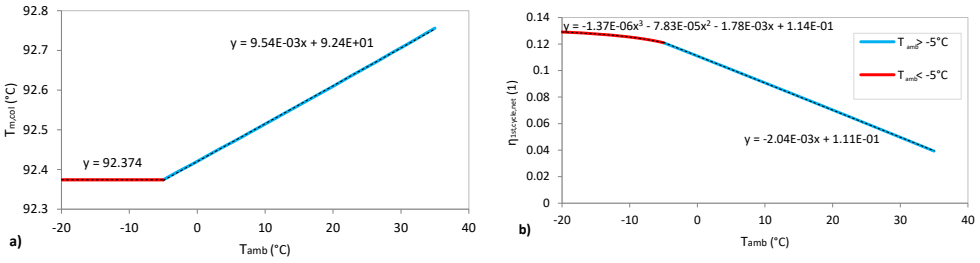

(a) (b)

Figure B.2: Mean collector temperature and cycle net efficiency for APC with collector outlet temperature 100°C.

Appendix C

Detailed results of APC comparison with alternatives to low temperature heat source

This appendix presents Tables C.1, C.2, C.3, C.4 with the resulting parameters of optimized thermodynamic cycles for given heat source temperatures and heat rejection method. Gross and net efficiency is presented for each cycle, where the net includes parasitic load represented by heat rejection fans and eventually pump. The efficiency is further referenced to the heat input (cycle efficiency) and to the heat content of the resource (utilization efficiency). In order to compare the obtained power to the thermodynamic potential of the heat input or heat source, exergy efficiency (2^{nd} law efficiency) is evaluated along the 1^{st} law energy efficiency. Lastly to illustrate one aspect of technical feasibility of different cycles, high and low pressures of the investigated cycles are presented in Tables C.5 and C.6.

Table C.1: Gross and net 1^{st} law cycle and heat source utilization efficiency when using the cooling tower (in %).

	$t_{hs,in}$ (°C)	60				80				100			
	w. fluid / η	gross cyc	net cyc	gross res	**net res**	gross cyc	net cyc	gross res	**net res**	gross cyc	net cyc	gross res	**net res**
APC	**LiBr P**	2.27	1.31	0.51	**0.29**	4.48	3.81	1.46	**1.24**	6.46	5.87	2.46	**2.24**
	LiBr K	2.27	1.30	0.50	**0.29**	4.53	3.82	1.48	**1.25**	6.61	5.84	2.51	**2.22**
	LiCl	2.17	1.37	0.53	**0.34**	4.39	3.85	1.47	**1.29**	6.43	5.99	2.48	**2.31**
	$CaCl_2$	2.29	1.47	0.58	**0.37**	4.30	3.82	1.49	**1.32**	6.30	5.82	2.43	**2.24**
	HN3-H_2O	1.90	0.96	0.44	**0.23**	4.07	3.32	1.38	**1.13**	6.09	5.33	2.46	**2.15**
RC1	**Water**	2.34	0.95	0.24	**0.10**	4.59	3.24	1.14	**0.81**	6.64	5.32	2.19	**1.76**
RC2	**Water**	2.34	0.95	0.27	**0.11**	4.60	3.25	1.22	**0.86**	6.65	5.34	2.29	**1.83**
(wet)	**R143a**	2.02	0.72	0.23	**0.08**	3.80	2.52	1.21	**0.80**	4.89*	3.63*	2.85*	**2.12***
	R152a	2.22	0.87	0.26	**0.10**	4.29	2.97	1.23	**0.85**	6.13	4.84	2.41	**1.90**
	Methanol	2.34	0.95	0.27	**0.11**	4.58	3.23	1.23	**0.87**	6.63	5.31	2.31	**1.85**
	NH_3	2.27	0.90	0.26	**0.10**	4.41	3.08	1.22	**0.85**	6.34	5.04	2.33	**1.85**
	R290	2.14	0.81	0.24	**0.09**	4.10	2.80	1.22	**0.83**	5.84	4.56	2.42	**1.89**
	R1234yf	1.94+	0.68+	0.15+	**0.05+**	4.12+	2.89+	1.12+	**0.79+**	5.79+	4.52+	2.37+	**1.85+**
RC3	**Isobutane**	2.22	0.87	0.23	**0.09**	4.29	2.97	1.16	**0.81**	6.12	4.84	2.32	**1.83**
(dry)	**n-Butane**	2.25	0.89	0.23	**0.09**	4.35	3.03	1.17	**0.81**	6.22	4.93	2.30	**1.82**
	RC318	2.16	0.83	0.23	**0.09**	4.11	2.82	1.18	**0.81**	5.81	4.55	2.39	**1.87**
	cyclohexane	2.30	0.93	0.24	**0.10**	4.49	3.15	1.17	**0.82**	6.46	5.15	2.27	**1.81**
	HFE7100	2.21	0.87	0.24	**0.09**	4.22	2.92	1.18	**0.81**	5.93	4.67	2.32	**1.83**
	R245fa	2.26	0.90	0.24	**0.09**	4.38	3.05	1.18	**0.82**	6.28	4.98	2.33	**1.85**
	MM	2.08	0.79	0.21	**0.08**	4.09	2.84	1.10	**0.76**	5.86	4.65	2.20	**1.74**
RC3R	**Isobutane**												
(dry. rec.)	**n-Butane**												
	RC318									6.00	4.71	2.40	**1.89**
	cyclohexane												
	HFE7100					4.32	3.00	1.18	**0.82**	6.33	5.02	2.34	**1.85**
	R245fa												
	MM					4.19	2.92	1.10	**0.76**	6.23	4.98	2.22	**1.77**
	$t_{hs,in}$ [d'ż"C]	120				140				160			
	w. fluid / η	gross cyc	net cyc	gross res	**net res**	gross cyc	net cyc	gross res	**net res**	gross cyc	net cyc	gross res	**net res**
APC	**LiBr P**	8.46	7.77	3.53	**3.25**	10.21	9.47	4.60	**4.26**	11.85	11.05	5.65	**5.27**
	LiBr K	8.45	7.85	3.57	**3.32**	10.27	9.59	4.57	**4.26**	11.90	11.23	5.66	**5.34**
	LiCl	8.34	7.77	3.53	**3.29**	10.63	9.93	4.56	**4.26**	13.17	12.32	5.50	**5.15**
	$CaCl_2$	8.07	7.47	3.41	**3.16**	9.93	9.14	4.44	**4.09**	11.65	10.71	5.51	**5.07**
	HN3-H_2O	7.97	7.08	3.68	**3.27**	9.66	8.89	4.82	**4.44**	11.56	10.52	6.35	**5.78**
RC1	**Water**	8.51	7.23	3.28	**2.78**	10.25	8.99	4.37	**3.83**	11.87	10.63	5.46	**4.89**
RC2	**Water**	8.54	7.25	3.37	**2.87**	10.28	9.02	4.46	**3.91**	11.90	10.67	5.53	**4.95**
(wet)	**R143a**	4.89*	3.63*	3.64*	**2.7***	4.87*	3.63*	3.83*	**2.86***	4.85*	3.64*	3.97*	**2.98***
	R152a	7.84	6.57	3.73	**3.13**	10.32*	9.09*	5.48*	**4.83***	10.35*	9.07*	8.49*	**7.45***
	Methanol	8.51	7.22	3.42	**2.91**	10.25	8.99	4.54	**3.99**	11.87	10.63	5.67	**5.08**
	NH_3	8.10	6.82	3.51	**2.96**	9.75	8.50	4.76	**4.15**	11.47	10.25	6.16	**5.51**
	R290	8.04*	6.8*	4*	**3.38***	8.07*	6.78*	6.35*	**5.33***	8.04*	6.8*	6.57*	**5.56***
	R1234yf	7.72*	6.44*	4.28*	**3.57***	7.74*	6.44*	5.95*	**4.95***	7.71*	6.45*	6.18*	**5.17***
RC3	**Isobutane**	7.80	6.53	3.62	**3.03**	9.49	8.24	4.94	**4.29**	11.02	9.80	6.50	**5.78**
(dry)	**n-Butane**	7.92	6.65	3.56	**2.99**	9.49	8.24	4.94	**4.29**	11.02	9.80	6.50	**5.78**
	RC318	7.37	6.14	3.85	**3.20**	10.36*	9.11*	6.36*	**5.6***	10.42*	9.09*	8.41*	**7.34***
	cyclohexane	8.24	6.96	3.45	**2.91**	9.87	8.62	4.68	**4.09**	11.37	10.14	5.96	**5.31**
	HFE7100	7.41	6.18	3.57	**2.98**	8.69	7.49	4.89	**4.22**	9.80	8.63	6.30	**5.55**
	R245fa	7.99	6.72	3.61	**3.04**	9.56	8.32	5.02	**4.36**	11.07	9.85	6.59	**5.87**
	MM	7.42	6.24	3.42	**2.87**	8.78	7.63	4.72	**4.10**	9.97	8.85	6.09	**5.40**
RC3R	**Isobutane**	7.83	6.56	3.62	**3.03**	9.54	8.28	5.09	**4.42**				
(dry. rec.)	**n-Butane**	8.00	6.72	3.57	**3.00**	9.72	8.46	4.95	**4.31**	11.45	10.21	6.51	**5.81**
	RC318	7.85	6.57	3.88	**3.24**	10.36*	9.11*	6.36*	**5.60***	10.42*	9.09*	8.41*	**7.34***
	cyclohexane	8.27	6.99	3.45	**2.92**	9.91	8.67	4.69	**4.10**	11.42	10.21	5.97	**5.34**
	HFE7100	8.22	6.92	3.60	**3.03**	10.02	8.73	4.95	**4.31**	11.74	10.47	6.38	**5.68**
	R245fa	8.05	6.77	3.61	**3.04**	9.77	8.51	5.02	**4.38**	11.47	10.22	6.61	**5.89**
	MM	8.19	6.94	3.45	**2.92**	10.04	8.81	4.76	**4.18**	11.82	10.60	6.15	**5.52**

* Cycles with maximal pressure limited to 90% of critical pressure
\+ Expansion ends in slightly superheated region

Table C.2: Gross and net 2^{nd} law cycle and heat source utilization efficiency when using the cooling tower (in %).

	$t_{hs,in}$ (°C)	60				80				100			
	w. fluid / η	gross cyc	net cyc	gross res	**net res**	gross cyc	net cyc	gross res	**net res**	gross cyc	net cyc	gross res	**net res**
APC	**LiBr P**	21.60	12.44	8.37	**4.82**	31.19	26.56	16.45	**14.01**	36.26	32.94	21.54	**19.57**
	LiBr K	21.50	12.29	8.26	**4.72**	31.71	26.76	16.77	**14.15**	37.07	32.73	21.96	**19.39**
	LiCl	20.87	13.18	8.76	**5.53**	30.74	26.94	16.57	**14.52**	36.15	33.68	21.64	**20.16**
	$CaCl_2$	22.07	14.16	9.56	**6.14**	30.28	26.87	16.76	**14.87**	35.41	32.74	21.21	**19.61**
	NH_3-H_2O	18.10	9.21	7.29	**3.71**	28.56	23.30	15.57	**12.70**	34.56	30.24	21.49	**18.80**
RC1	**Water**	20.94	8.53	3.92	**1.59**	30.75	21.70	12.90	**9.10**	36.28	29.07	19.16	**15.35**
RC2	**Water**	23.58	9.60	4.89	**1.99**	33.50	23.66	14.87	**10.50**	38.70	31.03	21.20	**17.00**
(wet)	**R143a**	20.32	7.25	4.22	**1.51**	28.46	18.90	14.79	**9.82**	32.62*	24.20*	26.45*	**19.62***
	R152a	22.35	8.72	4.70	**1.83**	31.60	21.86	15.05	**10.41**	36.58	28.87	22.31	**17.60**
	Methanol	23.54	9.57	4.90	**1.99**	33.45	23.60	14.96	**10.55**	38.65	30.97	21.41	**17.16**
	Ammonia	22.85	9.08	4.76	**1.89**	32.35	22.59	14.87	**10.38**	37.34	29.67	21.59	**17.16**
	R290	21.52	8.13	4.49	**1.70**	30.35	20.71	14.83	**10.12**	35.30	27.58	22.48	**17.56**
	R1234yf	17.24+	6.04+	2.51+	**0.88+**	28.02+	19.68+	12.66+	**8.89+**	33.04+	25.82+	20.79+	**16.25+**
RC3	**Isobutane**	19.95	7.81	3.81	**1.49**	29.17	20.20	13.18	**9.13**	34.36	27.13	20.29	**16.02**
(dry)	**n-Butane**	20.21	7.99	3.86	**1.53**	29.55	20.55	13.21	**9.19**	34.78	27.53	20.20	**15.99**
	RC318	19.34	7.42	3.76	**1.44**	28.06	19.22	13.30	**9.12**	33.13	25.93	20.93	**16.38**
	cyclohexane	20.68	8.32	3.93	**1.58**	30.35	21.29	13.19	**9.25**	35.72	28.48	19.88	**15.85**
	HFE7100	19.92	7.83	3.87	**1.52**	28.80	19.91	13.31	**9.20**	33.51	26.37	20.32	**16.00**
	R245fa	20.31	8.07	3.90	**1.55**	29.77	20.75	13.35	**9.30**	35.10	27.84	20.45	**16.22**
	MM	18.67	7.09	3.40	**1.29**	27.75	19.26	12.39	**8.60**	32.84	26.04	19.27	**15.28**
RC3R	**Isobutane**												
(dry. recup.)	**n-Butane**												
	RC318									34.05	26.72	21.06	**16.53**
	cyclohexane												
	HFE7100					29.42	20.40	13.34	**9.25**	35.35	28.03	20.48	**16.24**
	R245fa												
	MM					28.36	19.74	12.43	**8.65**	34.57	27.59	19.41	**15.50**
	$t_{hs,in}$ [d'ż"C]	120				140				160			
	w. fluid / η	gross cyc	net cyc	gross res	**net res**	gross cyc	net cyc	gross res	**net res**	gross cyc	net cyc	gross res	**net res**
APC	**LiBr P**	40.33	37.05	25.53	**23.46**	42.91	39.77	28.57	**26.48**	44.93	41.89	31.07	**28.97**
	LiBr K	40.34	37.47	25.84	**24.00**	43.04	40.18	28.39	**26.50**	45.08	42.52	31.10	**29.33**
	LiCl	39.85	37.15	25.48	**23.76**	44.18	41.28	28.33	**26.47**	48.48	45.36	30.23	**28.28**
	$CaCl_2$	38.59	35.70	24.65	**22.81**	41.65	38.36	27.62	**25.44**	44.06	40.53	30.30	**27.87**
	HN3-H_2O	38.88	34.56	26.60	**23.64**	41.66	38.34	29.97	**27.58**	45.53	41.45	34.91	**31.78**
RC1	**Water**	39.91	33.87	23.69	**20.10**	42.55	37.32	27.17	**23.83**	44.59	39.96	30.01	**26.89**
RC2	**Water**	41.96	35.63	25.53	**21.68**	44.28	38.86	28.76	**25.24**	46.10	41.32	31.35	**28.10**
(wet)	**R143a**	29.78*	22.06*	27.54*	**20.40***	26.14*	19.51*	24.74*	**18.46***	23.47*	17.60*	22.52*	**16.89***
	R152a	40.22	33.72	28.22	**23.66**	46.88*	41.28*	35.40*	**31.18***	50.16*	43.98*	48.18*	**42.25***
	Methanol	41.95	35.61	25.90	**21.98**	44.36	38.91	29.33	**25.73**	46.29	41.48	32.17	**28.83**
	NH_3	40.60	34.21	26.55	**22.37**	43.24	37.70	30.75	**26.81**	46.19	41.27	34.97	**31.24**
	R290	41.78*	35.29*	30.27*	**25.56***	43.31*	36.40*	40.97*	**34.43***	38.88*	32.86*	37.30*	**31.51***
	R1234yf	39.7*	33.12*	30.96*	**25.83***	39.47*	32.83*	36.96*	**30.75***	35.65*	29.81*	33.92*	**28.37***
RC3	**Isobutane**	38.05	31.87	26.14	**21.90**	41.35	35.88	31.62	**27.44**	48.53*	43.75*	38.17*	**34.41***
(dry)	**n-Butane**	38.35	32.21	25.76	**21.63**	41.31	35.89	30.71	**26.68**	44.29	39.39	35.67	**31.72**
	RC318	37.19	30.97	27.82	**23.16**	45.64*	39.96*	39.29*	**34.40***	44.82*	39.23*	42.67*	**37.35***
	cyclohexane	39.26	33.16	24.94	**21.07**	41.89	36.57	29.07	**25.38**	44.04	39.28	32.69	**29.16**
	HFE7100	36.51	30.45	25.80	**21.52**	38.75	33.41	30.41	**26.22**	40.67	35.82	34.57	**30.45**
	R245fa	38.74	32.58	26.12	**21.97**	41.72	36.29	31.17	**27.11**	44.66	39.73	36.19	**32.20**
	MM	36.14	30.39	24.71	**20.78**	38.57	33.52	29.31	**25.46**	40.58	36.01	33.42	**29.65**
RC3R	**Isobutane**	38.17	31.98	26.15	**21.90**	41.92	36.41	31.66	**27.50**				
(dry. recup.)	**n-Butane**	38.65	32.47	25.78	**21.66**	42.05	36.60	30.76	**26.77**	45.49	40.54	35.76	**31.87**
	RC318	38.94	32.60	28.03	**23.46**	47.66*	41.90*	39.54*	**34.77***	48.36*	42.21*	46.14*	**40.27***
	cyclohexane	39.37	33.30	24.95	**21.10**	42.03	36.77	29.12	**25.47**	44.20	39.53	32.76	**29.30**
	HFE7100	39.58	33.33	26.05	**21.94**	42.98	37.46	30.75	**26.81**	45.96	40.97	34.99	**31.20**
	R245fa	38.98	32.79	26.14	**21.99**	42.39	36.92	31.22	**27.19**	45.74	40.78	36.27	**32.34**
	MM	39.06	33.13	24.94	**21.15**	42.63	37.41	29.60	**25.97**	45.70	40.99	33.78	**30.30**

* Cycles with maximal pressure limited to 90% of critical pressure
+ Expansion ends in slightly superheated region

Table C.3: Gross and net 1^{st} law cycle and heat source utilization efficiency when using ACC (in %).

	$t_{hs,in}$ (°C)	60				80				100			
	w. fluid / η	gross cyc	net cyc	gross res	**net res**	gross cyc	net cyc	gross res	**net res**	gross cyc	net cyc	gross res	**net res**
APC	**LiBr P**	2.38	0.55	0.52	**0.12**	4.68	3.40	1.57	**1.14**	6.47	5.47	2.55	**2.16**
	LiBr K	2.37	0.45	0.52	**0.10**	4.59	3.36	1.55	**1.13**	6.28	5.41	2.47	**2.12**
	LiCl	2.27	0.51	0.63	**0.14**	4.38	3.35	1.60	**1.22**	6.58	5.69	2.64	**2.28**
	$CaCl_2$	2.43	0.74	0.68	**0.21**	4.53	3.45	1.65	**1.25**	6.36	5.42	2.61	**2.23**
	NH_3-H_2O	2.15	0.33	0.42	**0.06**	4.31	2.96	1.45	**1.00**	6.06	4.88	2.54	**2.04**
RC1	**Water**	2.51	0.34	0.09	**0.01**	4.74	2.64	0.97	**0.54**	6.78	4.72	2.00	**1.40**
RC2	**Water**	2.51	0.34	0.10	**0.01**	4.75	2.64	1.03	**0.57**	6.79	4.73	2.09	**1.46**
(wet)	**R143a**	2.11	0.12	0.05	**0.00**	3.76	1.81	0.99	**0.47**	4.54*	2.59*	2.57*	**1.47***
	R152a	2.35	0.26	0.08	**0.01**	4.37	2.33	1.03	**0.55**	6.17	4.16	2.18	**1.47**
	Methanol	2.50	0.34	0.10	**0.01**	4.73	2.62	1.04	**0.58**	6.76	4.70	2.11	**1.47**
	Ammonia	2.42	0.30	0.09	**0.01**	4.53	2.46	1.03	**0.56**	6.42	4.40	2.12	**1.45**
	R290	2.26	0.21	0.07	**0.01**	4.16	2.15	1.01	**0.52**	5.83	3.85	2.19	**1.45**
	R1234yf	2.05+	0.10+	0.03+	**0.00+**	4.11+	2.11+	1.02+	**0.52+**	5.76+	3.79+	2.25+	**1.48+**
RC3	**Isobutane**	2.53	0.25	0.09	**0.01**	4.38	2.33	1.04	**0.56**	6.17	4.17	2.21	**1.50**
(dry)	**n-Butane**	2.39	0.28	0.09	**0.01**	4.45	2.39	1.05	**0.57**	6.28	4.27	2.20	**1.50**
	RC318	2.27	0.23	0.08	**0.01**	4.16	2.17	1.05	**0.55**	5.81	3.86	2.28	**1.51**
	cyclohexane	2.45	0.32	0.10	**0.01**	4.61	2.53	1.06	**0.58**	6.55	4.51	2.18	**1.50**
	HFE7100	2.34	0.27	0.09	**0.01**	4.30	2.29	1.05	**0.56**	5.97	4.01	2.21	**1.48**
	R245fa	2.40	0.29	0.09	**0.01**	4.48	2.42	1.06	**0.57**	6.33	4.32	2.23	**1.52**
	MM	2.22	0.21	0.07	**0.01**	4.18	2.23	0.98	**0.52**	5.92	4.03	2.10	**1.43**
RC3R	**Isobutane**												
(dry. recup.)	**n-Butane**												
	RC318									6.05	4.04	2.29	**1.53**
	cyclohexane												
	HFE7100					4.45	2.38	1.06	**0.57**	6.43	4.39	2.24	**1.53**
	R245fa												
	MM					4.32	2.33	0.98	**0.53**	6.35	4.38	2.12	**1.46**
	$t_{hs,in}$ [d'ż"C]	120				140				160			
	w. fluid / η	gross cyc	net cyc	gross res	**net res**	gross cyc	net cyc	gross res	**net res**	gross cyc	net cyc	gross res	**net res**
APC	**LiBr P**	8.58	7.51	3.63	**3.17**	10.19	9.10	4.66	**4.16**	11.96	10.74	5.72	**5.14**
	LiBr K	8.40	7.38	3.64	**3.19**	10.21	9.15	4.66	**4.18**	12.11	10.97	5.68	**5.15**
	LiCl	8.65	7.67	3.66	**3.24**	10.76	9.57	4.68	**4.16**	13.35	12.00	5.58	**5.02**
	$CaCl_2$	7.99	7.07	3.53	**3.12**	9.71	8.64	4.47	**3.98**	11.32	10.10	5.46	**4.88**
	HN3-H_2O	7.94	6.76	3.68	**3.13**	9.70	8.42	4.94	**4.29**	11.37	9.84	6.41	**5.55**
RC1	**Water**	8.64	6.63	3.08	**2.36**	10.36	8.39	4.17	**3.37**	11.96	10.04	5.25	**4.40**
RC2	**Water**	8.66	6.65	3.17	**2.44**	10.39	8.43	4.25	**3.44**	12.00	10.07	5.32	**4.46**
(wet)	**R143a**	4.54*	2.59*	3.27*	**1.87***	4.51*	2.60*	3.46*	**2.00***	4.48*	2.60*	3.60*	**2.09***
	R152a	7.81	5.85	3.49	**2.61**	10.03*	8.12*	5.26*	**4.26***	10.07*	8.10*	8.13*	**6.54***
	Methanol	8.61	6.61	3.22	**2.47**	10.33	8.37	4.33	**3.51**	11.93	10.01	5.46	**4.58**
	NH_3	8.14	6.16	3.29	**2.49**	9.75	7.81	4.53	**3.63**	11.44	9.54	5.93	**4.94**
	R290	7.74*	5.80*	3.78*	**2.83***	7.77*	5.79*	5.98*	**4.46***	7.74*	5.80*	6.21*	**4.66***
	R1234yf	7.43*	5.50*	4.21*	**3.12***	7.45*	5.50*	5.80*	**4.28***	7.42*	5.51*	6.01*	**4.46***
RC3	**Isobutane**	7.79	5.78	3.60	**2.62**	9.33	7.41	5.00	**3.97**	11.35	9.28	6.95	**5.68**
(dry)	**n-Butane**	7.93	5.96	3.47	**2.61**	9.46	7.53	4.86	**3.87**	10.95	9.06	6.42	**5.31**
	RC318	7.31	5.40	3.74	**2.76**	9.41*	7.54*	6.25*	**5.01***	9.41*	7.54*	7.63*	**6.12***
	cyclohexane	8.31	6.32	3.37	**2.56**	9.91	7.96	4.61	**3.70**	11.39	9.47	5.90	**4.91**
	HFE7100	7.41	5.50	3.46	**2.57**	8.65	6.79	4.79	**3.76**	9.74	7.92	6.18	**5.03**
	R245fa	8.00	6.03	3.52	**2.66**	9.54	7.61	4.93	**3.93**	11.01	9.11	6.51	**5.39**
	MM	7.44	5.59	3.32	**2.50**	8.77	6.97	4.62	**3.67**	9.94	8.17	5.99	**4.93**
RC3R	**Isobutane**	7.88	5.90	3.52	**2.64**	9.56	7.60	5.01	**3.99**	11.56	9.64	6.88	**5.73**
(dry. recup.)	**n-Butane**	8.06	6.07	3.48	**2.62**	9.76	7.80	4.87	**3.89**	11.47	9.53	6.44	**5.35**
	RC318	7.86	5.87	3.78	**2.82**	10.19*	8.23*	6.32*	**5.11***	10.18*	8.23*	7.72*	**6.24***
	cyclohexane					10.22	8.24	4.62	**3.72**	11.92	9.96	5.91	**4.94**
	HFE7100	8.31	6.29	3.52	**2.66**	10.09	8.09	4.87	**3.91**	11.80	9.82	6.30	**5.24**
	R245fa	8.10	6.11	3.53	**2.66**	9.80	7.84	4.95	**3.95**	11.47	9.53	6.54	**5.43**
	MM	8.28	6.33	3.37	**2.58**	10.12	8.19	4.70	**3.80**	11.87	9.96	6.10	**5.12**

* Cycles with maximal pressure limited to 90% of critical pressure
\+ Expansion ends in slightly superheated region

Table C.4: Gross and net 2^{nd} law efficiency of cycle and of heat source utilization when ACC is employed (in %).

	$t_{hs,in}$ (°C)	**60**				**80**				**100**			
	w. fluid / η	gross cyc	net cyc	gross res	**net res**	gross cyc	net cyc	gross res	**net res**	gross cyc	net cyc	gross res	**net res**
APC	**LiBr P**	25.20	5.83	9.61	**2.22**	35.39	25.70	19.21	**13.95**	38.60	32.62	23.61	**19.96**
	LiBr K	25.07	4.71	9.55	**1.79**	34.56	25.28	18.81	**13.76**	37.42	32.21	22.82	**19.64**
	LiCl	24.68	5.51	11.50	**2.57**	33.45	25.62	19.37	**14.84**	39.36	34.04	24.38	**21.08**
	$CaCl_2$	26.50	8.09	12.50	**3.81**	34.63	26.32	20.05	**15.24**	38.25	32.60	24.14	**20.57**
	NH_3-H_2O	22.48	3.47	7.68	**1.19**	32.45	22.27	17.67	**12.12**	36.60	29.46	23.45	**18.87**
RC1	**Water**	21.78	2.98	1.53	**0.21**	31.10	17.28	10.93	**6.07**	36.41	25.36	17.51	**12.19**
RC2	**Water**	24.44	3.35	1.90	**0.26**	33.80	18.79	12.62	**7.02**	38.77	27.03	19.38	**13.51**
(wet)	**R143a**	20.41	1.21	0.85	**0.05**	27.40	13.16	12.07	**5.79**	29.93*	17.13*	23.82*	**13.63***
	R152a	22.87	2.53	1.56	**0.17**	31.41	16.73	12.58	**6.70**	36.05	24.34	20.24	**13.66**
	Methanol	24.37	3.32	1.90	**0.26**	33.70	18.70	12.69	**7.04**	38.67	26.91	19.57	**13.62**
	Ammonia	23.53	2.87	1.70	**0.21**	32.40	17.59	12.51	**6.79**	37.10	25.40	19.65	**13.45**
	R290	21.89	2.01	1.29	**0.12**	29.95	15.47	12.27	**6.34**	34.46	22.77	20.31	**13.42**
	R1234yf	19.69+	0.94+	0.50+	**0.02+**	29.66+	15.22+	12.40+	**6.37+**	34.31+	22.60+	20.83+	**13.72+**
RC3	**Isobutane**	24.54	2.47	1.67	**0.17**	31.47	16.79	12.74	**6.80**	36.15	24.43	20.51	**13.86**
(dry)	**n-Butane**	23.22	2.74	1.68	**0.20**	31.95	17.19	12.81	**6.89**	36.66	24.91	20.43	**13.88**
	RC318	22.08	2.20	1.43	**0.14**	30.14	15.69	12.78	**6.65**	34.64	23.01	21.09	**14.01**
	cyclohexane	23.88	3.08	1.83	**0.24**	32.98	18.08	12.87	**7.05**	37.87	26.10	20.19	**13.92**
	HFE7100	22.75	2.58	1.64	**0.19**	31.00	16.49	12.83	**6.82**	35.19	23.67	20.47	**13.76**
	R245fa	23.33	2.80	1.71	**0.21**	32.18	17.39	12.95	**7.00**	37.00	25.25	20.71	**14.13**
	MM	21.47	1.99	1.21	**0.11**	30.01	16.02	11.93	**6.37**	34.63	23.54	19.45	**13.22**
RC3R	**Isobutane**												
(dry. recup.)	**n-Butane**												
	RC318									35.85	23.96	21.25	**14.20**
	cyclohexane												
	HFE7100					31.97	17.13	12.90	**6.91**	37.50	25.60	20.73	**14.16**
	R245fa												
	MM					30.92	16.63	12.01	**6.46**	36.77	25.35	19.70	**13.58**
	$t_{hs,in}$ [d'ż"C]	**120**				**140**				**160**			
	w. fluid / η	gross cyc	net cyc	gross res	**net res**	gross cyc	net cyc	gross res	**net res**	gross cyc	net cyc	gross res	**net res**
APC	**LiBr P**	42.83	37.48	27.42	**23.99**	44.57	39.81	30.10	**26.88**	46.81	42.05	32.52	**29.22**
	LiBr K	42.15	37.02	27.49	**24.15**	44.65	40.02	30.14	**27.01**	47.18	42.74	32.27	**29.23**
	LiCl	43.17	38.28	27.67	**24.54**	46.52	41.36	30.25	**26.90**	50.69	45.58	31.69	**28.50**
	$CaCl_2$	40.28	35.62	26.66	**23.58**	42.52	37.85	28.87	**25.70**	44.39	39.62	31.03	**27.70**
	HN3-H_2O	40.52	34.48	27.82	**23.67**	43.63	37.88	31.93	**27.72**	46.59	40.32	36.41	**31.51**
RC1	**Water**	39.93	30.64	22.25	**17.08**	42.49	34.43	25.90	**20.98**	44.49	37.33	28.86	**24.21**
RC2	**Water**	41.93	32.20	23.99	**18.43**	44.19	35.83	27.42	**22.23**	45.97	38.59	30.15	**25.31**
(wet)	**R143a**	27.17*	15.53*	24.76*	**14.15***	23.86*	13.77*	22.35*	**12.90***	21.44*	12.45*	20.41*	**11.85***
	R152a	39.45	29.53	26.41	**19.76**	45.39*	36.73*	33.94*	**27.46***	48.33*	38.87*	46.13*	**37.10***
	Methanol	41.85	32.10	24.34	**18.67**	44.18	35.78	27.97	**22.65**	46.06	38.64	30.95	**25.96**
	NH_3	40.18	30.40	24.88	**18.82**	42.69	34.18	29.26	**23.43**	45.58	38.00	33.62	**28.02**
	R290	39.99*	29.98*	28.59*	**21.43***	41.20*	30.68*	38.62*	**28.76***	36.98*	27.75*	35.22*	**26.43***
	R1234yf	40.22*	29.78*	31.86*	**23.59***	39.76*	29.32*	37.46*	**27.62***	35.66*	26.49*	34.09*	**25.32***
RC3	**Isobutane**	40.21	29.32	27.24	**19.86**	42.49	33.72	33.27	**25.61**	47.73	39.02	38.44	**32.25**
(dry)	**n-Butane**	39.86	29.96	26.27	**19.75**	42.55	33.86	31.35	**24.95**	45.35	37.50	36.40	**30.10**
	RC318	38.29	28.30	28.29	**20.90**	46.35*	37.14*	40.35*	**32.34***	45.27*	36.27*	43.30*	**34.69***
	cyclohexane	41.04	31.21	25.51	**19.39**	43.41	34.87	29.76	**23.91**	45.37	37.74	33.45	**27.83**
	HFE7100	37.82	28.10	26.18	**19.45**	39.80	31.25	30.89	**24.25**	41.53	33.79	35.08	**28.54**
	R245fa	40.27	30.35	26.66	**20.09**	42.98	34.27	31.84	**25.38**	45.72	37.84	36.94	**30.57**
	MM	37.57	28.25	25.15	**18.90**	39.74	31.57	29.84	**23.71**	41.55	34.18	33.99	**27.96**
RC3R	**Isobutane**	39.78	29.78	26.66	**19.95**	43.25	34.41	32.36	**25.74**	48.12	40.12	39.00	**32.52**
(dry. recup.)	**n-Butane**	40.36	30.39	26.30	**19.80**	43.55	34.77	31.44	**25.11**	46.83	38.91	36.56	**30.37**
	RC318	40.46	30.21	28.61	**21.36**	48.80*	39.43*	40.81*	**32.97***	47.11*	38.07*	43.77*	**35.37***
	cyclohexane					44.43	35.82	29.80	**24.03**	46.91	39.22	33.50	**28.01**
	HFE7100	41.43	31.36	26.60	**20.13**	44.62	35.77	31.44	**25.21**	47.45	39.47	35.76	**29.75**
	R245fa	40.66	30.68	26.68	**20.13**	43.84	35.06	31.92	**25.52**	47.04	39.09	37.08	**30.81**
	MM	40.95	31.31	25.52	**19.51**	44.29	35.85	30.33	**24.54**	47.20	39.60	34.58	**29.02**

* Cycles with maximal pressure limited to 90% of critical pressure
+ Expansion ends in slightly superheated region

Table C.5: High and low pressure levels in all investigated cycles for maximal heat source utilization efficiency - when cooling tower is used (in kPa)

	$t_{hs,in}$ (°C) w. fluid	**60**		**80**		**100**		**120**		**140**		**160**	
		p_a	p_e	p_a	p_e	p_a	p_e	p_a	p_e	p_a	p_e	p_a	p_e
APC	**LiBr P**	4.2	2.5	7.2	2.6	12.5	2.8	24.1	3.6	38.3	3.9	58.7	4.3
	LiBr K	4.8	2.8	8.2	2.9	16.3	3.7	24.4	3.7	39.9	4.0	59.0	4.2
	LiCl	2.2	1.3	5.4	1.9	12.1	2.6	22.6	3.3	43.9	4.0	85.4	4.6
	$CaCl_2$	1.4	0.8	4.2	1.4	11.3	2.4	24.0	3.5	42.9	4.5	67.0	5.1
	NH_3-H_2O	1213.0	937.7	1639.0	978.2	2292.0	1091.0	3050.0	1174.0	3760.0	1159.0	5054.0	1289.0
RC1	**Water**	10.2	6.2	16.4	6.2	5809.0	7249.0	37.7	6.2	54.5	6.2	76.7	6.2
RC2 (wet)	**Water**	10.2	6.2	16.5	6.2	25.7	6.2	38.8	6.2	56.9	6.2	81.4	6.2
	R143a	2133.0	1709.0	2707.0	1709.0	3385*	1708*	3385*	1707*	3385*	1714*	3385*	1719*
	R152a	1072.0	835.8	1377.0	836.1	1760.0	836.4	2275.0	836.6	4068*	836.7*	4068*	832.3*
	Methanol	45.9	29.7	70.2	29.7	104.1	29.7	150.5	29.8	212.9	29.8	296.4	29.8
	Ammonia	1839.0	1421.0	2377.0	1421.0	3030.0	1422.0	3840.0	1423.0	4893.0	1423.0	6559.0	1424.0
	R290	1581.0	1275.0	1971.0	1275.0	2472.0	1275.0	3822*	1275*	3822*	1270*	3822*	1275*
	R1234yf	1219.0+	947.6+	1544.0+	947.4+	1961.0+	940.2+	3044*	944.3*	3044*	941.8*	3044*	946.3*
RC3 (dry)	**Isobutane**	623.1	488.1	797.7	488.3	1013.0	488.6	1288.0	488.6	1664.0	488.8	3276*	488.7*
	n-Butane	449.2	346.4	583.0	346.6	748.4	346.8	955.9	346.9	1225.0	347.1	1604.0	347.2
	RC318	586.2	449.9	769.2	450.5	1008.0	451.0	1347.0	451.5	2500*	451.6*	2500*	451.4*
	cyclohexane	31.3	21.6	45.3	21.6	63.9	21.6	88.5	21.6	120.4	21.6	161.8	21.7
	HFE7100	63.4	44.8	89.6	44.9	124.2	45.0	169.3	45.2	227.8	45.3	303.4	45.4
	R245fa	304.8	224.2	414.7	224.3	556.4	224.4	740.7	224.6	985.9	224.7	1334.0	224.8
	MM	15.1	10.3	22.7	10.3	33.6	10.3	48.7	10.3	69.3	10.4	97.1	10.4
RC3R (dry recup.)	**Isobutane**							1292.0	488.3	1668.0	487.9		
	n-Butane					1012.0	449.3	959.1	346.5	1229.0	346.2	1608.0	345.9
	RC318							1351.0	448.4	2500*	447.9*	2500*	443.8*
	cyclohexane							88.8	21.6	120.9	21.6	162.5	21.5
	HFE7100			90.1	44.7	124.8	44.6	170.2	44.5	229.1	44.4	305.4	44.4
	R245fa							743.5	224.3	989.4	224.1	1338.0	223.9
	MM			22.8	10.2	33.7	10.2	48.9	10.2	69.7	10.2	97.7	10.1

* Cycles with maximal pressure limited to 90% of critical pressure
\+ Expansion ends in slightly superheated region

Table C.6: High and low pressure levels in all investigated cycles for maximal heat source utilization efficiency - when ACC is used (in kPa)

	$t_{hs,in}$ (°C)	60		80		100		120		140		160	
	w. fluid	p_a	p_e	p_a	p_e	p_a	p_e	p_a	p_e	p_a	p_e	p_a	p_e
APC	**LiBr P**	5.2	3.0	7.2	2.4	12.5	2.8	21.2	2.9	34.8	3.4	57.6	4.0
	LiBr K	5.0	2.9	8.2	2.9	12.4	2.9	19.1	2.7	33.8	3.3	60.2	4.0
	LiCl	1.7	0.9	3.7	1.2	9.6	1.9	21.3	2.8	44.1	3.9	85.4	4.2
	$CaCl_2$	1.7	1.0	5.4	1.8	10.9	2.3	20.7	2.9	38.3	3.8	61.8	4.4
	NH_3-H_2O	1470.0	1112.0	1711.0	985.3	2113.0	989.3	2856.0	1074.0	3760.0	1148.0	4973.0	1286.0
RC1	**Water**	11.5	6.8	18.5	6.8	28.5	6.8	42.2	6.8	60.7	6.8	85.2	6.8
RC2	**Water**	11.5	6.8	18.6	6.8	28.8	6.8	43.2	6.8	63.1	6.8	89.9	6.8
(wet)	**R143a**	2276.0	1799.0	2866.0	1799.0	3385*	1799*	3385*	1798*	3385*	1807*	3385*	1813*
	R152a	1145.0	879.8	1464.0	880.3	1862.0	880.7	2393.0	881.0	4068*	881.5*	4068*	875.1*
	Methanol	51.2	32.2	78.0	32.3	115.1	32.3	165.4	32.4	232.9	32.4	322.6	32.4
	Ammonia	1967.0	1495.0	2533.0	1497.0	3217.0	1498.0	4059.0	1499.0	5152.0	1499.0	6911.0	1500.0
	R290	1677.0	1336.0	2082.0	1336.0	2596.0	1336.0	3822*	1336*	3822*	1329*	3822*	1337*
	R1234yf	1290+	1003+	1616+	992.3+	2071+	992.3+	3044*	992.4*	3044*	989*	3044*	995.3*
RC3	**Isobutane**	665.5	503.5	847.6	503.5	1072.0	503.5	1354.0	503.5	1741.0	503.5	2559.0	503.5
(dry)	**n-Butane**	480.9	365.3	621.1	365.6	793.5	365.8	1008.0	366.1	1286.0	366.3	1675.0	366.5
	RC318	630.0	476.9	821.1	477.7	1068.0	478.4	1417.0	479.1	2500*	479*	2500*	478.9*
	cyclohexane	34.5	23.2	49.5	23.3	69.5	23.3	95.6	23.3	129.3	23.3	172.8	23.3
	HFE7100	69.5	48.2	97.5	48.4	134.2	48.6	181.7	48.8	243.0	49.0	322.0	49.2
	R245fa	330.1	238.7	446.4	238.9	595.4	239.1	787.4	239.3	1041.0	239.5	1400.0	239.6
	MM	16.8	11.2	25.1	11.2	36.8	11.2	52.9	11.3	74.8	11.3	104.0	11.4
RC3R	**Isobutane**							1359.0	513.1	1746.0	512.4	2539.0	511.8
(dry. recup.)	**n-Butane**							1013.0	365.0	1292.0	364.5	1681.0	363.9
	RC318			0.0	0.0	1074.0	474.6	473.1	1424.0	2500*	472.2*	2500*	472.3*
	cyclohexane									130.1	23.2	23.1	174.0
	HFE7100			98.0	48.0	135.0	47.8	182.9	47.7	244.7	47.5	324.7	47.4
	R245fa							791.6	238.6	1047.0	238.2	1406.0	237.8
	MM			25.2	11.1	37.0	11.1	53.2	11.0	75.2	11.0	104.8	10.9

* Cycles with maximal pressure limited to 90% of critical pressure
\+ Expansion ends in slightly superheated region

Appendix D

Detailed results of APCC and its benchmark systems

This appendix contains supplementary results for the study of the combined power and cooling thermodynamic cycles. Thermodynamic parameters are presented in each nodes of the systems in Tables D.1, D.2, D.3 and D.4 for the proposed absorption system and for the benchmark system consisting of ORC and vapour compression chiller. These results are presented for two cases, first for a baseline case of fixed heat source temperature difference and second for a case optimized for heat source utilization. Lastly there are additional results of the sensitivity analysis of the absorption cycle parameters in Figures D.1 and D.2, particularly on heat source temperature (two cases, when temperature difference of heat source is constant and outlet temperature is constant), on ambient temperature and evaporator temperature.

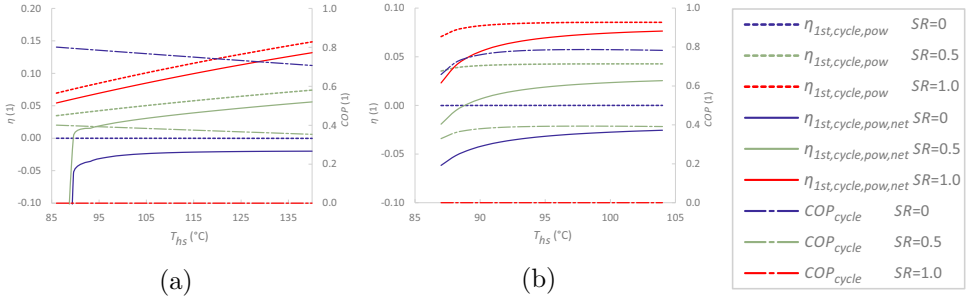

(a) (b)

Figure D.1: COP and gross and net APCC system efficiency at varied heat source temperature when (a) temperature difference of heat source is constant (10 °C) and (b) outlet temperature of the heat source is constant (85 °C).

Table D.1: Parameters of the APCC in its nodes for baseline conditions (imposed values in underscored bold).

Node	T (°C)	p (kPa)	h (kJ·kg^{-1})	$\dot{m}$ (kg $\cdot s^{-1}$)	s (kJ·kg^{-1}·K^{-1})	ξ (1)	x (1)
1	36.4	8.683	92	0.499	0.221	0.560	subc
2	79.1	8.683	179	0.499	0.484	0.560	subc
3	80.1	8.683	181	0.499	0.490	0.560	0
4	90.0	8.683	389	0.499	1.072	0.560	0.030
5	90.0	8.683	2669	0.035	8.463	0.000	sup
6	90.0	8.683	2669	0.018	8.463	0.000	1
7	5.0	0.8725	2417	0.018	8.689	0.000	0.963
8	90.0	8.683	2669	0.018	8.463	0.000	sup
9	43.1	8.683	180	0.018	0.613	0.000	**0**
10	5.0	0.8725	180	0.018	0.649	0.000	0.109
11	5.0	0.8725	2510	0.018	9.025	0.000	**1**
12	5.0	0.8725	2463	0.035	8.857	0.000	0.981
13	90.0	8.683	215	0.463	0.508	0.603	0
14	41.4	8.683	122	0.463	0.231	0.603	subc
15	41.4	0.8725	122	0.463	0.232	0.603	0.017
16	44.7	0.8725	288	0.499	0.847	0.560	0.028
17	36.4	0.8725	92	0.499	0.221	0.560	**0**
21	**95**.0	**800**	399	**2.500**	1.250		
22	85.1	800	357	2.500	1.135		
23	**85.0**	800	357	2.500	1.134		
30	30.0	**200**	126	3.665	0.437		
31	30.0	200	126	2.404	0.437		
32	39.7	200	167	2.404	0.569		
33	30.0	200	126	1.261	0.437		
34	38.4	200	161	1.261	0.550		
35	39.3	200	164	3.665	0.563		
41	**25.0**	**101.3**	61	14.86	5.823		
42	34.3	101.3	70	14.86	5.855		
51	**15.0**	**200**	63	1.969	0.224		
52	10.0	200	42	1.969	0.151		

Table D.2: Parameters of the ORC-VCC in its nodes for baseline conditions (imposed values in underscored bold).

Node	T (°C)	p (kPa)	h (kJ·kg^{-1})	$\dot{m}$ (kg ·s^{-1})	s (kJ·kg^{-1}·K^{-1})	x (1)
1	43.3	841.7	257	0.524	1.192	subc
2	47.4	841.7	263	0.524	1.210	subc
3	82.5	841.7	313	0.524	1.358	**0**
4	82.5	841.7	463	0.524	1.781	**1**
5	53.9	275.3	447	0.524	1.794	sup
6	48.3	275.3	441	0.524	1.776	sup
7	43.0	275.3	436	0.524	1.759	**1**
8	43.0	275.3	257	0.524	1.192	**0**
11	35.0	831.5	249	0.158	1.165	subc
12	5.0	261.2	249	0.158	1.174	0.23
13	5.0	261.2	388	0.158	1.674	**1**
14	45.3	831.5	415	0.158	1.691	sup
15	43.0	831.5	412	0.158	1.682	**1**
16	43.0	831.5	260	0.158	1.202	**0**
21	**95.0**	**800**	399	**2.500**	1.250	
22	87.5	800	367	2.500	1.163	
23	**85.0**	800	357	2.500	1.134	
30	30.0	**200**	126	3.584	0.437	
31	30.0	200	126	2.811	0.437	
32	38.0	200	159	2.811	0.546	
33	38.2	200	160	2.811	0.549	
34	30.0	200	126	0.773	0.437	
35	38.0	200	159	0.773	0.546	
36	38.2	200	160	0.773	0.548	
37	38.2	200	160	3.584	0.549	
41	**25.0**	**101.3**	61	14.530	5.823	
42	33.2	101.3	69	14.530	5.852	
51	**15.0**	**200**	63	1.052	0.224	
52	10.0	200	42	1.052	0.151	

Table D.3: Parameters of the APCC in its nodes after optimisation for heat source utilisation (imposed values in underscored bold).

Node	T (°C)	p (kPa)	h (kJ·kg^{-1})	$\dot{m}$ (kg ·s^{-1})	s (kJ·kg^{-1}·K^{-1})	ξ (1)	x (1)
1	35.5	8.089	88	0.502	0.218	0.555	subc
2	77.5	8.089	174	0.502	0.479	0.555	subc
3	77.6	8.089	174	0.502	0.479	0.555	0
4	90.0	8.089	435	0.502	1.211	0.555	0.030
5	90.0	8.089	2669	0.045	8.496	0.000	sup
6	90.0	8.089	2669	0.022	8.496	0.000	1
7	5.0	0.8725	2424	0.022	8.715	0.000	0.963
8	90.0	8.089	2669	0.022	8.496	0.000	sup
9	41.7	8.089	175	0.022	0.595	0.000	**0**
10	5.0	0.8725	175	0.022	0.629	0.000	0.109
11	5.0	0.8725	2510	0.022	9.025	0.000	1
12	5.0	0.8725	2467	0.045	8.870	0.000	0.981
13	90.0	8.089	218	0.458	0.502	0.609	**1**
14	40.5	8.089	124	0.458	0.224	0.609	subc
15	40.5	0.8725	124	0.458	0.224	0.609	0.017
16	45.9	0.8725	331	0.502	0.993	0.555	0.028
17	35.5	0.8725	88	0.502	0.218	0.555	**0**
21	**95.0**	**800**	399	**2.500**	1.250		
22	82.5	800	346	2.500	1.105		
23	82.5	800	346	2.500	1.105		
30	30.0	200	126	4.624	0.437		
31	30.0	200	126	2.717	0.437		
32	40.8	200	171	2.717	0.582		
33	30.0	200	126	1.907	0.437		
34	37.0	200	155	1.907	0.532		
35	39.2	200	164	4.624	0.562		
41	**25.0**	**101.3**	61	18.75	5.823		
42	34.2	101.3	70	18.75	5.855		
51	**15.0**	**200**	63	2.480	0.224		
52	10.0	200	42	2.480	0.151		

Table D.4: Parameters of the ORC-VCC in its nodes after optimisation for heat source utilisation (imposed values in underscored bold).

Node	T (°C)	p (kPa)	h (kJ·kg^{-1})	$\dot{m}$ (kg ·s^{-1})	s (kJ·kg^{-1}·K^{-1})	x (1)
1	43.3	725.7	257	0.905	1.192	subc
2	46.2	725.7	261	0.905	1.205	subc
3	76.6	725.7	304	0.905	1.334	**0**
4	76.6	725.7	460	0.905	1.777	**1**
5	52.3	275.3	445	0.905	1.788	sup
6	48.3	275.3	441	0.905	1.776	sup
7	43.0	275.3	436	0.905	1.759	**1**
8	43.0	275.3	257	0.905	1.192	**0**
11	35.0	831.5	249	0.237	1.165	subc
12	5.0	261.2	249	0.237	1.174	0.23
13	5.0	261.2	388	0.237	1.674	**1**
14	45.3	831.5	415	0.237	1.691	sup
15	43.0	831.5	412	0.237	1.682	**1**
16	43.0	831.5	260	0.237	1.202	**0**
21	**95.0**	**800**	399	**2.500**	1.250	
22	81.6	800	342	2.500	1.094	
23	77.9	800	327	2.500	1.050	
30	30.0	200	126	3.584	0.437	
31	30.0	200	126	4.854	0.437	
32	38.0	200	159	4.854	0.546	
33	38.2	200	160	4.854	0.549	
34	30.0	200	126	1.155	0.437	
35	38.0	200	159	1.155	0.546	
36	38.2	200	160	1.155	0.548	
37	38.2	200	160	6.009	0.549	
41	**25.0**	**101.3**	61	24.36	5.823	
42	33.2	101.3	69	24.36	5.852	
51	**15.0**	**200**	63	1.571	0.224	
52	10.0	200	42	1.571	0.151	

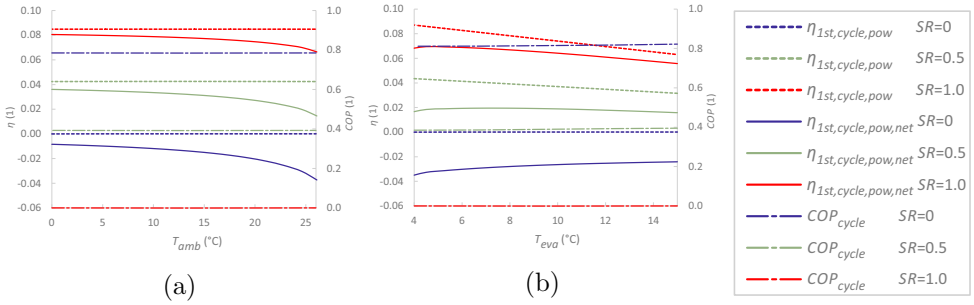

(a) (b)

Figure D.2: COP and gross and net APCC system efficiency at (a) varied ambient temperature and (b) varied evaporator temperature.

Appendix **E**

APC 1^{st} test rig design details

Sizing of the 1^{st} test rig has been done for the operation at pressure 20-100 kPa and concentrations chosen for simplicity and comfort of operation. With the heat input 10.5 kW and using 30% LiBr weak solution and desorber inlet 30°C and outlet at 155°C the liquid concentration will be 60% and mass flow will be half of the overall weak solution flow 7 $g \cdot s^{-1}$. Heat transfer calculations for single phase fluid are well documented. In highly turbulent flows the commonly known Dittus Boelter correlations are used while in lower Reynolds numbers (especially thermo-oil) is used Gnielinski correlation, Equation (E.1) to improve the accuracy. In heat exchangers with highly changing properties of fluids and flow regime, especially LiBr solution desorption and absorption, heat exchangers are divided into discrete elements (in most cases 30), where heat transfer and specific properties are calculated for each element separately.

$$Nu_i = (f_i/8) \cdot (Re_i - 1000) \cdot \left[\frac{\mathrm{Pr}_i}{1 + 12.7 \cdot (f_i/8)^{0.5} \cdot \left(\mathrm{Pr}_i^{0.67} - 1\right)} \right] \tag{E.1}$$

The desorber (a in the scheme in Figure 7.1) is conceptually designed as three segments of a modified tube in tube heat exchanger. The LiBr solution is inside an inner tube and is being partially boiled, while the thermal oil flows in the spiral channel created in the annulus between the pipes. Thermocouple measurements are evenly distributed to monitor temperature development of both fluids. Between the segments are unheated sections for additional measurement and instrumentation ports and especially sight glass for visual observation. The thermal design of heat transfer is modelled based on flow boiling correlations described in [225]. Here a single phase heat transfer coefficient is calculated first and it is then multiplied by a ratio expressed by Equations (E.2), (E.3), where the higher value should be used. *f(Fr)* is

a stratification parameter depending on Froude number *Fr* (Unity for *Fr* 0.04 and vertical pipes). Specific surface fluid combination G_{sf} is here unity. Nucleate boiling heat flux q_s" is given by Equation (E.4) where the coefficient C_{sf} and the exponent n depend on the experimentally determined solid-fluid combination. Values of these coefficients are approximated as ones for water on polished stainless steel, as more detailed information is not available. Solving these equations simultaneously together with fluid properties and parameters for each element obtains the heat transfer coefficients. Subsequently, heat transfer area and finally element length can be obtained.

$$\frac{\alpha}{\alpha_{liq}} = 0.6683 \left(\frac{\rho_{liq}}{\rho_{\text{vap}}}\right)^{0.1} x^{0.16}(1-x)^{0.64} f(Fr) + 1058 \left(\frac{q''_s}{m'' h_{fg}}\right)^{0.7} (1-x)^{0.8} G_{sf} \tag{E.2}$$

$$\frac{\alpha}{\alpha_{liq}} = 1.136 \left(\frac{\rho_{liq}}{\rho_{\text{vap}}}\right)^{0.45} x^{0.72}(1-x)^{0.08} f(Fr) + 667.2 \left(\frac{q''_s}{m'' h_{fg}}\right)^{0.7} (1-x)^{0.8} G_{sf} \tag{E.3}$$

$$q''_s = \mu_{liq} h_{fg} \left[\frac{g\left(\rho_{liq} - \rho_{vap}\right)}{\sigma}\right]^{0.5} \left(\frac{c_{p,liq}\left(T_{surf} - T_{sat}\right)}{C_{sf} h_{fg} Pr_{liq}^{n}}\right)^{3} \tag{E.4}$$

Design of the two phase fluid separator *b* in the scheme to vapour and liquid stream follows a design of cyclone centrifuge separators used in geothermal plants. The methodology follows recommendations of Crabtree [168] with a schematic diagram in Figure E.1. Two phase fluid enters tangentially; liquid content impinges the wall due to centrifugal force and then flows downward towards liquid outlet; vapour moves up and finally exits through a vertical pipe in the centre. This design is supposed to have moisture removal efficiency above 99.995% for inlet flow velocity of 35 m/s.

Condenser (*f* in the scheme) is designed as a vessel (shell) with a bank of horizontal tubes inside where the heat transfer coefficient is based on commonly accepted correlation with the Nusselt number in form of Equation (E.5) with a value of constant *C* as 0.729 for tubes and modified latent heat h_{fg}' obtained from Equation (E.6). Heat exchange in the liquid phase cooler *(c)* steam cooler as expander emulator *(g)* and feed tank *(d)* are simple tasks of a single phase flow.

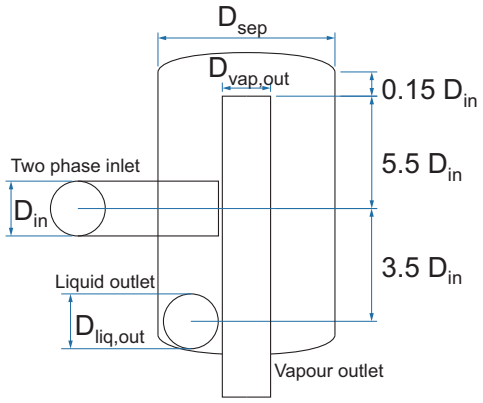

Figure E.1: Schematic representation of two phase geothermal centrifugal separator (modified from [20])

$$Nu_{\text{cond}} = C \cdot \left(\frac{\rho_{\text{liq}}\, g\, (\rho_l - \rho_{\text{vap}})\, h'_{fg} D^3}{\mu_{\text{liq}}\, k_{\text{liq}}\, (T_{\text{sat}} - T_{\text{surf}})} \right)^{1/4} \tag{E.5}$$

$$h'_{fg} = h_{fg} + 0.68 c_{p,liq} (T_{sat} - T_{surf}) \tag{E.6}$$

Sizing of desorber has been done for the operation at pressure 15-100 kPa and concentrations have been chosen for simplicity and comfort of operation. With the heat input 12.9 kW, LiBr weak solution concentration at desorber inlet 30% and temperature of inlet 30°C, for an outlet at 120°C the liquid concentration will be 60%, and mass flow will be half of the overall weak solution flow 7 $g \cdot s^{-1}$. Tube-in-tube design with LiBr solution inside requires a spiral from a steel rod in the annulus for higher oil velocities and thus higher heat transfer coefficients. With inner tube 57x2 mm and outer tube 70x2 mm there is a required heated length of about 3 m. Custom made thermocouple wells are inbuilt into both LiBr solution and oil streams respectively, to obtain temperature development of each medium. One of the desorber elements is shown in Figure E.2. Desorber is installed into the rig in a way that allows modification of its angle to get flow pattern that is most beneficial for the temperature glide of bulk fluid flow.

Separator resulting design has outer dimension as 293 mm high pipe 219.1x3 mm, input pipe dimensions is 38x3 mm and steam outlet pipe 168.3x2 mm. The top lid is arched while the bottom lid covering only the annular space is flat. As the liquid outlet volume is very small, the liquid outlet pipe is used in dimension G1/2".

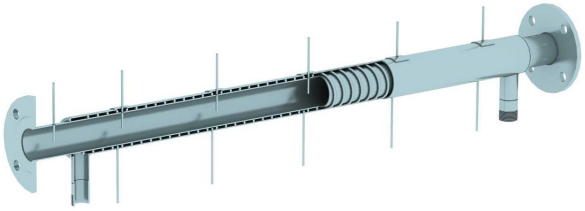

Figure E.2: Element of the desorber.

Other equipment in the LiBr rig includes a condenser requiring heat transfer area 0.12 m^2, where a coil for cooling water from approximately 2 m of G1/2" CATS pipe is inserted into a vessel. In the bottom part is kept a space for sufficient water level for conductivity measurement. Heat exchanger for a separated liquid solution requires 0.07 m2 of heat transfer area and will be of pipe-in-pipe design. Several passes of G1/2" pipe will also be within the collection tank as about 0.3 kW of heat needs to be rejected during a nominal operation and further temperature adjusting of feed solution temperature may prove as beneficial. A magnetically driven micropump MG204 from Topsflo is used as a feeding pump. Thermal oil electric boiler is designed in serial pass configuration with six 2.25 kW heaters. Oil is then circulated by an off the shelf hydraulic gear pump with modified seals to sustain higher temperatures.

Sizing of absorber has been performed as well, however the design has not been manufactured. As the methodology is similar to (and partly simplified from) the design of the absorber in the second test rig, it is not described in this section.

Appendix F

APC proof of concept unit (2^{nd} testrig) design details

This appendix contains supplementary material to the key heat exchangers design of the proof of concept APC unit. Presented are construction details of desorber and absorber along with illustration of the modelled development of selected parameters of interest across them, Figures F.1, F.2, F.3 and F.4.

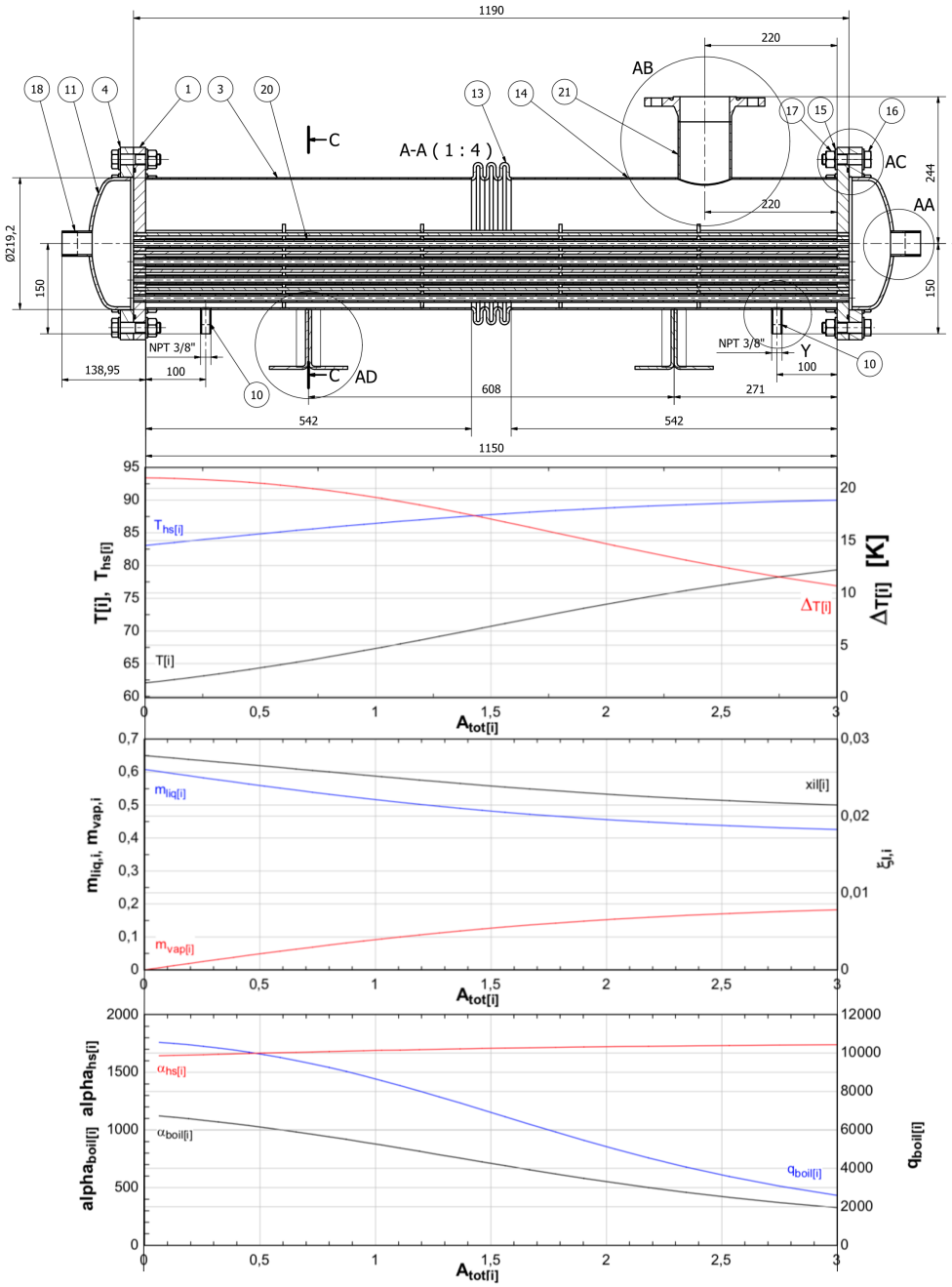

Figure F.1: Front view on the drawing of the desorber assembly with graph of the properties/parameters along the desorber length

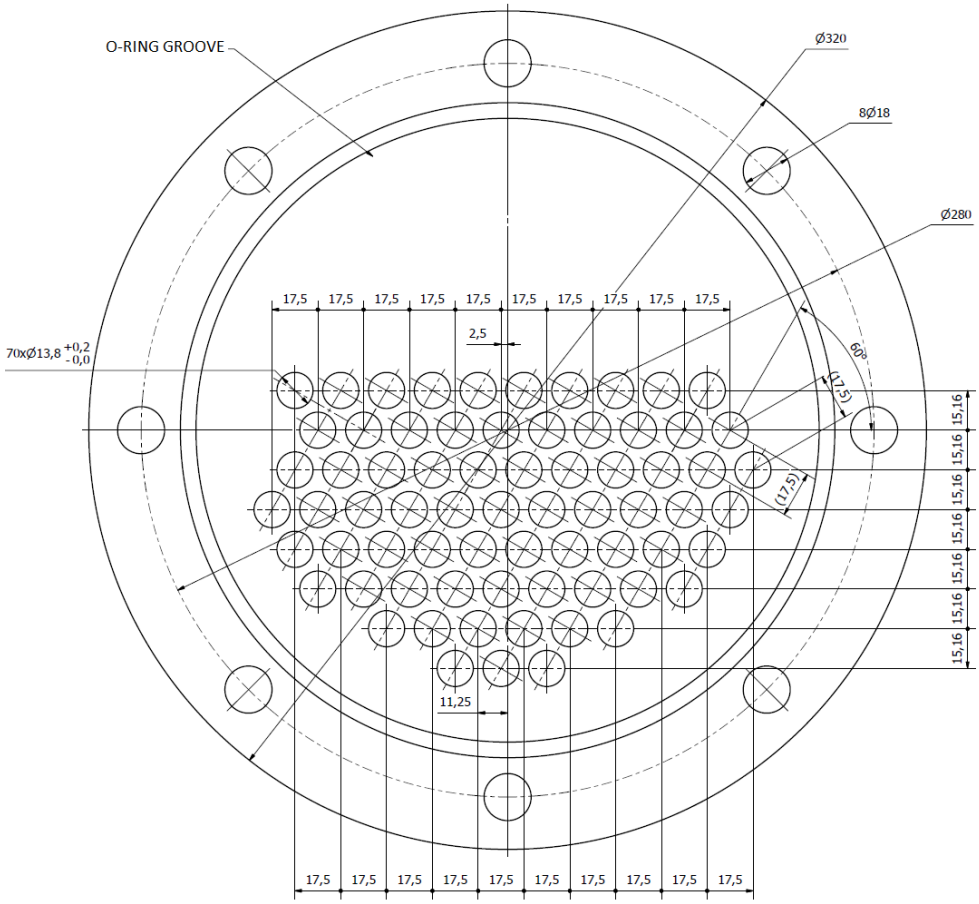

Figure F.2: Tubes arrangement demonstrated on the flange cap of the desorber

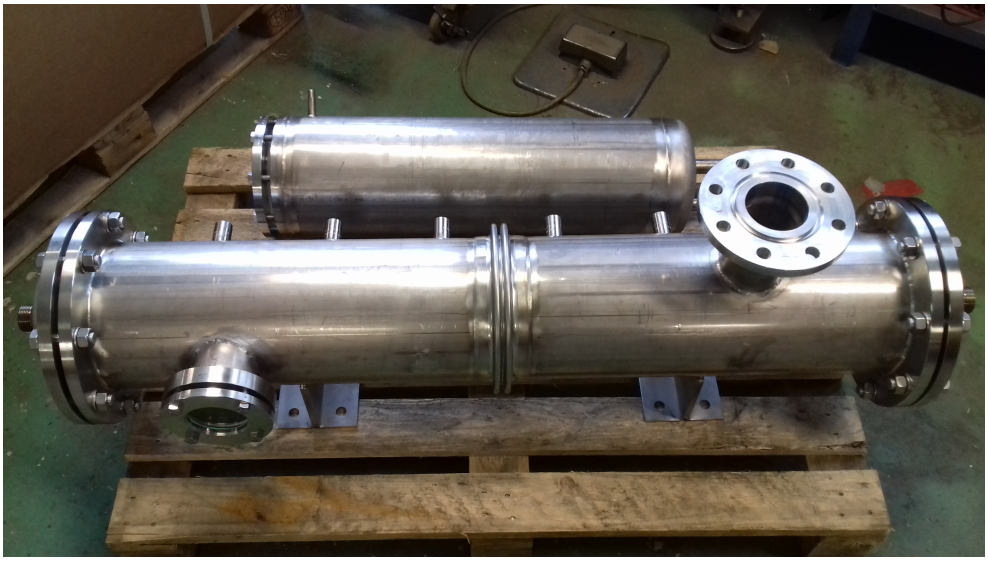

Figure F.3: A photograph of the fabricated desorber (front) and of the solution tank (back)

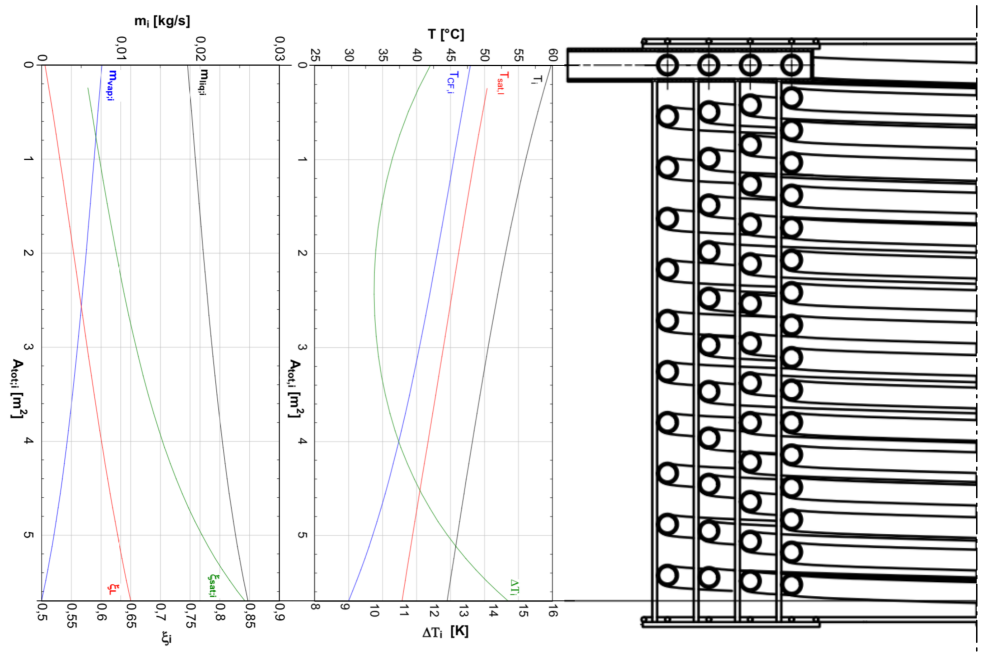

Figure F.4: Front view on a half cut cooling coils bundle alongside with the graphs of temperature and mass flow properties relative to the total surface area

Appendix G

Experimental APC results – charts with full uncertainty error bars

In order to assess the performance with respect to the uncertainties of the measurements and their impact, this section presents the previously provided experimental results including the error bars, Figures G.1, G.2, G.3, G.4, G.5, G.6, G.7, G.8, G.9 and G.10. When two parameters are presented in single chart, e.g. cycle and utilization efficiency below, the uncertainty of the x-axis value is for sake of readability presented only for one of these values. In several cases, only a selection of certain charged solution concentration is presented with uncertainties separately, highlighting the effect of it and related cycle parameters.

The high spread of certain uncertainties comes from several sources. First, mass flow rate of steam is not measured directly but needs to be obtained from solving a system of energy and mass balance equations. Then, some sensors, especially regarding pressure, have at the very low pressures in the vacuum rather high relative error. At the same time however pressure sensors capable of withstanding air overpressures used for leak detection need to be used. Last but not least, since temperature differences of the heat source fluid are often low, this further increases the relative error in heat input into the cycle.

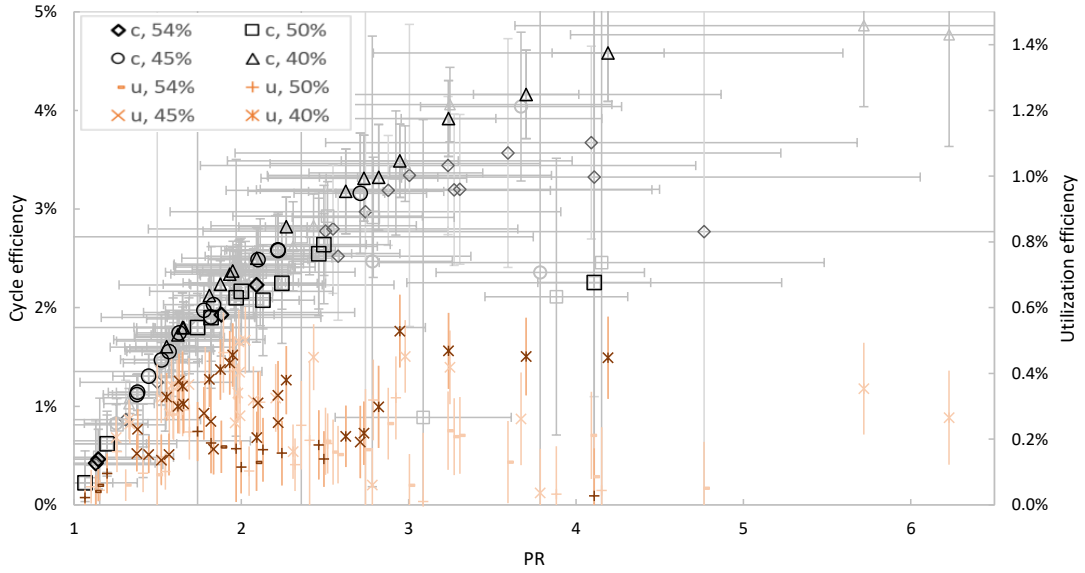

Figure G.1: Cycle and utilization efficiencies (c and u) with included uncertainties as a function of charged LiBr concentration (40-54%) and cycle pressure ratio (PR). Values for hypothetical 65% expander efficiency with "more accurate" states in bold

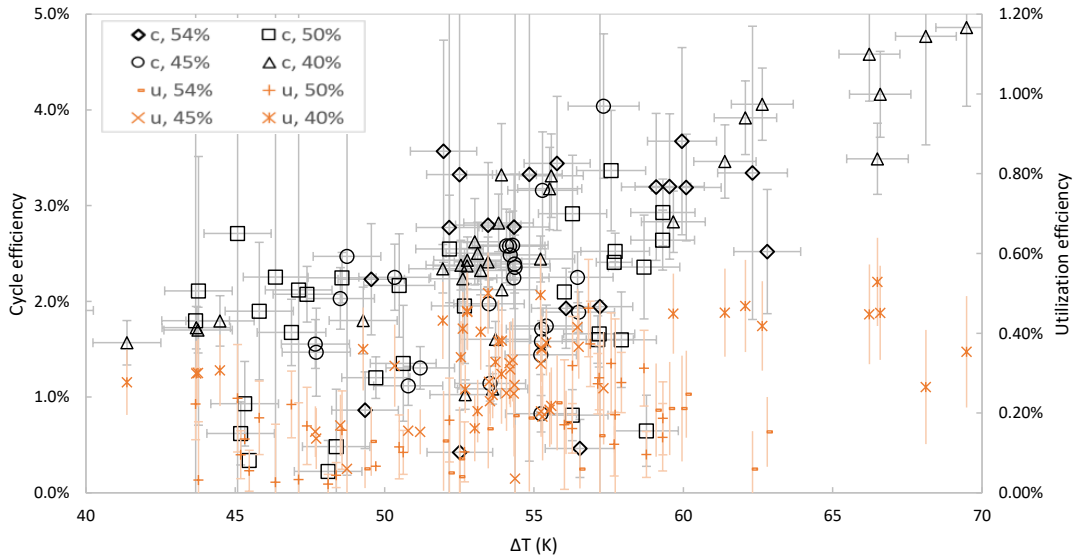

Figure G.2: Cycle and utilization efficiencies (c and u) with included uncertainties as a function of charged LiBr concentration (40-54%) and of the temperature difference ΔT between the heat source and heat sink for hypothetical 65% expander efficiency

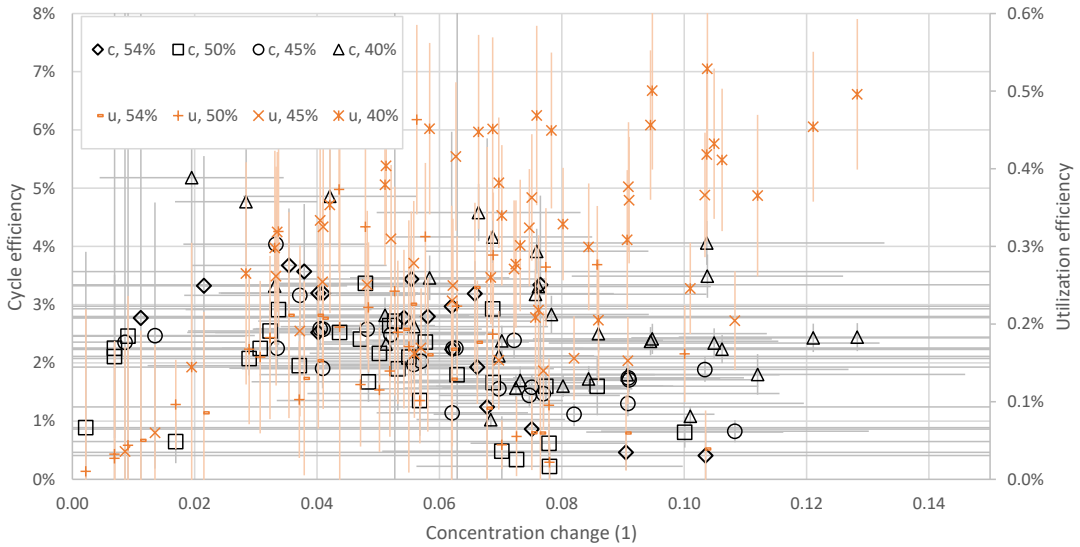

Figure G.3: Cycle and utilization efficiencies (c and u) as a function of charged LiBr concentration (40-54%) and of a concentration change in the cycle for hypothetical 65% expander efficiency, uncertainty plotted for all datapoints

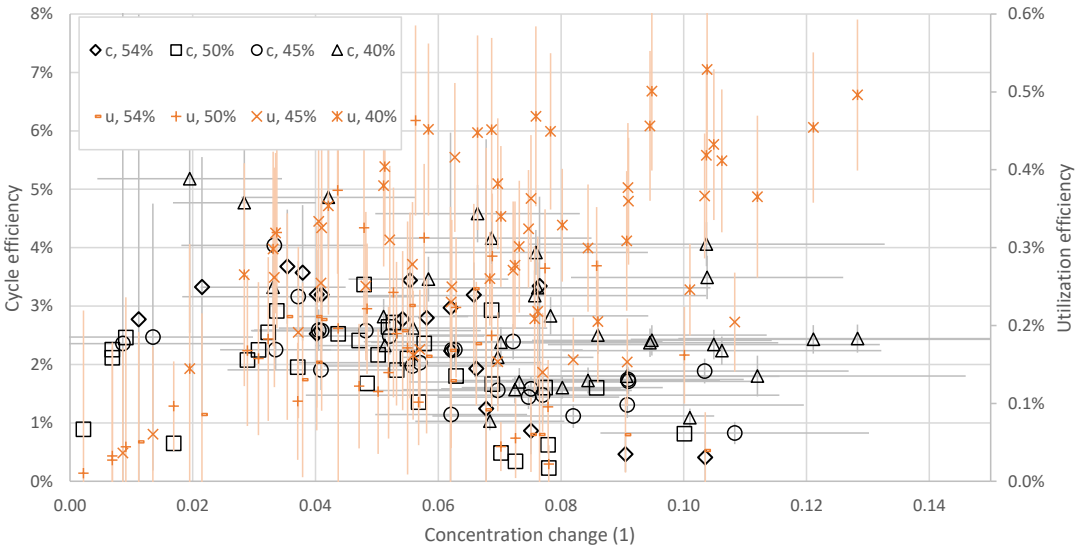

Figure G.4: Cycle and utilization efficiencies (c and u) as a function of charged LiBr concentration (40-54%) and of a concentration change in the cycle for hypothetical 65% expander efficiency, uncertainty plotted only for datapoints of charged concentration 45% and 40%

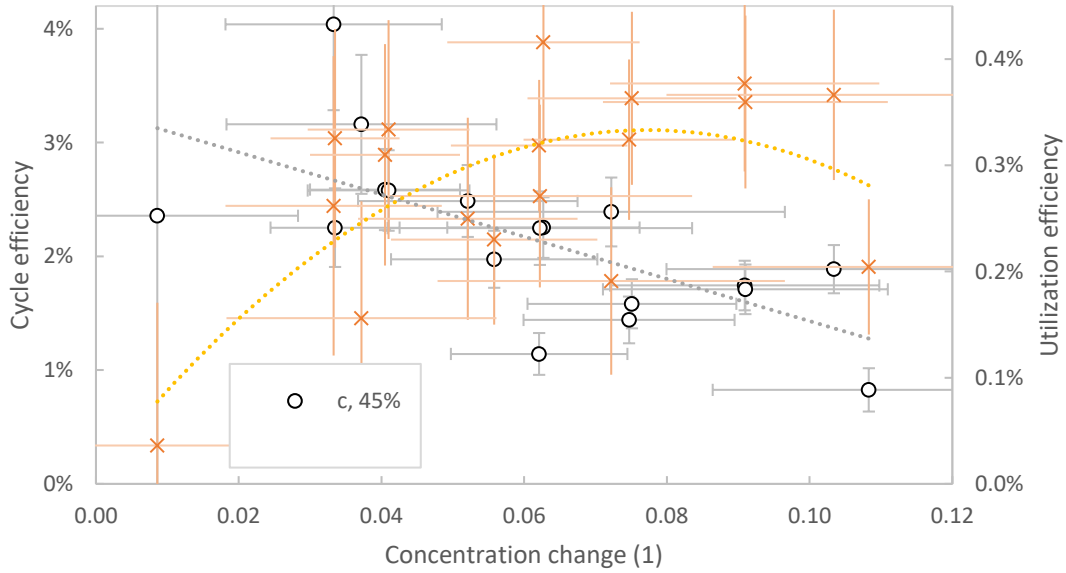

Figure G.5: Detail of cycle and utilisation efficiencies as a function of the solution concentration difference for cases with low heat source and sink inlet temperature and mass flow rate variation

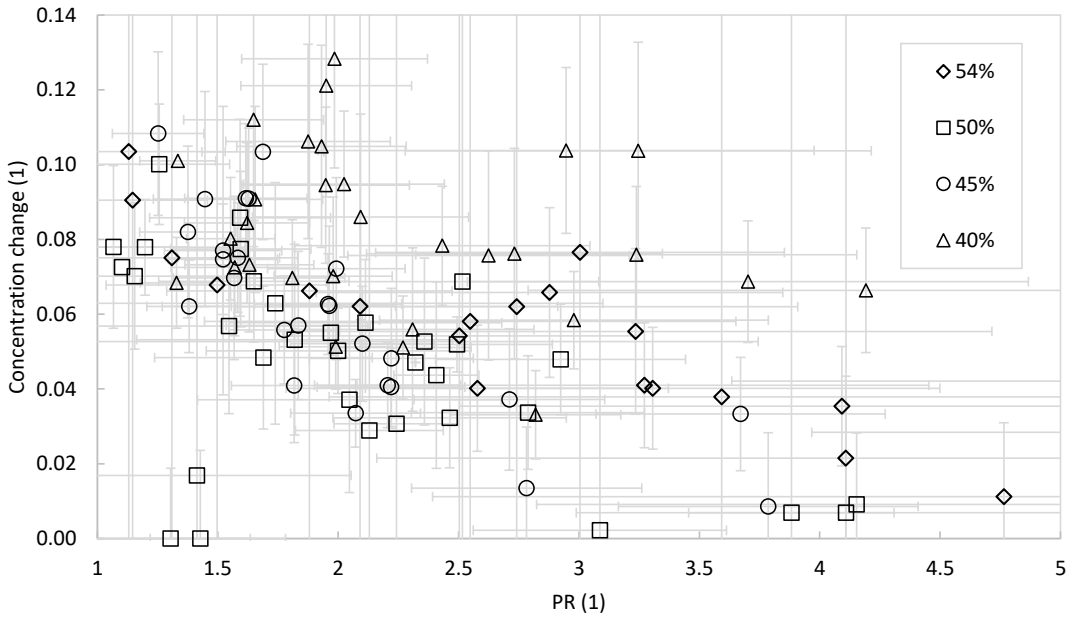

Figure G.6: Concentration change as a function of pressure ratio for all measured states, uncertainty plotted for all datapoints

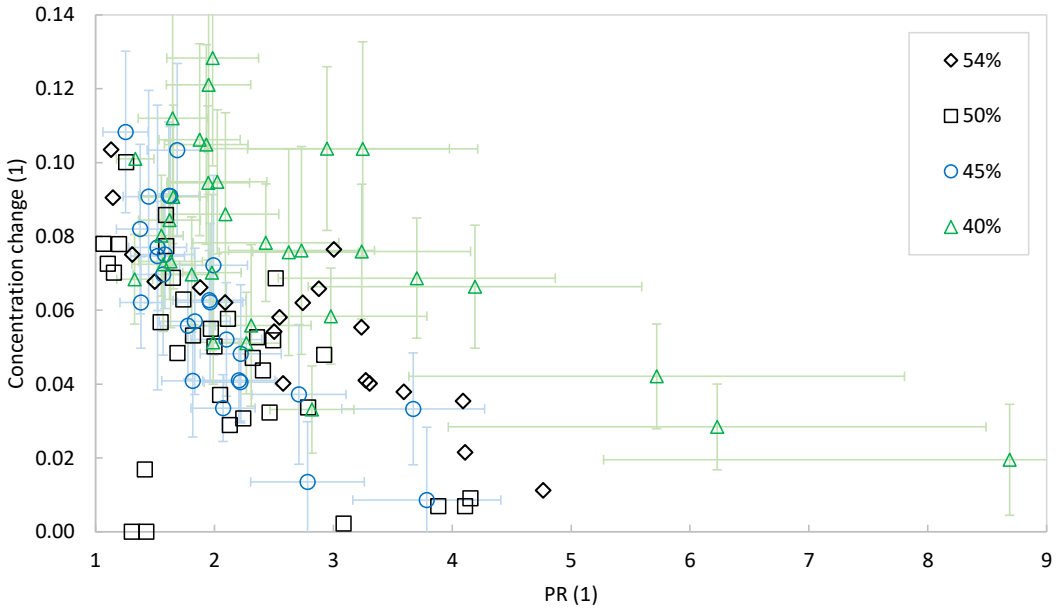

Figure G.7: Concentration change as a function of pressure ratio for all measured states, displayed additional points of very high pressure ratio, uncertainty plotted only for datapoints of charged concentration 45% and 40%

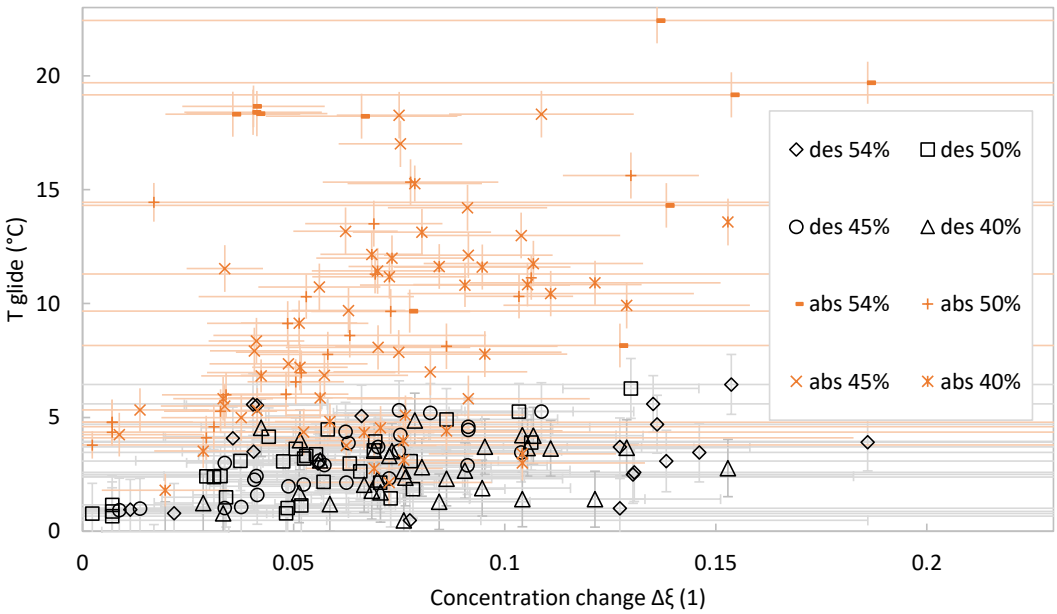

Figure G.8: Temperature glide as a function of concentration change for all measured states, uncertainty plotted for all datapoints

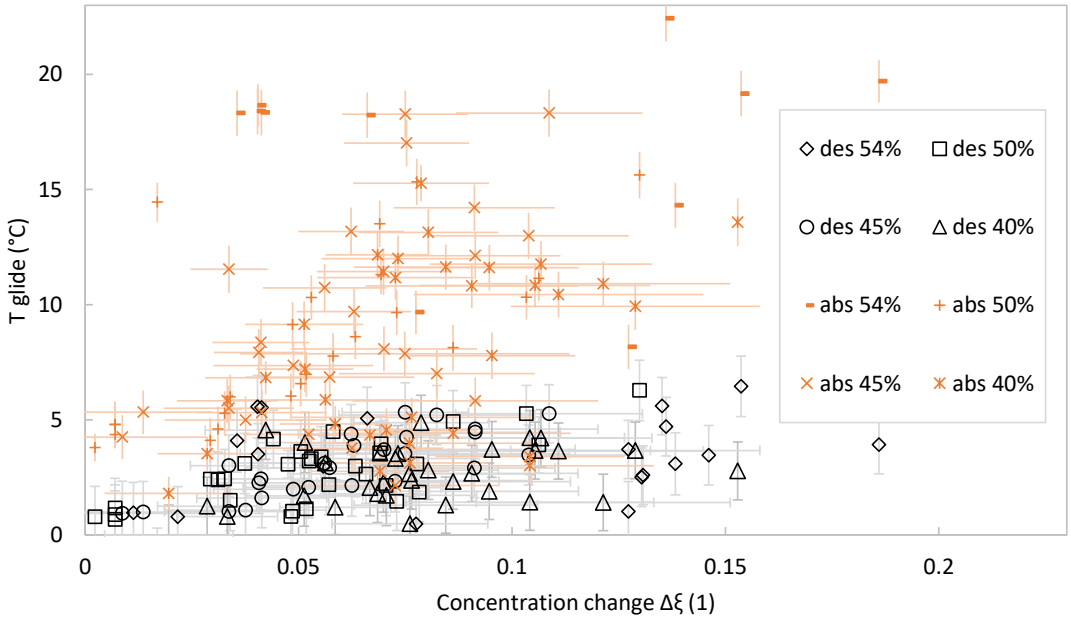

Figure G.9: Temperature glide as a function of concentration change for all measured states, uncertainty in x-axis plotted only for datapoints of charged concentration 45% and 40%

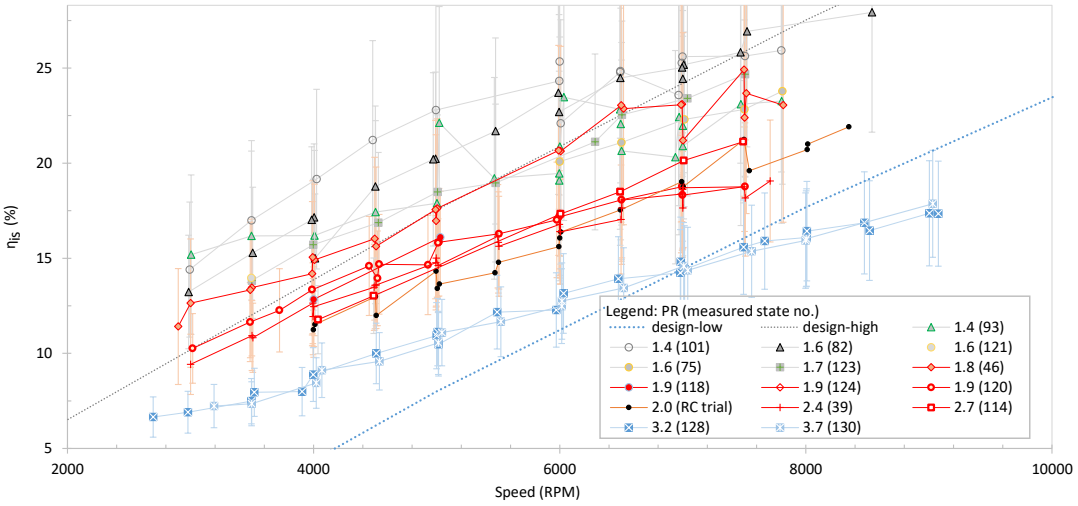

Figure G.10: Measured turbine characteristics from APC operation for states with higher accuracy with included uncertainties

Appendix H

Axial turbine design

Computation models and supplementary results regarding designing of the turbines are in detail described here. First, a detailed description of the axial air turbine model is presented. Following is a sensitivity analysis of the air turbine results for a nominal case. Finally modifications used in design of the APC turbine are provided.

H.1 Axial air turbine model

The model of the turbine, described also in author's work [Sc15] is based on a mass and energy balance in the stator and rotor vanes and accounting for major pressure and energy losses. The principle of calculation follows a traditional methodology developed by the turbine manufacturer, Skoda Power company, and in detail described by Kadrnozka [220] or Ambroz [221]. The model was built in the Engineering Equation Solver, in which also the sensitivity analysis and optimization with respect to its parameters took place. In the model, the nozzles entry is denoted as state 0. The absolute velocity component of the fluid after the nozzles (in turbine stages denoted as state 1) is given by Equation (H.1) with reaction degree R considered zero. Then, it is decreased to actual velocity by friction, reflected in calculation by velocity coefficient φ and from energy balance is then determined steam enthalpy after expansion, Equation (H.2). Tangential velocity component is in relation with chosen speed (revolutions per second) n and mean diameter of vanes D_1 given by Equation (H.3). Relative velocity w_1 and subsequently relative velocity in the exit from rotor blades (in turbine stages denoted as state 2) w_2 is then obtained from velocity triangle and velocity coefficient ψ given by Equation (H.4).

$$c_{1,is} = \sqrt{{c_0}^2 + 2 \cdot (1 - R) \cdot \Delta h_{is} \cdot 1000} = \frac{c_1}{\varphi} \tag{H.1}$$

$$h_1 = h_{1,is} + 0.5\left(c_{is,1}^2 - c_1^2\right)/1000 \tag{H.2}$$

$$u = 0.5 \cdot D_1 \cdot \omega \tag{H.3}$$

$$w_1 = \sqrt{c_1^2 + u^2 - 2 \cdot c_1 \cdot u \cdot \cos\alpha_1} = w_{2,is} = \frac{w_2}{\psi} \tag{H.4}$$

Stator vanes length without partial admission (theoretical) $l_{1,th}$ is based on continuity equation, Equation (H.5) with outflow coefficient μ_1 and flow angle α_1 (angles are referenced to radial plane and taken for both rotor and stator as positive). The ratio of theoretical and actual blade length defines the partial admission parameter e. Actual blade length is then subject to optimization. Rotor blades are based on the rule of thumb 1 mm longer than stator vanes. Mean diameter is used same for the stator vanes and rotor blades. Continuity Equation (H.6) in the relative system is used to determine exit angle of steam from rotor blades β_2. Absolute outlet velocity is determined from the velocity triangle, Equation (H.7). Subsequently, there are determined energy losses. First, so-called primary losses are given by friction (and related velocity loss) in turbine nozzles z_s, in rotor blades z_r and by outlet kinetic energy z_v, Equation (H.8)–(H.10), summed then to $\sum z$. Following that are for the stage determined additional losses, Equation (H.11)- (H.15), namely secondary flow loss due to limited blade length ξ_o, partial admission loss ξ_{pa}, windage loss ξ_w, disc friction loss ξ_k, loss by variable velocity field along constant angle (non-twisted) blade length ξ_{vv}, altogether $\sum \xi$. Eventually, other correlations for many these losses exist when subsequent evaluation of their suitability is also a subject of experimental evaluation. As it is impulse stage, leakage flow is at this point neglected, however, in reality, some will also take place. Turbine "primary" efficiency (used for ξ_{pa}) is given by Equation (H.16) and finally isentropic efficiency by Equation (H.17). Mechanical and electrical efficiency is at design point unknown and will be dependent on the generator as will be described further. Constants and parameters assumed or estimated from the reference in the design of the turbine are summarized in Table H.1.

$$m \cdot v_{1,is} = \mu_1 \cdot \pi \cdot D_1 \cdot l_{1,th} \cdot c_{1,is} \cdot \sin\alpha_1 \tag{H.5}$$

$$m \cdot v_{1,is} = \mu_2 \cdot \pi \cdot D_2 \cdot l_2 \cdot w_{2,is} \cdot \sin\beta_2 \cdot e \tag{H.6}$$

$$c_2 = \sqrt{w_2^2 + u^2 - 2 \cdot w_2 \cdot u \cdot \cos\beta_2} \tag{H.7}$$

Table H.1: Non-dimensional coefficients used for turbine design

φ	ψ	μ_1	μ_2	K
0.98	0.95	0.98	0.94	0.0314

$$z_S = \frac{c_{1,is}^2}{2} \cdot \left(1 - \varphi^2\right) \tag{H.8}$$

$$z_r = \frac{w_{2,is}^2}{2} \cdot \left(1 - \psi^2\right) \tag{H.9}$$

$$z_v = \frac{c_2^2}{2} \tag{H.10}$$

$$\xi_o = 9.9 \cdot \frac{\left(u/c_{1,is}\right)^2}{l_1} \tag{H.11}$$

$$\xi_{pa} = 0.25 \cdot \frac{{l_2}^2}{\pi \cdot D_1 \cdot l_1 \cdot \sin\left(\alpha_1\right) \cdot e} \cdot \frac{u}{c_{1,is}} \cdot i \cdot \eta_u \tag{H.12}$$

$$\xi_w = \left(0.04 + 0.5 \cdot \frac{l_1}{D_1}\right) \cdot \frac{1 - e}{e \cdot \sin\left(\alpha_1\right)} \cdot \left(\frac{u}{c_{1,is}}\right)^3 \tag{H.13}$$

$$\xi_k = K \cdot \frac{\left(D_1 - l_2\right)^2}{\pi \cdot D_1 \cdot l_1 \cdot e \cdot \sin\left(\alpha_1\right)} \cdot \left(\frac{u}{c_{1,is}}\right)^3 \tag{H.14}$$

$$\xi_{vv} = 0.77 \cdot \left(\frac{l_2}{D_2}\right)^2 \tag{H.15}$$

$$\eta_u = \frac{\Delta h_{is} - z_r - z_o - z_v}{\Delta h_{is}} \tag{H.16}$$

$$\eta_{is} = \frac{\Delta h_{is} - z_r - z_o - z_v}{\Delta h_{is}} - \left(\xi_o + \xi_{pa} + \xi_w + \xi_k + \xi_{vv}\right) \tag{H.17}$$

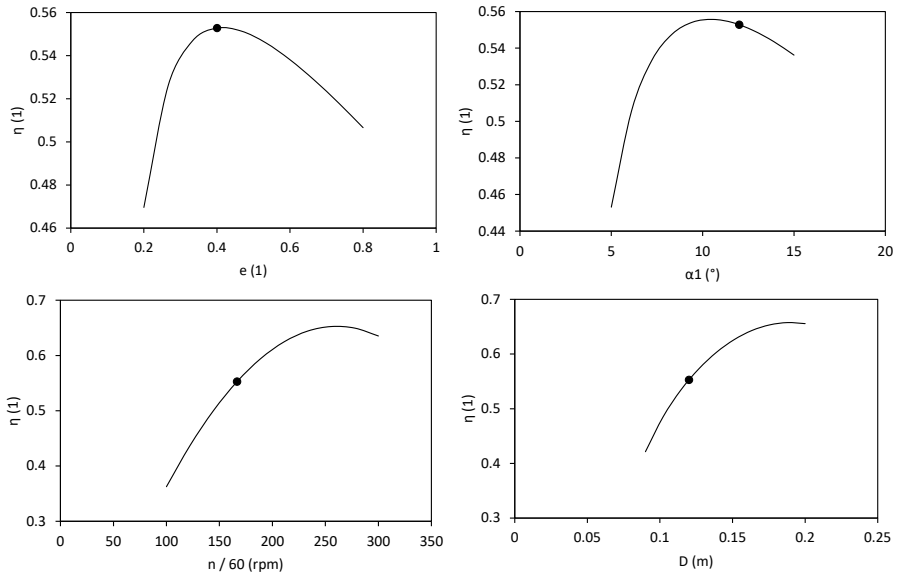

Figure H.1: Sensitivity analysis of efficiency for partial admission, nozzle outlet angle, speed and diameter. Orange point shows the design point.

H.2 Sensitivity analysis of axial air turbine parameters

Additionally to previous results, Figure H.1 shows a sensitivity analysis of the efficiency on main parameters based on the 1D model (for the 2.2 kW design). It shows that the model is optimized with respect to partial admission (blade length balances between secondary flow loss and loss caused by partial admission), is a bit behind the maximum regarding nozzles the nozzle outlet angle (due to manufacturability). Limitation by both diameter and speed shows that both of these parameters are below optimal values and for further analyses would be beneficial to increase one or another.

H.3 Alternative correlations used in APC turbine

According to the design of the turbine model, the isentropic velocity is corrected by velocity coefficients which, together with correlations for other secondary losses (partial admission, secondary flow – horseshoe vortex loss, passage vortex loss, disc friction-ventilation loss and profile loss) and flow coefficients taken again from [221]. Several aspects are however different and at some points different correlations were used. Specifically, these are:

- Disc friction loss was neglected due to its extremely small contribution in comparison to other losses

Table H.2: Alternative parameters in turbine design used for the APC turbine

φ	φ_{conv}	ψ	μ_1	μ_2
0.9	0.94	0.88	0.9	0.8

- Several combinations of loss models were applied to provide a range of results (based on previous air turbine results)
- Velocity coefficients were taken as one alternative from specific charts in the reference (but then secondary loss should be included in the value). Additionally stator nozzle was split to convergent and overall section, each with different velocity coefficient – see Table H.2.
- Effect of alternative approach of secondary flow loss suggested for short blades in following form was explored:

$$\xi_o = \frac{1.5}{l_2} \, (l_2 \text{ in mm}) \tag{H.18}$$

- Since the design is supersonic, the throat area was determined iteratively by a solver as a point of a real expansion, where the actual velocity (isentropic corrected by convergent nozzle velocity coefficient) was identical with calculated speed of sound. The enthalpy in that point is then obtained as the inlet enthalpy lower by the energy content in the fluid velocity

Appendix I

Isentropic efficiency evaluation method for air turbines

To obtain the isentropic power for the fluid isentropic expansion process, mass flow rate is evaluated from the measured volumetric flow rate. Enthalpy and entropy at the inlet are calculated using fluid properties and for the inlet enthalpy, isentropic outlet enthalpy is evaluated. Isentropic power is then Equation (I.1):

$$\dot{W}_{is} = \dot{m} \cdot (h_1 - h_{3is}) \tag{I.1}$$

The measured power output is evaluated from the electrical current and voltage as Equation (I.2):

$$\dot{W}_{el_{meas}} = U \cdot I \tag{I.2}$$

Power loss at the rectifier is added to that, assuming a constant voltage drop of 1.5 V over two low-drop diodes in a rectifier bridge Equation (I.3):

$$\dot{W}_{\text{rect}} = \Delta U_{\text{rect}} \cdot I \tag{I.3}$$

From the electrical power and rotational speed, initial guess of the torque is calculated Equation (I.4):

$$T = \frac{\left(\dot{W}_{el_{\text{meas}}} + \dot{W}_{\text{rect}}\right)}{\omega} \tag{I.4}$$

Electrical efficiency of the generator is calculated by the measured characteristics provided by tool E-Calc for certain rotational speed and torque and is generally characterised by Equation (I.5). These data have been obtained experimentally for each generator (BLDC motor) type. An assumption of equal efficiency in motor and generator regime is presumed for the same mechanical power on the shaft.

$$\eta_g = f(n, T) \tag{I.5}$$

With the electrical efficiency (including also bearing friction losses), a new value of torque is calculated, and this process is repeated iteratively. This process was automated using VBA macros and GoalSeek function. The generator efficiency 2-D plot is illustrated in Figure I.1. The automatic iteration loop then uses this 2-D map for bilinear interpolation of the efficiency value according to the formula in Equation (I.6) below with indexes correspond to a matrix 2,2 within of which bordering value the torque and speed are.

$$\begin{aligned}\eta_g(n,T) \approx \frac{1}{\{(n_{\{2\}}-n_{\{1\}})(T_{\{2\}}-T)\}} \cdot (\eta_{g\{11\}} \cdot (n_{\{2\}} - n) \cdot (T_{\{2\}} - T) \\ +\eta_{g\{21\}} \cdot (n - n_{\{1\}}) \cdot (T_{\{2\}} - T) + \eta_{g\{12\}} \cdot (n_{\{2\}} - n) \cdot (T - T_{\{1\}}) \\ +\eta_{g\{22\}} \cdot (n - n_{\{1\}}) \cdot (T - T_{\{1\}}))[-]\end{aligned} \tag{I.6}$$

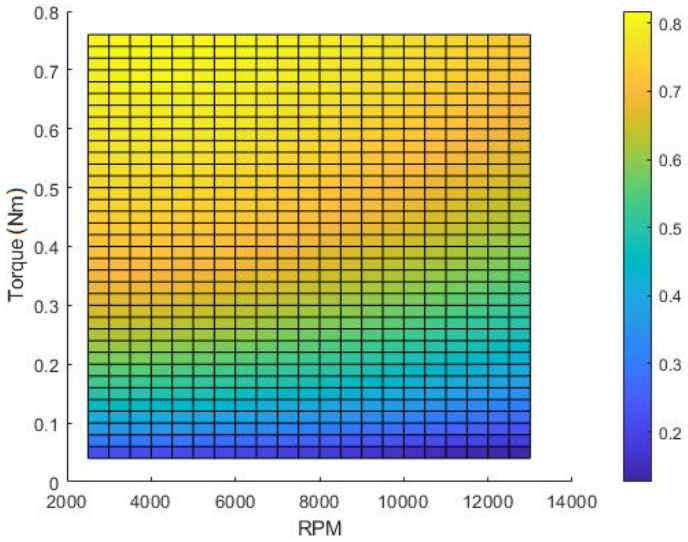

Figure I.1: Electrical efficiency map of Turnigy SK3-6364-245 generator as a function of rpm and torque, obtained from the E-Calc tool.

Mechanical power can be then calculated using the iterated electrical efficiency of the generator as in Equation (I.7):

$$\dot{W}_{\text{mech}} = \frac{(W_{\text{el meas}} + W_{\text{rect}})}{\eta_g} \tag{I.7}$$

Mechanical power divided by isentropic power gives the final and desired value of the isentropic efficiency at each steady state of each assembly at a given pressure ratio, as seen in Equation (I.8). These values are then used to plot the efficiency charts as a function of the rotational speed at a certain pressure ratio. Note that mechanical losses such as in bearing are included in generator efficiency. In the nominator the term can be substituted by respective electrical output to evaluate net or gross electrical efficiency of the turbogenerator. Primary aim of the work at this point focuses however on expander isentropic efficiency.

$$\eta_{is} = \frac{\dot{W}_{mech}}{W_{is}} \tag{I.8}$$

Author's Scopus / WoS publications

[Sc1] V. Novotny, V. Basta, P. Smola, J. Spale, Review of carnot battery technology commercial development, Energies 15 (2) (2022). doi:10.3390/en15020647.

[Sc2] V. Novotny, J. Spale, D. Szucs, H.-Y. Tsai, M. Kolovratnik, Direct integration of an organic rankine cycle into an internal combustion engine cooling system for comprehensive and simplified waste heat recovery, Energy Reports 7 (2021) 644–656, cited By 0. doi:10.1016/j.egyr.2021.07.088.
URL https://www.scopus.com/inward/record.uri?eid=2-s2.0-85119612595&doi=10.1016%2fj.egyr.2021.07.088&partnerID=40&md5=7970da7d797273fe07d07aaaef6aa945

[Sc3] V. Novotny, D. Szucs, J. Spale, H.-Y. Tsai, M. Kolovratnik, Absorption power and cooling combined cycle with an aqueous salt solution as a working fluid and a technically feasible configuration, Energies 14 (12), cited By 0 (2021). doi:10.3390/en14123715.
URL https://www.scopus.com/inward/record.uri?eid=2-s2.0-85109023466&doi=10.3390%2fen14123715&partnerID=40&md5=73bbb3110ec6bc0d1ec4cb9b942b0b5d

[Sc4] V. Novotny, J. Spale, D. Suchna, J. Pavlicko, M. Kolovratnik, A. Weiss, Absorption power cycle with a 3d-printed plastic micro turboexpander - considerations, design and first experimental results, Vol. 2323, 2021, cited By 1. doi:10.1063/5.0041429.
URL https://www.scopus.com/inward/record.uri?eid=2-s2.0-85102741879&doi=10.1063%2f5.0041429&partnerID=40&md5=559f861fb7ed56ebc4580ae8c6cf1f72

[Sc5] J. Spale, V. Novotny, V. Mares, A. Weiss, 3d printed radial impulse cantilever micro-turboexpander for preliminary air testing, Vol. 2323, 2021, cited By 1. doi:10.1063/5.0041433.
URL https://www.scopus.com/inward/record.uri?eid=2-s2.0-85102736059&doi=10.1063%2f5.0041433&partnerID=40&md5=fe9897781b714ed24c416bf5ea4e1fa8

[Sc6] J. Mascuch, V. Novotny, J. Spale, V. Vodicka, Z. Zeleny, Experience from set-up and pilot operation of an in-house developed biomass-fired orc microcogeneration unit, Renewable Energy 165 (2021) 251–260, cited By 4. doi:10.1016/j.renene.2020.11.021.
URL https://www.scopus.com/inward/record.uri?eid=2-s2.0-85096169840&doi=10.1016%2fj.renene.2020.11.021&partnerID=40&md5=edf50c5e7ec452fc06e718e47e33e38e

[Sc7] A. Weiss, V. Novotny, T. Popp, P. Streit, J. Spale, G. Zinn, M. Kolovratnik, Customized orc micro turbo-expanders - from 1d design to modular construction kit and prospects of additive manufacturing, Energy 209, cited By 8 (2020). doi:10.1016/j.energy.2020.118407.
URL https://www.scopus.com/inward/record.uri?eid=2-s2.0-85089280227&doi=10.1016%2fj.energy.2020.118407&partnerID=40&md5=c4bc463c06afd32f3b1d993c90343dcb

[Sc8] S. Roussanaly, M. Vitvarova, R. Anantharaman, D. Berstad, B. Hagen, J. Jakobsen, V. Novotny, G. Skaugen, Techno-economic comparison of three technologies for pre-combustion co2 capture from a lignite-fired igcc, Frontiers of Chemical Science and Engineering 14 (3) (2020) 436–452, cited By 10. doi:10.1007/s11705-019-1870-8.
URL https://www.scopus.com/inward/record.uri?eid=2-s2.0-85067044729&doi=10.1007%2fs11705-019-1870-8&partnerID=40&md5=5be0be82d22e922138f830f202c2a667

[Sc9] J. Mascuch, V. Novotny, V. Vodicka, J. Spale, Z. Zeleny, Experimental development of a kilowatt-scale biomass fired micro â chp unit based on orc with rotary vane expander, Renewable Energy 147 (2020) 2882–2895, cited By 22. doi:10.1016/j.renene.2018.08.113.
URL https://www.scopus.com/inward/record.uri?eid=2-s2.0-85052945950&doi=10.1016%2fj.renene.2018.08.113&partnerID=40&md5=10f5d4413671a142f23ac3750a3a9a23

[Sc10] V. Novotny, M. Vitvarova, J. Spale, J. Jakobsen, Intermediate pressure reboiling in geothermal flash plant for increased power production and more effective non-condensable gas abatement, Energy Reports 6 (2020) 20–27, cited By 0. doi:10.1016/j.egyr.2019.10.014.
URL https://www.scopus.com/inward/record.uri?eid=2-s2.0-

85075485344&doi=10.1016%2fj.egyr.2019.10.014&partnerID=40&md5=056d6d1a5f1322896681a09aa1eb4d7a

[Sc11] A. Weiss, P. Streit, T. Popp, P. Shoemaker, T. Hildebrandt, V. Novotny, J. Spale, Uncommon turbine architectures for distributed power generation - development of a small velocity compounded radial re-entry turbine, Archives of Thermodynamics 41 (4) (2020) 235–253, cited By 2. doi:10.24425/ather.2020.135862.
URL https://www.scopus.com/inward/record.uri?eid=2-s2.0-85107388514&doi=10.24425%2father.2020.135862&partnerID=40&md5=fbfc41da4746b1eb23b5d43922c599d5

[Sc12] V. Novotny, D. Szucs, M. Kolovratnik, T. Matuska, Simulation of absorption power cycle and organic rankine cycle using evacuated tube solar collectors, Vol. 2020-July, 2020, pp. 600–607, cited By 0. doi:10.18462/iir.rankine.2020.1227.
URL https://www.scopus.com/inward/record.uri?eid=2-s2.0-85099297323&doi=10.18462%2fiir.rankine.2020.1227&partnerID=40&md5=912a8038a7948b4f76f6ac43747c897b

[Sc13] V. Novotny, D. Szucs, J. Spale, V. Vodicka, J. Mascuch, M. Kolovratnik, Investigation of novel configuration for dual organic rankine cycle configurations for maximization of waste heat utilization, Vol. 2020-July, 2020, pp. 36–43, cited By 0. doi:10.18462/iir.rankine.2020.1108.
URL https://www.scopus.com/inward/record.uri?eid=2-s2.0-85099287207&doi=10.18462%2fiir.rankine.2020.1108&partnerID=40&md5=fcd9654eb3ccea23c1d027efa41f76f5

[Sc14] V. Vodicka, V. Novotny, Z. Zeleny, J. Mascuch, M. Kolovratnik, Theoretical and experimental investigations on the radial and axial leakages within a rotary vane expander, Energy 189, cited By 16 (2019). doi:10.1016/j.energy.2019.116097.
URL https://www.scopus.com/inward/record.uri?eid=2-s2.0-85072619522&doi=10.1016%2fj.energy.2019.116097&partnerID=40&md5=de749ad39001c702b2afc29f79fecaa7

[Sc15] V. Novotny, M. Vitvarova, M. Kolovratnik, B. Stunova, V. Vodicka, J. Spale, P. Zikmund, M. Drasnar, E. Schastlivtseva, Design and manufacturing of a metal 3d printed kw scale axial turboexpander, Vol. 8, 2019, cited By 4. doi:10.1115/GT2019-91822.
URL https://www.scopus.com/inward/record.uri?eid=2-s2.0-85075807438&doi=10.1115%2fGT2019-91822&partnerID=40&md5=550115481e816b79861d49f8d7ab9bbd

[Sc16] V. Novotny, D. Suchna, M. Kolovratnik, Experimental rig for libr-water absorption power cycle - design and first experimental results, Vol.

2047, 2018, cited By 1. doi:10.1063/1.5081646.
URL https://www.scopus.com/inward/record.uri?eid=2-s2.0-85060859320&doi=10.1063%2f1.5081646&partnerID=40&md5=d8e07f5bd591ade18553e2f7daeb79db

[Sc17] J. Mascuch, V. Novotny, M. Tobias, Economic aspects of micro-cogeneration systems - insight into investors' approaches, 2018, pp. 1–5, cited By 2. doi:10.1109/SCSP.2018.8402654.
URL https://www.scopus.com/inward/record.uri?eid=2-s2.0-85050312176&doi=10.1109%2fSCSP.2018.8402654&partnerID=40&md5=7857124cd394220aa5f9b897bc481d60

[Sc18] V. Novotny, J. Dobes, D. Hrabal, Implementing large scale electromobility infrastructure as a profitable virtual electricity storage plant: A case study, system alise, 2018, pp. 1–6, cited By 1. doi:10.1109/SCSP.2018.8402647.
URL https://www.scopus.com/inward/record.uri?eid=2-s2.0-85050303332&doi=10.1109%2fSCSP.2018.8402647&partnerID=40&md5=3a9d6ad237584f56739ed1f7576176d2

[Sc19] V. Vodicka, V. Novotny, J. Mascuch, Wear behaviour of vanes for a rotary vane expander with various graphite materials under dry sliding conditions, Acta Polytechnica 58 (5) (2018) 315–322, cited By 3. doi:10.14311/AP.2018.58.0315.
URL https://www.scopus.com/inward/record.uri?eid=2-s2.0-85063225648&doi=10.14311%2fAP.2018.58.0315&partnerID=40&md5=9abcfe1f47b8d5705d021d4e00f81f72

[Sc20] V. Novotny, M. Vitvarova, M. Kolovratnik, Absorption power cycles with various working fluids for exergy-efficient low-temperature waste heat recovery, Green Energy and Technology (2018) 99–111Cited By 3. doi:10.1007/978-3-319-89845-2_8.
URL https://www.scopus.com/inward/record.uri?eid=2-s2.0-85051107235&doi=10.1007%2f978-3-319-89845-2_8&partnerID=40&md5=c87fb95459a554b395c138be3e71725f

[Sc21] V. Novotny, M. Kolovratnik, Absorption power cycles for low-temperature heat sources using aqueous salt solutions as working fluids, International Journal of Energy Research 41 (7) (2017) 952–975, cited By 25. doi:10.1002/er.3671.
URL https://www.scopus.com/inward/record.uri?eid=2-s2.0-85028254425&doi=10.1002%2fer.3671&partnerID=40&md5=326621401aea73321491c73de46a7e75

[Sc22] V. Vodicka, V. Novotny, J. Mascuch, M. Kolovratnik, Impact of major leakages on characteristics of a rotary vane expander for orc, Vol. 129,

2017, pp. 387–394, cited By 22. doi:10.1016/j.egypro.2017.09.249.
URL https://www.scopus.com/inward/record.uri?eid=2-s2.0-85029767415&doi=10.1016%2fj.egypro.2017.09.249&partnerID=40&md5=92a52a3d50a1fc638c44d4b7166c96aa

[Sc23] V. Novotny, V. Vodicka, J. Mascuch, M. Kolovratnik, Possibilities of water-lithium bromide absorption power cycles for low temperature, low power and combined power and cooling systems, Vol. 129, 2017, pp. 818–825, cited By 11. doi:10.1016/j.egypro.2017.09.104.
URL https://www.scopus.com/inward/record.uri?eid=2-s2.0-85029764885&doi=10.1016%2fj.egypro.2017.09.104&partnerID=40&md5=1cf6e8aaf45c4311b4d29877312cedc4

[Sc24] Z. Zeleny, V. Vodicka, V. Novotny, J. Mascuch, Gear pump for low power output orc - an efficiency analysis, Vol. 129, 2017, pp. 1002–1009, cited By 19. doi:10.1016/j.egypro.2017.09.227.
URL https://www.scopus.com/inward/record.uri?eid=2-s2.0-85029764359&doi=10.1016%2fj.egypro.2017.09.227&partnerID=40&md5=42372595ac7c3a6976546cd234888908

[Sc25] J. Mascuch, V. Novotny, V. Vodicka, Z. Zeleny, Towards development of 1-10 kw pilot orc units operating with hexamethyldisiloxane and using rotary vane expander, Vol. 129, 2017, pp. 826–833, cited By 16. doi:10.1016/j.egypro.2017.09.196.
URL https://www.scopus.com/inward/record.uri?eid=2-s2.0-85029742581&doi=10.1016%2fj.egypro.2017.09.196&partnerID=40&md5=892260a183741455296d8d80c823f6da

[Sc26] V. Novotny, J. Mascuch, H.-Y. Tsai, M. Kolovratnik, Design of experimental rig for validation of absorption power cycle concept, Vol. 105, 2017, pp. 4990–4996, cited By 2. doi:10.1016/j.egypro.2017.03.998.
URL https://www.scopus.com/inward/record.uri?eid=2-s2.0-85020726505&doi=10.1016%2fj.egypro.2017.03.998&partnerID=40&md5=6728ab24d1dd3e13d64e30d38c3ff161

[Sc27] V. Novotny, M. Vitvarova, M. Kolovratnik, Z. Hrdina, Minimizing the energy and economic penalty of ccs power plants through waste heat recovery systems, Vol. 108, 2017, pp. 10–17, cited By 9. doi:10.1016/j.egypro.2016.12.184.
URL https://www.scopus.com/inward/record.uri?eid=2-s2.0-85016107852&doi=10.1016%2fj.egypro.2016.12.184&partnerID=40&md5=df9a55db5ebca5022c649483fe341f81

[Sc28] M. Son, V. Novotny, H. Choi, Thin-film nanocomposite membrane with vertically embedded carbon nanotube for forward osmosis, Desalination and Water Treatment 57 (55) (2016) 26670–26679, cited By 10.

doi:10.1080/19443994.2016.1190110.
URL https://www.scopus.com/inward/record.uri?eid=2-s2.0-84975259873&doi=10.1080%2f19443994.2016.1190110&partnerID=40&md5=24a75518abd6d0485679e95416648950

[Sc29] V. Novotny, M. Kolovratnik, M. Vitvarova, J. Jakobsen, Analysis and design of novel absorption power cycle plants, Vol. 1, 2016, cited By 6. doi:10.1115/ES2016-59272.
URL https://www.scopus.com/inward/record.uri?eid=2-s2.0-85002397930&doi=10.1115%2fES2016-59272&partnerID=40&md5=d8697d3a26137ae6f2bdfe252c699074

[Sc30] L. Vesely, V. Dostal, O. Bartos, V. Novotny, Pinch point analysis of heat exchangers for supercritical carbon dioxide with gaseous admixtures in ccs systems, Vol. 86, 2016, pp. 489–499, cited By 27. doi:10.1016/j.egypro.2016.01.050.
URL https://www.scopus.com/inward/record.uri?eid=2-s2.0-84971278232&doi=10.1016%2fj.egypro.2016.01.050&partnerID=40&md5=7d835b50b863872558d7390b6b624db9

[Sc31] V. Novotny, J. Mascuch, Model of small family house with micro cogeneration unit [model maleho rodinneho domu s mikrokogeneracni jednotkou], Vytapeni, Vetrani, Instalace 25 (1) (2016) 12–17, cited By 2.
URL https://www.scopus.com/inward/record.uri?eid=2-s2.0-84957620809&partnerID=40&md5=3aaae2407477a6d5d59eca152519e1cf

[Sc32] V. Novotny, M. Vitvarova, Effect of different configurations of physical solvent based acid gas removal and CO2 capture for IGCC CCS power plants, in: M. Vesely, Z. Hrdlicka, J. Hanika, J. Lubojacky (Eds.), 4th International Conference on Chemical Technology, Mikulov, Czech Republic, CZECH SOC INDUSTRIAL CHEMISTRY, Mikulov, CZECH REPUBLIC, 2016, pp. 308–314.

[Sc33] L. Vesely, G. Skaugen, M. Vitvarova, S. Roussanaly, V. Novotny, Case study of transport options for co2 from igcc coal power plant in the czech republic for storage, in: M. Vesely, Z. Hrdlicka, J. Hanika, J. Lubojacky (Eds.), PROCEEDINGS OF THE 4TH INTERNATIONAL CONFERENCE ON CHEMICAL TECHNOLOGY, 1ST EDITION, CZECH SOC INDUSTRIAL CHEMISTRY, Mikulov, CZECH REPUBLIC, 2016, pp. 315–320.